Thomas C. Taucher

INVESTIGATION OF COLLECTIVE ELECTROSTATIC EFFECTS AND THEIR IMPACT ON PHYSICAL OBSERVABLES OF METAL-ORGANIC SYSTEMS

DISSERTATION

to achieve the university degree of
Doktor der Naturwissenschaften

submitted to
GRAZ UNIVERSITY OF TECHNOLOGY

SUPERVISOR:
Ao.Univ.-Prof. Dipl.-Ing. Dr.techn. Egbert Zojer

Institute of Solid State Physics

Graz, June 2021

AFFIDAVIT

I declare that I have authored this thesis independently, that I have not used other than the declared sources/resources, and that I have explicitly indicated all material which has been quoted either literally or by content from the sources used. The text document uploaded to TUGRAZonline is identical to the present dissertation.

Date

Signature

EIDESSTATTLICHE ERKLÄRUNG

Ich erkläre an Eides statt, dass ich die vorliegende Arbeit selbstständig verfasst, andere als die angegebenen Quellen/Hilfsmittel nicht benutzt, und die den benutzten Quellen wörtlich und inhaltlich entnommenen Stellen als solche kenntlich gemacht habe. Das in TUGRAZonline hochgeladene Textdokument ist mit der vorliegenden Dissertation identisch.

Datum

Unterschrift

ABSTRACT

Computational modeling is a major cornerstone in the highly active field of materials physics. Being able to reliably model systems quantum mechanically from first principles gives rise to novel possibilities for investigating material properties. Some of the most successful and widely used approaches in condensed matter physics are based on ab-initio density functional theory, which is also used in the field of organic electronics, photovoltaics and battery systems. Experimentally, X-ray photoelectron spectroscopy plays an important role in the investigation of the chemical composition and electronic structure of nano materials and surfaces. Here, ab-initio simulations provide crucial support for the interpretation of complex spectra and are able to produce additional insights concerning the expected properties of hybrid inorganic-organic systems without the need to synthesize them first.

In the first part of this thesis, the applicability of slab-type density functional theory-based band structure calculations to model X-ray photoelectron spectra using the final state approach is investigated. When simulating core-hole excitations in hybrid inorganic-organic systems the calculations can be flawed by introducing spurious collective electrostatic effects due to the applied periodic boundary conditions utilized by the computational methodology.

In the second part of this thesis, the potential of X-ray photoelectron spectroscopy measurements for determining interface dipoles of organic self-assembled monolayers on metal substrates is investigated. It is shown that for densely packed monolayers the interface dipole can be directly assessed via the shifts of the X-ray photoelectron specta. Furthermore, these shifts also directly correlate with the adsorption-induced work function change in the absence of polar tail groups in the adsorbate molecules.

In the third part of this thesis, the impact of the aforementioned collective electrostatic effects is investigated within the realms of molecular electronics by assessing the applicability of a single level model to determine the transition voltage. For this, different molecular junctions, comprised of molecular clusters of varying size and molecules arranged in an orderly fashion with different coverages are investigated. The transition voltage can be acquired by means of a Fowler–Nordheim-like plot utilizing the current-voltage characteristics as long as collective electrostatic effects do not shift the energetic level alignment in such a way that Fermi level pinning occurs.

Finally, a brief outlook is given of how collective electrostatic effects could be used to create novel quantum structures in molecular electronics.

ZUSAMMENFASSUNG

Im hochaktuellen Forschungsgebiet der Materialphysik spielen Computersimulationen eine fundamentale Rolle. Mit Hilfe von quantenmechanischen ab-initio Simulationen können auch komplexe Materialeigenschaften berechnet werden. Einige der vielseitigsten und erfolgreichsten Methoden für die Modellierung von organisch-anorganischen Nanomaterialien, die auch in der organischen Elektronik, Photovoltaik und Batterietechnik Anwendung finden können, beruhen auf der Dichtefunktionaltheorie (DFT). Bei der experimentiellen Untersuchung der chemischen Zusammensetzung sowie der elektronischen Struktur von Nanomaterialien spielt die Röntgenphotoelektronenspektroskopie (XPS) eine besondere Rolle. Für die Interpretation von komplexen Röntgenphotoelektronenspektren (XP-Spektren) leisten Simulationen einen nicht zu unterschätzenden Beitrag und sind darüber hinaus in der Lage, experimentiell nicht zugängliche Größen zu bestimmen, sowie Aussagen über Eigenschaften von Materialien noch vor deren Synthese zu treffen.

In der vorliegenden Arbeit wird im ersten Teil die Anwendbarkeit der sogenannten *final-state* Methode untersucht, welche bei der Berechnung der Anregungsenergie quantenmechanische Relaxationseffekte und Abschirmeffekte berücksichtigt. Diese nutzt Bandstrukturberechnungen als Grundlage um XP-Spektren zu simulieren. Es wird gezeigt, dass diese Methode falsche Ergebnisse liefern kann, weil der simulationstechnische Ansatz eine künstliche und unphysikalische Schicht von dicht gepackten Dipolen an der Grenzfläche erzeugen kann, welche die simulierten Elektronenbindungsenergien stark verfälscht.

Im zweiten Teil wird mittels DFT-Simulationen untersucht, inwieweit sich XPS dazu eignet, den Dipol an der Grenzfläche zwischen Metallsubstrat und organischem Adsorbat zu bestimmen. Für den Fall einer dicht gepackten Monolage korreliert die Verschiebung des XP-Spektrums direkt mit der Größe des Grenzflächendipols. Überdies hängt auch die Änderung der Austrittsarbeit auf Grund der Adsorption einer Monolage direkt mit der Verschiebung des Spektrums zusammen, solange die adsorbierten Moleküle ihrerseits keine polaren Gruppen enthalten.

Der dritte Teil der Dissertation befasst sich mit dem Einfluss kollektiver elektrostatischer Effekte auf die Transporteigenschaften in der organischen Elektronik mit Fokus auf die sogenannte Übergangsspannung. Dafür werden die Strom-Spannungs Kennlinien molekularer elektronischer Systeme untersucht, wobei sowohl einzelne organische Moleküle zwischen zwei Metallelektroden, als auch verschieden große Cluster und selbstassemblierte Monolagen diskutiert werden. Abschließend wird ein kurzer Ausblick gegeben, wie kollektive elektrostatische Effekte genutzt werden können, um neuartige Quantenstrukturen in der molekularen Elektronik zu realisieren.

PREFACE

This Thesis is compiled as a semi-cumulative PhD thesis and as such includes both peer-reviewed papers I contributed to and additional work not yet published.

First, an introduction providing an overview of the highly active field of materials physics with special emphasis on hybrid inorganic-organic systems and organic electronics is given to put the investigated topics into perspective. Additionally, the work is motivated and a summary of the current advancements in the field is given. The introductory chapter is followed by discussing the theoretical basics of density functional theory, non-equilibrium Greens function technique and collective electrostatic effects. Furthermore, the applied computational implementations including concepts concerning the modeling of interfaces are explained. In the results section the projects pursuit during my PhD study are presented, including the papers I wrote as a verbatim copy, as well as an additional chapter investigating the impact of spurious collective electrostatic effects when simulating real-world systems. The last part consists of an investigation of the impact of collective electrostatic effects in the realms of molecular electronics not yet published in a peer-reviewed journal. Finally, an outlook and concluding remarks are given alongside a summary of the work.

As scientific work is done mostly collaboratively, before each included paper my contribution is specified in detail. Additionally, each publication is put in context within this thesis.

ACKNOWLEDGMENTS

I want to express my deepest gratitude to everyone who supported me throughout my studies. Such an endeavor builds on the help and support of others.

First of all, I want to thank my supervisor *Egbert Zojer*. Your patient support, outstanding supervision and constructive criticism has been crucial to my success. I benefited a lot from your experience, knowledge and advice during the course of my thesis. Thank you for having me as part of such an unrivaled group.

Furthermore, I want to thank *Oliver T. Hofmann* for fruitful discussions mentioning the occasional counter-argument, as well as all former and current members of the Advanced Materials Modeling Team at TU Graz, with special emphasis on the *EgbertInnen*. Thank you for always being helpful, encouraging and for all the conversations about any (more or less scholarly) topic coming to our minds. Enjoying your company pre-COVID-19 at the office, during lunch and the occasional coffee break made working even more fun.

I would like to thank *Reinhard J. Maurer* from the University of Warwick for hosting me during my research stay and inviting me to the Surface Science Workshop about Structure and Spectroscopy of Hybrid Metal-Organic Interfaces. It was a pleasure giving a talk and discussing with you and your group members.

Moreover, I would like to thank *Nick R. Papior* from the Technical University of Denmark (then at ICN2 in Barcelona) for allowing me to be part of a workshop within the Open Knowledge Program about TBtrans and TranSiesta: Non-equilibrium Green Functions - from Tight-Binding to Self-Consistency.

For providing computational resources and technical support I would like to thank the teams at the VSC Research Center and at the Information Technology Solutions of TU Wien who jointly operate the Vienna Scientific Cluster 3, where most of the simulations for this thesis were done.

Financial support by the Austrian Science Fund (FWF) is gratefully acknowledged for projects P28051-N36, P24666-N20 and I937-N19.

Finally, I am deeply grateful for the unconditional support of my friends and family. Many thanks to my parents, you have always encouraged me in my decisions and supported me along my way.

CONTENTS

Part I

Fundamental aspects

1

INTRODUCTION AND MOTIVATION

Modern materials science cannot be imagined without computational physics any more. There is a variety of methods for investigating material properties at different time and length scales, starting at a macroscopic description, going down to a microscopic scale and finally arriving at an atomistic picture.[1] The investigations done in this work are conducted using an atomistic description of the systems of interest. One of the most successful and widely used method for investigating material properties quantum-mechanically at an atomistic length scale, based on an ab-initio description, is density functional theory (DFT). This is mainly due to its advantageous compromise between accuracy and efficiency.[2] It not only helps interpreting experimental data, but is also used as a powerful tool to gain additional insights not accessible via experimental measurements. Furthermore, due to the ever increasing computational power available, the design of completely new materials with specific properties suited for all kind of applications by means of high throughput studies is possible utilizing DFT.[3] Density functional theory also proofed to be able to predict new materials, which were later confirmed experimentally, e. g., in the highly interesting field of renewable energy materials.[4, 5] The fields in which it is used for investigating materials are remarkably diverse and range from superconductors over batteries to (organic) photovoltaic and (opto)electronic devices.

As the characteristics of organic (opto)electronic devices are mainly dominated by the interfaces between their constituents, describing such interfaces correctly is highly relevant.[6, 7] Organic semiconductors are a research topic of high interest, due to being widely used for vastly different applications, ranging from thin-film transistors [8, 9] (whose interface consists of organic semiconductors (OSCs) and dielectrics) to multi-layer stacks in organic light emitting diodes (OLEDs) [10, 11] and (hybrid) solar cells [12, 13]. But not only the interfaces in the heart of such devices are of crucial importance, also the interfaces to the electrodes connecting the outside circuitry are of utmost importance. These usually comprise a metal-organic interface. This has triggered widespread investigations of hybrid inorganic-organic systems (HIOSs) as these lie at the foundation of organic electronics.[6, 14] The crucial parameters of an interface in an electronic device are the energy level alignment between the electronic states in the materials the interface is comprised of.[6, 15] In hybrid organic-inorganic devices one key parameter is the work function of the electrodes. The possibility to modify the work function by self-assembled monolayers (SAMs) has been a highly investigated research topic since the work of Campbell *et al.* [16, 17] back in 1996.[18–33] The electronic properties of metal substrates are impacted by such SAMs via dipolar layers which occur, e. g., due to bond dipoles at the metal-substrate interfaces or due to polar groups, either embedded in the molecules or as tail group substituents of the adsorbate layer.[21, 26, 28, 32, 34–43]

These adsorbate layers are routinely investigated by X-ray photoelectron spectroscopy (XPS), which is an invaluable tool to study and characterize all kind of surfaces.[44–48] It provides qualitative and quantitative information about the composition of the surface by probing the core-level binding energies. Furthermore, the chemical neighborhood of the excited core-level can be deduced from the shift of the measured binding energy.[49–52] For interpreting complex experimental spectra as well as for being able to computationally model them, a fundamental understanding and a constant development and improvement of the computational methods available for simulating such experiments is of utmost importance.[48, 52–55] Up to know, different approaches have been proposed, also based on highly sophisticated methods like GW, which are able to acquire even absolute values for core-level binding energies.[54, 56] Unfortunately, these are computationally not feasible for the systems we are interested in.

Therefore, the quantum-mechanical modeling of relative core-level shifts within the framework of DFT is investigated and comprises a major part of this theses. To be precise, I examined the advantages and caveats of modeling core-level binding energies within the final-state approximation [57, 58] for extended surfaces by applying periodic boundary conditions.[59] When utilizing this approach one must be aware of possible artifacts due to spurious collective electrostatic effects, which are explained in great detail in Chapter 4.4.

Furthermore, the potential of XPS for determining interface dipoles between a metal substrate and an organic, self-assembled monolayer is explored in Chapter 5. The X-ray photoelectron spectrum is shifted by collective electrostatic effects, which occur right at the interface due to the densely packed adsorbate layer and, therefore, correlate with the interface dipole.[60]

As these collective electrostatic effects have an impact on the position of the electronic levels, they also play a role in molecular electronics. In Chapter 6 the role of the transition voltage [61, 62] and its relation to the intrinsic electronic properties of molecular and monolayer junctions is investigated with a special focus on how they are influenced by said collective electrostatic effects. Thereafter, a brief outlook is given in Chapter 6.7 how collective electrostatic effects could be utilized in molecular electronics to create novel quantum structures.

Finally, at the end of this thesis in Chapter 7, concluding remarks are formulated for the presented work.

2

THEORETICAL BASICS AND COMPUTATIONAL METHODS

In this chapter a brief introduction to the theoretical methods and computational approaches applied in this work is given. First, the Schrödinger equation will be discussed, which forms the basis for doing quantum-mechanical calculations. Subsequently, the main ideas of density functional theory (DFT) are explained. Nowadays, this is the most successful, and, thus, most widely used, computational approach for electronic structure calculations in condensed matter physics and is used throughout this work. Furthermore, the basic principles of the non-equilibrium Greens function technique are presented as it is used for the transport calculations done in Chapter 6. Finally, the used software packages and the concept utilized for the computational modeling of the systems investigated are discussed.

For the sections dealing with fundamental aspects the following books served as reference: [2, 63, 64].

2.1 THE SCHRÖDINGER EQUATION

As the Schrödinger equation builds a fundamental part of the foundation of modern physics, solving it analytically for an arbitrary system has been a challenge of great interest ever since. But up to today, calculating the solution analytically is only possible for a number of limited systems. If dealing with systems as they occur in *real world*-problems, one is still limited to various numerical approximations to solve the Schrödinger equation, which in its most general form is given as:

$$i\hbar\frac{\partial}{\partial t}\psi(\mathbf{r},t) = \hat{H}\psi(\mathbf{r},t), \tag{1}$$

where $\hbar$ is the reduced Planck constant, ψ denotes the time-dependent wave function and $\hat{H}$ the Hamiltonian. Written in its time-independent form using the bra-ket notation it is probably the most widely known formula in modern physics:

$$\hat{H}|\psi\rangle = E|\psi\rangle. \tag{2}$$

In this eigenvalue equation, $|\psi\rangle$ denotes an eigenstate of $\hat{H}$ and E represents its eigenvalue. In solid state physics and quantum chemistry one would like to solve the non-relativistic, time-independent Schrödinger equation

$$\hat{H}\psi(\mathbf{r}_1,\ldots,\mathbf{r}_n,\mathbf{R}_1,\ldots,\mathbf{R}_M) = E\psi(\mathbf{r}_1,\ldots,\mathbf{r}_n,\mathbf{R}_1,\ldots,\mathbf{R}_M) \tag{3}$$

for the many-electron wave function ψ. Here $\hat{H}$ denotes the Hamiltonian for a molecular system in the absence of a magnetic field containing M nuclei and n electrons, and $\mathbf{r}_i$ and $\mathbf{R}_I$ are the positions of the electrons and nuclei, respectively. Already back in 1927 Born and Oppenheimer developed an approximation [65] in which they suggested to separate the nuclear and electronic part of the wave function

$$\psi_{total} = \psi_{electrons} \cdot \psi_{nuclei} \,. \tag{4}$$

This can be justified due to the nucleus having a mass around 2000 times bigger in comparison to an electron, which allows to describe the latter moving in a fixed potential of the former without practically influencing it. Keeping this in mind, we can rewrite the Schrödinger equation to describe the time-independent, many-electron problem as follows:

$$\begin{aligned} \hat{H}\psi = \left[\hat{V} + \hat{T} + \hat{U}\right]\psi = \left[\sum_i^N V(\mathbf{r}_i) + \sum_i^N -\frac{\hbar^2}{2m}\nabla_i^2 + \sum_{i<j}^N U(\mathbf{r}_i, \mathbf{r}_j)\right]\psi \\ = E\psi, \end{aligned} \tag{5}$$

where $\hat{V}$ denotes an external (time independent) potential, which the electrons experience, $\hat{T}$ describes their kinetic energy and $\hat{U}$ the electron-electron interaction. This gives the total energy of the system, denoted by E. As one can see, it introduces $3N$ variables per particle (even only considering the three spatial coordinates and neglecting, e. g., the N spin coordinates of each electron). Taking into account that interesting physical problems deal with systems containing $N = \mathcal{O}(10^{24})$ particles, one can grasp easily that this is not a simple *pen and paper*-problem. As a matter of fact, this equation is still not solvable in practice, due to its extremely large number of variables. To conquer this challenge, there exist nowadays two widely used, but contrary approaches, namely wave function based methods and density functional theory (DFT). In the next sections DFT will be discussed in more detail, as it was used for all band structure calculations done in this work.

2.2 DENSITY FUNCTIONAL THEORY

Arguably, the most important method for modeling materials is density functional theory (DFT). It is a quantum mechanical modeling method, using a first-principles approach to calculate the quantities of interest. It is nowadays the most widely used method in physics and chemistry to investigate the electronic structure of complex many-body systems.[66–68] In solid state physics it is the de facto standard approach to describe ground state properties of metals, semiconductors and insulators. Yet the success of DFT nowadays not only encompasses bulk materials, but also complex (organic) structures such as proteins and carbon nanotubes.[69–72] Furthermore, it was successfully used to predict new materials which were subsequently confirmed experimentally.[4, 5] Building on this, an important next step to advance materials design is the possibility to use collaborative ab-initio databases.[73–75]

The main idea behind DFT is to describe an interacting system of fermions via its electron density instead of its many-body wave function. This means, for N electrons in a solid, which obey the Pauli exclusion principle [76] and interact with each other via the Coulomb potential, the system depends only on the three spatial coordinates rather than on $3N$ degrees of freedom. As a consequence, it would generally be possible to solve a given problem in an exact manner if the analytical form of the exchange-correlation (XC) functional would be known (vide infra).

2.2.1 *Hohenberg-Kohn theorem*

One of the fundamental ideas DFT relies on is the fact that it is possible to reformulate the energy of an atomic system as a functional of its ground state electron density instead of its electron wave function. This goes back to the seminal work of Pierre Hohenberg and Walter Kohn in 1964 [77], who built on the concept introduced by Llewellyn Thomas [78] and Enrico Fermi [79] known as the Thomas-Fermi model. The first Hohenberg-Kohn theorem asserts that there exists *one unique mapping* between the ground-state electron density of a system and its ground-state wave function.

THEOREM 1. The ground state energy of a system of interacting electrons is a unique functional of the electron density.[77]

This is expressed mathematically in Equation (6) and means that the ground-state electron density n_0 determines all ground-state properties of a system, which are described by its wave function ψ_0.

$$\psi_0(\mathbf{r}_1, \ldots, \mathbf{r}_N) \leftrightarrow n_0(\mathbf{r}) \tag{6}$$

As stated in Theorem 1, the ground-state electron density $n_0(\mathbf{r})$ is a functional of the ground-state wave function $\psi_0(\mathbf{r}_1, \ldots, \mathbf{r}_N)$:

$$n_0(\mathbf{r}) = n_0[\psi_0(\mathbf{r}_1, \ldots, \mathbf{r}_N)] \tag{7}$$

As a consequence, changing the external potential $\hat{V}$ in Equation (5) means changing the wave function of the system, and, subsequently, the electron density $n_0(\mathbf{r})$. Furthermore, the ground state energy E_0 is also a functional of the ground-state wave function:

$$E_0(\mathbf{r}) = E_0[\psi_0(\mathbf{r}_1, \ldots, \mathbf{r}_N)] = \langle\psi_0|\, \hat{H}\, |\psi_0\rangle \tag{8}$$

This means, we can calculate the ground-state energy with only three variables instead of $3N$.

The second theorem by Hohenberg and Kohn states that there exists a variational principle for the above mentioned energy density functional $E[n_0(\mathbf{r})]$, namely:

THEOREM 2. The electron density that minimizes the energy of the overall functional is the true ground-state electron density.

$$\left.\frac{\delta E[n(\mathbf{r})]}{\delta n}\right|_{n=n_0} = 0 \qquad s.t. \quad \int d^3r\, n(r) = N \tag{9}$$

This variational problem can be solved using the so-called Ritz method [80] to finally get the ground-state electron density and, more importantly, the ground-state energy.

For actual calculations, the total ground-state energy can be written as

$$E[n(\mathbf{r})] = V[n(\mathbf{r})] + T[n(\mathbf{r})] + U[n(\mathbf{r})], \tag{10}$$

but is not known analytically; only the external potential can be expressed as

$$V[n(\mathbf{r})] = \int d\mathbf{r}\; v(\mathbf{r})\, n(\mathbf{r}), \tag{11}$$

whereas the kinetic part $T[n_0]$ and the interaction part $U[n_0]$ cannot be determined exactly for an interacting system, yet. Finding analyitcal forms of these two functionals would mean solving any DFT-problem exactly.

2.2.2 *Kohn-Sham equation*

Walter Kohn and Lu Jeu Sham tackled the problem of not knowing the exact form of the functionals and suggested to split the problem into exact, non-interacting terms for the kinetic and interaction functionals, and putting everything that is not known analytically into the *exchange-correlation* functional E_{XC}. They used the standard kinetic energy operator for a Slater-determent basis for the kinetic part $T[n(\mathbf{r})]$, i. e., the kinetic energy as if dealing with non-interacting particles. Furthermore, they split the interaction part $U[n(\mathbf{r})]$ up into a known part, derived from the Hartree-Fock approach (representing the exact local Coulomb interaction) and into an unknown, which is accounted for in the aforementioned exchange-correlation functionall E_{XC}. This results in Equation (12) for the kinetic part, where also the unknown exchange-correlation functional is added, and Equation (13) for the interaction part.

$$U[n(\mathbf{r})] = \frac{e^2}{2} \int d^3r \int d^3r' \, \frac{n(\mathbf{r})\, n(\mathbf{r}')}{|\mathbf{r} - \mathbf{r}'|} + E_{XC}[n(\mathbf{r})] \tag{12}$$

$$T[n(\mathbf{r})] = \sum_{i}^{N} \int d^3r\, \psi_i^*(\mathbf{r}) \left(-\frac{\hbar^2}{2m}\nabla^2 \right) \psi_i(\mathbf{r}) \tag{13}$$

Equation (13) expresses the kinetic term for *non-interacting* particles, where $\psi_i(\mathbf{r})$ and $\psi_i^*(\mathbf{r})$ represent the atomic orbitals which create the wave-function by a Slater-determinant and it is summed over all N particles. Using Slater-determinants ensures that the wave-function is anti-symmetric [81] and, hence, the Pauli exclusion principle [76] is obeyed. This approach can be used, because as stated above, everything that goes beyond the Hartree-Fock model is already included in the exchange-correlation functional E_{XC} in Equation (12). To finally arrive at the Kohn-Sham equation, one has to use Lagrange multipliers for the variational Ansatz, which yields

$$\epsilon_i\psi_i(\mathbf{r}) = \left[-\frac{\hbar^2}{2m}\nabla_i^2 + v(\mathbf{r}) + e^2 \int d^3r' \,\frac{n(\mathbf{r})\, n(\mathbf{r}')}{|\mathbf{r}-\mathbf{r}'|} + \frac{\delta E_{XC}[n(\mathbf{r})]}{\delta n(\mathbf{r})} \right] \psi_i(\mathbf{r}) \tag{14}$$

for equation (10). With this it is in principal possible - if the E_{XC} would be known - to exactly solve our problem by calculating the ground-state electron density and, subsequently, the ground-state energy, as stated in Theorem 1. This has to be done in a self-consistent manner, meaning that the Kohn-Sham equation is solved iteratively starting with an educated guess for the initial electron density $n(\mathbf{r})$. Knowing the Kohn-Sham orbitals allows then to calculate a new electron density by summing over the occupied orbitals via

$$n(\mathbf{r}) = \sum_{i}^{occ} \|\psi_i(\mathbf{r})\|^2. \tag{15}$$

This cycle has to be repeated until convergence is reached and the true ground-state electron density is found as stated in Theorem 2. As mentioned above, the exact solution can only be found in theory, because the analytical expression for the exchange-correlation functional E_{XC} is not known, meaning that only an approximate solution can be obtained.

2.2.3 *The exchange-correlation functional*

Finding the most universal expression for the exchange-correlation (XC)-functional, E_{XC}, is one of the major challenges in DFT and nowadays there exist several different approaches to tackle this obstacle. The most widely used approaches are the local density approximation (LDA) [82, 83] and the semi-local general gradient approximation (GGA) [84], whereas the latter builds on the former and additionally includes the gradient of the electron density to yield more accurate results. A comparison of different functionals covering the range from LDA to GGA-based functionals can be found in the work of Ziesche et al.[85]. For this thesis the widely used and highly successful Perdew-Burke-Ernzerhof (PBE)-functional [86, 87] was employed, which is a GGA based functional. On the next step up on Jacob's ladder [88] are the so-called hybrid functionals, introduced by Becke [89] in 1993, which include a portion of exact exchange from Hartree–Fock theory. These, in a lot of cases semi-empirical, hybrid functionals can improve the calculated properties like bond lengths and atomization energies, as well as vibrational frequencies compared to pure ab-initio functionals.[90] Quite recently, (optimally tuned) screened range-separated hybrid functionals have been introduced, which seem to have overcome the traditional problem of DFT-calculations of underestimating the fundamental gap and describe charge-transfer more accurately, and, therefore, are of great interest for the calculations of, e. g., (organic) semiconductors.[91–95] Since the dawn of density functional theory a wide variety of functionals has been developed and the quest for a universal density functional is still an ongoing endeavor.[96, 97]

Unfortunately, the additional computational costs that come with these more sophisticated hybrid functionals still prevents them from being used routinely nowadays, especially for problems which are tackled accurately enough using GGA-based functionals like PBE.

2.2.4 *Long range van der Waals forces*

Van der Waals (vdW) forces are crucial for the stability, the geometric structure and the function of a wide range of molecules, clusters, and materials in general.[98–100] Furthermore, they are of utmost importance for the correct description of (physisorbed) molecules on surfaces, as without considering these long-range vdW-interactions, semi-local functionals will often predict no bonding at all.[101] Unfortunately, these vdW-forces need to be considered explicitly to correctly describe the physics of an interface when modeling them within DFT.[101–104] This is due to DFT-calculations applying mostly local and semi-local exchange-correlation functionals, e. g., LDA- and GGA-based functionals, respectively, where these long range dispersion forces are not considered inherently by the standard approximations. For a correct description by the exchange-correlation functional an overlap of the electron densities is required, which is mostly not the case for dispersion forces due to their non-local nature. There have been several dispersion correction schemes developed.[101] One of the most basic approaches includes the dispersion energy by adding so-called C_6/r^{-6} pairwise interaction terms to the total energy of the system in a non self-consistent manner. This energy correction term is commonly written as

$$E_{vdW} = -\frac{1}{2}\sum_{A,B} f_{\text{damp}}(r_{AB}, r_A, r_B) C_6^{A,B} r_{A,B}^{-6}, \tag{16}$$

where f_{damp} is a short range damping function to prevent the overall term from diverging for small distances, r_{AB} is the distance between atom A and B, r_A and r_B is the vdW-radius of atom A and B, respectively, and $C_6^{A,B}$ denotes the corresponding C_6 coefficient. This C_6 correction can be improved by including higher order terms or adjusting the C_6 terms depending on the atomic environment.[105–107] More sophisticated methods which go beyond a pairwise interaction correction have also been developed, i. a., many-body dispersion (MBD) [108, 109], non-local functionals [110, 111], or approaches based on the fluctuation dissipation theorem (FDT) [112].

For the simulations done in the course of this thesis, long range vdW-forces were considered by utilizing the Tkatchenko-Scheffler dispersion correction scheme vdW-TS [106] whose C_6 coefficients and vdW-radii are based on the ground state charge density and are, therefore, environment-dependent. The vdW-TS scheme was applied via the so-called $\mathrm{vdW}^{\mathrm{Surf}}$ [113] modification in the implementation of Al-Saidi *et al.*[114], which is specifically designed for the investigation of adsorbates on surfaces by including Coulomb screening via the Lifshitz-Zaremba-Kohn theory.[115, 116]

2.3 GREENS FUNCTION TECHNIQUE

For investigating transport phenomena at the nanoscale, DFT can be combined with the non-equilibrium Greens function technique (NEGF) in conjunction with the Landauer approach.

2.3.1 *Landauer approach*

The Landauer approach [117], which was first introduced in 1957, can be used to study ballistic transport. In his work, Landauer showed that at length scales where the wave nature of an electron cannot be ignored, i. e., when quantum effects dominate the transport, *conductance is transmission*. This means, to find the total conductance one has to solve the Schrödinger equation to get the current-carrying eigenmodes, calculate their transmission values, and, finally, sum up their contributions. Mathematically speaking, this results in the following equation for the total conductance:

$$G = \frac{2e^2}{h} \sum_{n=1}^{N} T_n \,, \tag{17}$$

where the summation is performed over all N available conduction modes and T_n denotes their individual transmissions. If the transmission of a mode is perfect, it contributes exactly one quantum unit of conductance, $G_0 = 2e^2/h \approx (12.9k\Omega)^{-1}$.

Furthermore, the total current between two leads with different chemical potentials, μ_L and μ_R, is given by the so-called Landauer equation

$$I(V) = \frac{2e}{h}\int_{-\infty}^{\infty} dE\, T(E)[f(E-\mu_L) - f(E-\mu_R)]\,, \tag{18}$$

where the factor 2 accounts for the spin degeneracy that usually exists, $f(E-\mu)$ is the Fermi function of the electron reservoirs of the left and right electrodes, and $T(E)$ is the transmission probability. This instructively shows the relation between current and transmission at nanoscales. At zero temperature, the Fermi function on the left, $f_L(E)$, and right, $f_R(E)$, side are step functions both equal to 1 below $E_F + eV/2$ and $E_F - eV/2$, respectively, and $f_L(E) = f_R(E) = 0$ above this energy.

The aforementioned approach is quite successful in explaining basic transport phenomena at small scales. Due to the fact that this is a one-electron theory, it is only valid as long as inelastic scattering can be neglected, though. This means, it is assumed that the electron propagation is a fully quantum coherent process over the entire sample. Such a description is only valid at zero temperature, as noted above, and, furthermore, assumes that the energy of the electrons in the electrodes is equal to the Fermi energy. At finite bias, the coherent propagation may be limited by inelastic scattering processes due to electron-phonon and electron-electron collisions. A more adequate model to describe the transport in such situations where inelastic interactions cannot be neglected requires, e. g., Greens function techniques, which will be discussed in section 2.3.2.

Quite recently, Maassen and Lundstrom[118] showed that this formalism can also be applied to diffuse transport regimes and provides a common language for electron and phonon transport.

2.3.2 *Non-equilibrium Greens function technique*

For obtaining the transmission function $T(E)$ the non-equilibrium Greens function technique can be used in conjunction with DFT-based methods. This approach partitions the molecular junction into semi-infinite electrodes acting as an electron reservoir and a central region consisting of the molecule and its interface to the leads (see Figure 1). The idea behind this is that now the Hamiltonian can be decomposed into the aforementioned parts.

Within this methodology, the transmission function in Equation (18) can be expressed as:

$$T(E) = \sum_k \omega_k Tr(\mathbf{G}_C^\dagger \mathbf{\Gamma}_R \mathbf{G}_C \mathbf{\Gamma}_L)\,, \tag{19}$$

where the sum is taken over all lateral k-points and weighted by ω_k, $\mathbf{G}_C$ denotes the retarded Greens function of the central region and $\mathbf{\Gamma}_{L,R} = i(\mathbf{\Sigma}_{L,R} - \mathbf{\Sigma}^\dagger_{\mathbf{L,R}})$ are

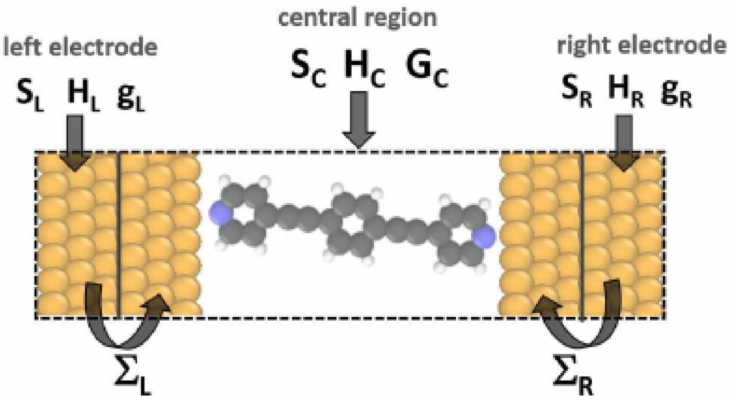

Figure 1: Partitioning of a molecular junction into semi-infinite electrodes (left and right) and a finite sized central region. The parts entering the transmission function in Equation (19) are shown accordingly. $S_{C,L,R}$ denote the overlap matrices of the central region as well as of the left and right electrode, respectively. $H_{C,L,R}$ indicate the Hamiltonian matrices of the aforementioned parts and G_C indicates the Greens function of the central region. $g_{L,R}$ denote the retarded Greens functions of the isolated semi-infinite left and right leads, respectively. $\Sigma_{L,R}$ denote the self-energies including all effects arising from the coupling between the central region and the left and right leads, respectively. Figure taken from [119]

the coupling matrices to the electrodes, with $\mathbf{\Sigma}_{L,R}$ being the self-energies of the left and right electrode, respectively.

The Greens function of the central region is constructed as:

$$\mathbf{G}_C^R = (E^+\mathbf{S}_C - \mathbf{H}_C - \mathbf{\Sigma}_L - \mathbf{\Sigma}_R)^{-1}, \tag{20}$$

where the Hamiltonian matrix $\mathbf{H}_C$ and the overlap matrix $\mathbf{S}_C$ of the central region is calculated with DFT. The self-energies $\mathbf{\Sigma}_{L,R}$ including all effects arising from the coupling between the central region and the leads are obtained independently for both electrodes using

$$\mathbf{\Sigma}_{L,R} = \boldsymbol{\tau}_{L,R}^{\dagger}\mathbf{g}_{L,R}\boldsymbol{\tau}_{L,R}\,, \tag{21}$$

where $\mathbf{g}_{L,R} = (E^+\mathbf{S}_{L,R} - \mathbf{H}_{L,R})^{-1}$ are the retarded Greens functions of the isolated semi-infinite left ($\mathbf{g}_L$) and right ($\mathbf{g}_R$) leads, i. e., the surface Greens functions of the uncoupled electrodes. $\boldsymbol{\tau}_{L,R}$ refer to the coupling of the central region to the surface Greens function corresponding to the left and right surface atoms, respectively. These can be calculated by an iterative method proposed by Sancho et al.[120] in 1985.

2.4 COMPUTATIONAL IMPLEMENTATIONS

In this chapter a brief overview of the software packages utilized for calculations presented in this work will be given. As already mentioned, the results discussed in this theses are acquired within the framework of DFT. Most of the DFT-simulations for all but Chapter 6 were done using the Fritz Haber Institute ab initio molecular simulations package (FHI-AIMS)[121–125]. Additionally, the Vienna Ab initio Simulation Package (VASP)[126–129] was used for test calculations and to double check the results computed with FHI-AIMS. Most of the electronic-structure calculations for the transport simulations were done using The Spanish Initiative for Electronic Simulations with Thousands of Atoms (SIESTA)[130, 131], and, consequently, TranSIESTA (TRANSIESTA), which is the module for modeling charge transport. The three DFT-based codes each use a different approach to represent the basis functions and treat the core and valence orbitals differently. In the next section, FHI-AIMS and SIESTA will be described in more detail, as these were mainly used in the course of this thesis.

2.4.1 *FHI-aims*

FHI-AIMS [121–125] is an all-electron, full potential code, which means that every electron in the system is considered explicitly in the calculations. This means that the full spectrum of energy levels is calculated including not only the valence, but also the core electrons. As a consequence, the computational resources needed for a given system depend on the elements it is comprised of, and, therefore, scale with the number of atoms and the number of electrons present in the system. The Kohn-Sham (KS)-eigenfunctions are constructed using a basis set of numeric atom-centered orbitals. Optimized basis sets are provided for all elements with three pre-defined default settings, namely *light*, *tight*, and *really tight*, with increasing accuracy, and, of course, increasing computational cost. In this work, the default *tight*-settings were routinely used for the calculations, as they provide accurate results at feasible computational costs. An advantage when using atom-centered orbitals is that their spatial extend can be tuned by cutting off the radial functions at larger distances. This means, they are zero beyond a certain radius, and, as a consequence, the vacuum region which is quite substantial when utilizing the repeated slab approach (cf. Chapter 2.5.1) comes at basically no additional computational cost. Another ansatz is used by, e. g., VASP, which uses plane waves and, therefore, the relevant quantity for the computational cost of a calculation is not only the number of electrons in the system, but the volume of the primitive unit cell, i. e., in this case the size of the vacuum region matters, besides the cutoff energy, of course. This needs to be considered when applying the repeated slab approach.[132]

2.4.2 *SIESTA and TranSIESTA*

The fundamental approach SIESTA[130, 131] builds on are strictly localized, pseudo-atomic orbitals as basis sets with norm-conserving pseudopotentials on a real-space grid to represent the charge density. This allows to tune the accuracy and cost of a calculation over a wide range, making it possible to quickly model systems as well as doing accurate simulations. For doing transport calculations the TranSIESTA module is used, which applies a three step process for this. First, the Hamiltonian and overlap matrices with the information needed to calculate the surface Greens function is acquired by doing a bulk calculation. The second step is to calculate the Hamiltonian, the overlap matrices, and the (energy) density matrix of the central region. Finally, the transmission is acquired using Equation (19). Quite recently, significant improvements to the TranSIESTA module have been made by introducing improved algorithms.[133] Due to technical difficulties of the version available at the time the investigations were carried out, for the work presented in Chapter 6 these new features could not be utilized. Instead, the focus of the work was shifted to a thorough analysis of the transition voltage for vastly different molecular junctions; ranging from single molecule junctions to such comprised of a full coverage organic monolayer. Consequently, the main aspect of the work presented in this thesis deals with the impact of collective electrostatic effects on the transition voltage.

Furthermore, interfaces to new solvers for the electronic structure problem have been added. This promises the possibility of being able to do even more advanced electronic structure simulations with SIESTA in the future.

2.5 CONCEPTS CONCERNING THE MODELING OF INTERFACES

One of the most important things when modeling interfaces quantum mechanically is to capture the physics correctly. This is due to the fact that it is not possible to describe a *real-world system* atom by atom, but certain choices have to be made on how to describe the system of interest quantum mechanically in a way that it is still possible to calculate it. As the systems treated in this thesis consist of highly ordered interfaces, the repeated slab approach (RSA) (see next chapter) was used in the DFT-calculations. For this, i. a., a commensurable unit cell of a suitable size has to be found.[132]

2.5.1 *The repeated slab approach*

When modeling extended systems, usually periodic boundary conditions (PBC) are applied to the commensurate unit cell. In most band-structure codes this means that the unit cell is periodically repeated in all three spatial directions. This poses a problem when the system of interest is, e. g., an interface or a surface, which can be described, in a first approximation, as two dimensional. The repeated slab

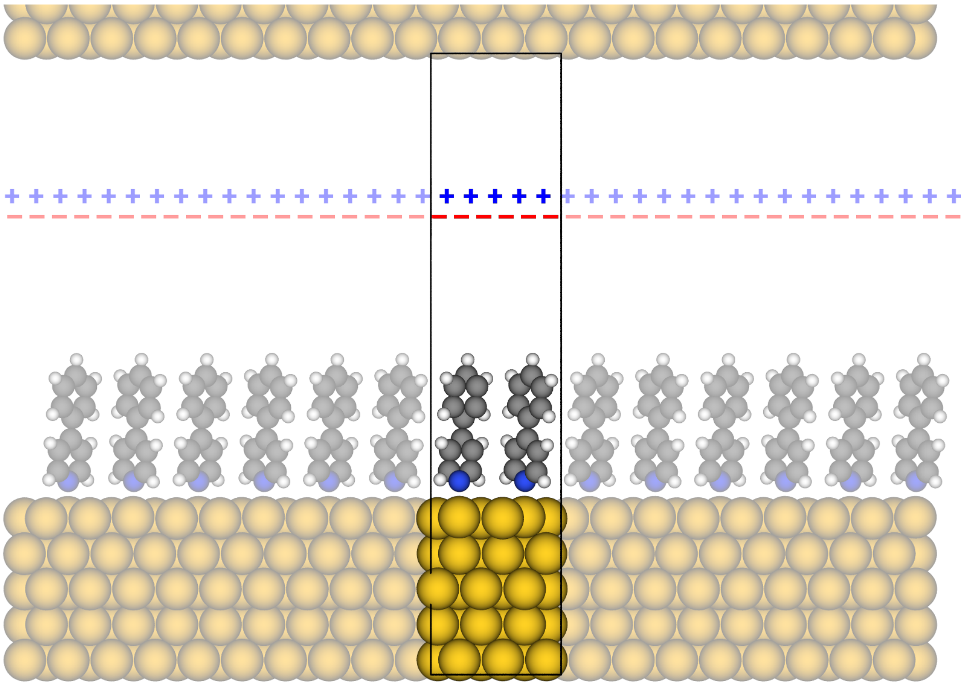

Figure 2: Schematic image of the repeated slab approach (RSA). The black box denotes the unit cell, which is repeated in all three spatial directions (visualized with desaturated replicas). The plus and minus sign indicate the dipole correction applied to decouple the system electronically in z-direction.

approach is a way of modeling such systems with PBC applied in all directions, yielding a system effectively periodic in only two directions. This is achieved by decoupling the system along the third direction. It is done in a twofold manner, namely quantum mechanically by inserting a vacuum region and electronically via an electrostatic correction. A quite extensive discussion about different approaches how to accomplish this, can be found in a paper recently published by Hofmann *et al.*[132]. The principles of the approach used for the calculations in this thesis are shown in Figure 2 for a unit cell containing two molecules which form a SAM on a metal slab.

As one can see, the gold substrate with its SAM of pyridines is quantum mechanically decoupled in the z-direction via a vacuum layer of about 25 Å. This ensures that there is no overlap of the wave functions. Furthermore, to eliminate spurious polarization effects due to the PBC in z-direction a self-consistent dipole correction [134, 135] is introduced in the vacuum region. The discontinuity in the electrostatic potential is depicted by the plus and minus signs in Figure 2. This ensures that any potential difference between the top and the bottom of the unit cell is compensated.

2.5.2 *Unit cell considerations*

As mentioned in the preceding section, when using the repeated slab approach, a suitable unit cell is needed. First of all, when applying periodic boundary conditions, a prerequisite is to have a commensurable unit cell of your system. Furthermore, the exact geometric structure of the interface needs to be determined. When dealing with hybrid inorganic-organic systems (HIOSs), the crystal structure of the metal substrate is normally known, but the geometry of the organic adsorbate needs to be optimized for every system investigated. First, the number of layers of the metal substrate has to be converged. To find the atomic geometry of the organic layer, the adsorbate is built on a first guess based on experimental measurements, chemical intuition, or, since recently, also based on geometries acquired through machine learning. Starting from there, a crucial step is to optimize the geometry of the whole system. This can be done utilizing different algorithms, in which long-range van der Waals-forces have to be considered to get reasonable results, as they are not covered by the most commonly used DFT-functionals (cf. Chapter 2.2.4). Having found the geometry for the primitive unit cell, there are still different aspects to consider when choosing the actual unit cell used for the simulations, depending on the actual calculations. Generally speaking, the smallest unit cell possible should be used, because of obvious computational reasons. But there are cases in which it is not enough to have found a commensurate unit cell, but quite large super cells need to be calculated to obtain physically correct results, as will be shown in Chapter 4.4.

3

BASIC ELECTROSTATICS AND COLLECTIVE ELECTROSTATIC EFFECTS

Collective electrostatic effects play a fundamental role in all projects investigated in this work. They arise upon adsorption of self-assembled monolayers (SAMs) due to the orderly array of bond dipoles right at the substrate-adsorbate interface, as is shown in Chapter 5 for organic adsorbates on metal substrates, and are fundamental for determining the interface dipole. As is shown in Chapter 4.4 they can also be artificially introduced by means of the computational method used, where they come into play as spurious effects due to the applied periodic boundary conditions when modeling core-level excitations in the final state approach. Furthermore, they also need to be considered in the realm of molecular electronics as is shown in Chapter 6, where their impact on the current voltage characteristics and, consequently, the transition voltage is investigated.

Even though emerging in different situations, these collective electrostatic effects are governed by the same underlying physical principles. Therefore, in this chapter a brief introduction considering collective electrostatic effects will be given. It will mostly build on the review paper by Zojer, Taucher, and Hofmann [136] published in 2019. As will be explained in the following, dipolar layers play an important role when determining the electronic structure of hybrid inorganic-organic systems (HIOSs) and their interfaces. Principally, dipolar layers can either occur due to interfacial charge rearrangements upon adsorption of an organic SAM, or when the adsorbate itself consists of polar molecules assembled in an orderly fashion.

In the next sections, first the impact of dipoles and layers thereof on the potential energy surface is explained to build the foundation for the second part, where it is discussed, how dipolar adsorbates influence the electronic structure of metal-organic interfaces.

3.1 IMPACT OF DIPOLE LAYERS

To be able to understand the impact of collective electrostatic effects as discussed in the course of this thesis, it is of vital importance to get a fundamental understanding of the effect of ordered polar layers on the electronic levels of an interface. Therefore, it is beneficial to describe the influence of isolated dipoles, ordered arrays of point dipoles, and sheets of point charges on the electrostatic energy of electrons in their vicinity.[40, 137]

In Figure 3 the electrostatic energy of an electron is plotted under the influence of different assemblies of dipoles. As can be seen in Figure 3(a), the electrostatic potential an electron feels is only disturbed right in the vicinity of a point dipole. Once the electron is farther away, the vacuum energy does not change anymore, i. e., its energy is uniquely defined in the far field. In stark contrast to this is the situation when an ordered array of dipoles is introduced. As is shown in part (b) of Figure 3, there is an abrupt jump in the potential right at the position of the infinitely extended dipole layer. This layer consists of point dipoles which are arranged in a quadratic lattice in the x-y plane, perpendicular to it. The abrupt jump in the potential is due to so-called collective electrostatic effects, also known as cooperative electrostatic effects.[35, 137–141] As a consequence, the vacuum level the electron feels differs between the left and the right side of the dipole layer. To quantify the difference of the vacuum level, the following equation, which is based on Poisson's equation, can be used:

$$\Delta VL = \frac{q_e \mu}{\epsilon_0 A} . \tag{22}$$

It states that the change of the vacuum level, ΔVL, is proportional to the dipole moment per area, μ / A, with q_e being the charge of an electron and ϵ_0 the vacuum permittivity. It should be noted that only the dipole moment perpendicular to, in this notation, the x-y plane contributes to the change of the vacuum level. When looking at an actual system consisting of a metal substrate and an adsorbate layer of polar molecules, the x- and y-components of any dipole are screened by the metal. Furthermore, the dipole per molecule in the adsorbate is different from the dipole of the isolated molecule due to depolarization effects. This depolarization can be described via an effective dielectric constant, ϵ_{eff}, which leads to the following equation [142] starting from Equation (22) and using the dipole moment of the isolated molecule μ_0:

$$\Delta VL = \frac{q_e \mu_0}{\epsilon_0 \epsilon_{eff} A} . \tag{23}$$

As can be seen in Figure 3 the potential jumps abruptly right at the layer of dipoles, and, therefore, consecutive layers of dipoles do not interfere if they are separated enough.[137, 143] As a consequence, it is possible to introduce SAMs with several polar groups which produce a step-wise potential energy surface [144] as is sketched in Figure 3(c).

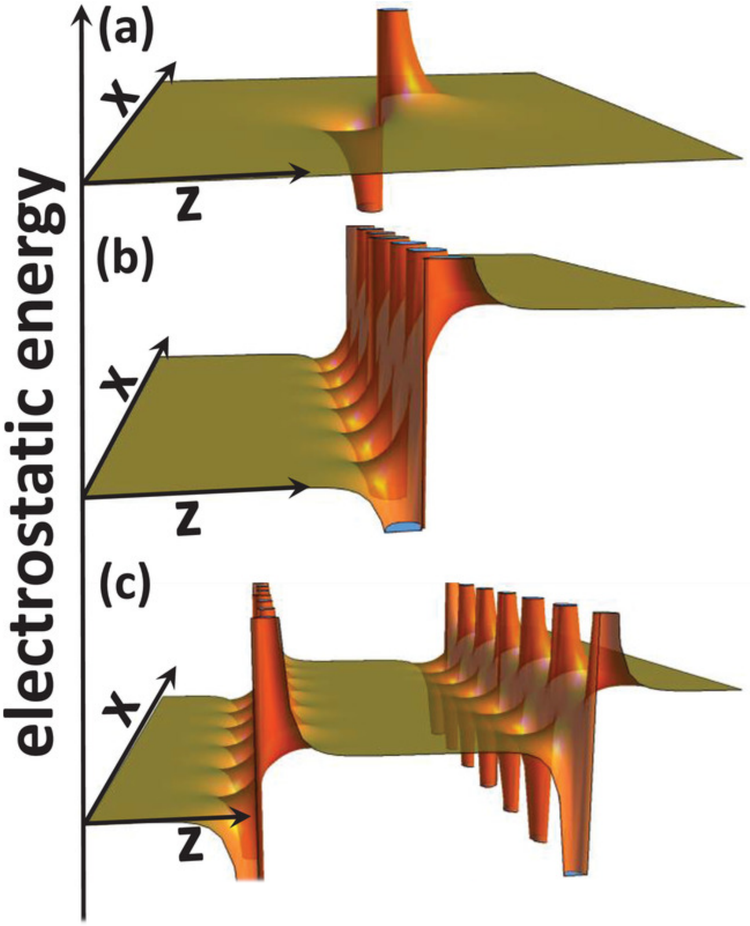

Figure 3: Electrostatic energy of an electron due to differently arranged assemblies of dipoles as follows: (a) Single dipole. (b) Infinitely extended 2D sheet of point dipoles on a quadratic grid with a lattice constant *a* in the xy-plane. The direction of the dipoles is perpendicular to the sheet. (c) Series of two infinitely extended sheets of point dipoles at a distance of *a*. The plotting range in all panels corresponds to $6a \times 6a$. A relative length scale is used, because the shape of the energy landscape is determined by the ratio between the distance from the dipole sheet and the interdipole distance. In the plot we also refrain from quantifying the changes in electrostatic energy, as these scale linearly with the magnitude of the point dipoles and point charges. Figure modified from [136].

3.2 ELECTRONIC STRUCTURE OF INTERFACES

Because the systems investigated in this thesis are almost exclusively comprised of organic adsorbates with and without polar groups placed on metal substrates, this kind of interface will be discussed in more detail in the following paragraphs.

To describe the electronic structure of such interfaces the energy level alignment of its constituents is used as shown in Figure 4. What should be noted is the fact that in this sketch no Fermi level pinning occurs. Furthermore, for the sake of clarity it is assumed that band bending effects within the organic semiconductor can be

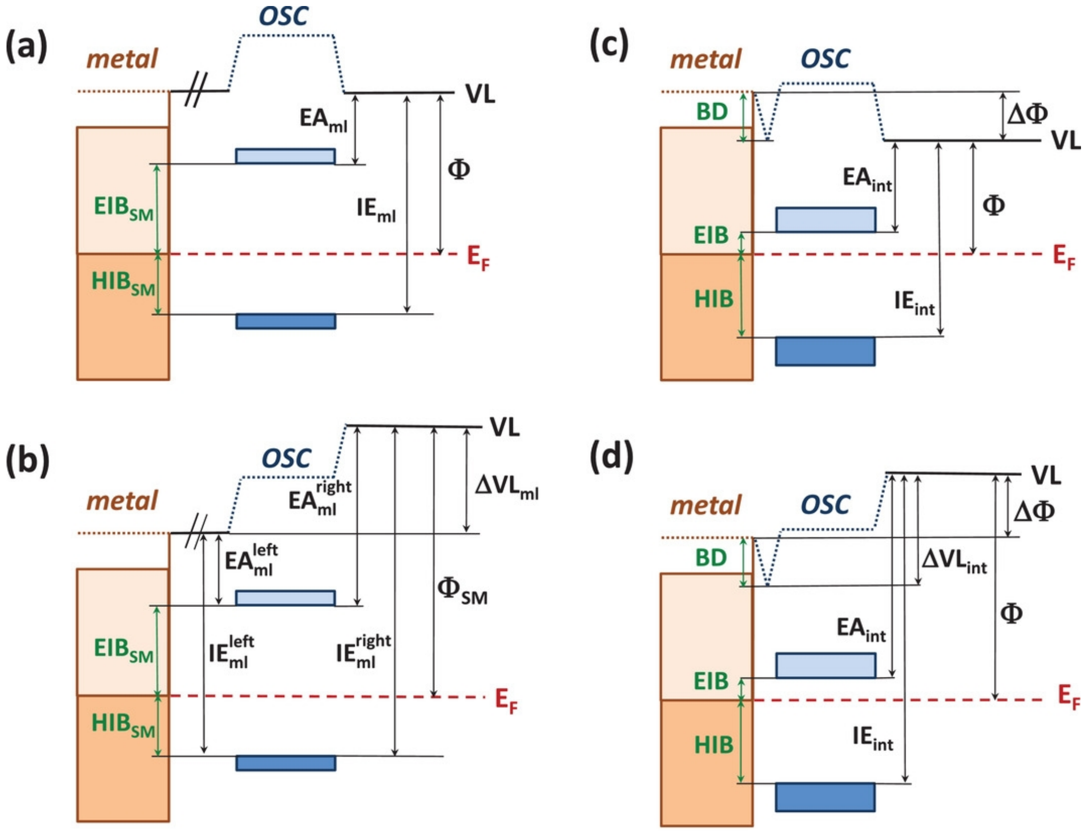

Figure 4: Energy level alignment of a hybrid inorganic/organic interface comprised of its constituents, namely an organic semiconductor (OSC) on a metal substrate. In the top part, i. e., panel (a) and (c), the adsorbate has no net dipole moment, whereas in the bottom part the situation is shown for an adsorption layer with a nonzero net dipole moment. In the left part, i. e., panels (a) and (b), the Schottky-Mott limit is depicted and in panels (c) and (d) an equilibrium situation (including the bond dipole BD) is shown. In this sketch it is assumed that no electrons are transferred from the metal to the unoccupied states of the adsorbate layer. The Fermi level is denoted as E_F. Dark shaded areas correspond to filled states whereas light shading indicates unoccupied states. The indicated quantities are explained in detail in the main text. Figure modified from [136].

neglected. The two schematic plots at the top of Figure 4 show the energy levels of the metal substrate and an OSC adsorbate without a net dipole moment, aligned at their respective vacuum levels. In panel (a) and (b) the situation in the Schottky-Mott limit [145–147] is depicted. This describes a non-interacting interface without any charge rearrangements or atomic relaxation, i. e., the pure physics utilizing the superposition principle to calculate the charge distribution from its constituents without considering any interface chemistry. Due to these limitations its relevance is rather limited for most experimentally observed metal-semiconductor interfaces, even though, it has been shown that, e. g., van der Waals metal-seminconductor junctions are approaching this ideal limit.[148] Furthermore, it is nonetheless worthwhile discussing it to better understand the principle electrostatics occurring at such interfaces. In the case of the Schottky-Mott limit, the energy level alignment can be expressed using the electron- and hole-injection barriers, EIB_{SM} and HIB_{SM}, respectively. [136]

$$EIB_{SM} = \Phi_{sub} - EA_{ml}^{left} \quad \text{and} \quad HIB_{SM} = IE_{ml}^{left} - \Phi_{sub}\,, \tag{24}$$

where Φ_{sub} denotes the work function of the pristine metal substrate, EA_{ml}^{left} the electron affinity and IE_{ml}^{left} the ionization energy on the left side of the molecular monolayer. Consequently, the work function of the combined system, Φ_{SM}, can be expressed as:

$$\Phi_{SM} = \Phi_{sub} + \Delta VL_{ml}\,, \tag{25}$$

where ΔVL_{ml} amounts to the change of the vacuum layer due to the organic adsorbate layer. This means, the work function in the Schottky-Mott limit, Φ_{SM}, does not change due to an adsorption of an adsorbate with no overall dipole moment as depicted in Figure 4(a). In the case of a polar adsorption layer, there is a work-function shift introduced according to Equation (25). This situation is shown in Figure 4(b).

Additionally, in Figure 4(c) and (d) the situation for an interacting system is shown. There, interfacial charge rearrangements are taken into account. Furthermore, the chemical interaction between the metal substrate and the OSC is considered as well as geometric changes of the adsorption layer due to the aforementioned charge rearrangements and upon bond formation, i. e., the creation of hybrid bands. Additionally, screening effects come into play by renormalizing the bandgap and, consequently, changing the electronic levels of the adsorbate. This means, the electron affinity as well as the ionization energy of the organic semiconductor change at the interface (in comparison to the hypothetical free standing monolayer as discussed above). Therefore, they are denoted as EA_{int} and IE_{int} in the right part of Figure 4. As a consequence, the vacuum level of the adsorbate layer also changes and is, therefore, denoted as ΔVL_{int}. Furthermore, also the work function changes upon the adsorption of the OSC, and is denoted as $\Delta\Phi$ in Figure 4(c) and (d).

As already explained, these charge rearrangements have an important impact on the energy level alignment at the interface and are commonly attributed to the so-called bond dipole, BD, of the interface. Although it is not unambiguously defined, in the course of this work, the BD includes also the electrostatic energy associated with geometric rearrangements of the metal substrate from, e. g., surface reconstructions and ad-atoms. Furthermore, effects due to the formation of chemical bonds are also included in this term. What should be noted, though, is that the change of the vacuum level, ΔVL_{int}, arising from the densely packed molecular layer's polar tail-groups is not part of the BD, i. e., these two dipole layers are spatially separated. The electrostatic situation thereof is depicted in Figure 3(c). As a consequence, the bond dipole causes a shift in the energetic landscape right at the interface as shown in Figure 4(c) and (d). When looking at the overall work function of the combined system, Φ, it is given by:

$$\Phi = \Phi_{sub} + \Delta\Phi = \Phi_{sub} + BD + \Delta VL_{int}\,. \tag{26}$$

Here the sign convention is applied that a bond dipole which reduces Φ is counted negative, As already mentioned, the bond dipole includes the effects right at the interface and it is assumed that it essentially drops between the substrate and the adsorbate. This definition is also commonly used when modeling systems within the framework of DFT.[35, 40, 144] For the adsorption of polar molecules the electron- and hole-injection barriers can be expressed including the bond dipole by the electron affinity and ionization energy as follows.

$$EIB = \Phi_{sub} - EA_{int}^{left} + BD \quad \text{and} \quad HIB = IE_{int}^{left} - \Phi_{sub} - BD\,. \tag{27}$$

Note that for both quantities the ones facing the metal need to be used; these are denoted as EA_{int}^{left} and IE_{int}^{left}, respectively.

Part II

Results

4

ON THE CALCULATION OF CORE-LEVEL EXCITATIONS

As already mentioned, this thesis deals with X-ray photoelectron spectroscopy (XPS) in a twofold way. In Chapter 4.4 spurious collective electrostatic effects are investigated which can occur when modeling core-hole excitations within the framework of density functional theory (DFT), and, furthermore, in Chapter 5 it is explored how XPS can be used to determine the bond dipole of an interface between a self-assembled monolayer (SAM) and a metal substrate. Therefore, a brief introduction on the principles of XPS from an experimental point of view is given, as well as how this translates to a theoretical point of view. As in this thesis the quantum-mechanical simulations are done using state-of-the-art density functional theory (DFT)-calculations, different methods of how to model XPS-measurements within the framework of DFT are presented.

Core-level spectroscopy is used to probe the local electrostatic environment, i. e., the chemical neighborhood, of atoms.[44–52] This can be done because of the sensitive nature of core levels with respect to their local electronic structure. The basic principle of determining the binding energy spectroscopically builds on an effect discovered by Hertz [149] and theoretically interpreted by Einstein and since then known as the photoelectric effect[150]. The experimentally measured binding energy of an electron is determined by the incident photon energy, $h\nu$, the kinetic energy of the emitted electron, E_{kin}, and the spectrometer's work function, Φ_{spect},

$$E_B = h\nu - E_{kin} - \Phi_{spect}\,. \tag{28}$$

Furthermore, the kinetic energy of the emitted electron depends on the orbital it was ejected from. A schematic plot for an XPS measurement is given in Figure 5, which also shows how the spectrometer's work function comes into play. Even though it actually is not a one-particle process, the basic principle can be described by an incident photon hitting the sample and ionizing a core electron. The ionized photoelectron's energy is subsequently detected by an analyzer, which shares a common Fermi level with the (conductive) sample. Therefore, the measured energy depends on the work function of the spectrometer.

The measured binding energy of the electron is characteristic for the atomic orbital it was ejected from. Furthermore, it depends also on the chemical neighborhood of the probed atom, which allows for a detailed chemical analysis of the investigated material. Hence the name *electron spectroscopy for chemical analysis* (ESCA), XPS was originally known as. The overall process is non-destructive and allows a

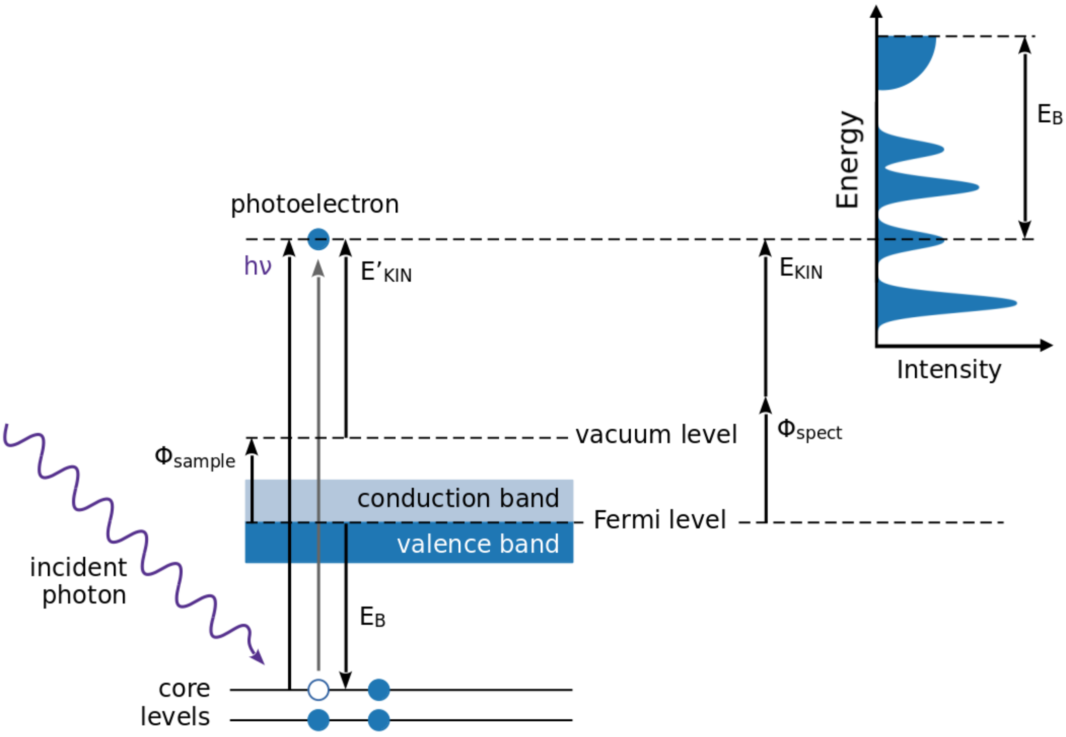

Figure 5: Schematics of an XPS-measurement. In the left part of the image the energy levels of a sample are depicted and on the right side the spectrometer and a prototypical spectrum is sketched. A core electron is ionized by absorbing an incident photon with an energy $h\nu$ and transitions above the vacuum level. The photoelectron's energy $h\nu$ is equal to the binding energy E_B, the work function of the sample Φ_{sample} and the kinetic energy E'_{KIN}. The kinetic energy E_{KIN} of the ejected photoelectron is then measured by a spectrometer with a work function Φ_{spect} and contributes to an overall X-ray photoelectron (XP)-spectrum. In an experiment, the sample and the spectrometer are aligned with respect to the Fermi level.

qualitative (as each element produces characteristic peaks due to its electron configuration) and a quantitative (a detection limit as low as 100 ppm can be achieved, depending on the element and the signal-to-noise ratio)[151] analysis of the sample. This means, by analyzing the spectrum and interpreting the chemical shifts occurring due to the local chemical potential, i. e., due to the bonding environment of the probed atom, the chemical composition of the surface can be determined. In a lab based system using monochromated Aluminum K_α X-rays a peak resolution of around 0.3 eV for the FWHM can be achieved. In comparison, if using a synchrotron for the generation of the incident photons, a remarkably higher accuracy, typically in the range of 0.02 eV is possible.[152] The measurements done at a synchrotron facility are known as high resolution X-ray photoelectron spectroscopy (HRXPS) and are carried out under UHV conditions.

In addition to the aforementioned chemical shifts due to the potential in the vicinity of the probed atom, shifted peaks can also stem from collective electrostatic effects introduced by a densely packed array of dipoles. This is, e. g., the case in self-assembled monolayers (SAMs) with an embedded polar group. We investigated these effects in great detail in ref. [153] and were able to explain why chemically absolutely identical atoms produce a double-peak structure. For this, we modeled XP-spectra of an ester containing alkyl thiolate SAM, namely a pentyl-11-sulfanylundecanoate (C10EC5), on a Au(111)-substrate. It should explicitly be noted that the alkyl chain below and above the embedded ester group is chemically absolutely identical, i. e., the segments are chemically equivalent, only separated by the polar ester group. As can be seen in Figure 6, in the full coverage system a distinctive double-peak structure (black) is produced in the calculated spectrum, which perfectly reflects the experimental measurements.[153] This double peak is due to collective electrostatic effects shifting the energy levels of the alkyl chain above the ester group with respect to the ones below of it. When the densely packed array of dipoles due to the embedded ester group is diluted enough, e. g., in the case of a hypothetical low-coverage system, these collective electrostatic effects vanish. It can be clearly seen that in the case of the low-coverage system, where no collective electrostatic effects are present, the double peak structure recovers into a single peak (red).

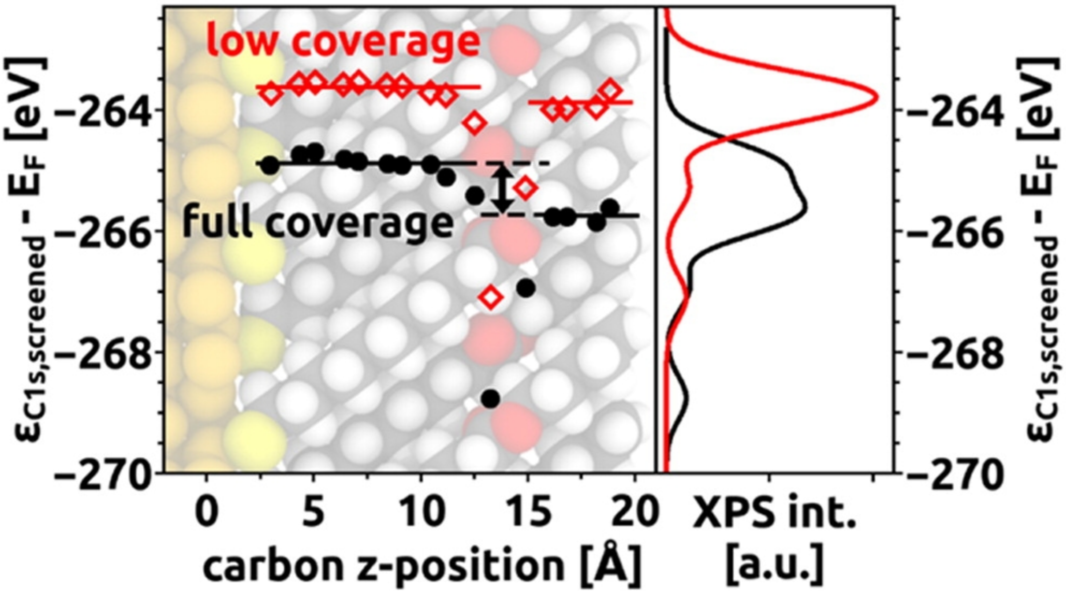

Figure 6: In the left part the calculated carbon 1s core-level energies of C10EC5 in a full coverage SAM (black) and for comparison a low-coverage system (red) are shown. Details are explained in the main text. The right plot shows the XP-spectra calculated from the individual 1s orbital energies of all carbon atoms in the system. Figure modified from [153].

In passing we note that the chemical shifts due to the incorporated oxygen atoms of the ester group are present in both, the full and low coverage, systems. The low-coverage system was realized by multiplying the full coverage unit cell in x- and y-direction and removing all but one molecule to acquire a molecular coverage of 1/32. Furthermore, the geometry was kept the same, i. e., the atoms were fixed at the positions of the optimized full coverage geometry to prevent the molecule from falling over in the simulations of the low-coverage system. Additionally, these collective electrostatic effects also come into play right at the metal-substrate interface, where due to charge-rearrangement a dipolar layer is induced in the case of the full-coverage system. That is the reason why the core-level energies of the system with the SAM are rigidly shifted to more negative binding energies with respect to the low-coverage system. As can be deduced from the relative shifts, the bond dipole and the dipole due to the embedded ester group are pointing in the same direction (cf. Chapter 3).

As one can imagine, the interpretation of XP-spectra can become quite complex, for which reason computational simulations are of great help and are widely used today.

When simulating such spectra, the core-level binding energy, E_{CL}, is - theoretically speaking - defined as the energy difference of two separate systems, namely one in its ground state (E_N), and a second, ionized system with one electron removed (E_{N-1}). This calculated energy difference acquired within a theoretical model, in the course of this theses calculated via DFT, is a measure for the experimentally measured core-level binding energy E_B:

$$E_{CL} = E_{N-1} - E_N \simeq E_B \, . \tag{29}$$

When calculating core-level energies within the DFT-framework, one can rely on several approaches, the two most important ones are more thoroughly discussed including their benefits and drawbacks in the next two chapters. What most methods based on DFT have in common is that they can describe relative core-level shifts quite accurately, but, generally, fail to predict absolute core-level energies. To obtain absolute core-level energies higher level theoretical methods such as GW [56] or Δ coupled-cluster approaches [54, 154, 155] are needed.

Nowadays, there have been quite a lot of different quantum chemical methods developed to describe core-level spectroscopy. Generally speaking, there is a wide variety of computational approaches which can be classified on the one hand as wave-function based and on the other hand as methods based on density functional theory. In the realms of wave-function based methods the Hartree-Fock (HF) approach describes the system in a single-particle picture of molecular orbitals. To recover the electron correlation, several ab-initio methods have been developed, e. g., second order Møller—Plesset perturbation theory (MP2) [156]. Principally speaking, even the exact solution for the energy of the many-electron initial and final state could be calculated within the framework of configuration interaction

(CI) by using a relativistic Hamiltonian and an infinitely complete basis set.[55] Practically this is not possible, though, and some kind of approximation is needed. In the course of this work we will focus on systems where one-body effects are dominant, i. e., each core-level contributes via a single peak with only weak satellite features (if any at all) to the overall XP-spectrum. In contrast to this would be systems where many-body effects dominate, i. e., the spectrum shows several intense peaks for a probed level. This multiplet splitting cannot be described by a single configuration wave function but rather needs to be treated considering many body effects.[55] Extending HF-theory based on Green's functions leads to the GW quasiparticle approach. [56, 157–163] There the HF equations are generalized via Green's functions (G) and the self-energy term is non-local and energy dependent. Furthermore, the electrostatic potential is dynamically screened (W), including many-body effects explicitly.[55, 157, 158] These GW-based methods can be applied self-consistently (with drastically increased computational cost), or non-self-consistently, meaning that they depend on the input electron density obtained from a standard DFT-calculation.[164] Additional wave-function based methods have emerged from the Green's functions formalism, building on a propagator theory, e. g., the second-order algebraic-diagrammatic construction (ADC2), [165, 166], where both the core-hole relaxation and the polarization effect are taken into account.

Furthermore, also more sophisticated DFT-based methods have been developed,[167] i. a., orthogonality constrained density functional theory [168, 169] and approaches based on time-dependent DFT [170–173], which allow to simulate excitation processes explicitly.[174, 175]

Unfortunately, the aforementioned methods are computationally way more expensive and, therefore, not applicable to the wide range of systems which can be calculated with DFT. Especially for investigating SAMs of organic adsorbates on metal substrates, DFT-based approaches are still the method of choice. In passing we note, that in recent studies by Pueyo Bellafont *et al.* they explored the performance of different functionals for determining core-level binding energies of molecules on metals,[177] and investigated the impact of different XC-functionals, specifically focusing on the core-level binding energy of a CO molecule.[176] They showed that the type of functional should be well-considered, i. e., whether to use a GGA, meta-GGA or hybrid functional should be chosen appropriately, depending on the investigated system.

When modeling core-level binding energies within the framework of density functional theory (DFT), the approaches can principally be categorized into so-called initial and final-state methods. These two fundamentally different approaches are explained in more detail in the next sections. First, the advantages and drawbacks of the initial-state approach, which neglects any final-state effects and electronic screening, are discussed. Second, the a priori more sophisticated final-state approach, which inherently considers the aforementioned effects, is explained. Additionally, the challenges needed to be addressed when utilizing periodic boundary conditions (PBC) in conjunction with final-state approaches are investigated in more detail in the included paper in Chapter 4.2.

4.1 THE INITIAL-STATE APPROACH

The most straightforward way to model XPS measurements when doing DFT-calculations is the so-called initial-state approach, which maps the Kohn-Sham (KS)-eigenvalues to the binding energy of an electron.

This approach is based on the ionization potential (IP)-theorem, which states that the negative unrelaxed ionization potential of a system equals the calculated KS-HOMO.[178] In passing we note that Koopmans' theorem [179] states the same for the unrelaxed ionization potential in the context of HF theory. The general use of the orbitals' KS-eigenvalues for determining the energies of their electrons is a heavily discussed topic, though, because the KS-states have per se no physical meaning.[52, 180–186] Chong *et al.* [183] argue that the KS orbital energies of occupied states ϵ_k approximate relaxed vertical ionization potentials, VIP_k, accurately for outer valence levels, $\epsilon_k \approx -VIP_k$, and become an exact identity for the highest occupied molecular orbital (HOMO), $\epsilon_{HOMO} = -VIP_{HOMO}$. As this approach neglects, i. a., correlation and relaxation effects upon ionization, it only works well for systems where these play only a minor role or cancel each other.[187] Therefore, it is of utmost importance to check whether an approach within the initial-state framework is applicable. It was shown for, e. g., surface core-level shifts and alloys, that methods considering final-state effects can be necessary to obtain correct results.[188–191] Despite these drawbacks and although the obtained values are not exact (as it is generally the case with DFT-calculations), the initial-state approach is quite successful for a vast range of different systems and, therefore, widely used.[28, 35, 153, 191–196] A more detailed description of it is given in the next paragraphs.

As mentioned above, for calculating core-level excitations within the initial-state approach a standard self-consistent field (SCF)-calculation is done and the KS-eigenstates are mapped to the electron binding energies of their respective orbitals. This means, the initial-state core-level energy $E_{CL}^{initial}$ can be reported with respect to the Fermi-energy:

$$E_{CL}^{initial} = \varepsilon_{KS} - \varepsilon_F \,, \tag{30}$$

where ε_{KS} is the eigenvalue of the KS-orbital from which the electron is ejected and ε_F the Fermi energy of the system. By aligning all calculated energies to the Fermi level it is possible to compare different DFT-calculations, because the Fermi level can act as a common reference energy level when investigating organic adsorbates on metal substrates. In passing we note that also experimental spectra are measured relative to the Fermi level as is shown in Figure 5.

As already mentioned, final-state effects and electronic screening is entirely neglected within the initial-state approach. Neglecting these bears the advantage of being able to acquire core-level binding-energies with a lot less computational resources due to the fact that only a single DFT-calculation is needed to get the orbital energies of all atoms in the unit cell. This is in stark contrast to the final-state approach, especially when investigating SAMs comprised of bigger molecules, where a full SCF-calculation is needed for every atomic orbital contributing to the overall spectrum. Utilizing the initial-state approach means, therefore, neglecting any relaxation effects due to the missing core electron, though, because no change of the potential is considered after removing the electron.[52, 55, 57, 58]

To mitigate the impact of neglecting the aforementioned final-state effects, screening effects due to mirror charges as well as the finite attenuation length of an actual electron can be corrected a posteriori via a classical electrostatic model.[197–199] The mirror charge screening due to the polarizable metal substrate can be accounted for via a classical electrostatic image charge model [197, 198]. This leads to the following equation for adjusting the calculated core-level energies in the initial-state approach:

$$\epsilon_{screened} = \epsilon_{KS} + \frac{1}{4\epsilon(z - z_0)}, \tag{31}$$

where $\epsilon_{screened}$ denotes the corrected core-level energy due to mirror charges in the metal and ϵ_{KS} the calculated KS-orbital energy. ϵ is the dielectric constant of the SAM and $z - z_0$ denotes the distance between the atom of the orbital in question and the mirror image plane of the metal. The position z_0 of the substrate's image plane depends on the metal it is comprised of.[200, 201] This correction shifts the calculated core-level binding energies to smaller binding energies, effecting the orbitals closest to the metal substrate the most.

To finally generate an XP-spectrum out of the calculated orbital energies, the delta peak of each orbital contributing to the spectrum has to be broadened. For this, a simple Gaussian function can be used. Additionally, a Lorentzians or a Voigt function, which is a convolution of a Gaussian and a Lorentzian function, are good options. Furthermore, Gaussian-Lorentzian sum (GLS) and Gaussian-Lorentzian product (GLP) functions can be useful for XPS peak fitting as Jain *et al.* argued in their perspective.[202] Over these individual contributions is then summed up, while weighting each orbital with an exponential attenuation factor, w_i,[199] to account for the finite escape depth of the ionized photoelectron, $\epsilon_{i,screened}$.

$$\sum_i w_i \epsilon_{i,screened} \quad \text{with} \quad w_i = w_0 e^{-\frac{d}{\lambda}}, \tag{32}$$

where the weighting factor w_i depends on the distance d between the atom in question and the topmost layer of atoms in the SAM, a scaling constant w_0, and the damping factor λ, which is given by [199]:

$$\lambda = 0.3 E_{kin} e^{\beta} , \tag{33}$$

where E_{kin} denotes the kinetic energy of the photoelectron, which itself is determined by the incident photon energy minus the calculated core-level binding-energy. The empirical attenuation factor β needs to be chosen in such a way that the calculated spectra reproduce the experimentally measured relative peak heights and, therefore, depends on the investigated SAM. This strategy allows to reproduce high resolution X-ray photoelectron spectroscopy (HRXPS) measurements quite well, though, only relative binding energies can be obtained. This means, to be able to compare the calculated core-level energies to experimentally measured binding energies, the former needs to be rigidly shifted to coincide with the latter.[15, 52, 53, 186, 191, 193, 203] In the case of organic adsorbates on metal substrates, the calculated core-level energies need to be shifted to higher binding energies. When dealing with hydrocarbon SAMs on a gold substrate, they need to be shifted by around 18.9 eV to 19.0 eV to match the values obtained at a synchrotron.[43, 195, 196, 204]

4.2 THE FINAL-STATE APPROACH

In the a priori more sophisticated final-state approach the remaining core electrons are allowed to relax after the photo-ionized electron is ejected from the atomic orbital. This means, quantum mechanical relaxation and screening effects are inherently considered in the final-state approach. As a matter of fact, final-state effects are quite crucial for surface core level shifts,[52, 188, 190, 191, 205, 206] in same cases even changing the sign of the core-level shift.[190] What should be noted is that in literature the terms initial state and final state *method* not always exclusively describe initial state and final state *effects*, respectively, as is discussed by Pueyo Bellafont *et al.*[57]. They argue, "we note that initial state effects on core-level BE's arise largely from the core and valence electron density at the nucleus of the ionized atom. As such, changes in the initial state contributions directly reflect changes in the chemical bonding. On the other hand, the final-state effects arise from the response, or relaxation, of the passive electrons to the presence of the core-hole and are less easy to relate to the changes in chemistry. Although there is some disagreement in the literature about suitable definitions of initial and final-state effects, the definitions given above have general acceptance."[57] There are different ways to consider the aforementioned final-state effects, the most prominent methods are removing 1 electron from the system (ΔSCF [55, 193, 207, 208]) or are removing ½ electron from the core level, the latter being known as the Slater-Janak transition state method [209]. The conceptional difference is that in the case of the ΔSCF-method the difference of the total energies is taken; i. e., the core-level binding energy is calculated by doing a full SCF-calculation of the system in its ground state and one with an electron removed from the core-level of interest, thereby letting the system adjust for the missing electron, and finally taking the difference of the total energy of both calculations. In comparison, in the case of the Slater-Janak transition-state method the KS-eigenvalue of the orbital of interest is taken from a full SCF-calculation with half an electron removed from the system as the core-level binding energy.

The Slater-Janak transition-state method builds on the theorem that the KS-eigenvalue of a half-occupied state equals the binding energy of its electron. This is strictly speaking only valid for the HOMO, which was shown by Jones and Gunnarsson [83]. They argue based on Koopman's theorem within HF theory, which states that

$$\epsilon_i^{HF} = E(n_1, \ldots, n_i, \ldots, n_N) - E(n_1, \ldots, n_i - 1, \ldots, n_N)\,. \tag{34}$$

Here ϵ_i^{HF} is a HF-eigenvalue and $E(n_1, \ldots, n_N)$ is the total energy of the system with the occupation numbers $n_1, \ldots, n_N$. The theorem is valid if the change of the occupancy of an orbital n_i does not affect the other orbitals and it identifies ϵ_i^{HF} as the energy required to remove an electron from the orbital i. This is not generally valid in DFT, where Slater and Janak state [209, 210]:

$$\frac{\partial E}{\partial n_i} = \epsilon_i(n_1, \ldots, n_N)\,. \tag{35}$$

The total energy difference in Equation 34 can now be written as:

$$\begin{aligned} &E(n_1, \ldots, n_i, \ldots, n_N) - E(n_1, \ldots, n_i - 1, \ldots, n_N) \\ &\qquad = \int_0^1 \epsilon_i(n_1, \ldots, n_i + n - 1, \ldots, n_n)\, dn\,. \end{aligned} \tag{36}$$

What should be noted is the fact that Equation (36) has a formal justification only if the occupation numbers refer to the ground state of the system with M and $M-1$ particles, where $M = \sum n_i$, i. e., ϵ_i refers to the highest occupied eigenstate of an M-electron system. Then Equation 36 can be simplified within the DFT-formalism by using the result for the HOMO:

$$\epsilon_N(n_1, \ldots, n_N = n) = \epsilon_N(n_1, \ldots, n_N = 1), \quad 0 < n \leq 1\,, \tag{37}$$

which was derived by Perdew and Norman using the $T \to 0$ limit of the finite T theory.[181] This means, we can use the following equation to determine the core-level energy:

$$E_{CL} = E_{N-1} - E_N = -\int_0^1 \epsilon(n)\, dn\,, \tag{38}$$

and on the assumption that the KS-eigenvalues are a linear function of the occupation number of the orbitals, which was shown by Göransson *et al.*[211] to hold in a first approximation, the core-level energy can be calculated by removing half an electron:

$$E_{CL} = -\int_0^1 \epsilon(n)\, dn = \epsilon(0) - \frac{1}{2}[\epsilon(1) - \epsilon(0)] = \epsilon(1/2)\,. \tag{39}$$

A thorough explanation and numerical investigation can be found in the aforementioned work of Göransson *et al.* [211] and the approach was generalized by Williams *et al.* who stated that "excitation energies of somewhat greater accuracy" can be obtained when the SCF-calculation is evaluated for a state at 2/3 of the transition rather than at 1/2 as in Slater's formulation.[212] This, however, will introduce larger spurious collective electrostatic effects when periodic boundary conditions (PBC) are applied as is explained in Chapter 4.4.

What a priori limits the applicability of final-state methods is that they are computationally way more costly compared to initial-state methods. This is due to having to run a full SCF-calculation for every single orbital which contributes to the overall spectrum, in contrast to the initial-state method where just one calculation is needed to acquire the whole spectrum.

Another crucial point, especially when investigating surfaces and interfaces by utilizing the repeated slab approach (RSA), is the fact that there arise computational artifacts due to the PBC applied to the unit cell. These spurious collective electrostatic effects are introduced by removing the charge from the core level and placing it, e. g., in the conduction band, as the unit cell itself cannot be charged when PBC are applied. Applying them to a charged system leads to a periodic arrangement of charges, which, consequently, leads to a diverging energy, and, therefore, the SCF-calculation would not converge. This means, the removed charge from the core-level needs either to be compensated within the unit cell, which can be done, e. g., by a uniform background charge, or the charged unit cell is not repeated at all, e. g., by utilizing some kind of embedding scheme. Both approaches have their own advantages and disadvantages, and are discussed in more detail, e. g., in the work of Hofmann *et al.*[132].

In the case of FHI-AIMS, which was used throughout this work, the charge is moved from the core-level to the lowest unoccupied orbital, i. e., in the case of an organic semiconductor (OSC) adsorbate on a metal substrate, this is somewhere at the Fermi edge of the metal. Consequently, this induces an artificial dipole between the core level and the metal surface. The size of the point dipole depends on the distance from the metal substrate to the atom probed, i. e., the distance to the positively charged core hole. As already discussed in Chapter 3, this creates a dipole, which modifies the potential energy surface. This poses per se no problem, as the influence of a single dipole is quite localized. But if periodic boundary conditions (PBC) are applied and the repeated unit cell is too small, an artificial, densely packed array of dipoles is introduced, which causes an abrupt jump in the potential. This contrasts the picture of an XPS-measurement, which is more appropriately described by a single dipole, i. e., only one atom is excited and its core-level electron is measured at the same time. We published a thorough investigation of these artificial effects in a peer-reviewed article, which is reproduced in Chapter 4.6.

4.3 CORE-LEVEL CALCULATIONS IN PRACTICE

In this section a brief hands-on tutorial will be given on how to model XPS, covering the most important points when simulating XP-spectra of SAMs on metal substrates. As throughout this work FHI-AIMS was used, also the following considerations are focusing solely on the workflow utilizing FHI-AIMS. In passing it is noted that this is not an exhaustive how to, but rather only points concerning the calculation of core-level energies are considered and other, equally important steps like, e. g., convergence tests, are not discussed.

First, the key steps for the initial-state approach will be discussed, and, second, the same will be done for the final-state approach.

4.3.1 *Self-consistent field (SCF)-calculations*

For the initial-state approach a single SCF-calculation is sufficient. If using FHI-AIMS, the following lines shown in Listing 1 should be added to your `control.in` input file. For evaluating carbon $1s$ core-level energies, e. g., in a methane molecule, the atom projected density of states (DOS) should be written out at the appropiate energy range, i. e., in this case around −270 eV, in addition to the total DOS. This can be done by including the keywords `output atom_proj_dos` and `output dos` with the desired energy window, the number of steps and the broadening. Furthermore, to be able to easily compare different calculations, a common reference level is needed, which the work function provides. It is only written out, though, if the keyword `evaluate_work_function` is included in the input file. Additionally, the `cube origin`, `cube edge` and `cube_content_unit` keywords should be set for every cube file to ensure they are written out in a consistent manner.

Listing 1: Lines to be added in the `control.in` file for calculating orbital energies within the initial-state appraoch. The lines commented with `fs` need to be additionally included to produce the necessary restart files for a subsequent final-state calculation.

```
restart_write_only restart_xps # fs - specifies the name of the restart files
KS_method serial # fs - needed with the aims version used
evaluate_work_function     # writes out the work function
use_dipole_correction      # needed for slab calculations
dos_kgrid_factors 10 10 1  # writes out the DoS on a denser grid
```

```
output dos -10 10 2000 0.1 # specifies the range for the
   ↪ total DoS
output species_proj_dos -10 10 2000 0.1   # specifies the
   ↪ range for the species projected DoS
output atom_proj_dos -350 -250 1000 0.1   # specifies the
   ↪ range for the atom projected DoS
output cube eigenstate_density X
   #the following lines have to be set for every cube file
   ↪ written out!
   cube filename eigenstateX.cube
   cube origin 2.0 2.0 10.0
   cube edge 400 0.01 0.0 0.0
   cube edge 400 0.0 0.01 0.0
   cube edge 1000 0.0 0.0 0.01
   cube_content_unit bohr
output cube hartree_potential # fs
output cube xc_potential      # fs
output cube total_density     # fs
```

The orbital energies can be found in the section called `Writing Kohn-Sham eigenvalues.` in the output file. There all KS-eigenvalues are written out in ascending order of their eigenvalue. This means, one needs to know beforehand, which eigenstate corresponds to the core-level of interest to be able to define the correct `eigenstate_density` to write out. The same holds for the energy range of the atom projected DOS, which can also be used to investigate the core-level orbital energies. As mentioned above, for a carbon 1s orbital in a methane molecule, this energy is about -270 eV. It should be checked if the KS-state is localized on a single atom instead of being delocalized over several atoms, which can be the case when dealing, e. g., with an alkyl chain. Once knowing the energy of the KS-eigenstate, the spectrum can be constructed as explained in Chapter 4.1.

When the SCF-calculation is converged and the needed restart files are written out, the additional SCF-calculations needed for the final-state approach can be started in parallel, as will be explained in the next chapter.

4.3.2 *SCF-calculations for the final-state approach*

As the final-state approach is a two-step process, first a SCF-calculation as explained in the previous chapter has to be done. In passing it is noted that usually overall computing time is saved when the convergence criteria for this SCF-calculation are quite tight, because than the restarted calculated converges faster compared to one, which is restarted using a less converged restart file. Once finished, the output should be validated and it needs to be checked if all required files for the final-state calculations are indeed written out. There should be an additional file per cpu-core used created, i. e., `restart_xps000` to `restart_xps015` when sixteen cores were utilized. Now another SCF-calculation has to be done for every core-level contributing to the overall spectrum. In the example given above in Listing 1 of the keywords to include in the `control.in` file, X denotes the eigenstate of the core-level of interest in the system. There should be a separate cube file written out for every orbital contributing to the spectrum, as these are needed to unambiguously assign an eigenstate to a specific atom. Furthermore, when assigning the KS-state to a specific atom, it should also be checked if the eigenstate in question is indeed localized. For the actual final-state calculation, the lines given in Listing 2 have to be additionally included in your `conrol.in` input file for evaluating excited core orbitals.

Listing 2: Lines to be added in the `control.in` file for calculating orbital energies within the final-state appraoch. The keyword `restart_write_only` needs to be changed to `restart` or `restart_read_only` in contrast to Listing 1.

```
restart restart_xps # restart file to start final-state scf
force_occupation_projector X 1 1.5 y z # eigenstate, spin
   ↪ channel, occupation, overlap-check start, check end
```

The keyword `force_occupation_projector` defines the electron occupation of the KS-eigenstate X. If applying the Slater-Janak transition-state theory, half an electron is removed from the core-level and the energy of the eigenstate of said core-level is used to generate the XP-spectrum. For this, the KS-state, the spin channel, the occupation, and a region to check for any overlap with the KS-state between different SCF-steps have to be given. Therefore, eigenstates with very similar energy should be included here, i. e., for the system investigated in Chapter 4.8 at least all carbon 1s states. In passing we note that if spin-unrestricted calculations are performed, the total occupation of a KS-state is 2, whereas in a spin restricted calculation it is 1. A more elaborate explanation about these constraining approaches is given in the FHI-AIMS manual.

When the SCF-calculation is finished, again it should be checked whether the eigenstate of interest is localized by examining the `eigenstatedensity.cube` file. Additionally, it should be checked, if any spurious collective electrostatic effects (cf. Chapter 4.4) impact the results. A quick and easy sanity check if dealing with upright standing molecules, is to verify that the (upper) work function stays the same for all the different final state calculations. If different values are reported, a probable cause is that the used unit cell was chosen not big enough to mitigate the aforementioned collective electrostatic effects arising due to the applied periodic boundary conditions (PBC). Additionally, convergence tests with a bigger super cell should be done to check whether the quantities of interest are converged.

For the generation of the spectrum, the Fermi level of each calculation is needed, as well as the eigenstates of all the core orbitals contributing to the spectrum. Furthermore, for considering the final escape depth of the photoelectrons, the z-position of each atom found in the `geometry.in` file is needed. Having acquired all of these values, the spectrum can finally be constructed as explained in Chapter 4.1.

4.4 CALCULATING CORE-LEVEL BINDING-ENERGIES WITHIN THE FINAL-STATE APPROACH

In the following paper we investigated spurious collective electrostatic effects which can occur when modeling hybrid metal-organic interfaces applying periodic boundary conditions (PBC) utilizing the final-state approach for describing the core-hole excitations. These spurious effects are due to the way the system is constructed utilizing the repeated slab approach (RSA). Even though the RSA is a standard way to calculate surfaces and interfaces in the field of solid state and condensed matter physics, in this specific case it incorrectly describes the physics of the system by introducing an artificial dipole layer. A more in-depth explanation of the electrostatic basics of these collective effects can be found in Chapter 3. In the following paper we investigated the drawbacks of final-state approaches with a special emphasis on the Slater-Janak transition-state method (cf. Chapter 4.2). Furthermore, we focused on physisorbed organic molecules on metal substrates as these are one of the most intensively studied systems in the surface science community. For explaining the aforementioned artificial effects we used a deliberately chosen model system, namely methane - representing the simplest organic molecule - on an aluminum slab in order to get a fundamental understanding of the computational artifacts.

4.5 AUTHOR CONTRIBUTIONS

The idea for this paper emerged while I was working on another manuscript [153] investigating different methodologies to calculate core-level excitations. During this work, preliminary results acquired within the final-state approach showed an interesting behavior which we deemed worth investigating more thoroughly.

I contributed to all stages of the following publication and performed all DFT-calculations presented in this paper as well as analyzed their results. I generated all Figures with the exception of Figure 2b and 6, which where created by Egbert Zojer. Oliver T. Hofmann contributed significantly to the interpretation of the data and helped overcome various technical challenges. Subsequently, the data was discussed and interpreted jointly by all authors.

I wrote the first draft of the manuscript, which was then modified and improved by all authors. Egbert Zojer supervised the research, was responsible for the coordination, the funding and had the original idea for the project.

Furthermore, I generated all the data for the Supporting Information and compiled the corresponding text, which was then revised by Egbert Zojer.

4.6 ORIGINAL MANUSCRIPT: FINAL-STATE SIMULATIONS OF CORE-LEVEL BINDING ENERGIES AT METAL-ORGANIC HYBRID INTERFACES: ARTIFACTS CAUSED BY SPURIOUS COLLECTIVE ELECTROSTATIC EFFECTS

http://pubs.acs.org/journal/acsodf Article

Final-State Simulations of Core-Level Binding Energies at Metal-Organic Hybrid Interfaces: Artifacts Caused by Spurious Collective Electrostatic Effects

Thomas C. Taucher, Oliver T. Hofmann, and Egbert Zojer*

Cite This: *ACS Omega* 2020, 5, 25868−25881

Read Online

ACCESS | Metrics & More | Article Recommendations | Supporting Information

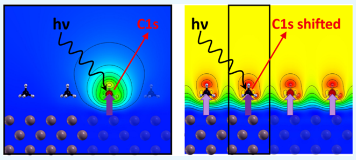

ABSTRACT: Core-level energies are frequently calculated to explain the X-ray photoelectron spectra of metal-organic hybrid interfaces. The current paper describes how such simulations can be flawed when modeling interfaces between physisorbed organic molecules and metals. The problem occurs when applying periodic boundary conditions to correctly describe extended interfaces and simultaneously considering core hole excitations in the framework of a final-state approach to account for screening effects. Since the core hole is generated in every unit cell, an artificial dipole layer is formed. In this work, we study methane on an Al(100) surface as a deliberately chosen model system for hybrid interfaces to evaluate the impact of this computational artifact. We show that changing the supercell size leads to artificial shifts in the calculated core-level energies that can be well beyond 1 eV for small cells. The same applies to atoms at comparably large distances from the substrate, encountered, for example, in extended, upright-standing adsorbate molecules. We also argue that the calculated work function change due to a core-level excitation can serve as an indication for the occurrence of such an artifact and discuss possible remedies for the problem.

1. INTRODUCTION

X-ray photoelectron spectroscopy (XPS), also known as electron spectroscopy for chemical analyses (ESCA), is a widely used technique to analyze the chemical structure of surfaces and interfaces, providing qualitative and quantitative information about the chemical neighborhood of specific atoms.[1,2] In addition to the chemical environment, core-level binding energies are also influenced by the local electrostatic potential at the position of the excited atom.[3−6] This effect is related to observations for ionic crystals that the differences in Madelung energies between the bulk and the surface can easily amount to ~1 eV.[7] Electrostatic shifts are also of particular relevance for interfaces in cases where large dipoles occur. This is very common for hybrid organic−inorganic interfaces (relevant, e.g., for the areas of organic and molecular electronics), where interfacial potential shifts are typically associated with collective (also termed cooperative) electrostatic effects.[4,5,8−12] Also in this context, electrostatically triggered core-level shifts on the order of 1 eV have been observed for polar self-assembled monolayers (SAMs) adsorbed on metal substrates.[3,4,13−15] For such systems, the electrostatic shifts can be straightforwardly rationalized by the periodic arrangement of polar entities at the interface. The superposition of their fields causes a step in the electrostatic energy that changes not only the sample work function but also the energetic positions of core levels relative to the Fermi level of the substrate, as described in detail in ref 5.

The interpretation of experimentally acquired spectra frequently relies on first-principle simulations.[2,16] There is a broad range of different approaches to simulate XP spectra.[2,17,18] The most simple strategy inspired by Koopmans' theorem[19] would be to associate core-level binding energies with the orbital energies of a ground-state calculation.[3,4,6,20−26] This approach, often referred to as the initial-state approach, does not provide absolute values of the core-level binding energies but yields relative shifts between different systems.[2,27−31] This is often sufficient for understanding molecular adsorbates, like self-assembled monolayers with atoms at rather large distances from a metal substrate. There, the trends obtained within the initial-state approach typically agree very favorably with experimental data[3,4,14,20,32] and core hole screening effects can be accounted for by electrostatic models.[33,34] The situation becomes more involved when considering surface core-level shifts, adsorbates in the immediate vicinity of the surface, or the effect of alloying: also there, initial-state calculations have provided valuable insights. Bagus et al.,[2] for instance, showed that surface core-level shifts at Al and Cu surfaces (as representatives for sp and transition metals) are primarily due to initial-state effects.[35,36] The neglect of (potentially site-dependent) screening in initial-state calculations can, however, cause problems: for example, Methfessel et al.[27] found for intermetallic MgAu compounds that the inclusion of screening effects "changes the picture

Received: July 3, 2020
Accepted: September 14, 2020
Published: September 29, 2020

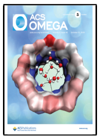

https://dx.doi.org/10.1021/acsomega.0c03209
ACS Omega 2020, 5, 25868−25881

drastically" with a sign change in the shift of the Mg 1s core state; Pehlke and Scheffler[37] observed "remarkably different" screening effects for the two atoms in the surface dimers of Si and Ge; Stierle et al.[38] reported that the inclusion of final-state effects changes the sign of surface core-level shifts in NiAl(110); and Birgersson et al.[39] found that "a large variation exists in the relative importance of initial- and final-state effects for CO on Rh(111)" and stressed the "dangers of interpreting core-level binding-energy shifts in a simple initial-state framework".

The resulting need to properly account for screening effects has triggered the development of a variety of more sophisticated tools,[17,18] including Green's function-based approaches,[40−42] techniques based on the GW approximation,[40,43,44] and the explicit simulation of excitation processes,[45] for example, in the framework of time-dependent density functional theory (DFT).[46−49] The most common strategies for complex, extended systems are based (i) either on calculating the difference in total energy between the (fully) ionized interface and the interface in its ground state—typically referred to as Δ self-consistent field (ΔSCF)[17,37,50−54]—(ii) or on the Slater–Janak transition-state approximation.[17,53,55−63] The latter relies on calculating the (Kohn–Sham) orbital energies of a partially ionized core level, whose occupation has been reduced by 0.5 electrons. These approaches are typically referred to as final-state approaches, as they include screening effects of the core hole by the polarization of the electron cloud of the substrate. In passing, we note that this screening can also be accounted for semiquantitatively in initial-state calculations by employing a mirror charge correction proportional to $1/[4\varepsilon(z - z_0)]$ (with $z - z_0$ denoting the distance of the excited core level from the image plane of the substrate and ε referring to the dielectric constant of the adsorbate layer).[4,14,20,34,64,65] One would, however, expect that an explicit consideration of screening effects in the quantum-mechanical simulations through final-state approaches should be superior. This suggests that the final-state calculations should typically provide improved results not only for surface core-level shifts but also for adsorbate layers. In the present paper, we will, however, show that the final-state calculations in conjunction with periodic boundary conditions (PBCs) can give rise to a potentially serious complication that is due to the periodic repetition of the core hole in every unit cell. In this context, we will focus on the practically relevant interfaces between metal substrates and physisorbed organic molecules, in which the distance of the generated core hole from the metal surface is comparably large. We will also primarily discuss results obtained within the Slater–Janak transition-state approximation.

2. MAPPING THE INTERFACE ON A SUITABLE MODEL SYSTEM AND THE ROLE OF COLLECTIVE ELECTROSTATICS

For understanding possible pitfalls of final-state calculations, it is crucial to consider yet another methodological aspect, namely, how the interface in question is mapped onto an atomistic model system. Usually, one possibility is to apply slab-type calculations, which apply periodic boundary conditions (PBCs) with the metal substrate represented by a two-dimensional (2D) periodic slab consisting of a finite number of metal layers onto which molecules are adsorbed. In the third dimension, periodic replicas of the slab are then decoupled quantum-mechanically by introducing a wide enough vacuum gap and electrostatically by a self-consistently determined dipole layer.[66] Alternatively, the system in question can be modeled by a finite size cluster employing open boundary conditions.

In the following discussion, we will focus on PBC simulations, as they straightforwardly account for collective electrostatic effects, which typically dominate the electronic properties of organic–inorganic hybrid interfaces.[5,8,11,67] These effects arise from the omnipresence of dipoles at surfaces and the fact that a periodic arrangement of dipoles causes a step in the electrostatic energy, shifting the energy landscapes above and below the dipole layer relative to each other (for a tutorial review, see ref 5). In this context, it should be mentioned that the actual interfacial charge distributions are typically more complex than mere dipoles but the latter term is still used as a "shorthand" for the actual situation, as often the true interface properties can be conveniently mapped onto a dipole model.[5,9] For organic–inorganic hybrid interfaces with typically rather large interfacial dipoles, it is well established that these effects significantly change substrate work functions and the alignment between electronic levels at the interface.[5,8−11] Most important in the present context is that the shift in the electrostatic energy also changes core-level binding energies. This has, for example, been measured as well as modeled for self-assembled monolayers formed by aliphatic[13,15,68,69] and aromatic molecules[3,15,20] containing polar entities embedded into their backbones.

As the above-described effects arise from the superposition of the electric fields of the periodically repeated dipoles at interfaces, their description is intrinsically well compatible with 2D periodic boundary conditions. Thus, it is also not surprising that PBCs are commonly employed when modeling core-level excitations at organic–inorganic hybrid interfaces.[4,5,7,20,61,62,70−73]

In this context, it should be noted that cluster calculations a priori miss the above-described effects, as they do not consider the periodically repeated polar entities present at the interface. As the impact of the interfacial dipoles in neighboring unit cells is primarily electrostatic in nature,[5] it should, however, be rather straightforward to include them via suitable electrostatic embedding schemes[74−78] (in analogy to what is done to account for the Madelung energies when studying ionic crystals[6,7]). Thus, properly corrected cluster calculations might indeed be an interesting strategy for modeling the said interfaces when employing final-state approaches, as will become evident from the data presented in this manuscript.

In fact, the key advantage of PBC calculations described above can become their Achilles heel, when it comes to final-state calculations: while periodic boundary conditions properly capture the impact of periodically repeated polar entities present at the interface, they also periodically replicate the core holes and the corresponding polarization effects in final-state calculations. This then gives rise to artificial collective electrostatic effects. A closely linked problem is that the unit cells in PBC calculations are typically charge neutral to prevent a divergence of the electrostatic energy (although there are also certain approaches to embed charged unit cells within periodic systems[78]). Thus the (half) electron excited from the core level in the final-state calculation is usually not entirely removed from the system but placed into the lowest unoccupied state, which for metal substrates resides right at the Fermi level.[61,62,79−81] Adding a (fractional) charge to a sufficiently thick metal slab should a priori not pose a sizable problem, as it does not noticeably modify the electronic structure of the substrate. Adding the excess charge to an unoccupied state is considerably more serious for semiconducting and insulating substrates, where the additional (half) electron is put into the conduction band (or into unoccupied states of the adsorbed molecules, if they are lower in energy). This is by no means consistent with what is actually happening at the interface as a consequence of the core-level excitation. The problem is further amplified by the fact that at semiconductor surfaces the additional electrons can be artificially localized in diffuse Rydberg orbitals close to the core holes, as described in ref 6. As a remedy to this specific problem, Bagus et al.[6] suggested compensating for the charge of the core hole via the virtual crystal approximation[82−85] rather than adding charge to the conduction band.

This, however, does not solve the problem that for semiconducting as well as metallic substrates the combination of the core hole and the compensation charge creates a polar unit cell, which in conjunction with periodic boundary conditions results in an artificial dipole layer. The resulting spurious collective electrostatic effects can have significant consequences, especially when the separation between the core hole and the compensation charge is large, as will be discussed below. In passing, we note that these are not the only spurious electrostatic interactions PBC calculations can suffer from,[86] as similar complications also occur when modeling charged defects.[87−90]

3. METHANE ON ALUMINUM: A SIMPLE, YET INSTRUCTIVE MODEL SYSTEM FOR METAL-ORGANIC HYBRID INTERFACES

To illustrate the consequences of the spurious dipole layer, we designed a prototypical test system for an interface consisting of a metal substrate and a physisorbed organic molecule. It consists of an Al(100) surface with methane molecules adsorbed in every 2 × 2 surface unit cell (see Figure 1). Methane represents the simplest organic molecule. Its frontier levels are far from the Fermi level of the substrate. Thus, Pauli pushback is the only origin of the actual interface dipole[5,91−94] and even when the (half) core hole has been formed, the lowest unoccupied molecular orbital (LUMO) of the ionized adsorbate molecule will (in most cases) remain well above the metal Fermi level. This prevents a transfer of electrons from the metal into the molecular LUMO as a consequence of the core-level excitation. Thus, one avoids Fermi-level pinning,[5,91] which would further complicate the situation (see below). Moreover, the small size of methane confines intramolecular screening effects to a very small volume. Consequently, the simulation artifacts arising from the spurious dipole layer can be shown without significant interference from additional effects, like massive interfacial charge transfer, Fermi-level pinning, or complex dielectric screening. Aluminum has been chosen as the substrate to minimize computational costs for our all-electron calculations. This is important, as to clearly demonstrate the impact of artificial collective electrostatic effects, the largest considered supercell contains 36 adsorbate molecules and 432 substrate atoms. Moreover, the exact nature of the metal substrate should only have a very minor impact on the results obtained here.

As parent unit cell, we chose a 2 × 2 surface unit cell of Al(100) containing a single methane molecule. For bigger supercells, the parent cell was repeated simultaneously in both the x- and y-directions, creating 4 × 4, 6 × 6, 8 × 8, 10 × 10, and 12 × 12 supercells with identical adsorbate densities and aspect ratios. The surface area of the investigated cells (cf. Figure 1) ranges from 33 Å^2 (for the 2 × 2 unit cell containing a single methane molecule) to 1181 Å^2 (for the 12 × 12 supercell containing 36 methane molecules). We emphasize that the trends discussed below are not dependent on the adsorbate density but rather are determined by the density of (half) core holes created on the surface. This is shown explicitly in the Supporting Information (Section 1), where we compare calculations on supercells containing only a single adsorbate molecule (which is also excited) with simulations on supercells with the same methane coverage as in the parent 2 × 2 unit cell (where only one carbon atom per supercell is excited). Both sets of calculations yield essentially the same results, which implies that the relevant quantity for the calculated core-level shift (at least for the present model interface) is the excitation density rather than the coverage of the adsorbate molecules. In the following, we will report data obtained for the full-coverage case with a single methane molecule per supercell excited, such that the inverse supercell size directly corresponds to the excitation density. The only exception is a 3 × 3 surface unit cell at slightly reduced coverage, which we calculated to generate an additional data point with an excitation density between the 2 × 2 and 4 × 4 cells.

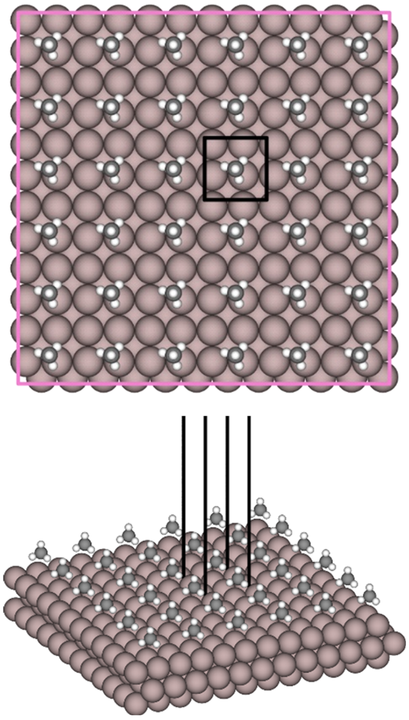

Figure 1. Largest supercell of the methane/Al(100) interface investigated in the present study. The black box indicates the smallest considered supercell (2 × 2 surface unit cell of Al(100); base area of 33 Å^2), while the colored box shows the biggest supercell (12 × 12, with a base area of 1181 Å^2 and containing 36 methane molecules). In the bottom image, only a part of the vacuum gap is shown.

4. METHODOLOGY

The quantum-mechanical modeling was done using density functional theory (DFT) employing the all-electron, full-potential FHI-aims code version 180808.[95−99] To perform the slab-type band-structure calculations on the interfaces, the Perdew−Burke−Ernzerhof (PBE)[100,101] functional was used for describing exchange and correlation. Long-range van der Waals interactions were accounted for by employing the Tkatchenko–Scheffler dispersion correction.[102] All calculations were done with tight settings for all atomic species (as supplied by FHI-aims). Details on the corresponding basis functions are described in the Supporting Information (Section 2.1). Reciprocal space was sampled by a Γ-centered $12 \times 12 \times 1$ grid for the 2×2 unit cell and by smaller grids for the larger cells ($8 \times 8 \times 1$ for the 3×3, $5 \times 5 \times 1$ for the 4×4, $4 \times 4 \times 1$ for the 6×6 and 8×8, and $2 \times 2 \times 1$ for the 10×10 and 12×12 supercells). These grids are very well converged (despite minor variations in the k-point density between different supercells), as shown in the Supporting Information (Section 2.2). The change in the electron density between subsequent iterations was converged to 10^{-5} e^{-}, and the change of the total energy of the calculated system was converged to 10^{-6} eV.

Interfaces were modeled employing the repeated-slab approach with the Al substrate represented by three metal layers. These are rather few layers but making this choice was inevitable to consistently calculate also the largest supercells (the 12×12 supercell containing 612 atoms). The Supporting Information (Section 2.3) contains layer-convergence tests for the 2×2 unit cell (the cell most strongly affected by the artifacts discussed here), which show that for the current system also three-layer slabs yield reliable core-level binding energies. The periodic replicas of the slabs were quantum-mechanically and electrostatically decoupled by a vacuum gap of 30 Å and a self-consistent dipole correction.[103] The geometries of the adsorbate molecules in the 2×2 and 3×3 unit cells were fully relaxed until the remaining forces on each atom were below 10^{-3} eV/Å. The geometries of the other supercells considered here were directly derived from the 2×2 cells. The obtained adsorption height amounts to 3.68 Å for the central C atom above the topmost Al layer. Whether the top Al layers are relaxed only negligibly impacts the obtained results (see the Supporting Information, Section 2.4); thus, we stick to unrelaxed surface layers.

The final-state calculations were done within the Slater–Janak transition-state approximation.[55−59] To that aim, half an electron is removed from the carbon 1s core orbital of one of the methane molecules in the supercell. The Slater–Janak theorem has a rigorous theoretical foundation for finite size systems,[104] but when employing periodic boundary conditions, a complication arises, as the unit cell needs to stay charge neutral (see the discussion in Section 2). Thus, in that case, the excited charge is moved to the lowest unoccupied level, which for the metal substrate considered here corresponds to a state right at the Fermi level. Notably, the region of electron accumulation following the core-level excitation is found right above the metal surface underneath the excited molecule, as will be discussed below. Correspondingly, one is dealing with one excitation per supercell and an excitation density that is inversely proportional to the size of the supercell. As each core hole excitation creates a dipole at the surface, this inverse relation also applies to the dipole density.

For supercells, special care had to be taken that in the ground-state calculations the orbital from which the charge was eventually removed was localized on only one carbon atom. To achieve that, in most cases, the translational symmetry within the supercells had to be broken by moving one methane molecule by −0.01 Å closer to the surface. The occupation of the selected orbital was then reduced and kept fixed in the following self-consistent field (SCF) cycles. All calculations were performed in a spin-unpolarized manner, as commonly done for such core-level excitation simulations.[6] Spin-polarized calculations on selected test systems yield equivalent trends, as shown in the Supporting Information (Section 2.5).

In addition to employing the Slater–Janak transition-state approximation, we also performed ΔSCF calculations on selected systems, as this approach has also been used repeatedly in conjunction with periodic boundary conditions for calculating core-level excitations at interfaces and surfaces.[17,51,53,54,63] In the ΔSCF approach, the core-level binding energy is obtained as the difference in total energy between the system with, in this case, a full electron excited from the core level and the system in its ground-state configuration. Notably, while in ΔSCF calculations on finite size clusters, the excited electron can be removed from the system, when employing periodic boundary conditions it is again typically put into the lowest unoccupied orbital. If that orbital is localized in the substrate, this again results in a spurious dipole layer. In the ΔSCF calculations, due to the excitation of a full electron, the magnitude of the dipole is essentially doubled compared to the Slater–Janak case (unless this is prevented by pinning effects; see below).

For the analysis and visual representation of the data, Python was used in conjunction with NumPy[105] and matplotlib.[106] Ovito[107] was applied for generating the three-dimensional (3D) view of the system, and VESTA[108] and XCrySDen[109] were used for producing isodensity plots. The figures were compiled with GIMP.[110] The graphs in Figures 2b and 6 have been compiled using Mathematica, version 11.3 from Wolfram Research.

5. RESULTS AND DISCUSSION

5.1. Impact of the Size of the Surface Unit Cell on the Calculated Core-Level Shifts. Figure 2a shows the calculated C 1s core-level binding energies as a function of the supercell size for the methane/Al(100) interface. Applying the Slater–Janak transition-state approximation, they are obtained as the orbital energy of the partially ionized C 1s orbital relative to the system's Fermi energy. The core-level binding energies vary by as much as 1.2 eV, with the most negative binding energy obtained for the 2×2 cell and the least negative binding energy calculated for the 12×12 cell. This happens in spite of the identical chemical nature of the studied interface for all supercells. The only appreciable difference between the different supercells is the density of the created core holes (i.e., the excitation density) with only one C 1s core hole generated per supercell.

The screening charge in the metal is found right above the topmost metal layer, as shown in the Supporting Information (Section 3). It is localized exclusively below the ionized methane molecule, such that an effective interfacial dipole is created (which is modified by screening effects within the methane molecule). Due to the required charge neutrality (see above), the screening charge can be associated with the half-electron added to the system right at the Fermi level, although even if the half-electron was entirely removed from the system, the metal would be polarized by the core hole.

The main problem is that the dipole formed by the core hole and the screening/compensation charge in the metal exists in every unit cell due to the periodic boundary conditions. This is in sharp contrast to the actual situation in the experiments, where neighboring core holes with their associated polarization charges are well separated. As a consequence of collective electrostatic effects,[3,4,20] the artificial array of core holes and their countercharges in the metal creates a gradient of the electrostatic energy across the interface. This is shown schematically in Figure 2b, where we compare the electrostatic

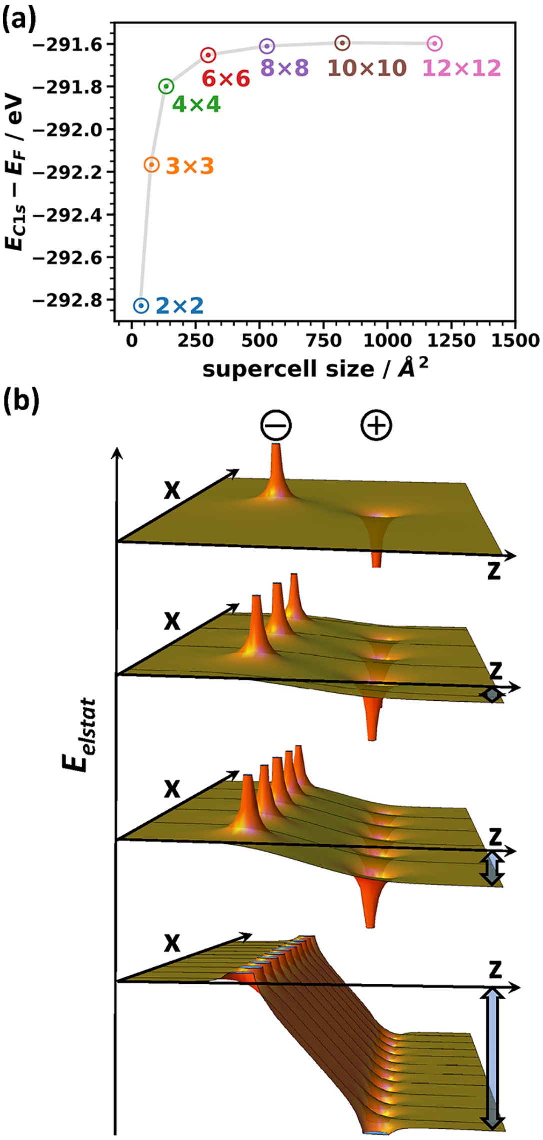

Figure 2. (a) C 1s core-level binding energy of methane adsorbed on Al(100) as a function of the chosen supercell size for calculations employing the final-state approach within the Slater−Janak transition-state approximation. (b) Electrostatic energy landscape for an electron generated by an isolated pair of a negative and a positive point charge (top panel) and by two oppositely charged, square periodic, 2D arrays of point charges (three lower panels). The distances between the charges in the arrays in the three lower panels scale as 3:2:1, and their packing densities scale as 1/9:1/4:1. While the electron electrostatic energy becomes constant for the isolated dipole in the top panel, there is a step in energy for the pairs of periodic charge arrays. These steps are schematically indicated by the blue arrows.

energy of an isolated pair of a negative and positive point charge (top panel), with the situation for 2D charge arrays of varying density. While for the single pair, the energy approaches a constant value far away from the point charges, there is a step in the electrostatic energy between the region left of the negative and right of the positive charges for all 2D charge arrays. As a consequence, the array of core holes and polarization charges causes a shift of all electronic states (including the core levels) in the adsorbate layer relative to the Fermi level of the substrate. The magnitude of that shift depends on the density of core holes, as shown in the three lower panels of Figure 2b. As discussed in the Supporting Information (Section 5), it also scales linearly with the amount of transferred charge (i.e., the effect doubles for a full- compared to a half core-hole calculation). This is insofar relevant, as Williams et al.[57] suggested that removing 2/3 instead of 1/2 of an electron (as in the original formulation by Slater) would yield numerically more accurate values for the core-level binding energies. According to the data in Section 5 of the Supporting Information, this would a priori increase the artificial electrostatic shift of the orbital energy by a factor of 4/3. It would, however, not increase the impact of artificial collective electrostatics on the core-level binding energy, as in the model by Williams et al., the orbital energy for the partially ionized system enters the expression for the ionization energy weighted by a factor of 3/4. Equivalent considerations also apply to approaches relying on the calculation of the slope of the dependence of the orbital energy on the fractional occupation, which have also been suggested by Williams et al. in ref 57.

Notably, not only final-state calculations based on the Slater−Janak transition-state approximation are adversely affected by the presence of the artificial, excitation-induced dipole layer, but also ΔSCF-type final-state calculations are significantly impacted, as is shown in the Supporting Information (Section 6). In that case, the origin of the problem is the additional energy cost associated with the creation of an artificial dipole layer instead of a single dipole.

The above considerations show that both types of final-state calculations (ΔSCF and Slater−Janak) are adversely affected by artificial collective electrostatic effects, which become stronger for high excitation densities. Naturally, the problem can be mended by considering larger supercells. In fact, as shown in Figure 2, for the system considered here, the core-level binding energy obtained with the 8 × 8 supercell is within ∼0.01 eV of the result for the 10 × 10 and 12 × 12 cells. This means that for a methane molecule in the immediate vicinity of the metal substrate, the calculation of the 8 × 8 supercell containing 16 molecules can be considered to be energetically converged.

5.2. Impact of the Creation of the Core Hole on the Global Energy Landscape.

As a next step, we discuss the direct impact of the excitation-induced dipoles on the electrostatic energy in more detail. As a starting point for that discussion, Figure 3a shows the plane-averaged electrostatic energies for the ground-state configurations of the 2 × 2 and 12 × 12 supercells. They coincide, underlining the identical physical and chemical natures of the two systems. The minima in the electrostatic energy at the positions of the Al planes as well as in the region of the adsorbate molecule are well resolved, and the minor methane-induced shift in the sample work function due to Pauli pushback[5,91,111,112] can be inferred from the energetic difference of the vacuum levels left and right of the slab (indicated by the dashed black line).

The situation changes fundamentally in the presence of core hole excitations (again half a core hole per supercell). This is shown in Figure 3b by the modification of the electrostatic energy due to the excitation of a half core-hole per unit cell (including the corresponding compensation charge in the metal). In particular, one sees that for smaller supercells (i.e.,

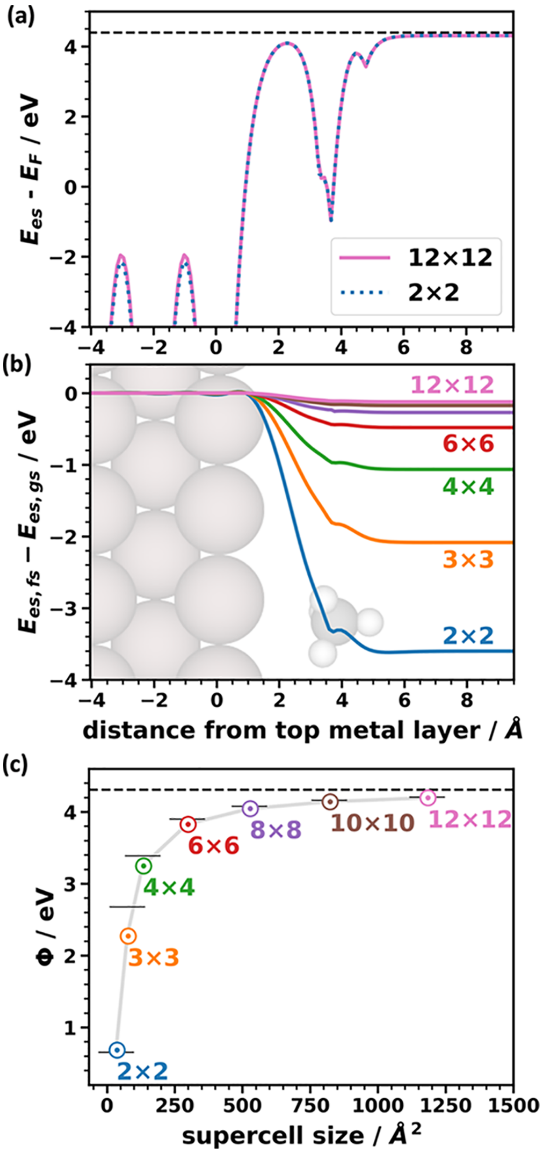

Figure 3. (a) Plane-averaged electrostatic energy of the methane/Al(100) interface for the smallest (2 × 2; dotted blue line) and largest (12 × 12; solid pink line) cells. The work function on the methane side of the slab amounts to 4.31 eV, while on the Al side it is 4.40 eV (yielding an adsorption-induced work function change of 0.09 eV; see the dashed horizontal line). (b) Calculated change in the plane-averaged electrostatic energy between a final-state calculation (including a half core-hole excitation), $E_{es,fs}$, and the ground state, $E_{es,gs}$ for different excitation densities caused by different supercell sizes. The latter are denoted directly in the graph (the lines for the 8 × 8 (violet) and 10 × 10 (brown) cells are not labeled due to the limited available space). (c) Work function, Φ, of the systems with a half core-hole excitation per supercell on the methane side of the slab. The work function obtained in the ground-state calculation is indicated by the dashed black line at 4.31 eV. The work functions on the Al side essentially do not change, as shown in the Supporting Information (Section 7). The values obtained with the simple electrostatic model in

Figure 3. continued

the main text are indicated as short horizontal lines for the corresponding supercells.

higher excitation and dipole densities in the final-state calculations) the change in the averaged electrostatic energy is more pronounced. Notably, the majority of that change occurs between the region of electron accumulation right above the topmost metal layer and the position of the carbon atom of the adsorbed methane molecules. When analyzing the work function of the system in the presence of a core hole excitation (given as the difference between the Fermi energy and the electrostatic energy far above the surface), one observes a strong, supercell-dependent change, as shown in Figure 3c. Even though this work function is not of immediate relevance for the studied interface, it is still useful for judging the collective electrostatic artifact: the overall trend for the evolution of the work function shift in Figure 3c is similar to that for the core-level binding energies in Figure 2a and, as discussed in the Supporting Information (Section 4), it is essentially inversely proportional to the size of the unit cell (depolarization effects notwithstanding).

In fact, it is even rather straightforward to obtain a rough estimate of the work function change due to the core-level excitation solely based on electrostatic and geometric arguments, i.e., without performing any quantum-mechanical simulations (see the Supporting Information, Section 4.2). Such a model yields the values indicated by the short horizontal lines in Figure 3c, which agree rather well with the actual work function changes and, thus, provide a first handle for estimating the adverse impact of the artificial electrostatic effects discussed here.

In this context, it is, however, worthwhile mentioning that the absolute magnitude of the work function shift is significantly larger than the shift of the core-level binding energies (as can be inferred from a comparison of Figures 2a and 3c). To understand that, one has to analyze the difference between the electrostatic energy at the location of the core level and in the far-field, high above the interface.

5.3. Local Impact of the Dipoles.

As a first step for analyzing locality effects, it is useful to provide a spatially resolved illustration of the differences in the change in electrostatic energy that occurs due to the presence of an isolated core hole and due to a dense layer of core holes. To that aim, Figure 4 compares the 2D cross sections of that energy change for the 2 × 2 and 12 × 12 cells. While for the 12 × 12 supercell, one essentially obtains the situation of an isolated dipole, which affects the energy landscape only locally, for the 2 × 2 cell, the above-discussed global shift of the electrostatic energy also (infinitely) far above the metal surface occurs.

Figure 4 also reveals that the change in electrostatic energy varies significantly in the lateral direction, especially at low coverage. A detailed analysis of the impact of these lateral fluctuations shows that they are responsible for the much smaller artificial shifts in core-level binding energies compared to the shifts in work functions (see above). This is a direct consequence of core-level binding energies being sensitive to the local electrostatic energy at the position of the orbital from which the electron is excited.[3,8,20] In contrast, the work function measures the electrostatic situation in the far-field, such that the lateral fluctuations of the potential energy are no longer relevant. This aspect is of practical relevance as it, for example, results in

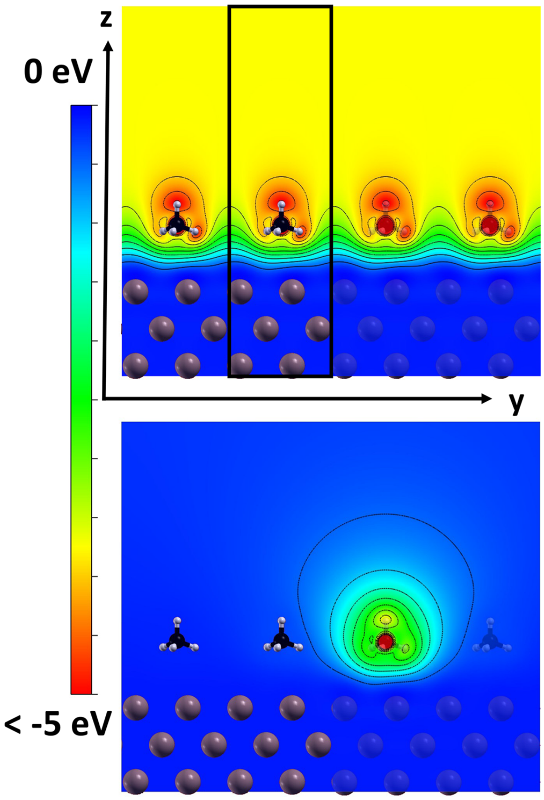

Figure 4. Calculated difference in electrostatic energy between the final-state and the ground-state calculations for the 2 × 2 (top) and the 12 × 12 (bottom) cells. The values are plotted for a plane parallel to one of the unit cell axes, containing the nuclei of the C atoms. The overlaid atomic structure of the interface is shaded in the right half of the plots to better resolve changes in electrostatic energy close to the nuclei. Furthermore, only part of the 12 × 12 supercell is shown and the 2 × 2 unit cell is repeated four times in the vertical direction.

core-level shifts in polar SAMs becoming sensitive to sample inhomogeneities.[20] In the present context, it means that averaging the electrostatic energy over the entire unit cell (like in Figure 3b) very well characterizes the situation for the work function but fails to properly capture the "locality" of core-level shifts. To show that also quantitatively, one has to analyze the electrostatic energy averaged over a much smaller area than in Figure 3b. This is done in the Supporting Information (Section 8), with the results fully supporting locality as the main reason for the smaller artifacts in the core-level energy calculations.

5.4. Impact of the Adsorption Distance on Core-Level Energies. The next aspect to be addressed is to what extent the discussed artifact depends on the geometrical structure of the interface. In particular, we will address how spurious collective electrostatic effects depend on the distance between the metal surface and the atom probed by XPS. This is, for example, relevant when bulky side groups lift the backbone of an adsorbed molecule from the metal substrate. It is also relevant for upright-standing adsorbates,[113−119] e.g., in self-assembled, covalently bonded monolayers.[120−126] To qualitatively assess the situation, we systematically varied the distance between the methane molecule and the surface. In this way, effects arising from (system-specific) screening by the upright molecular backbones between the probed atom and the substrate are not accounted for. Still, the model serves to illustrate the impact of an increased charge-transfer distance.

Figure 5 shows the dependence of the core-level binding energy on the adsorption distance of the methane molecules (specified relative to the equilibrium distance) for differently sized supercells. This plot reveals several interesting aspects:

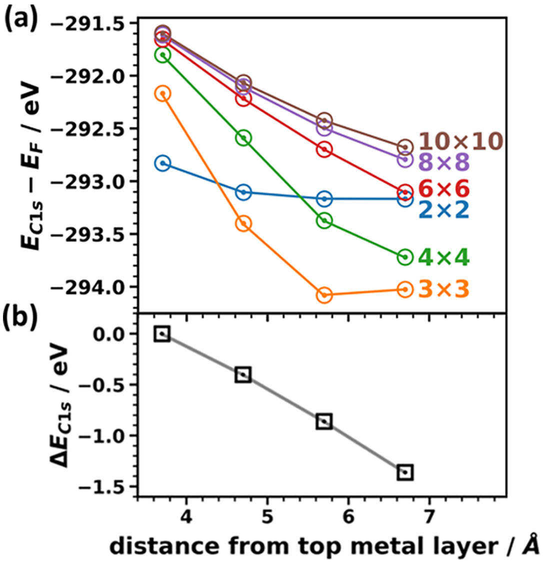

Figure 5. (a) C 1s core-level energies for methane on Al(100) relative to the Fermi level for different unit cell sizes and different adsorption heights of the methane molecule (blue: 2 × 2 unit cell, orange: 3 × 3 supercell, green: 4 × 4 supercell, red: 6 × 6 supercell, violet: 8 × 8 supercell, brown: 10 × 10 supercell). No data points for 12 × 12 supercells could be included in this plot, as for this very large cell we failed to converge the SCF cycle in the calculations for increased adsorption distances. (b) Difference in core-level energies between the 10 × 10 and the 4 × 4 supercells.

(i) The data points for the 10 × 10 and 8 × 8 supercells essentially coincide at small distances. This implies that there the 8 × 8 and 10 × 10 data display the true effect of core hole and screening. For larger distances, the deviations between the 10 × 10 and 8 × 8 unit cells increase, and at 3 Å above the equilibrium distance (i.e., at an adsorption distance of 6.69 Å) they exceed 0.1 eV; notably, at that adsorption distance also the excitation-induced work function change reaches 0.5 eV, even in the 10 × 10 cell. This is attributed to the growth of the dipole per unit cell upon increasing the charge-transfer distances. In view of the observation that at large adsorption distances even the 10 × 10 data are impacted by artificial collective electrostatic shifts, we refrain from fitting the data with simple electrostatic image charge corrections (where the shift of the core-level binding energies would be inversely proportional to the distance of the excited atom from the mirror charge plane).[34]

(ii) The calculated distance dependence of the core-level binding energies clearly deteriorates for the 6 × 6 and 4 ×

4 unit cells. In fact, the deviations between the 10 × 10 simulations and the 4 × 4 simulations skyrocket for larger distances, as is shown in Figure 5b. These results imply that to mitigate the adverse impact of artificial collective electrostatic effects, at larger adsorption distances, one would have to simulate even larger supercells than those studied here. Considering that already the calculation of the 10 × 10 cell is reaching the limits of present computational capacities, studying further enlarged cells is far from trivial. In fact, we failed to achieve convergence in the SCF procedure for 12 × 12 cells at larger distances.

(iii) For the smallest considered cells, the situation changes fundamentally. Especially for the 2 × 2 unit cell, the core-level binding energy becomes essentially independent of the adsorption distance. This behavior is reminiscent of the situation encountered for Fermi-level pinning,[5,30,91,112,127−132] as for the smallest unit cells, the shift in electrostatic energy due to the artificial dipole layer becomes so strong that the lowest unoccupied states of the adsorbed molecules would get pushed below the Fermi level of the substrate. This is counteracted by electrons being transferred from the metal into the formerly unoccupied molecular states, significantly modifying the net charge rearrangements (see the Supporting Information, Section 9). The ensuing counterdipole prevents any further increase of the potential step across the interface. Consequently, the energetic positions of the electronic states become independent of the adsorption distance. Such a behavior is inconsistent with the experimental situation for two reasons: first, at least in the present model system, the pinning situation is solely a consequence of the artificial collective electrostatic effects resulting from unrealistically high excitation densities in the simulations. Second, even if the core hole locally shifted unoccupied states below the Fermi level (for example, because of a much smaller energy gap of the adsorbate), for many interfaces, the time scales of the photoelectron experiments[133,134] would be such that the (partial) filling of these states with electrons would be too slow to affect the measured kinetic energies of the escaping electrons (and, thus, the core-level binding energies).

An aspect that is somewhat surprising about the pinned situation for the 2 × 2 unit cell is that pinning occurs at core-level binding energies that are significantly less negative than for some of the considered 3 × 3 and 4 × 4 cells. On the one hand, we attribute this to the different degrees of localization of the core levels and the much more delocalized unoccupied states at which pinning occurs. Consequently, the different orbitals "probe" shifts in the electrostatic energy in different spatial regions and are, thus, differently affected. On the other hand, we observe a more broadened low-lying unoccupied density of states in the 2 × 2 cell compared to the larger supercells. This can also result in Fermi-level pinning already for smaller energetic shifts. The relevant factor here is that pinning occurs at the unoccupied states primarily localized at the excited molecules, as these lie lowest in energy due to the dipole-induced shifts. For the 2 × 2 cell, all adsorbate molecules are excited and, thus, all unoccupied states are shifted by the same amount, favoring a strong intermolecular coupling. Conversely, for 4 × 4 and larger supercells, all excited molecules are surrounded by molecules in their ground state, effectively preventing such a coupling. A more detailed discussion of the impact of the excitation density and the adsorption distance on the shape of the unoccupied density of states can be found in the Supporting Information (Section 9). There, one also finds a discussion of the impact of the choice of the basis set on the unoccupied states of methane, which can quantitatively (albeit not qualitatively) change the situation.

5.5. Possible Strategies for Avoiding Spurious Electrostatic Effects in Final-State Calculations Employing Periodic Boundary Conditions. Considering that the discussed artifacts are electrostatic in nature, the question arises whether one could also devise an electrostatic correction scheme. The simplest approach would be to employ a plate-capacitor model like that used in Section 5.2. Such a correction only describes the situation in the far-field (i.e., at a sufficient distance from the interface) and does not reproduce the shift of the local electrostatic potential at the position of the excited atom. The latter is, however, what counts for the core-level shifts, as discussed in Section 5.3.

A solution to the locality problem would be to explicitly consider the spurious shifts in electrostatic energy due to the periodic replicas of the (half) core holes and their image charges.[87,103] In view of the employed dipole correction (see Section 4), periodicity is considered here only in the directions parallel to the surface. The resulting correction for the electrostatic energy of an electron at the position of the central core hole placed at the origin of the coordinate system (at $i = j = 0$), E_{corr}, is then given by

$$E_{\mathrm{corr}} = \frac{1}{4\pi\varepsilon_0\varepsilon}\sum_{i,j\neq 0}\frac{Q}{\sqrt{(i\cdot a)^2 + (j\cdot a)^2}} - \frac{Q}{\sqrt{(i\cdot a)^2 + (j\cdot a)^2 + D^2}} \tag{1}$$

Here, a square lattice (like in the studied model system) with lattice constant a is assumed. For the half core-hole calculations, the charge of the core hole and the mirror charge are both set to $Q = 0.5e$ (with e being the elementary charge). D corresponds to the distance between a core hole and its mirror charge and is given by $D = 2(z - z_0)$, where z denotes the position of the core hole above the top metal layer and z_0 refers to the position of the image plane set to 1.59 Å for Al(100).[135] ε is an effective dielectric constant that describes the screening within the adsorbate layer. When setting ε to 2.1, one obtains correction energies of 1.20 and 0.17 eV for the 2 × 2 and 4 × 4 supercells, respectively. This, indeed, provides an excellent correction of the artificial shifts in Figure 2 (see also Figure 6a). A complication in this context is, however, that the correct value of ε is a priori not known, while especially for small unit cells its value rather significantly impacts the correction (see Figure 6b).

This raises the question of whether one could avoid the spurious dipoles in neighboring unit cells by achieving charge neutrality in every unit cell via some static compensation charge rather than by placing the excited (half) electron into an unoccupied level. A homogeneous background charge often employed in bulk calculations[137] will typically still create an artificial dipole layer, whose magnitude depends on the size of the unit cell and, thus, on the size of the vacuum gap separating periodic replicas of the slab.[83] This should become particularly problematic when comparing core-level excitations from atoms at different positions within the unit cell. Another possibility would be to account for the compensation charge via the virtual

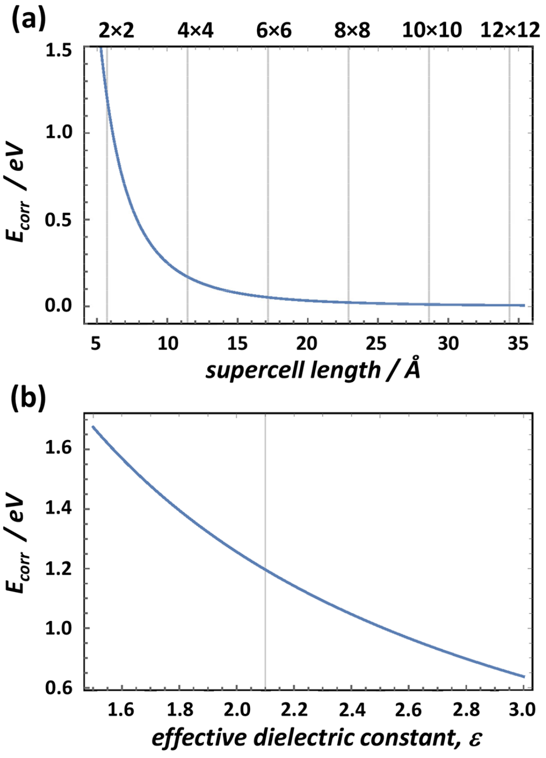

Figure 6. (a) Dependence of the point-charge-derived correction energy calculated employing eq 1, E_{corr}, on the size of the unit cell, with ε set to 2.1. The vertical lines denote supercells considered in the present manuscript. In the simulation, the actual lattice constant of our model system (5.728 Å), the optimized adsorption distance of 3.678 Å, an image plane of 1.59 Å above the topmost Al layer,[135] and half an elementary charge at every point charge position have been used. (b) Dependence of the point charge-derived correction energy calculated employing eq 1, E_{corr}, on the effective dielectric constant describing screening processes at the interface. The vertical line at a dielectric constant of 2.1 indicates the situation quoted in the main manuscript. The simulations have been performed using Mathematica.[136]

crystal approximation.[82−85] As shown by Bagus et al.,[2] this eliminates certain artifacts occurring when the compensation charge is put into the conduction band of a semiconductor substrate (see Section 1). As it does not eliminate the spurious interfacial dipole layer, it, however, also does not remove the spurious potential drop between the substrate and the adsorbate.

A strategy for avoiding that drop would be to put compensation charges into a charged sheet above the adsorbate layer (in analogy to the charge reservoir electrostatic sheet technique (CREST) used to model the band bending in the extended depletion regions of semiconductor surfaces; albeit there, the charged sheet is placed below the slab).[138,139] This would, however, also result in an incorrect description of the screening potential between the actually generated core hole and the metal substrate, as the charged sheet tends to concentrate the electric field in the region between the core hole and the sheet. In the region of the metal, this results in a too small field due to the core hole, with the deviation being particularly large for smaller unit cells (like the 2×2 cell, as shown in the Supporting Information, Section 11).

Likewise, the problem could not be solved by putting the compensation charge into some higher-lying unoccupied levels within the molecules. This would largely avoid the artificial dipoles, but it would also render all molecules essentially charge neutral (including the one that is actually excited); i.e., in such a calculation, screening by the metal would be eliminated altogether, which would again not represent the actual situation encountered in an experiment.

Thus, we envision four strategies (with varying strengths and weaknesses) that have the potential to either avoid or correct for the spurious collective electrostatic effects discussed in this paper:

(i) Employing the electrostatic correction scheme described at the beginning of this section.

(ii) Increasing the supercell size in final-state simulations applying periodic boundary conditions until the artificial core-level shifts are below a certain threshold (see above). In this process, the coverage has to be kept at its initial value while exciting only one atom per supercell. Converging the supercell size will typically be feasible for flat-lying adsorbates, where charge-transfer distances (and, thus, spurious dipoles) are rather small (albeit at significantly increased computational costs). For studying upright-standing adsorbate layers of spatially extended molecules, which are often relevant for practical applications, the required supercells will, however, often be computationally not accessible.

(iii) Especially for atoms far from the surface, initial-state calculations with an a posteriori mirror charge correction proportional to $1/(4\varepsilon(z - z_0))$ are a viable strategy to account for screening effects. We have, in fact, routinely and successfully employed this approach for modeling core-level shifts in self-assembled monolayers.[4,14,20,32,68] This approach, however, poses the disadvantage that it describes screening on purely electrostatic grounds, disregarding, e.g., quantum-mechanical effects, which might become relevant especially for atoms that are part of or close to the surface (see Section 1). Moreover, the determination of the relevant parameters (like the dielectric constant of the monolayer) is not necessarily straightforward.

(iv) Another strategy to avoid spurious electrostatics would be to refrain from employing periodic boundary conditions and to study finite size clusters as a model for the interface. True collective electrostatic effects at the interface could then be accounted for by properly designed electrostatic embedding schemes,[76−78] like the "periodic electrostatic embedded cluster method" (PEECM).[74,75] As far as the properties of the extended interface vs the cluster are concerned, such corrections would, however, only account for purely electrostatic effects.

6. CONCLUSIONS

The above data show that spurious electrostatic effects can come into play when simulating XP spectra within the final-state framework in combination with periodic boundary conditions. The screening/compensation charge in the metal creates a dipole, which due to the periodic boundary conditions is spuriously repeated in every unit cell. This creates an artificial, dense layer of dipoles, which shifts all electronic states in the adsorbed molecule relative to the metal Fermi level. Consequently, also their core-level binding energies are increased. Therefore, one observes a pronounced shift in the calculated core-level binding energies as a function of the employed supercell size (and the resulting excitation density). For the methane/Al(100) system studied here, this shift amounts to 1.2 eV when comparing calculations for 2 × 2 cells (with an area of 33 Å^2) and 12 × 12 cells (with an area of 1081 Å^2), when in each cell a single molecule is ionized. A similar effect is obtained when comparing the total energies of the systems in their ground and excited states (i.e., when applying the ΔSCF procedure; see the Supporting Information, Section 6).

Another quantity that is significantly changed by the interfacial dipole layer due to the core-level excitations is the work function obtained in the final-state calculations. Even though this quantity is not of practical relevance for the actual experimental situation, it is still useful for illustrating the artifacts discussed in this paper. Moreover, a significant work function change in a final-state calculation is a strong indication for artificial core-level shifts. This has the advantage that one can predict, whether problems occur, already on the basis of a single calculation without the need to converge supercell sizes.

When increasing the distance of the excited core hole from the metal substrate, the artificial collective electrostatic effects increase even further, such that performing trustworthy final-state calculations in conjunction with periodic boundary conditions becomes virtually impossible.

For cases in which converging the lateral size of the unit cell in final-state calculations becomes impossible, we suggest a simple electrostatic correction, whose application, however, requires a reasonable guess for the effective dielectric constant of the interface. Alternative strategies for studying such situations would be to perform initial-state calculations with an a posteriori mirror charge screening or to join cluster calculations with electrostatic embedding schemes, where each of the suggested approaches has its own strengths and limitations.

■ ASSOCIATED CONTENT

Supporting Information

The Supporting Information is available free of charge at https://pubs.acs.org/doi/10.1021/acsomega.0c03209.

> Further details of the computational methodology, projected densities of states of methane monolayers for different supercell sizes and adsorption distances, C 1s core-level energies for different methane coverages, additional data of test calculations and convergence tests, charge rearrangements for different excitation densities and adsorption heights as well as the corresponding cumulative charge rearrangements, work function and core-level shifts as a function of the inverse supercell size, core-level shifts with respect to the charge removed from the core hole and with respect to the unit cell size, electrostatic energy plane averaged over differently sized areas, calculations underlining the dependence of core-level shifts on the local electrostatic energy, simple electrostatic model for estimating work function changes, energies of the frontier orbitals of methane as a function of the used basis set, and electric fields at various excitation densities for a CREST-like correction scheme (PDF)

■ AUTHOR INFORMATION

Corresponding Author

Egbert Zojer − *Institute of Solid State Physics, Graz University of Technology, 8010 Graz, Austria;* orcid.org/0000-0002-6502-1721; Phone: +43-316-873-8475; Email: egbert.zojer@tugraz.at

Authors

Thomas C. Taucher − *Institute of Solid State Physics, Graz University of Technology, 8010 Graz, Austria;* orcid.org/0000-0002-0071-1799

Oliver T. Hofmann − *Institute of Solid State Physics, Graz University of Technology, 8010 Graz, Austria;* orcid.org/0000-0002-2120-3259

Complete contact information is available at: https://pubs.acs.org/10.1021/acsomega.0c03209

Notes

The authors declare no competing financial interest.

■ ACKNOWLEDGMENTS

The authors are thankful to R. Maurer, G. S. Michelitsch, and C. Winkler for their stimulating discussions. Financial support by the Austrian Science Fund (FWF): P28051-N36 is gratefully acknowledged. The quantum-mechanical calculations have been performed using the Vienna Scientific Cluster (VSC3).

■ REFERENCES

(1) Egelhoff, W. F. Core-Level Binding-Energy Shifts at Surfaces and in Solids. *Surf. Sci. Rep.* **1987**, *6*, 253−415.

(2) Bagus, P. S.; Ilton, E. S.; Nelin, C. J. The Interpretation of XPS Spectra: Insights into Materials Properties. *Surf. Sci. Rep.* **2013**, *68*, 273−304.

(3) Abu-Husein, T.; Schuster, S.; Egger, D. A.; Kind, M.; Santowski, T.; Wiesner, A.; Chiechi, R.; Zojer, E.; Terfort, A.; Zharnikov, M. The Effects of Embedded Dipoles in Aromatic Self-Assembled Monolayers. *Adv. Funct. Mater.* **2015**, *25*, 3943−3957.

(4) Taucher, T. C.; Hehn, I.; Hofmann, O. T.; Zharnikov, M.; Zojer, E. Understanding Chemical versus Electrostatic Shifts in X-Ray Photoelectron Spectra of Organic Self-Assembled Monolayers. *J. Phys. Chem. C* **2016**, *120*, 3428−3437.

(5) Zojer, E.; Taucher, T. C.; Hofmann, O. T. The Impact of Dipolar Layers on the Electronic Properties of Organic/Inorganic Hybrid Interfaces. *Adv. Mater. Interfaces* **2019**, *6*, No. 1900581.

(6) Bagus, P. S.; Nelin, C. J.; Zhao, X.; Levchenko, S. V.; Davis, E.; Weng, X.; Späth, F.; Papp, C.; Kuhlenbeck, H.; Freund, H.-J. Revisiting Surface Core-Level Shifts for Ionic Compounds. *Phys. Rev. B* **2019**, *100*, No. 115419.

(7) Nelin, C. J.; Uhl, F.; Staemmler, V.; Bagus, P. S.; Fujimori, Y.; Sterrer, M.; Kuhlenbeck, H.; Freund, H.-J. Surface Core-Level Binding Energy Shifts for MgO(100). *Phys. Chem. Chem. Phys.* **2014**, *16*, 21953−21956.

(8) Natan, A.; Kronik, L.; Haick, H.; Tung, R. T. Electrostatic Properties of Ideal and Non-Ideal Polar Organic Monolayers: Implications for Electronic Devices. *Adv. Mater.* **2007**, *19*, 4103−4117.

(9) Heimel, G.; Rissner, F.; Zojer, E. Modeling the Electronic Properties of π-Conjugated Self-Assembled Monolayers. *Adv. Mater.* **2010**, *22*, 2494−2513.

(10) Heimel, G.; Salzmann, I.; Duhm, S.; Koch, N. Design of Organic Semiconductors from Molecular Electrostatics. *Chem. Mater.* **2011**, *23*, 359−377.

(11) Monti, O. L. A. Understanding Interfacial Electronic Structure and Charge Transfer: An Electrostatic Perspective. *J. Phys. Chem. Lett.* **2012**, *3*, 2342−2351.

(12) Chen, X.; Annadata, H. V.; Kretz, B.; Zharnikov, M.; Chi, X.; Yu, X.; Egger, D. A.; Nijhuis, C. A. Interplay of Collective Electrostatic

Effects and Level Alignment Dictates the Tunneling Rates across Halogenated Aromatic Monolayer Junctions. *J. Phys. Chem. Lett.* **2019**, *10*, 4142−4147.

(13) Cabarcos, O. M.; Shaporenko, A.; Weidner, T.; Uppili, S.; Dake, L. S.; Zharnikov, M.; Allara, D. L. Physical and Electronic Structure Effects of Embedded Dipoles in Self-Assembled Monolayers: Characterization of Mid-Chain Ester Functionalized Alkanethiols on Au{111}. *J. Phys. Chem. C* **2008**, *112*, 10842−10854.

(14) Gärtner, M.; Sauter, E.; Nascimbeni, G.; Petritz, A.; Wiesner, A.; Kind, M.; Abu-Husein, T.; Bolte, M.; Stadlober, B.; Zojer, E.; Terfort, A.; Zharnikov, M. Understanding the Properties of Tailor-Made Self-Assembled Monolayers with Embedded Dipole Moments for Interface Engineering. *J. Phys. Chem. C* **2018**, *122*, 28757−28774.

(15) Sauter, E.; Gilbert, C.-O.; Morin, J.-F.; Terfort, A.; Zharnikov, M. Mixed Monomolecular Films with Embedded Dipolar Groups on Ag(111). *J. Phys. Chem. C* **2018**, *122*, 19514−19523.

(16) Kirchhuebel, T.; Monti, O. L. A.; Munakata, T.; Kera, S.; Forker, R.; Fritz, T. The Role of Initial and Final States in Molecular Spectroscopies. *Phys. Chem. Chem. Phys.* **2019**, *21*, 12730−12747.

(17) Viñes, F.; Sousa, C.; Illas, F. On the Prediction of Core Level Binding Energies in Molecules, Surfaces and Solids. *Phys. Chem. Chem. Phys.* **2018**, *20*, 8403−8410.

(18) Maurer, R. J.; Freysoldt, C.; Reilly, A. M.; Brandenburg, J. G.; Hofmann, O. T.; Björkman, T.; Lebègue, S.; Tkatchenko, A. Advances in Density-Functional Calculations for Materials Modeling. *Annu. Rev. Mater. Res.* **2019**, *49*, 1−30.

(19) Koopmans, T. Über die Zuordnung von Wellenfunktionen und Eigenwerten zu den Einzelnen Elektronen Eines Atoms. *Physica* **1934**, *1*, 104−113.

(20) Hehn, I.; Schuster, S.; Wächter, T.; Abu-Husein, T.; Terfort, A.; Zharnikov, M.; Zojer, E. Employing X-Ray Photoelectron Spectroscopy for Determining Layer Homogeneity in Mixed Polar Self-Assembled Monolayers. *J. Phys. Chem. Lett.* **2016**, *7*, 2994−3000.

(21) Baerends, E. J.; Gritsenko, O. V.; van Meer, R. The Kohn−Sham Gap, the Fundamental Gap and the Optical Gap: The Physical Meaning of Occupied and Virtual Kohn−Sham Orbital Energies. *Phys. Chem. Chem. Phys.* **2013**, *15*, 16408.

(22) Joubert, D. P. Mapping Kohn-Sham Eigenenergies onto Vertical Ionization Energies and Electron Affinities. *Phys. Rev. A* **2012**, *85*, No. 1174.

(23) Perdew, J. P.; Norman, M. R. Electron Removal Energies in Kohn-Sham Density-Functional Theory. *Phys. Rev. B* **1982**, *26*, 5445−5450.

(24) Pueyo Bellafont, N.; Bagus, P. S.; Illas, F. Prediction of Core Level Binding Energies in Density Functional Theory: Rigorous Definition of Initial and Final State Contributions and Implications on the Physical Meaning of Kohn-Sham Energies. *J. Chem. Phys.* **2015**, *142*, No. 214102.

(25) Stowasser, R.; Hoffmann, R. What Do the Kohn-Sham Orbitals and Eigenvalues Mean? *J. Am. Chem. Soc.* **1999**, *121*, 3414−3420.

(26) Chong, D. P.; Gritsenko, O. V.; Baerends, E. J. Interpretation of the Kohn−Sham Orbital Energies as Approximate Vertical Ionization Potentials. *J. Chem. Phys.* **2002**, *116*, 1760−1772.

(27) Methfessel, M.; Fiorentini, V.; Oppo, S. Connection between Charge Transfer and Alloying Core-Level Shifts Based on Density-Functional Calculations. *Phys. Rev. B* **2000**, *61*, 5229−5236.

(28) Heimel, G.; Romaner, L.; Brédas, J.-L.; Zojer, E. Organic/Metal Interfaces in Self-Assembled Monolayers of Conjugated Thiols: A First-Principles Benchmark Study. *Surf. Sci.* **2006**, *600*, 4548−4562.

(29) Giesbers, M.; Marcelis, A. T. M.; Zuilhof, H. Simulation of XPS C1s Spectra of Organic Monolayers by Quantum Chemical Methods. *Langmuir* **2013**, *29*, 4782−4788.

(30) El-Sayed, A.; Borghetti, P.; Goiri, E.; Rogero, C.; Floreano, L.; Lovat, G.; Mowbray, D. J.; Cabellos, J. L.; Wakayama, Y.; Rubio, A.; Ortega, J. E.; de Oteyza, D. G. Understanding Energy-Level Alignment in Donor−Acceptor/Metal Interfaces from Core-Level Shifts. *ACS Nano* **2013**, *7*, 6914−6920.

(31) Pueyo Bellafont, N.; Illas, F.; Bagus, P. S. Validation of Koopmans' Theorem for Density Functional Theory Binding Energies. *Phys. Chem. Chem. Phys.* **2015**, *17*, 4015−4019.

(32) Ishiwari, F.; Nascimbeni, G.; Sauter, E.; Tago, H.; Shoji, Y.; Fujii, S.; Kiguchi, M.; Tada, T.; Zharnikov, M.; Zojer, E.; Fukushima, T. Triptycene Tripods for the Formation of Highly Uniform and Densely Packed Self-Assembled Monolayers with Controlled Molecular Orientation. *J. Am. Chem. Soc.* **2019**, *141*, 5995−6005.

(33) Jackson, J. D. *Classical Electrodynamics*, 3rd ed.; Wiley: New York, 1999.

(34) Neaton, J. B.; Hybertsen, M. S.; Louie, S. G. Renormalization of Molecular Electronic Levels at Metal-Molecule Interfaces. *Phys. Rev. Lett.* **2006**, *97*, No. 98.

(35) Bagus, P. S.; Pacchioni, G.; Parmigiani, F. Surface Core-Level Spectroscopy of Cu(100) and Al(100). *Phys. Rev. B* **1991**, *43*, 5172−5175.

(36) Bagus, P. S.; Pacchioni, G. Surface-Bulk Core-Level Binding-Energy Shifts for Al(100). *Phys. Rev. B* **1993**, *48*, 15274−15282.

(37) Pehlke, E.; Scheffler, M. Evidence for Site-Sensitive Screening of Core Holes at the Si and Ge (001) Surface. *Phys. Rev. Lett.* **1993**, *71*, 2338−2341.

(38) Stierle, A.; Tieg, C.; Dosch, H.; Formoso, V.; Lundgren, E.; Andersen, J. N.; Köhler, L.; Kresse, G. Surface Core Level Shift Observed on NiAl(1 1 0). *Surf. Sci.* **2003**, *529*, L263−L268.

(39) Birgersson, M.; Almbladh, C.-O.; Borg, M.; Andersen, J. N. Density-Functional Theory Applied to Rh(111) and CO/Rh(111) Systems: Geometries, Energies, and Chemical Shifts. *Phys. Rev. B* **2003**, *67*, No. B864.

(40) Onida, G.; Reining, L.; Rubio, A. Electronic Excitations: Density-Functional versus Many-Body Green's-Function Approaches. *Rev. Mod. Phys.* **2002**, *74*, 601−659.

(41) Danovich, D. Green's Function Methods for Calculating Ionization Potentials, Electron Affinities, and Excitation Energies: GF Methods for Calculating IPs, EAs, and Excitation Energies. *Wiley Interdiscip. Rev.: Comput. Mol. Sci.* **2011**, *1*, 377−387.

(42) Peng, B.; Kowalski, K. Green's Function Coupled-Cluster Approach: Simulating Photoelectron Spectra for Realistic Molecular Systems. *J. Chem. Theory Comput.* **2018**, *14*, 4335−4352.

(43) Golze, D.; Wilhelm, J.; van Setten, M. J.; Rinke, P. Core-Level Binding Energies from *GW*: An Efficient Full-Frequency Approach within a Localized Basis. *J. Chem. Theory Comput.* **2018**, *14*, 4856−4869.

(44) van Setten, M. J.; Costa, R.; Viñes, F.; Illas, F. Assessing *GW* Approaches for Predicting Core Level Binding Energies. *J. Chem. Theory Comput.* **2018**, *14*, 877−883.

(45) Besley, N. A.; Asmuruf, F. A. Time-Dependent Density Functional Theory Calculations of the Spectroscopy of Core Electrons. *Phys. Chem. Chem. Phys.* **2010**, *12*, 12024.

(46) Casida, M. E. Time-Dependent Density Functional Response Theory for Molecules. *Recent Advances in Computational Chemistry*; World Scientific, 1995; Vol. *1*, pp 155−192.

(47) Dreuw, A.; Head-Gordon, M. Single-Reference Ab Initio Methods for the Calculation of Excited States of Large Molecules. *Chem. Rev.* **2005**, *105*, 4009−4037.

(48) Burke, K.; Werschnik, J.; Gross, E. K. U. Time-Dependent Density Functional Theory: Past, Present, and Future. *J. Chem. Phys.* **2005**, *123*, No. 062206.

(49) Runge, E.; Gross, E. K. U. Density-Functional Theory for Time-Dependent Systems. *Phys. Rev. Lett.* **1984**, *52*, 997−1000.

(50) Boman, M.; Aagren, H.; Stafstroem, S. A Delta Self-Consistent-Field Study of Core Electron Binding Energies of Model Molecules for the Aluminum/Polythiophene Interface. *J. Phys. Chem. A* **1995**, *99*, 16597−16601.

(51) Köhler, L.; Kresse, G. Density Functional Study of CO on Rh(111). *Phys. Rev. B* **2004**, *70*, No. 13.

(52) Morikawa, Y.; Hayashi, T.; Liew, C. C.; Nozoye, H. First-Principles Theoretical Study of Alkylthiolate Adsorption on Au. *Surf. Sci.* **2002**, *507−510*, 46−50.

(53) Happel, M.; Luckas, N.; Viñes, F.; Sobota, M.; Laurin, M.; Libuda, J. SO_2 Adsorption on Pt(111) and Oxygen Precovered Pt(111): A Combined Infrared Reflection Absorption Spectroscopy and Density Functional Study. *J. Phys. Chem. C* **2011**, *115*, 479−491.

(54) Susi, T.; Kaukonen, M.; Havu, P.; Ljungberg, M. P.; Ayala, P.; Kauppinen, E. I. Core Level Binding Energies of Functionalized and Defective Graphene. *Beilstein J. Nanotechnol.* **2014**, *5*, 121−132.

(55) Slater, J. C. Statistical Exchange-Correlation in the Self-Consistent Field. *Advances in Quantum Chemistry*; Elsevier, 1972; Vol. *6*, pp 1−92.

(56) Slater, J. C. *Quantum Theory of Molecules and Solids*; McGraw-Hill, 1974; Vol. *4*.

(57) Williams, A. R.; deGroot, R. A.; Sommers, C. B. Generalization of Slater's Transition State Concept. *J. Chem. Phys.* **1975**, *63*, 628−631.

(58) Janak, J. F. Proof That $\partial E \partial n i = \varepsilon$ in Density-Functional Theory. *Phys. Rev. B* **1978**, *18*, 7165−7168.

(59) Hadjisavvas, N.; Theophilou, A. Rigorous Formulation of Slater's Transition-State Theory for Excited States. *Phys. Rev. A* **1985**, *32*, 720−724.

(60) Triguero, L.; Plashkevych, O.; Pettersson, L. G. M.; Ågren, H. Separate State vs. Transition State Kohn-Sham Calculations of X-Ray Photoelectron Binding Energies and Chemical Shifts. *J. Electron Spectrosc. Relat. Phenom.* **1999**, *104*, 195−207.

(61) Lizzit, S.; Baraldi, A.; Groso, A.; Reuter, K.; Ganduglia-Pirovano, M. V.; Stampfl, C.; Scheffler, M.; Stichler, M.; Keller, C.; Wurth, W.; Menzel, D. Surface Core-Level Shifts of Clean and Oxygen-Covered Ru(0001). *Phys. Rev. B* **2001**, *63*, No. 205419.

(62) Fujimori, Y.; Zhao, X.; Shao, X.; Levchenko, S. V.; Nilius, N.; Sterrer, M.; Freund, H.-J. Interaction of Water with the CaO(001) Surface. *J. Phys. Chem. C* **2016**, *120*, 5565−5576.

(63) Diller, K.; Maurer, R. J.; Müller, M.; Reuter, K. Interpretation of X-Ray Absorption Spectroscopy in the Presence of Surface Hybridization. *J. Chem. Phys.* **2017**, *146*, No. 214701.

(64) Li, Y.; Lu, D.; Galli, G. Calculation of Quasi-Particle Energies of Aromatic Self-Assembled Monolayers on Au(111). *J. Chem. Theory Comput.* **2009**, *5*, 881−886.

(65) Biller, A.; Tamblyn, I.; Neaton, J. B.; Kronik, L. Electronic Level Alignment at a Metal-Molecule Interface from a Short-Range Hybrid Functional. *J. Chem. Phys.* **2011**, *135*, No. 164706.

(66) Neugebauer, J.; Scheffler, M. Adsorbate-Substrate and Adsorbate-Adsorbate Interactions of Na and K Adlayers on Al(111). *Phys. Rev. B* **1992**, *46*, 16067−16080.

(67) Deutsch, D.; Natan, A.; Shapira, Y.; Kronik, L. Electrostatic Properties of Adsorbed Polar Molecules: Opposite Behavior of a Single Molecule and a Molecular Monolayer. *J. Am. Chem. Soc.* **2007**, *129*, 2989−2997.

(68) Cabarcos, O. M.; Schuster, S.; Hehn, I.; Zhang, P. P.; Maitani, M. M.; Sullivan, N.; Giguère, J.-B.; Morin, J.-F.; Weiss, P. S.; Zojer, E.; Zharnikov, M.; Allara, D. L. Effects of Embedded Dipole Layers on Electrostatic Properties of Alkanethiolate Self-Assembled Monolayers. *J. Phys. Chem. C* **2017**, *121*, 15815−15830.

(69) Sauter, E.; Gilbert, C.-O.; Boismenu-Lavoie, J.; Morin, J.-F.; Zharnikov, M. Mixed Aliphatic Self-Assembled Monolayers with Embedded Polar Group. *J. Phys. Chem. C* **2017**, *121*, 23017−23024.

(70) Baby, A.; Fratesi, G.; Vaidya, S. R.; Patera, L. L.; Africh, C.; Floreano, L.; Brivio, G. P. Anchoring and Bending of Pentacene on Aluminum (001). *J. Phys. Chem. C* **2015**, *119*, 3624−3633.

(71) Setvin, M.; Shi, X.; Hulva, J.; Simschitz, T.; Parkinson, G. S.; Schmid, M.; Di Valentin, C.; Selloni, A.; Diebold, U. Methanol on Anatase TiO_2 (101): Mechanistic Insights into Photocatalysis. *ACS Catal.* **2017**, *7*, 7081−7091.

(72) Wang, H.; Levchenko, S. V.; Schultz, T.; Koch, N.; Scheffler, M.; Rossi, M. Modulation of the Work Function by the Atomic Structure of Strong Organic Electron Acceptors on H-Si(111). *Adv. Electron. Mater.* **2019**, *5*, No. 1800891.

(73) Zhang, R.; Hensley, A. J.; McEwen, J.-S.; Wickert, S.; Darlatt, E.; Fischer, K.; Schöppke, M.; Denecke, R.; Streber, R.; Lorenz, M.; Papp, C.; Steinrück, H.-P. Integrated X-Ray Photoelectron Spectroscopy and DFT Characterization of Benzene Adsorption on Pt(111), Pt(355) and Pt(322) Surfaces. *Phys. Chem. Chem. Phys.* **2013**, *15*, 20662.

(74) Burow, A. M.; Sierka, M.; Döbler, J.; Sauer, J. Point Defects in CaF2 and CeO2 Investigated by the Periodic Electrostatic Embedded Cluster Method. *J. Chem. Phys.* **2009**, *130*, No. 174710.

(75) Ammal, S. C.; Heyden, A. Modeling the Noble Metal/TiO2(110) Interface with Hybrid DFT Functionals: A Periodic Electrostatic Embedded Cluster Model Study. *J. Chem. Phys.* **2010**, *133*, No. 164703.

(76) Berger, D.; Logsdail, A. J.; Oberhofer, H.; Farrow, M. R.; Catlow, C. R. A.; Sherwood, P.; Sokol, A. A.; Blum, V.; Reuter, K. Embedded-Cluster Calculations in a Numeric Atomic Orbital Density-Functional Theory Framework. *J. Chem. Phys.* **2014**, *141*, No. 024105.

(77) Boese, A. D.; Sauer, J. Embedded and DFT Calculations on the Crystal Structures of Small Alkanes, Notably Propane. *Cryst. Growth Des.* **2017**, *17*, 1636−1646.

(78) Tölle, J.; Severo Pereira Gomes, A.; Ramos, P.; Pavanello, M. Charged-Cell Periodic DFT Simulations via an Impurity Model Based on Density Embedding: Application to the Ionization Potential of Liquid Water. *Int. J. Quantum Chem.* **2019**, *119*, No. e25801.

(79) Aizawa, T.; Suehara, S.; Hishita, S.; Otani, S.; Arai, M. Surface Core-Level Shift and Electronic Structure on Transition-Metal Diboride (0001) Surfaces. *Phys. Rev. B* **2005**, *71*, No. 165405.

(80) Ganduglia-Pirovano, M. V.; Scheffler, M. Structural and Electronic Properties of Chemisorbed Oxygen on Rh(111). *Phys. Rev. B* **1999**, *59*, 15533−15543.

(81) Olovsson, W.; Göransson, C.; Pourovskii, L. V.; Johansson, B.; Abrikosov, I. A. Core-Level Shifts in Fcc Random Alloys: A First-Principles Approach. *Phys. Rev. B* **2005**, *72*, No. 064203.

(82) Scheffler, M. Lattice Relaxations at Substitutional Impurities in Semiconductors. *Phys. B+C* **1987**, *146*, 176−186.

(83) Moll, N.; Xu, Y.; Hofmann, O. T.; Rinke, P. Stabilization of Semiconductor Surfaces through Bulk Dopants. *New J. Phys.* **2013**, *15*, No. 083009.

(84) Richter, N. A.; Sicolo, S.; Levchenko, S. V.; Sauer, J.; Scheffler, M. Concentration of Vacancies at Metal-Oxide Surfaces: Case Study of MgO(100). *Phys. Rev. Lett.* **2013**, *111*, No. 045502.

(85) Sinai, O.; Kronik, L. Simulated Doping of Si from First Principles Using Pseudoatoms. *Phys. Rev. B* **2013**, *87*, No. 235305.

(86) Dabo, I.; Kozinsky, B.; Singh-Miller, N. E.; Marzari, N. Electrostatics in Periodic Boundary Conditions and Real-Space Corrections. *Phys. Rev. B* **2008**, *77*, No. 115139.

(87) Freysoldt, C.; Neugebauer, J.; Van de Walle, C. G. Fully *Ab Initio* Finite-Size Corrections for Charged-Defect Supercell Calculations. *Phys. Rev. Lett.* **2009**, *102*, No. 016402.

(88) Lany, S.; Zunger, A. Assessment of Correction Methods for the Band-Gap Problem and for Finite-Size Effects in Supercell Defect Calculations: Case Studies for ZnO and GaAs. *Phys. Rev. B* **2008**, *78*, No. 235104.

(89) Taylor, S. E.; Bruneval, F. Understanding and Correcting the Spurious Interactions in Charged Supercells. *Phys. Rev. B* **2011**, *84*, No. 075155.

(90) Komsa, H.-P.; Rantala, T. T.; Pasquarello, A. Finite-Size Supercell Correction Schemes for Charged Defect Calculations. *Phys. Rev. B* **2012**, *86*, No. 045112.

(91) Ishii, H.; Sugiyama, K.; Ito, E.; Seki, K. Energy Level Alignment and Interfacial Electronic Structures at Organic/Metal and Organic/Organic Interfaces. *Adv. Mater.* **1999**, *11*, 605−625.

(92) Bagus, P. S.; Staemmler, V.; Wöll, C. Exchangelike Effects for Closed-Shell Adsorbates: Interface Dipole and Work Function. *Phys. Rev. Lett.* **2002**, *89*, No. 559.

(93) Mizushima, H.; Koike, H.; Kuroda, K.; Ishida, Y.; Nakayama, M.; Mase, K.; Kondo, T.; Shin, S.; Kanai, K. Effect of Physisorption of Inert Organic Molecules on Au(111) Surface Electronic States. *Phys. Chem. Chem. Phys.* **2017**, *19*, 18646−18651.

(94) Öström, H.; Triguero, L.; Nyberg, M.; Ogasawara, H.; Pettersson, L. G. M.; Nilsson, A. Bonding of Saturated Hydrocarbons to Metal Surfaces. *Phys. Rev. Lett.* **2003**, *91*, No. 6209.

(95) Blum, V.; Gehrke, R.; Hanke, F.; Havu, P.; Havu, V.; Ren, X.; Reuter, K.; Scheffler, M. Ab Initio Molecular Simulations with Numeric Atom-Centered Orbitals. *Comput. Phys. Commun.* **2009**, *180*, 2175−2196.

(96) Havu, V.; Blum, V.; Havu, P.; Scheffler, M. Efficient Integration for All-Electron Electronic Structure Calculation Using Numeric Basis Functions. *J. Comput. Phys.* **2009**, *228*, 8367−8379.

(97) Marek, A.; Blum, V.; Johanni, R.; Havu, V.; Lang, B.; Auckenthaler, T.; Heinecke, A.; Bungartz, H.-J.; Lederer, H. The ELPA Library: Scalable Parallel Eigenvalue Solutions for Electronic Structure Theory and Computational Science. *J. Phys.: Condens. Matter* **2014**, *26*, No. 213201.

(98) Togo, A.; Tanaka, I. Spglib: A Software Library for Crystal Symmetry Search, ArXiv180801590. arXiv.org e-Print archive. https://arxiv.org/abs/1808.01590 (submitted August 5, 2018).

(99) Yu, V. W.; Corsetti, F.; García, A.; Huhn, W. P.; Jacquelin, M.; Jia, W.; Lange, B.; Lin, L.; Lu, J.; Mi, W.; Seifitokaldani, A.; Vázquez-Mayagoitia, Á.; Yang, C.; Yang, H.; Blum, V. ELSI: A Unified Software Interface for Kohn−Sham Electronic Structure Solvers. *Comput. Phys. Commun.* **2018**, *222*, 267−285.

(100) Perdew, J. P.; Burke, K.; Ernzerhof, M. Generalized Gradient Approximation Made Simple. *Phys. Rev. Lett.* **1996**, *77*, 3865−3868.

(101) Perdew, J. P.; Burke, K.; Ernzerhof, M. ERRATA: Generalized Gradient Approximation Made Simple [Phys. Rev. Lett. 77, 3865 (1996)]. *Phys. Rev. Lett.* **1997**, *78*, 1396.

(102) Tkatchenko, A.; Scheffler, M. Accurate Molecular Van Der Waals Interactions from Ground-State Electron Density and Free-Atom Reference Data. *Phys. Rev. Lett.* **2009**, *102*, No. 073005.

(103) Freysoldt, C.; Eggert, P.; Rinke, P.; Schindlmayr, A.; Scheffler, M. Screening in Two Dimensions: G W Calculations for Surfaces and Thin Films Using the Repeated-Slab Approach. *Phys. Rev. B* **2008**, *77*, No. 235428.

(104) Chong, D. P. Accurate Calculation of Core-Electron Binding Energies by the Density-Functional Method. *Chem. Phys. Lett.* **1995**, *232*, 486−490.

(105) van der Walt, S.; Colbert, S. C.; Varoquaux, G. The NumPy Array: A Structure for Efficient Numerical Computation. *Comput. Sci. Eng.* **2011**, *13*, 22−30.

(106) Hunter, J. D. Matplotlib: A 2D Graphics Environment. *Comput. Sci. Eng.* **2007**, *9*, 90−95.

(107) Stukowski, A. Visualization and Analysis of Atomistic Simulation Data with OVITO−the Open Visualization Tool. *Modell. Simul. Mater. Sci. Eng.* **2010**, *18*, No. 015012.

(108) Momma, K.; Izumi, F. *VESTA 3* for Three-Dimensional Visualization of Crystal, Volumetric and Morphology Data. *J. Appl. Crystallogr.* **2011**, *44*, 1272−1276.

(109) Kokalj, A. XCrySDen—a New Program for Displaying Crystalline Structures and Electron Densities. *J. Mol. Graphics Modell.* **1999**, *17*, 176−179.

(110) The GIMP Development Team.*GIMP*, 2019.

(111) Hofmann, O. T.; Rangger, G. M.; Zojer, E. Reducing the Metal Work Function beyond Pauli Pushback: A Computational Investigation of Tetrathiafulvalene and Viologen on Coinage Metal Surfaces. *J. Phys. Chem. C* **2008**, *112*, 20357−20365.

(112) Hofmann, O. T.; Egger, D. A.; Zojer, E. Work-Function Modification beyond Pinning: When Do Molecular Dipoles Count? *Nano Lett.* **2010**, *10*, 4369−4374.

(113) Bröker, B.; Hofmann, O. T.; Rangger, G. M.; Frank, P.; Blum, R.-P.; Rieger, R.; Venema, L.; Vollmer, A.; Müllen, K.; Rabe, J. P.; Winkler, A.; Rudolf, P.; Zojer, E.; Koch, N. Density-Dependent Reorientation and Rehybridization of Chemisorbed Conjugated Molecules for Controlling Interface Electronic Structure. *Phys. Rev. Lett.* **2010**, *104*, No. 246805.

(114) Lercher, C.; Röthel, C.; Roscioni, O. M.; Geerts, Y. H.; Shen, Q.; Teichert, C.; Fischer, R.; Leising, G.; Sferrazza, M.; Gbabode, G.; Resel, R. Polymorphism of Dioctyl-Terthiophene within Thin Films: The Role of the First Monolayer. *Chem. Phys. Lett.* **2015**, *630*, 12−17.

(115) Lorch, C.; Banerjee, R.; Frank, C.; Dieterle, J.; Hinderhofer, A.; Gerlach, A.; Schreiber, F. Growth of Competing Crystal Phases of α-Sexithiophene Studied by Real-Time *in Situ* X-Ray Scattering. *J. Phys. Chem. C* **2015**, *119*, 819−825.

(116) Hofmann, O. T.; Glowatzki, H.; Bürker, C.; Rangger, G. M.; Bröker, B.; Niederhausen, J.; Hosokai, T.; Salzmann, I.; Blum, R.-P.; Rieger, R.; Vollmer, A.; Rajput, P.; Gerlach, A.; Müllen, K.; Schreiber, F.; Zojer, E.; Koch, N.; Duhm, S. Orientation-Dependent Work-Function Modification Using Substituted Pyrene-Based Acceptors. *J. Phys. Chem. C* **2017**, *121*, 24657−24668.

(117) Pachmajer, S.; Jones, A. O. F.; Truger, M.; Röthel, C.; Salzmann, I.; Werzer, O.; Resel, R. Self-Limited Growth in Pentacene Thin Films. *ACS Appl. Mater. Interfaces* **2017**, *9*, 11977−11984.

(118) Pithan, L.; Nabok, D.; Cocchi, C.; Beyer, P.; Duva, G.; Simbrunner, J.; Rawle, J.; Nicklin, C.; Schäfer, P.; Draxl, C.; Schreiber, F.; Kowarik, S. Molecular Structure of the Substrate-Induced Thin-Film Phase of Tetracene. *J. Chem. Phys.* **2018**, *149*, No. 144701.

(119) Spreitzer, H.; Kaufmann, B.; Ruzié, C.; Röthel, C.; Arnold, T.; Geerts, Y. H.; Teichert, C.; Resel, R.; Jones, A. O. F. Alkyl Chain Assisted Thin Film Growth of 2,7-Dioctyloxy-Benzothienobenzothiophene. *J. Mater. Chem. C* **2019**, *7*, 8477−8484.

(120) Ulman, A. Formation and Structure of Self-Assembled Monolayers. *Chem. Rev.* **1996**, *96*, 1533−1554.

(121) Schreiber, F. Structure and Growth of Self-Assembling Monolayers. *Prog. Surf. Sci.* **2000**, *65*, 151−257.

(122) Heister, K.; Zharnikov, M.; Grunze, M.; Johansson, L. S. O. Adsorption of Alkanethiols and Biphenylthiols on Au and Ag Substrates: A High-Resolution X-Ray Photoelectron Spectroscopy Study. *J. Phys. Chem. B* **2001**, *105*, 4058−4061.

(123) Schreiber, F. Self-Assembled Monolayers: From Simple Model Systems to Biofunctionalized Interfaces. *J. Phys. Condens. Matter* **2004**, *16*, R881−R900.

(124) Love, J. C.; Estroff, L. A.; Kriebel, J. K.; Nuzzo, R. G.; Whitesides, G. M. Self-Assembled Monolayers of Thiolates on Metals as a Form of Nanotechnology. *Chem. Rev.* **2005**, *105*, 1103−1170.

(125) Vericat, C.; Vela, M. E.; Benitez, G.; Carro, P.; Salvarezza, R. C. Self-Assembled Monolayers of Thiols and Dithiols on Gold: New Challenges for a Well-Known System. *Chem. Soc. Rev.* **2010**, *39*, 1805.

(126) Lee, H. J.; Jamison, A. C.; Lee, T. R. Surface Dipoles: A Growing Body of Evidence Supports Their Impact and Importance. *Acc. Chem. Res.* **2015**, *48*, 3007−3015.

(127) Amsalem, P.; Niederhausen, J.; Wilke, A.; Heimel, G.; Schlesinger, R.; Winkler, S.; Vollmer, A.; Rabe, J. P.; Koch, N. Role of Charge Transfer, Dipole-Dipole Interactions, and Electrostatics in Fermi-Level Pinning at a Molecular Heterojunction on a Metal Surface. *Phys. Rev. B* **2013**, *87*, No. 244704.

(128) Braun, S.; Salaneck, W. R. Fermi Level Pinning at Interfaces with Tetrafluorotetracyanoquinodimethane (F4-TCNQ): The Role of Integer Charge Transfer States. *Chem. Phys. Lett.* **2007**, *438*, 259−262.

(129) Tengstedt, C.; Osikowicz, W.; Salaneck, W. R.; Parker, I. D.; Hsu, C.-H.; Fahlman, M. Fermi-Level Pinning at Conjugated Polymer Interfaces. *Appl. Phys. Lett.* **2006**, *88*, No. 053502.

(130) Ge, Y.; Weidner, T.; Ahn, H.; Whitten, J. E.; Zharnikov, M. Energy Level Pinning in Self-Assembled Alkanethiol Monolayers. *J. Phys. Chem. C* **2009**, *113*, 4575−4583.

(131) Hofmann, O. T.; Atalla, V.; Moll, N.; Rinke, P.; Scheffler, M. Interface Dipoles of Organic Molecules on Ag(111) in Hybrid Density-Functional Theory. *New J. Phys.* **2013**, *15*, No. 123028.

(132) Braun, S.; Salaneck, W. R.; Fahlman, M. Energy-Level Alignment at Organic/Metal and Organic/Organic Interfaces. *Adv. Mater.* **2009**, *21*, 1450−1472.

(133) Ratner, B. D.; Castner, D. G. In *Surface Analysis: The Principal Techniques*; Vickerman, J. C., Ed.; Wiley-VCH: New York, 1997.

(134) Zharnikov, M. Probing Charge Transfer Dynamics in Self-Assembled Monolayers by Core Hole Clock Approach. *J. Electron Spectrosc. Relat. Phenom.* **2015**, *200*, 160−173.

(135) Inglesfield, J. E. The Screening of an Electric Field at an Al(001) Surface. *Surf. Sci.* **1987**, *188*, L701−L707.

(136) Wolfram Research, Inc. Mathematica, *Version 11.3; Champaign, IL*, 2018.

(137) Ihm, J.; Zunger, A.; Cohen, M. L. Momentum-Space Formalism for the Total Energy of Solids. *J. Phys. C: Solid State Phys.* **1979**, *12*, 4409−4422.

(138) Sinai, O.; Hofmann, O. T.; Rinke, P.; Scheffler, M.; Heimel, G.; Kronik, L. Multiscale Approach to the Electronic Structure of Doped Semiconductor Surfaces. *Phys. Rev. B* **2015**, *91*, No. 075311.

(139) Erker, S.; Rinke, P.; Moll, N.; Hofmann, O. T. Doping Dependence of the Surface Phase Stability of Polar O-Terminated $(000\bar{1})$ ZnO. *New J. Phys.* **2017**, *19*, No. 083012.

4.7 SUPPORTING INFORMATION

In the Supporting Information we present further details of the computational methodology, projected densities of states of methane monolayers for different supercell sizes and adsorption distances, C 1s core-level energies for different methane coverages, additional data of test calculations and convergence tests, charge rearrangements for different excitation densities and adsorption heights as well as the corresponding cumulative charge rearrangements, work function and core-level shifts as a function of the inverse supercell size, core-level shifts with respect to the charge removed from the core hole and with respect to the unit cell size, electrostatic energy plane averaged over differently sized areas, calculations underlining the dependence of core-level shifts on the local electrostatic energy, simple electrostatic model for estimating work-function changes, energies of the frontier orbitals of methane as a function of the used basis set, electric fields at various excitation densities for a CREST-like correction scheme.

Supporting Information for

Final-State Simulations of Core-Level Binding Energies at Metal-Organic Hybrid Interfaces: Artifacts Caused by Spurious Collective Electrostatic Effects

Thomas C. Taucher, Oliver T. Hofmann, and Egbert Zojer*

Institute of Solid State Physics, Graz University of Technology, NAWI Graz, Petersgasse 16, 8010 Graz, Austria.

*Corresponding author: egbert.zojer@tugraz.at

Table of Content

1. Dependence of the core-level binding energies on molecular coverage

In the main manuscript we show that the C 1s core-level binding energies of methane adsorbed on a Al(100) surface calculated employing the final-statefinal-state approach strongly depends on the density of core holes present in the simulation. These results (shown in Figure 2a of the main manuscript) have been obtained when modeling the binding energies as a function of supercell size with one excitation per supercell. In these simulations, the coverage of the methane molecules was kept constant. In Figure S1 we show that essentially the same results are obtained when also varying the coverage of the methane molecules (i.e., when changing the methane density for different unit cells - see Figure S2). The bigger unit cells with different coverages were created by multiplying the 2×2 unit cell and removing every forth methane molecule in the system for the ones with a coverage of 25% and by removing all but one molecule in the case of the 10×10 system, creating a coverage of only 4.0%. For the 3×3 unit cell an aluminum layer with 9 surface atoms per unit cell was created. The adsorption site of the methane molecule was obtained in the same way as in the full coverage 2×2 case, namely by placing the methane molecule on the surface and fully relaxing its geometry (keeping only the positions of the Al atoms fixed). The resulting coverages are summarized in Table S1. This shows that what primarily counts for the described effect is the density of excited core holes.

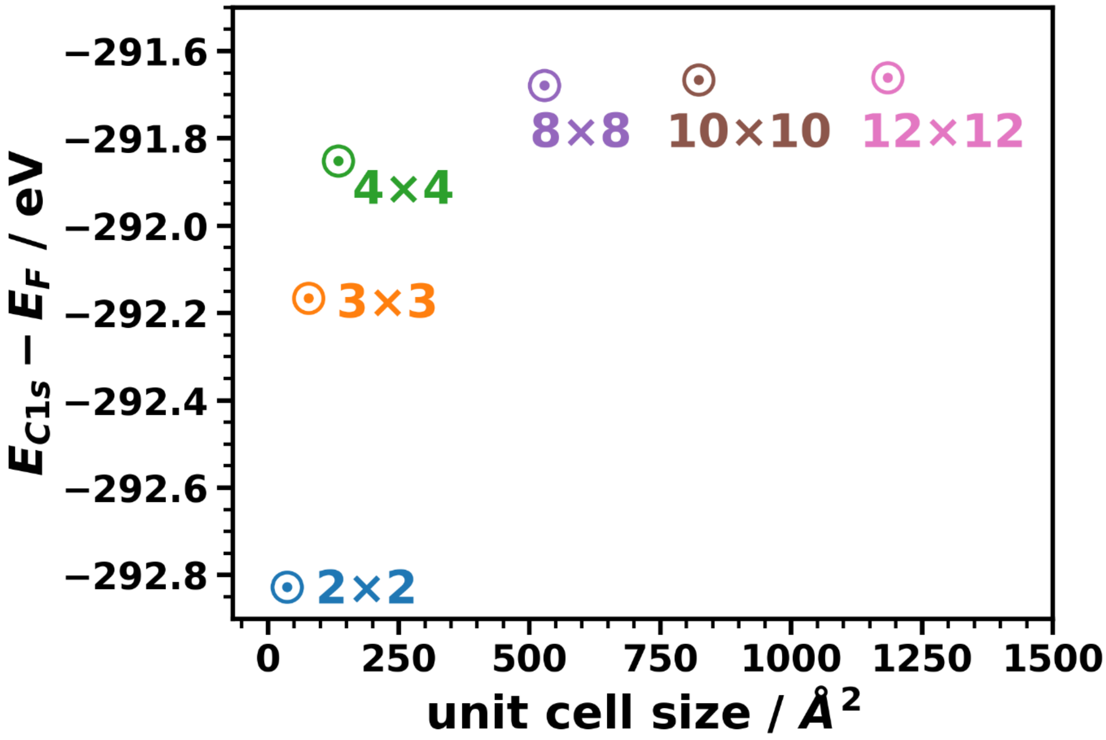

__Figure S1.__ C 1s core-level binding energy of methane adsorbed on Al(100) as a function of the chosen unit cell size with different methane coverages (see Table S1). The calculations were done employing the final-state approach within the Slater-Janak transition-state approximation.

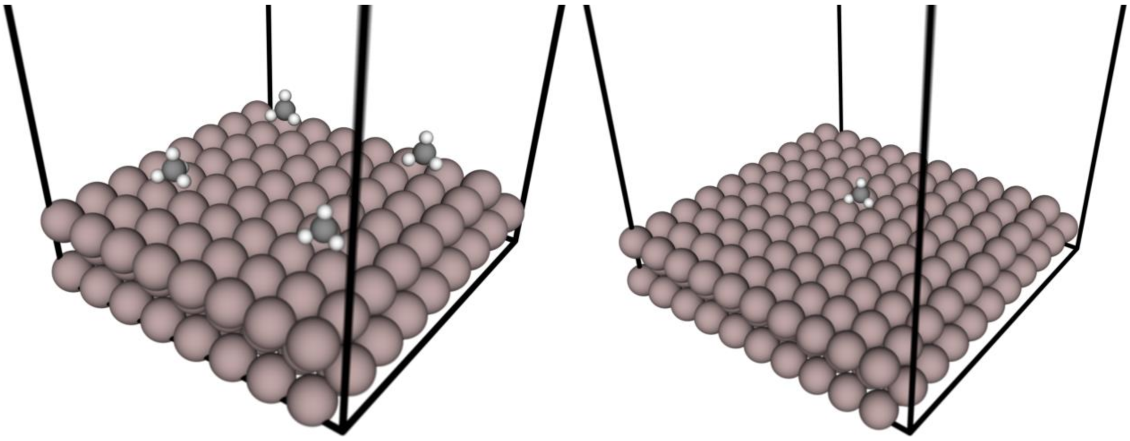

__Figure S2.__ Left: Unit cell of the 8×8 system with a methane coverage of 25%. Right: Unit cell of the 10×10 system with a methane coverage of 4%.

Table S1. *methane coverage of differently sized supercells.*

Supercell size	methane density / molecules per Å²	methane density / % of full coverage
2×2	0.0303	100.0
3×3	0.0135	44.6
4×4	0.0076	25.0
8×8	0.0076	25.0
10×10	0.0012	4.0
12×12	0.0076	25.0

2. Methodological details and tests

2.1.Information on the employed basis functions

The basis functions employed in the FHI-aims simulations have the format

$$\Phi(r) = \frac{u(r)}{r} * Y_{lm}(\Theta, \Phi)$$

in spherical coordinates (r, Θ, Φ) relative to a given atomic center. FHI-aims provides for every atomic species a preconstructed *species_defaults* file. The used tight basis sets were not further adjusted, because they afforded the required accuracy and efficiency. Note: If a higher tier for the basis set, i.e. when using tight settings, is used, all lower basis functions must be used as well.

Table S2. *Basis functions that have been used for all calculations performed with FHI-aims*[1]. *The abbreviations read as follows*[a]*: X(nl, z), where X describes the type of basis function where H stands for hydrogen-like functions and ionic for a free-ion like radial function. The parameter n stands for the main/radial quantum number, l denotes the angular momentum quantum number (s, p, d, f, …), and z denotes an effective nuclear charge, which scales the radial function in the defining Coulomb potential for the hydrogen-like function. In the case of free-ion like radial functions, z specifies the onset radius of the confining potential. If auto is specified instead of a numerical value, the default onset is used.*

	H	C	Al
Minimal	valence(1s, 1.0)	valence(2s, 2.0) valence(2p, 2.0)	valence(3s, 2.0) valence(3p, 1.0)
First tier	H(2s, 2.1) H(2p, 3.5)	H(2p, 1.7) H(3d, 6) H(2s, 4.9)	ionic(3d, auto) ionic(3p, auto) H(4f, 4.7) ionic(3s, auto)
Second tier	H(1s, 0.85) H(2p, 3.7) H(2s, 1.2) H(3d, 7.0)	H(4f, 9.8) H(3p, 5.2) H(3s, 4.3) H(5g, 14.4) H(3d, 6.2)	H(5g, 7) H(H3d, 6)

2.2. Convergence of the k-point grid

The Γ-centered k-point mesh was evenly split along the reciprocal lattice vectors of the unit cell with the same number of k-points in x- and y-direction and 1 k-point in z-direction. This was done because of the quadratic unit cell and the repeated slab approach. When applying the repeated slab approach, only 1 k-point in z-direction is used, as the interface is not periodic in that direction. Due to the fact that the k-point mesh samples reciprocal space, smaller unit cells require the use of more k-points. Therefore, when the unit cell size was doubled in a given direction, the number of k-points in that direction was halved. To find the number of k-points in x- and y-direction per unit cell length, which are needed to get converged results, several calculations were done with an increasing

---

[a] As described in the FHI-aims manual, version January 23, 2017.

number of k-points for the two smallest systems until the obtained values of interest did not change beyond a certain threshold. This procedure yielded that 400 k-points per topmost aluminum atom - i.e. 4 Al atoms at the surface in the case of the 2×2 unit cell, 16 surface atoms in the case of the 4×4 supercell, and 9 surface atoms in the case of the 3×3 unit cell - were enough to get orbital energies converged to at least ±0.002 eV. The exact number of k-points used for each supercell and the k-point density per surface atom is shown in Table S3.

Table S3. *Details on the used k-point grid for the different supercells calculated.*

System name	Number of surface Al atoms in x- and y-direction	k-points in x- & y- direction	k-points in z-direction	K-points per surface atom
2×2	2	12	1	576
3×3	3	8	1	576
4×4	4	5	1	400
6×6	6	4	1	576
8×8	8	4	1	1024
10×10	10	2	1	400
12×12	12	2	1	576

2.3. Impact of the number of layers contained in the slab

Owing to the very extended supercells required for the present manuscript, all data presented in the main manuscript rely on metal slabs consisting of only three Al layers. To ensure that this is sufficient for calculating the core-level binding energies of the present system (where there is no significant substrate/adsorbate charge transfer) test calculations for the smallest 2×2 unit cell containing 6 Al layers were also performed. As can be seen in Table S4, the C 1s orbital energies for the two slab thicknesses differed by only ~ 0.01-0.02 eV, even in cases, where the methane atom was moved farther away from the surface slab resulting in a bigger dipole. This suggests that the consideration of three-layer slabs is sufficient for the present purpose.

Table S4. *carbon 1s orbital energies calculated for the 2×2 unit cell within the Slater-Janak transition-state approach for different adsorption heights of the methane molecule on two slabs differing only in the number of aluminum layers used to represent the metal slab.*

Adsorption distance	C 1s orbital energy – E_F / eV	
	3 layer slab	6 layer slab
Equilibrium	-292.83	-292.82
+1 Å	-293.10	-293.08
+2 Å	-293.16	-293.14
+3 Å	-293.15	-293.14

2.4. Impact of the geometric relaxation of the topmost metal layer

The aluminum slab was constructed with ASE[2], utilizing the function to create a fcc(100) surface slab with a tabulated lattice constant of 4.05 Å. To mimic the metal slab, the lowest layer of aluminum atoms was always fixed. To test whether the other layers need to be relaxed, two additional systems were calculated. One with the topmost layer and one with the two topmost layers allowed to relax during a full geometric optimization. Again, this hardly affected the core-level binding energies (see Table S5). Thus, for all calculations the slab with the aluminum atoms in the ideal bulk lattice positions was used.

Table S5. *Fermi-level aligned carbon 1s orbital energies of an adsorbed methane molecule on differently geometrically optimized aluminum slabs calculated for the 2×2 system.*

Relaxed Al layers of the metal slab	C 1s orbital energy – E_F / eV
none	-292.83
topmost layer	-292.81
2 topmost layers	-292.80

2.5. Spin polarized calculations

To test whether one needs to perform spin polarized calculations, selected supercells were calculated with spin unrestricted settings. Therefore, in the *control.in* file to start the FHI-aims[1] calculations, the spin parameter was set to collinear and the force_occupation parameter was set by the following lines in the case of a calculation of the 4×4 system:

```
force_occupation_projector 49 1 0.5 49 52
force_occupation_projector 49 2 1.0 49 52
```

Additionally, an initial guess for the spin of the excited atom needs to be set with the keyword `initial_moment` in the *geometry.in* file in the line following the specification of the excited carbon atom. The results obtained with unrestricted spin settings yielded the same qualitative trend (see Figure S3) as the spin restricted calculations. In fact, the mean value of the spin up and spin down orbitals is close to the energy of the C 1s orbital in the restricted calculations.

What is more relevant in the present context is, however, that the energy difference between the 2×2 and 4×4 unit cells is essentially the same for the spin up, spin down, and spin unrestricted channels (1.017 eV; 1.019 eV; 1.019 eV).

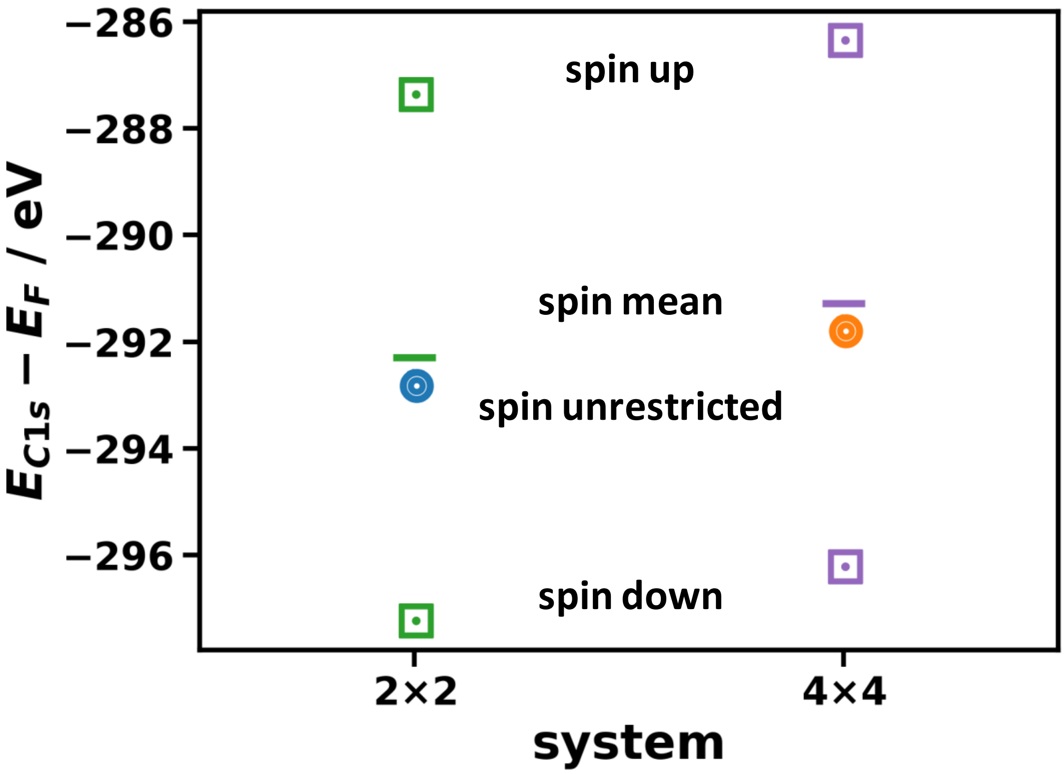

Figure S3. *Carbon 1s core orbital energies calculated within the Slater-Janak transition-state theory with spin restricted, i.e. Kohn-Sham eigenvalue set to 1.5e$^-$ (circles) and spin unrestricted (squares) for two different systems. Furthermore, the arithmetic mean of the spin down (occupation set to 1 e$^-$) and the spin up (occupation set to 0.5 e$^-$) eigenstate is plotted.*

3. Charge rearrangements due to the excitation

When utilizing the Slater-Janak transition-state theory, half an electron is removed from the excited core hole. This charge is then placed into the lowest unoccupied orbital in the calculated system. In the case of a system with a metal substrate, as considered in this manuscript, this corresponds to a state right at the Fermi level. Notably, the region of electron accumulation following the core-level excitation is found right above the metal surface underneath the excited molecule, as shown in Figure S4. Please note that the blue feature in Figure S4 in the region of methane is a consequence of electron depletion due to the polarization of the molecule. Consequently, there is one excitation per supercell and the excitation density is inversely proportional to the size of the chosen supercell.

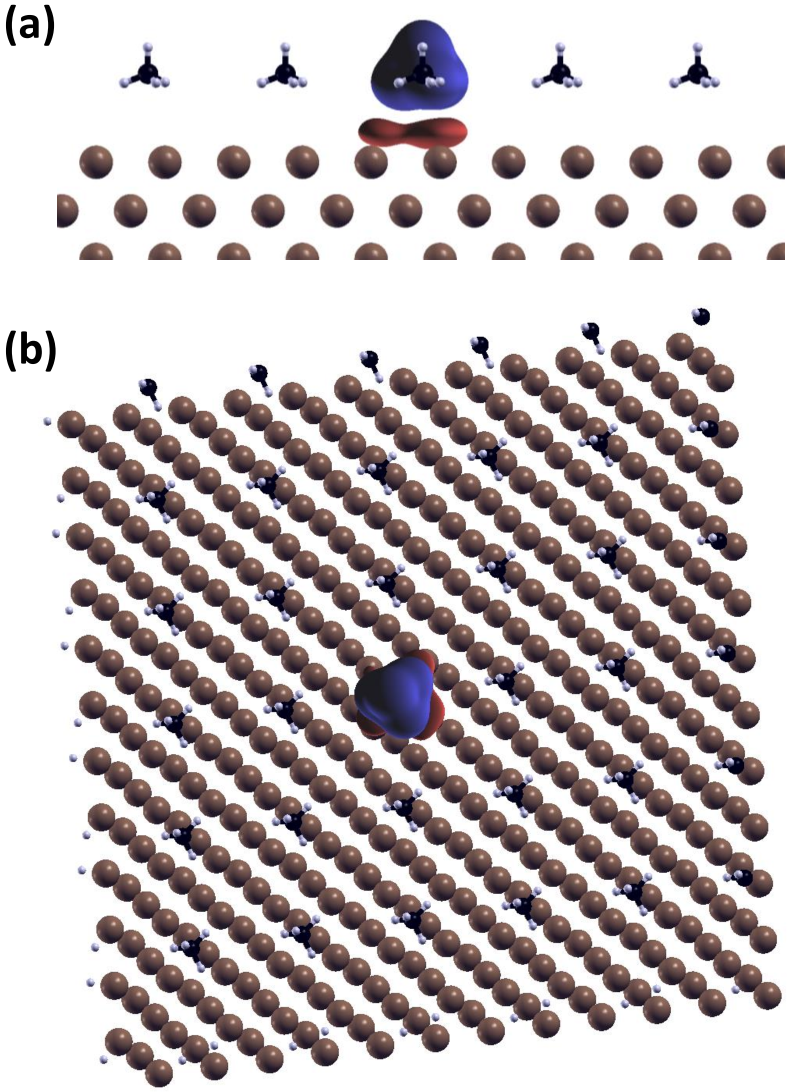

Figure S4. *Isodensity plot – front view (a) and top view (b) of the 12×12 supercell showing the electron depletion (blue) and accumulation (red) due to the removal of half an electron from the carbon 1s orbital of the excited molecule. This charge is moved to the lowest unoccupied level in the system by FHI-aims. As can be seen this is localized directly underneath the excited molecule.*

3.1. Plane-integrated charge rearrangements

Notably, the shapes of the calculated plane-integrated charge rearrangements are independent of the supercell size (cf., data for the 4×4 and 12×12 cells), with minor deviations for the smallest 2×2 cell (solid blue line in Figure S5). The latter we attribute to a somewhat different electronic structure in the 2×2 case, in which all adsorbate molecules are excited. In contrast, in the calculations of larger cells the excited methane molecule is surrounded by inequivalent molecules (i.e., by molecules in their electronic ground state), which minimizes hybridization effects between the molecules. This aspect will be discussed in more detail later, when discussing Fermi-level pinning effects.

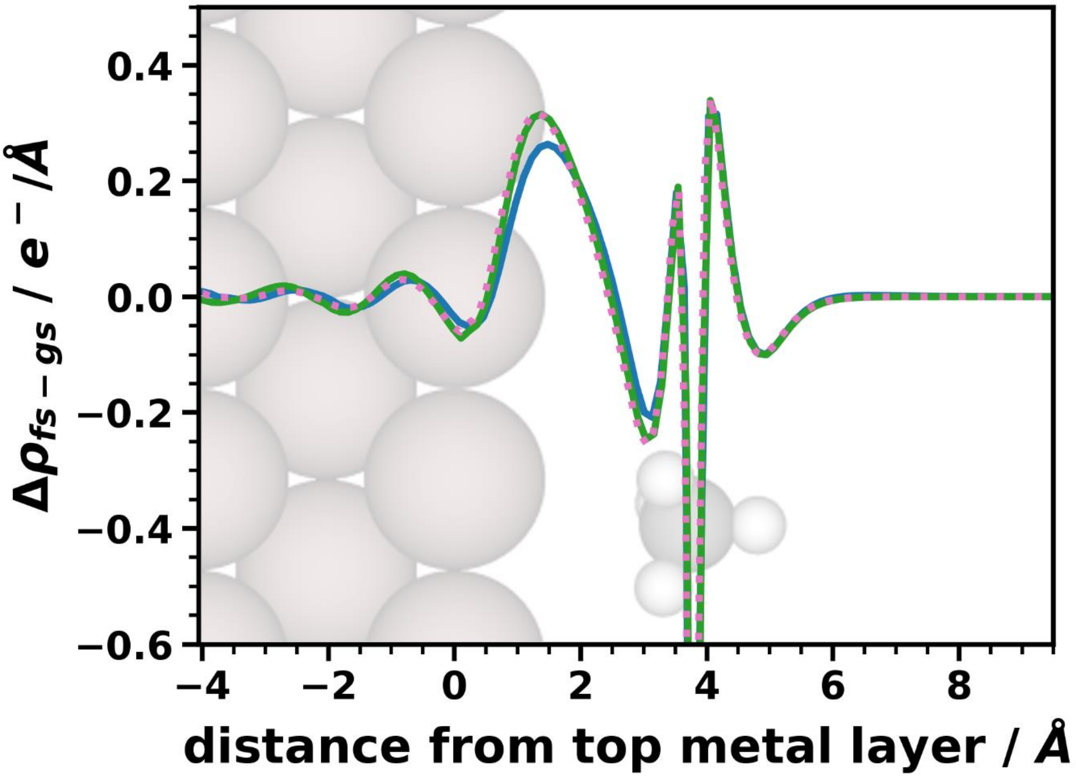

Figure S5. *Charge rearrangements between the initial- and final-state calculation, $\Delta\rho_{fs\text{-}gs}$, integrated over the unit cell for the 2×2 (blue, solid line), 4×4 (green, solid line), and 12×12 (pink, dotted line) surface supercell as a function of the adsorption height. The 4×4 and 12×12 data lie exactly on top of each other and the 2×2 data deviate only weakly, especially next to the metal surface.*

3.2. Plane integrated rearrangements as a function of the adsorption distance

In the previous section we show the charge rearrangements ($\Delta\rho_{fs\text{-}gs}$) in final-state calculations relative to the ground state charge density for different excitation densities (cf. Figure 5). Here we show the charge rearrangements due to different adsorption heights. As can be seen in Figure S6 the charge density difference in and right above the metal slab stays largely the same, no matter how far away the excited methane molecules are moved away from the substrate. Furthermore, the qualitative (and quantitative) charge rearrangements at the molecule prevail, when it is moved away from the metal slab.

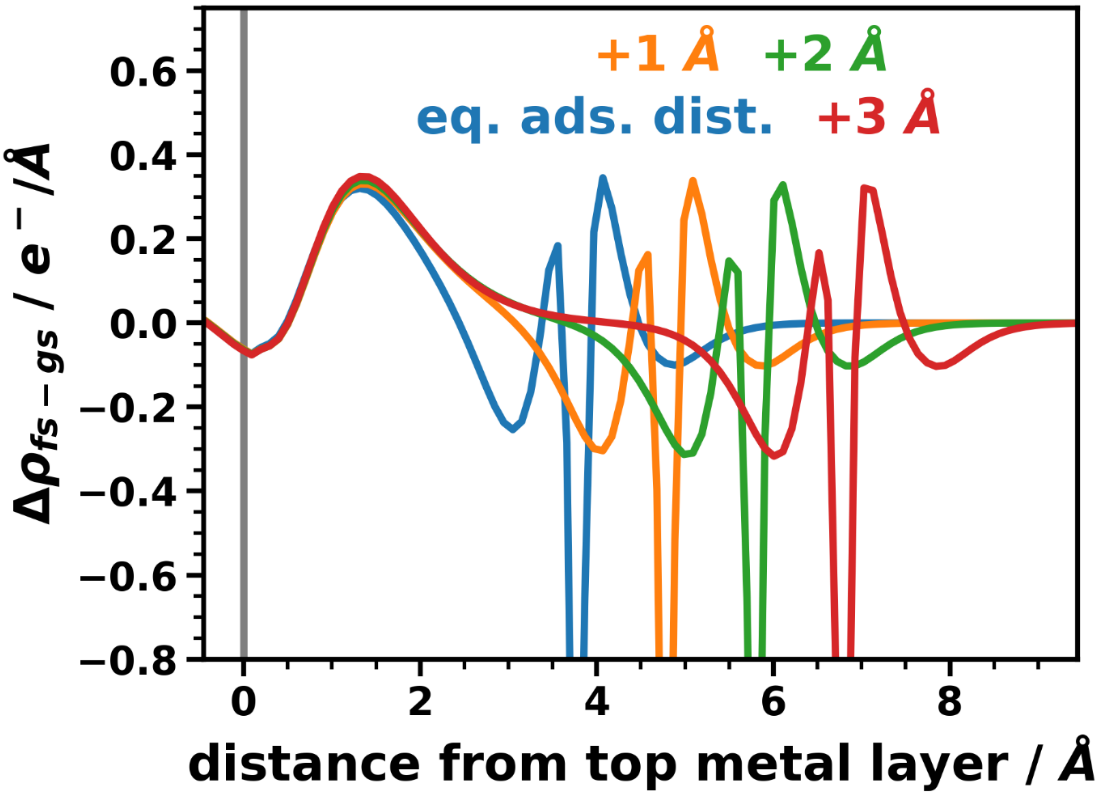

Figure S6. *Plane-integrated charge rearrangement due to the excitation - i.e. difference of the charge density of the final-state and the ground state calculation – for different adsorption heights of the methane molecule, calculated for the 10×10 supercell in units of the electron charge. Negative values mean electron depletion and positive vales electron accumulation. The grey line indicates the position of the topmost aluminum layer.*

3.3. Cumulative charge rearrangements as a function of the adsorption distance

Figure S7 shows the integral of $\Delta\rho_{fs\text{-}gs}$ (the quantity plotted in Figure S6) over the z coordinate of the unit cell as a function of the position up to which the integration has been performed. This integral can either be interpreted as a quantity proportional to the electric field resulting from $\Delta\rho_{fs\text{-}gs}$, or, more useful in the present context, as $\Delta Q_{fs\text{-}gs}$, the cumulative charge rearrangement, which quantifies, how many electrons have been transferred from below to above a plane at position z due to the excitation. Figure S7 shows that the maximum cumulative charge rearrangement somewhat increases with increasing adsorption height, which we attribute to the fact that at larger adsorption distances the overlap between the screening charges in the metal and the polarization charges in the adsorbate diminishes. This observation explains, the slightly superlinear increase of $\Delta E_{C\ 1s}$ with adsorption distance observed in Figure 6b.

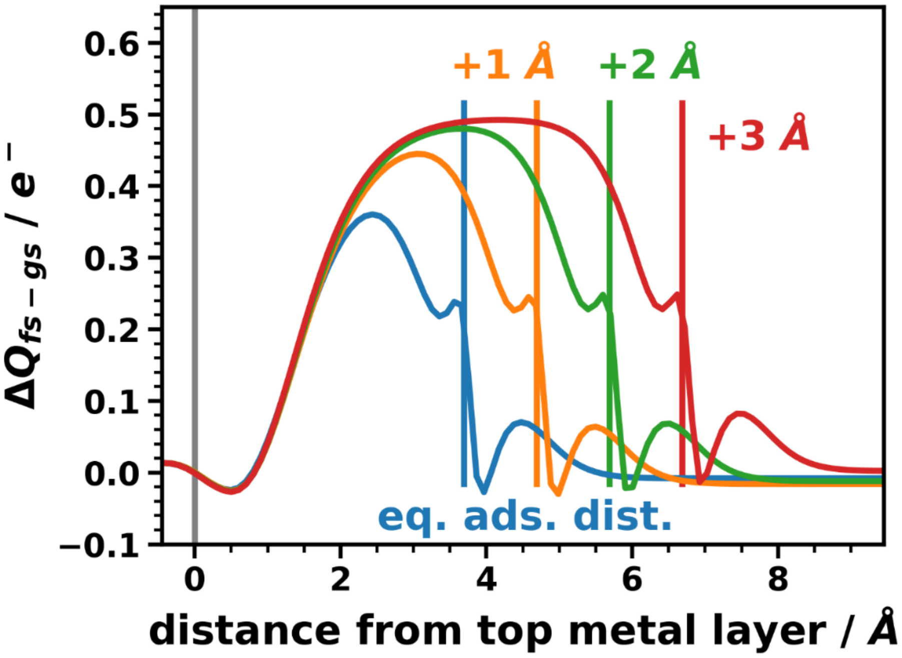

Figure S7. *Cumulative charge rearrangement due to the excitation – i.e. integrated difference of the charge density of the final-state and the ground state calculation (see Figure S6) - for the 10×10 supercell for different adsorption heights of the methane molecules. The grey line indicates the position of the topmost aluminum layer and the blue, orange, green and red line represent the position of the carbon atom of the methane molecule in equilibrium position, and moved farther away by 1, 2, and 3 Å, respectively.*

4. Shift of electronic levels

Due to collective electrostatic effects arising from the artificial dipole array in the calculations, all electronic states in the adsorbate layer are shifted relative to the Fermi level of the substrate.

4.1. Work function shifts

As a result of collective electrostatic effects, also the work function is shifted depending on the supercell size, i.e. the excitation density. The impact of this shift on the work function is inversely proportional to the base area of the supercell. In Figure S8 the work function change due to the artificial dipole layer in the final-state calculation is plotted over the inverse supercell size. As one can see all datapoints are essentially linear with the exception of the 2×2 unit cell, for which the evolution becomes sublinear. This is due to depolarization effects[3–8].

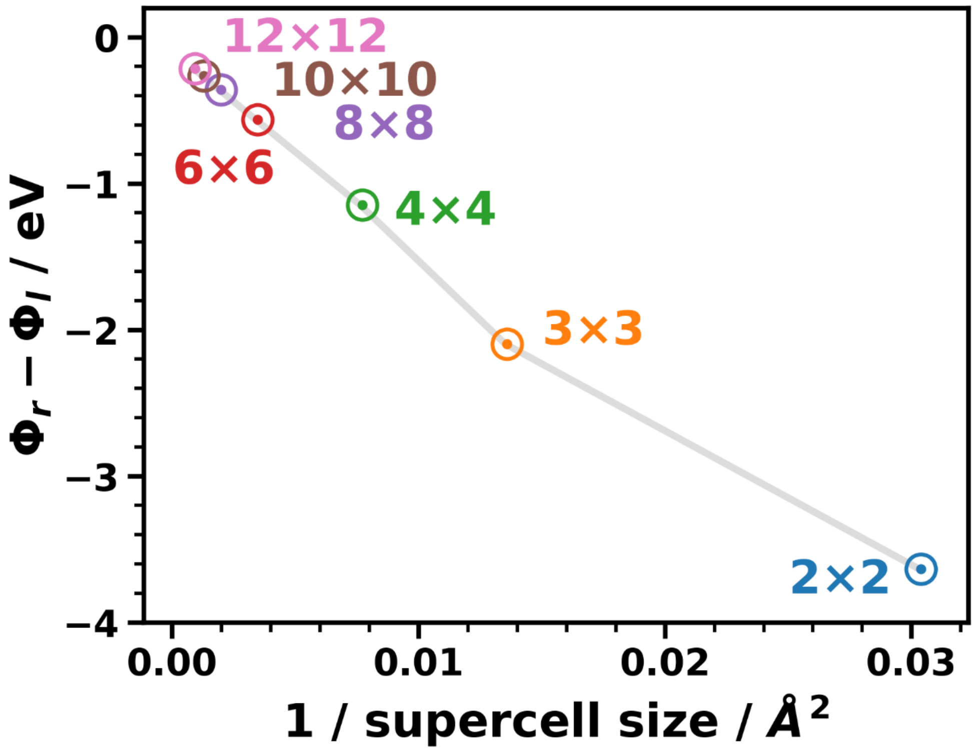

Figure S8. *Work function change of methane adsorbed on an Al(100) slab as a function of the inverse supercell size for calculations employing the final-state approach within the Slater-Janak transition-state approximation.*

4.2. Electrostatic model for estimating work-function changes

Starting from the Helmholtz solution to the Poisson equation one obtains the following numerical relation between Φ, the work function including the artificial dipole layer, Φ_0, the work function in the electronic ground state, Q·Δz, the dipole moment of one dipole (expressed via the transferred charge, Q, and the charge-transfer distance, Δz), ε_r, the dielectric constant of the organic layer, and A, the area per dipole:

$$\Phi = \Phi_0 - \frac{q_e Q \cdot \Delta z}{\varepsilon_0 \varepsilon_r A}$$

Here q_e is the charge of an electron and ε_0 is the vacuum permittivity. When providing energies in eV, lengths in Å, areas in Å^2, and Q in multiples of the elementary charge, the following numerical value equation is obtained (with 180.92 being a unit-conversion factor):

$$\Phi = \Phi_0 - 180.92 \frac{Q \cdot \Delta z}{\varepsilon_r A}$$

In the case of Slater-Janak transition-state calculations, Q is set to 0.5 times the elementary charge. For the system discussed in the present manuscript, Δz amounts to 2 Å as the approximate distance over which the potential drops in Fig. 4b, and ε_r is set to 1.5 (to account for screening effects within the methane layer).

4.3. Carbon 1s core-level binding energies

Furthermore, also the core-level binding energies are shifted. The magnitude of that shift again depends on the dipole density, i.e. the excitation density, which is inversely proportional to the size of the supercell. In Figure S9 the core-level energies are plotted over the inverse supercell size. As one can see, in this case an essentially linear relation is obtained. The "linearity" condition is, however, less well fulfilled than for the work-function change. We attribute this to the "locality" character of the core-level shifts, i.e., the fact that for core-level binding energies also lateral variations in the electrostatic energy are highly relevant.

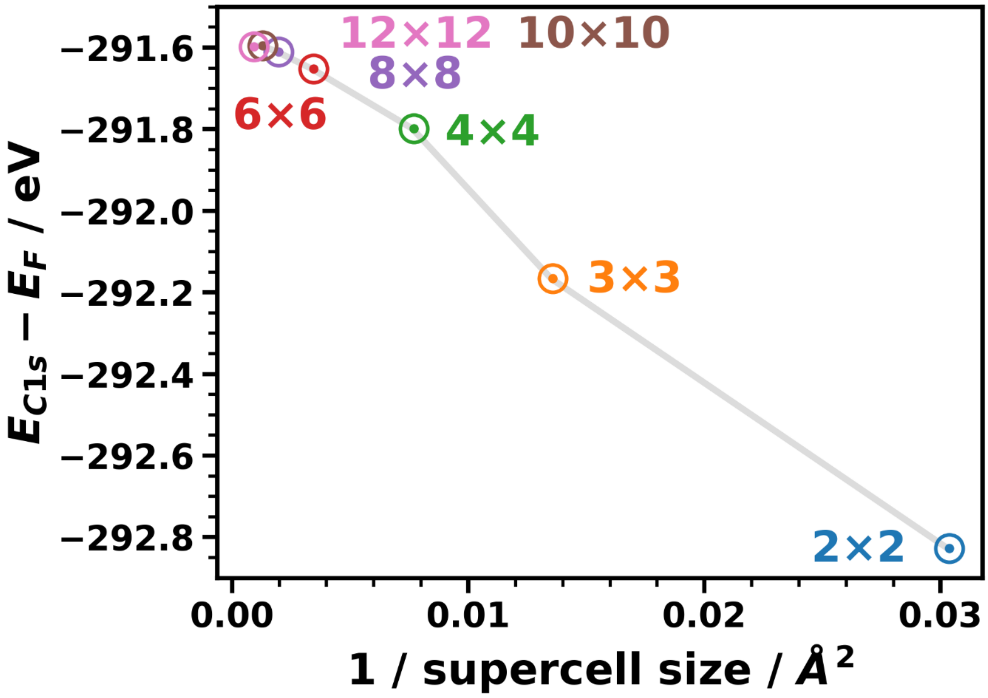

Figure S9. *Carbon 1s core-level binding energy of methane adsorbed on an Al(100) slab as a function of the inverse supercell size for calculations employing the final-state approach within the Slater-Janak transition-state approximation.*

5. Half core-hole vs. full core-hole calculations

If the observed shifts of the calculated core-level binding energies are indeed a consequence of electrostatic effects, their magnitude should depend linearly on the amount of transferred charge moved from the C 1s orbital to the Fermi level, i.e. to the metal's surface. This means in the case of a full core-hole calculation, the shift of the orbital energies should be twice as large as in calculations where half an electron is removed from the core orbital. Such a linear increase can indeed be observed, as shown in Figure S10 (at least as long as no Fermi-level pinning occurs, as discussed in chapter 10 of this Supporting Information).

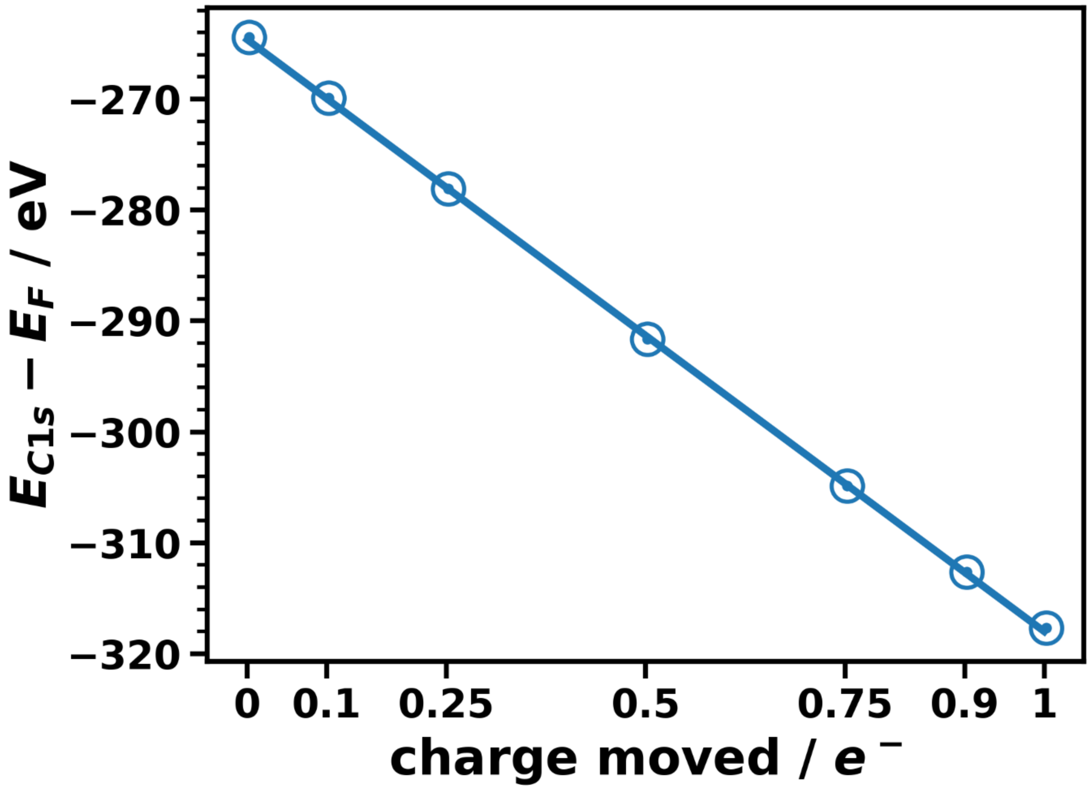

Figure S10. *Carbon 1s orbital energies for different amounts of charge moved from the core level to the lowest unoccupied level of the 8×8 supercell, and a linear fit. Zero charge transfer corresponds to a ground state calculation and a transfer of 0.5 electrons represents Slater's transition-state theory. The other points were calculated to show that this shift depends linearly on the transferred charge.*

6. Final-state calculations relying on the ΔSCF approach

Figure S11 compares the carbon 1s orbital energies calculated with two different final-state methodologies, namely the Slater-Janak transition-state theory and the ΔSCF method. In the former, half an electron is removed from the core hole and placed in the lowest unoccupied orbital of the system (in this case at the Fermi level, i.e. somewhere at the metal's surface) and in the latter a full electron is removed from the core orbital and in our case placed into the lowest unoccupied orbital. In the ΔSCF method, the core-level binding energies are then associated with the energy differences of the systems in their excited and ground state, respectively. For all but the smallest unit cell, the core-level binding energies obtained with the two different methodologies are essentially rigidly shifted relative to each other. This shows that the artificial collective electrostatic shifts are similar for both methods. This is insofar intrieguing, as the artefacts play out differently in the two approaches: When applying the Slater-Janak transition-state theory, the collective electrostatic shifts directly affect the energetic positions of the C 1s orbitals relative to the Fermi energy. Conversely, in the ΔSCF method they manifest themselves as the "charging energy" of an interfacial capacitor (cf. main manuscript).

The only exception from the overall trend is the 2×*2* unit cell, for which the C 1s core-level binding energy calculated within the ΔSCF approach is shifted significantly less than when applying the Slater-Janak transition-state theory. The reason for that is Fermi-level pinning similar to the effects observed in Figure 5a of the main manuscript. The reason why Fermi-level pinning for the ΔSCF approach occurs alrady at the equilibrium distance, while in Figure 5a it occurs especially for larger distances is the increased amount of charge transfer in the ΔSCF (a full electron instead of half an electron), which results in an increased dipole density.

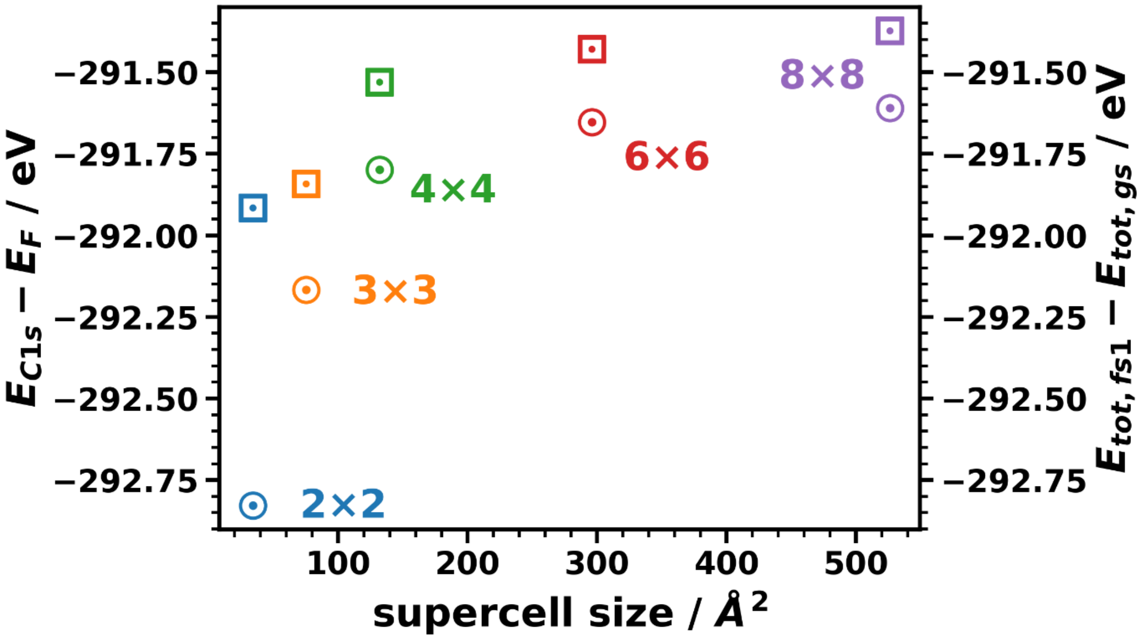

Figure S11. *C 1s core-level binding energies calculated within the Slater-Janak transition-state theory (circles) and by applying a ΔSCF approach (squares) for varying supercell sizes and excitation densities.*

7. Impact of the core-hole excitations on the work function on the Al-side of the slab

Due to the nature of final-state calculations, where charge is moved from the core orbital of an adsorbate to the lowest unoccupied level of the system, i.e., in this case to the metal slab, it is necessary to check that the latter does not deteriorate the description of the electronic structure of the substrate. To test that, we calculated to what extent the work function at the bottom side of the metal slab (i.e., the side not covered by the adsorbate) is affected by the added charge. This is done for different supercell sizes (and, thus, excitation densities). The results shown in Table S6 confirm that in none of the considered cases the bottom-side work function is changed significantly, further confirming the notion that the 3-layer Al slab is sufficiently thick for the studies reported in the present manuscript.

Table S6. *Left (aluminum-side) and right (adsorbate-side) work function of the system calculated within the final-state approach for different supercells.*

Supercell size	Φ_{Left} / eV	Φ_{Right} / eV
2×2	4.32	0.69
3×3	4.37	2.27
4×4	4.40	3.25
6×6	4.39	3.83
8×8	4.40	4.04
10×10	4.41	4.14
12×12	4.40	4.19

8. Impact of locality effects of the electrostatic energy on core-level binding energies

Here we show quantitatively that for properly capturing the impact of collective electrostatics on core-level shifts, one has to average the electrostatic energy over much smaller areas than the cross-section of the unit cell. Correspondingly, Figure S12 shows the electrostatic energy averaged over an area of only 0.08 Å^2 parallel to the surface (as an estimate for the "extent" of a C 1s orbital; see section 8.1) for the 2×2 and 12×12 cells. Both graphs reveal the pronounced dip in electrostatic energy around the core hole. Far enough above the methane molecule, the averaged electrostatic energy gradually approach the far-field values, like in Figure 3b, albeit at a much slower rate. The latter is fully consistent with the data in Figure 4. A disadvantage of the way the data are plotted in Figure S12a is, however, that the massive drops in the energy around the carbon atoms obscures the differences between different excitation densities.

Thus, in Figure S12b we plot the difference between the two curves contained in Figure S12a. Then, the 12×12 supercell can be viewed as the situation in the absence of artificial collective electrostatic effects (due to the highly diluted dipole density), while these effects are maximized for the 2×2 cell. Consequently, this plot illustrates their impact on a lateral length-scale consistent with the extent of the C 1s electron. In this way it accounts for the local nature at which core-level excitations probe the electrostatic landscape. From these data one learns that the artificial shift in electrostatic energy at the position of the C atom is, indeed, way smaller than the shift of the energy far above the interface. This reconciles the data from Figures 2a and 3c. In particular, it confirms the notion that the different magnitudes of the artificial shifts of the core-level binding energies (in Figure 2) and the work-function changes (in Figure 3c) solely arise from different "locality" with which these quantities probe the electrostatic energy across the interface.

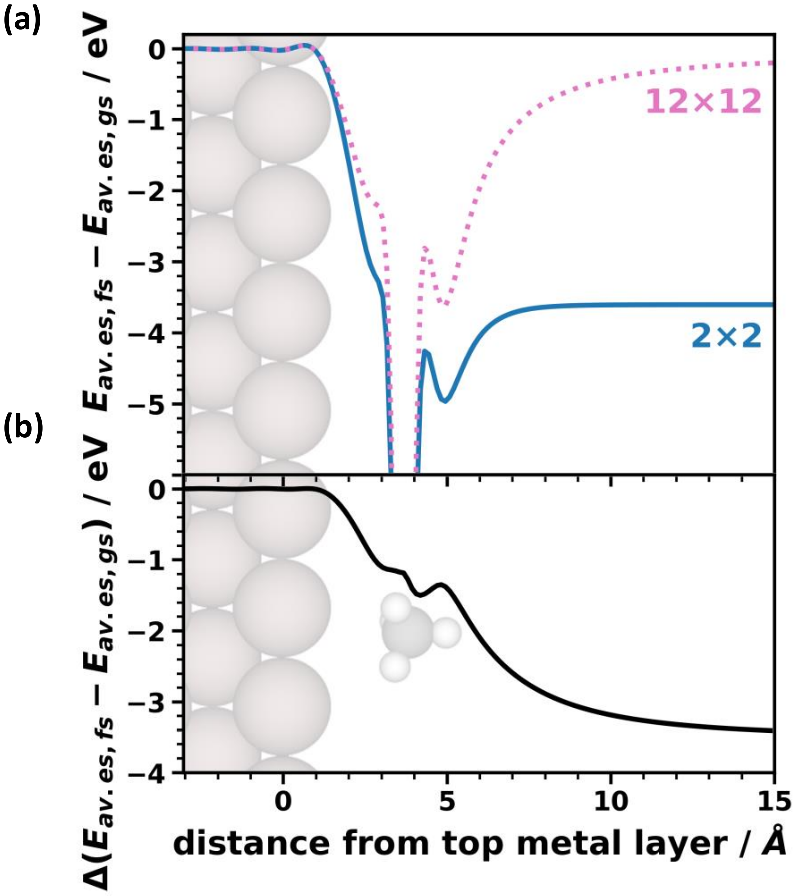

Figure S12. *(a) Difference in electrostatic energy between final-state and ground state calculations averaged over quadratic areas of 0.286 Å × 0.286 Å parallel to the substrate surface for the 2×2 (blue, solid) and 12×12 (pink, dotted) supercells. The average electrostatic energy is plotted as a function of the distance from the topmost metal layer and the area over which is averaged is chosen such that at the adsorption distance of the methane molecules, the excited carbon atom lies at the center of the square. (b) Difference of the data in panel (a) between the 2×2 and 12×12 unit cells. As the 12×12 supercell represents an essentially isolated excited dipole, these data characterize the change in the local electrostatic energy due to the surrounding excited dipoles for the 2×2 cells. In this context it is important to point out that the general shape of the curve in this figure does not depend on the specific area over which the electrostatic energy is averaged (as long as it is small enough). This is shown in the next section.*

8.1. Dependence of evolution of the local electrostatic energy on the size over which the lateral averaging occurs

To approximate electronic wavefunctions, Slater proposed the use of hydrogen-like orbitals with an effective nuclear charge. He also compiled rules for aquiring the effective nuclear charge (Z_{eff}) that should be used to take the screening of the core electrons into account. For a carbon 1s orbital this effective nuclear charge is $Z_{eff} = 5.7$,[9] which results in a radius of ~0.16 Å within which 2/3 of the C 1s charge density are contained. From this an effective cross-sectional area of the C 1s orbital of 0.08 Å^2 can be estimated analogous to the area used in the main manuscript (although there, for technical reasons, the averaging occurs over square voxels). In fact, when calculating the plane-averaged charge density associated with the C 1s orbital in the actual interface (see Figure S13) a consistent value is obtained.

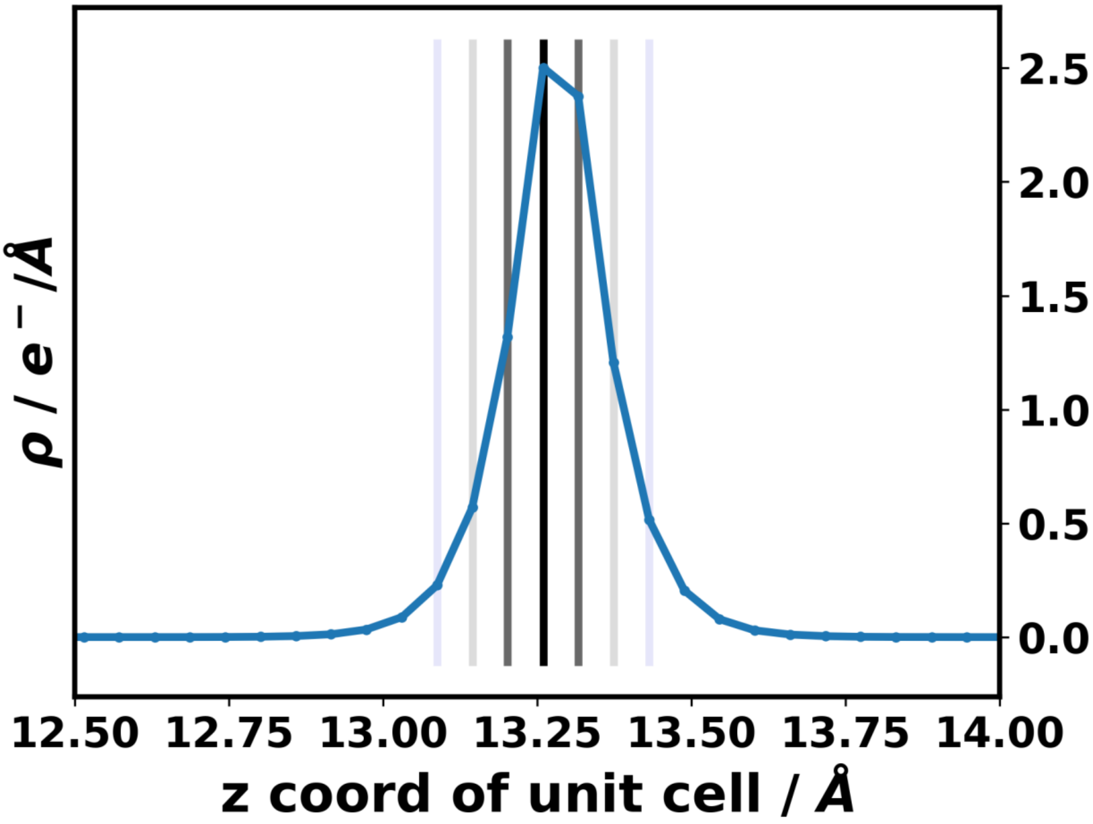

Figure S13. *Plane averaged charge density of the C 1s orbital. The vertical grey lines indicate the extent of the voxels of the grid on which the charge density was written out.*

The exact size of the area over which the electrostatic energy is averaged is, however, only of minor relevance: As shown in Figure S14 the depth of the potential well associated with the core hole, as expected, depends strongly on the area over which the averaging occurs. The actually relevant quantity, namely the difference in averaged potentials for the 2×2 and 12×12 supercells shown in Figure S15 is, however, not affected significantly.

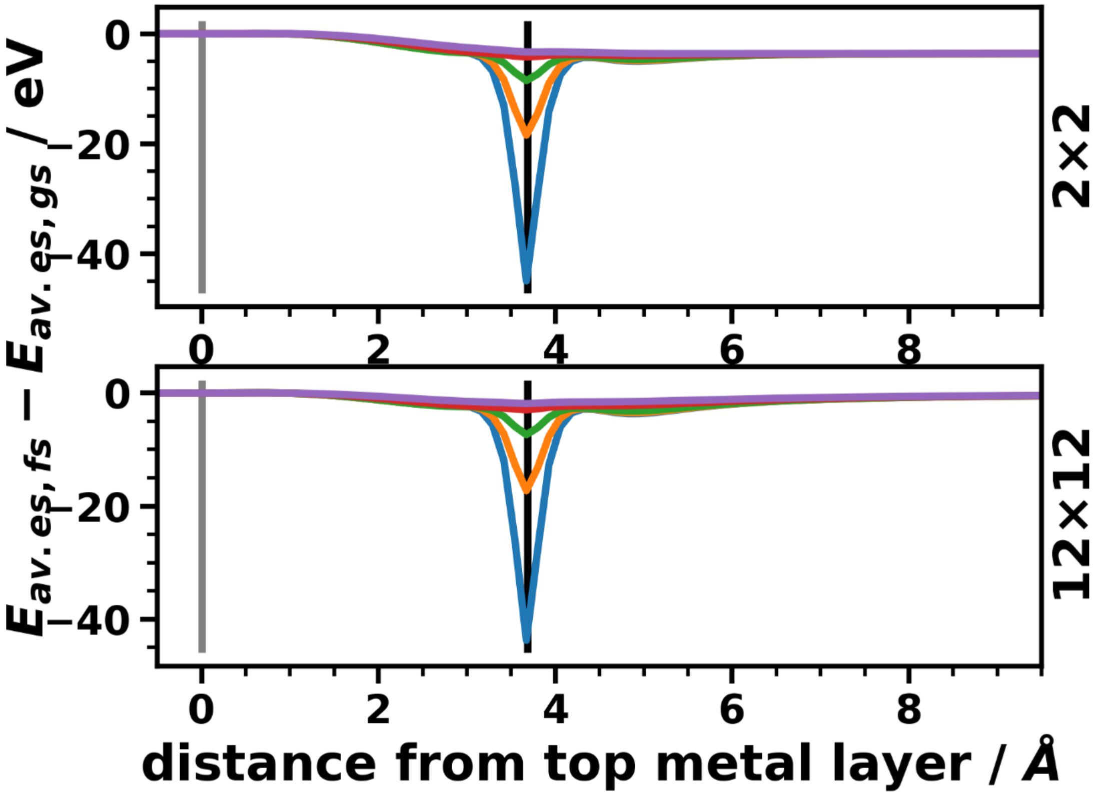

Figure S14. *Electrostatic energy averaged over differently sized areas for the 2×2 (top part) and the 12×12 (bottom part) supercell. Areas plotted: blue: 0.03 Å^2, orange: 0.40 Å^2, green: 1.45 Å^2, red: 12.20 Å^2, violet: 32.15 Å^2 (representing the total area of the 2×2 unit cell). The grey line indicates the position of the topmost aluminum layer and the black one shows the position of the carbon atom.*

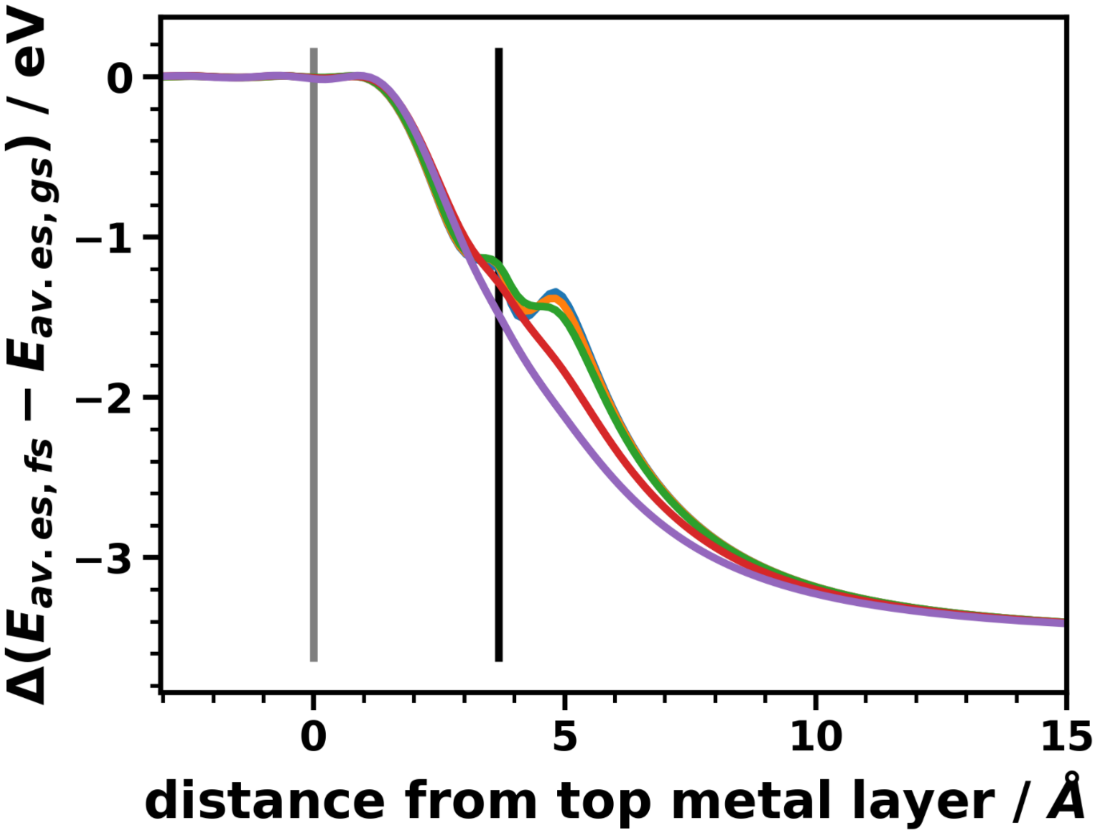

Figure S15. *Difference of the averaged electrostatic energy between the 2×2 and 12×12 supercells plotted for differently sized areas over which was averaged. Areas plotted: blue: 0.03 Å^2, orange: 0.40 Å^2, green: 1.45 Å^2, red: 12.20 Å^2, violet: 32.15 Å^2 (representing the total area of the 2×2 unit cell). The grey line indicates the position of the topmost aluminum layer and the black one shows the position of the carbon atom.*

9. Fermi-level pinning for large adsorption heights and small unit cells

As can be seen in Figure 5a of the main manuscript, for the 2×2 unit cell, the adsorption distance has hardly any impact on the C 1s energies. Conversely, for the 3×3 unit cell upon increasing the adsorption distance the orbital energies are shifted up to a certain value (significantly more negative than for the 2×2) and then pin. In other words, the pinning occurs not only at different distances, but also at very different energies. I.e., a priori, it is not clear, why the core-level in the 3×3 unit cell and in larger supercells can get shifted to energies that are significantly more negative than the energy at which pinning already occurs in the 2×2 unit cell. We here propose differences in orbital hybridization as the explanation for this effect.

Figure S16 shows the occupied and unoccupied density of states (DOS) for the 2×2 unit cell at the equilibrium adsorption distance for the ground state and for the final-state calculations. Here we also plot the unoccupied density of states at energies higher than the vacuum level above the adsorbate layer (indicated by colored vertical lines in the following plots). A priori the corresponding states cannot be properly described by an orbital-centered basis set. Nevertheless, we include it here, as it still allows the assessment of similarities between different systems (prone to the same inaccuracies due to the basis set).

The data in Figure S16 show to relevant aspects: First, the unoccupied states hybridize and broaden much more strongly than the occupied ones (as can be understood from the particularly delocalized character of the LUMO of methane shown in the top panel of Figure S16). Secondly, in the final-state calculations, in which every methane molecule is excited, the DOS is shifted essentially rigidly to higher binding energies by ~4.6 eV. As a consequence, the unoccupied DOS is shifted to the Fermi level and pinning occurs. Therefore, increasing the charge-transfer distance hardly changes the shift, as is shown for the unoccupied DOS of the 2×2 unit cell in Figure S17. Notably, also the shape of the unoccupied DOS hardly changes upon moving the molecules further away from the surface, indicating that the broadening of the unoccupied DOS in the 2×2 unit cell is really a consequence of inter-molecular (rather than molecule-substrate) interactions.

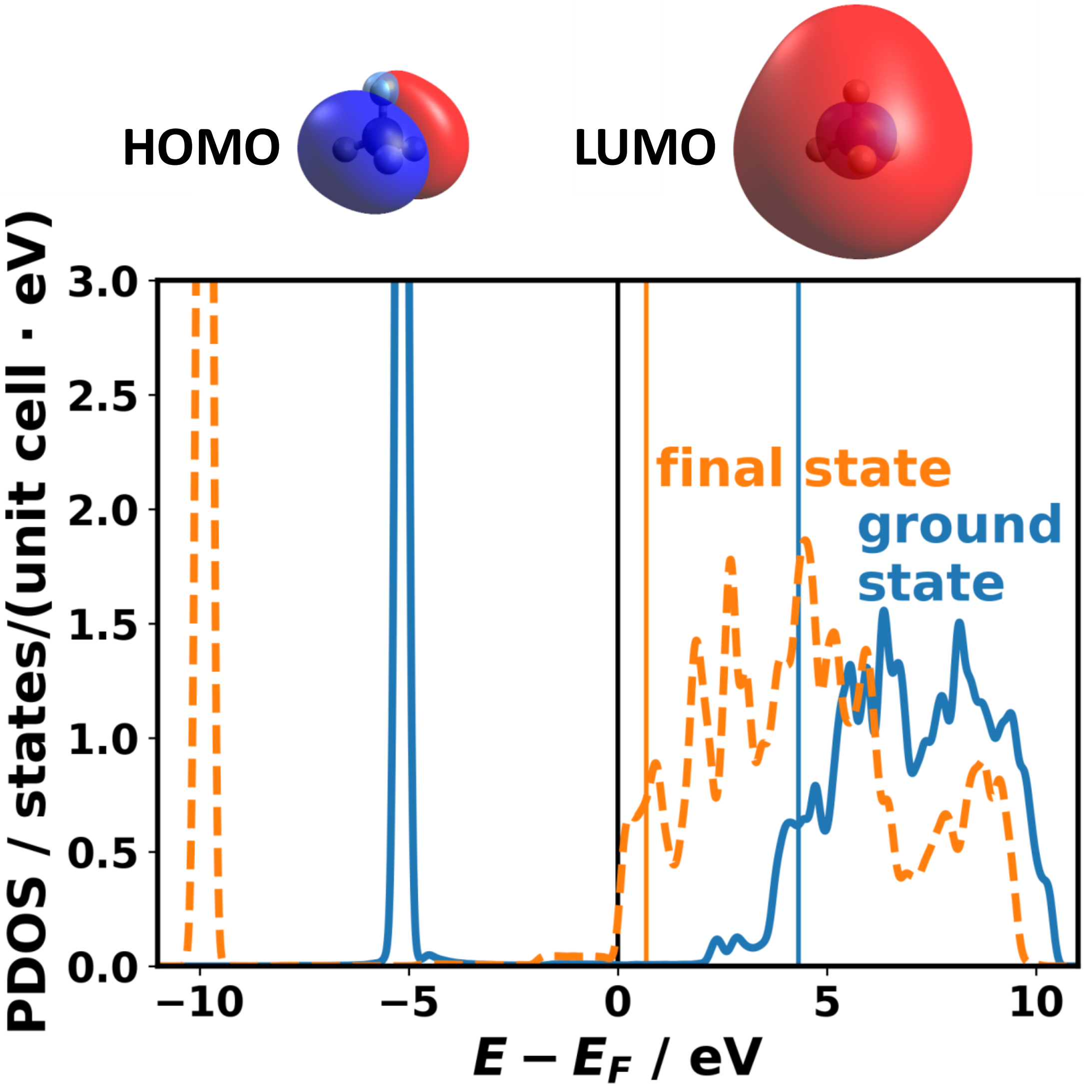

Figure S16. *Occupied and unoccupied projected density of states (PDOS) of the methane molecule, adsorbed at equilibrium distance and calculated utilizing the 2×2 unit cell. The solid, blue line is the PDOS of the ground state and the orange, dashed line the PDOS of the final-state calculation. The black line indicates the Fermi level and the orange and blue lines indicate the vacuum level of the final-state and ground state calculations, respectivly, above the adsorbate layer. Note that the states above the vaccum level are not correctly described with the employed basis set, but are still included for the sake of comparison. The top panel shows isodensity representations (isodensity value of 0.02 eV) of the highest occupied (HOMO) and lowest unoccupied molecular orbitals (LUMO) of a methane molecule calculated using gaussian16/RevA.03*[10] *employing the PBE functional and a 6-311G(d,p) basis set.*

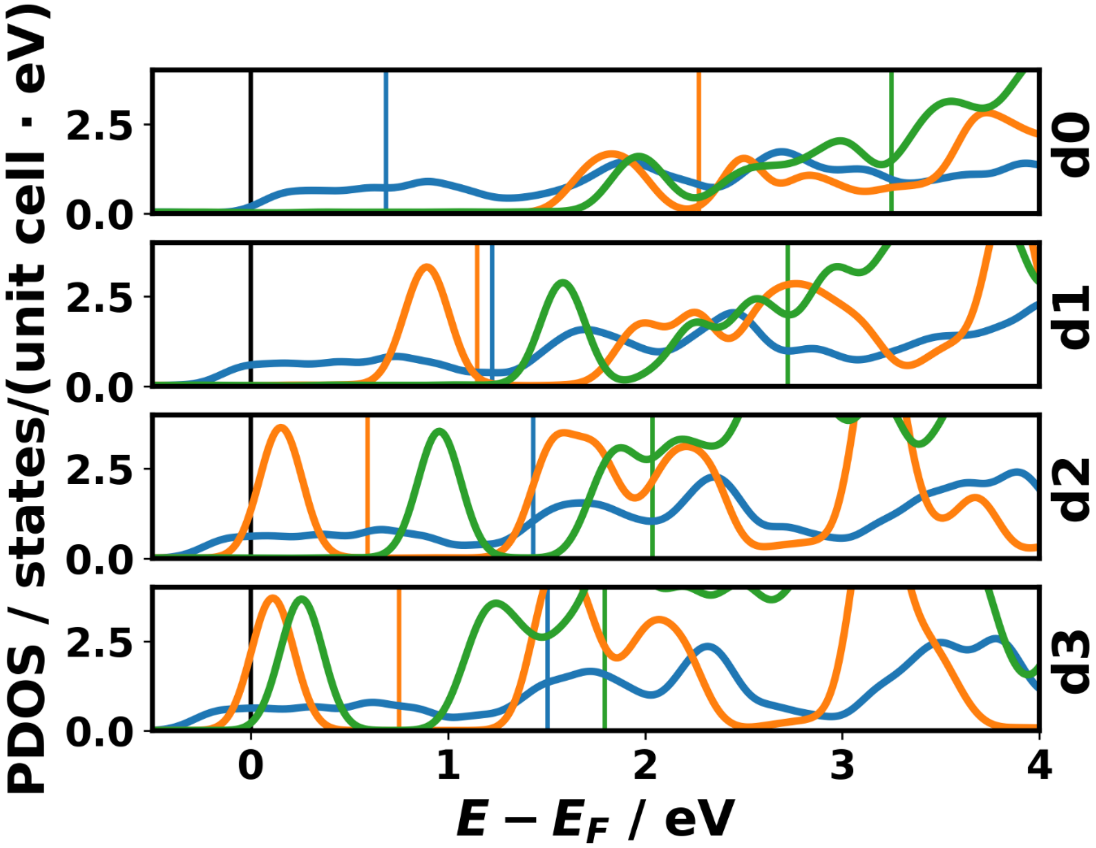

Figure S17. *Density of states of the methane monolayer calculated for different adsorption heights with different supercells. The 2×2 (blue) system is pinned already at the equilibrium adsorption distance, whereas the 3×3 (orange) methane peaks shift up to the Fermi level (from d2 on). The 4×4 methane DOS is also shifted, in the case of moving the molecule 3 Å farther away from the equilibrium adsorption distance (d3) right to the Fermi level. The black line indicates the Fermi level and the orange, blue, and green lines indicate the vacuum level following the aforementioned color code. Note that the states above that vaccum level are not correctly described with the employed basis set, but are still included for the sake of comparison.*

The situation is fundamentally different for the larger supercells. Starting from the 4x4 supercell, every excited molecule has only molecules in the ground state as nearest neighbors. Still, the orbitals of the excited molecules are stabilized by the electrostatic potential of the dipoles (albeit to a lesser degree than for the 2×2 case). Due to this shift, the unoccupied orbitals of the excited molecules would still be the ones that could cause pinning. Another consequence of the shift is, however, that, energetically, they come to lie below the orbitals of the surrounding molecules, as shown by projected densities of states in Figure S18 for the 4x4 supercell. This effectively reduces the coupling between neighboring molecules and, consequently, the DOS feature that is shifted towards E_F for all larger unit cells is a rather sharp peak, as shown in Figures S17 and S19 (with the effect particularly well visible for the 4x4 cell at larger distances).

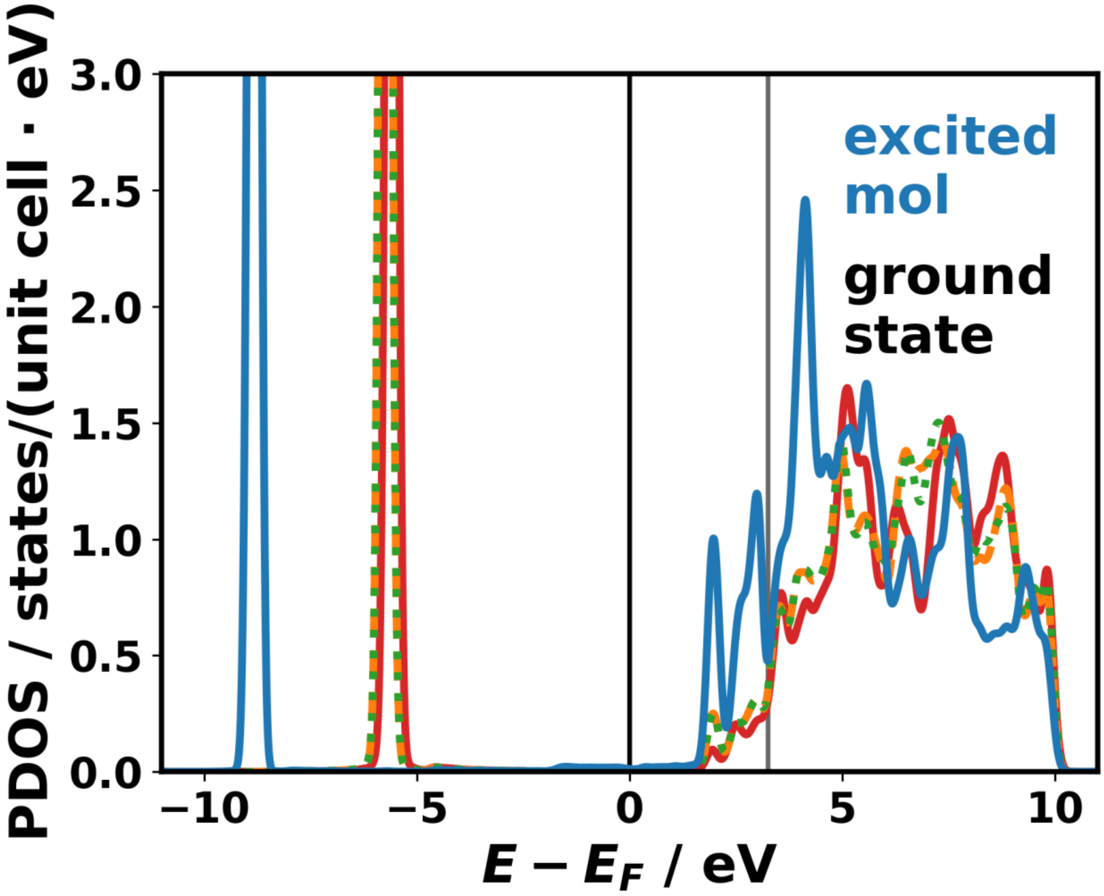

Figure S18. *Density of states of the 4×4 supercell with one molecule excited projected onto the four contained methane molecules. The PDOS of the excited methane molecule is plotted as a solid, blue line. The PDOSes of the three non-excited mlecules are plotted in orange, green, and red, respectively. An analysis of the less broadened, occupied DOS reveals that the features associated with the excited molecule are typically shifted by 3.1 eV. The black line indicates the Fermi level and the grey line indicates the vacuum level above the adsorbate* *layer following the aforementioned color code. Note that the states above that vaccum level are not correctly described with the employed basis set, but are still included for the sake of comparison.*

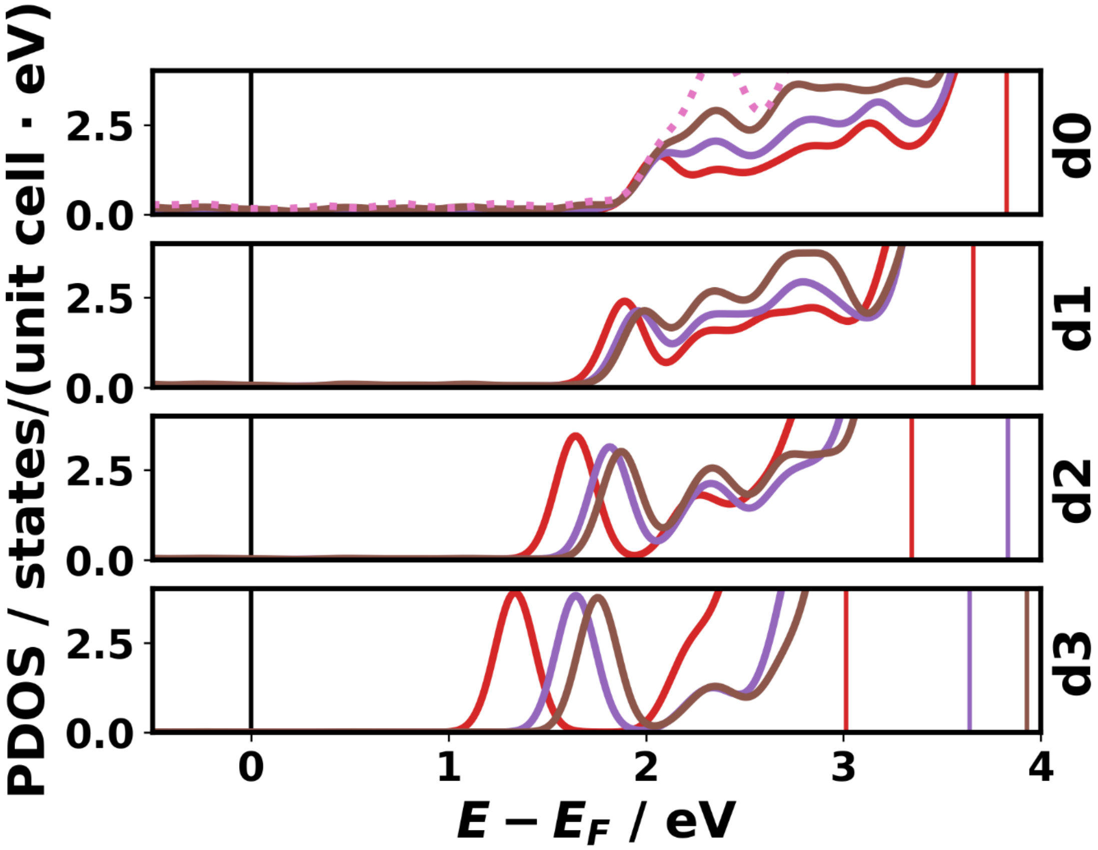

Figure S19. *Density of states of the 6×6 (red), 8×8 (violet), 10×10 (brown) and 12×12 (pink dotted, only at equilibrium distance) supercell. The methane DOS shifts also in the case of the bigger supercells plotted in this figure, but not as far as in the case of the smaller supercells. The black line indicates the Fermi level and the red, violet, and brown lines indicate the vacuum level accordingly to the before mentioned color codes. The higher-lying orbitals are not properly described with the employed basis set.*

10. HOMO – LUMO gap

Several test calculations were done with FHI-aims, Gaussian v16[10] and VASP v5.4.4[11–14] to understand the impact of the choice of the basis set on the energies of the frontier orbitals and on the gap. The results of these tests are shown in the following table. The data show that the energies of the LUMO (and correspondingly also the value of the gap) vary somewhat with the chosen basis set, with the LUMO in the FHI-aims simulations using the tight basis set (see section 2.1) significantly lies below that of all Gaussian calculations disregarding diffuse basis functions and somewhat above the values obtained with Gaussian including diffuse basis functions as well as with VASP and a plane-wave basis set. These data suggest that pinning at the LUMO would occur at somewhat higher fields in final-state calculations using FHI-aims with a tight basis set compared to equivalent simulations using a plane-wave basis in VASP. The effect is, however, not particularly strong and by no means changes the qualitative picture.

Table S7. *Highest occupied molecular orbital (HOMO) and lowest unoccupied molecular orbital (LUMO) energies and their respective gand gap calculated with different methodologies and basis sets applying open (OBC) and periodic boundary conditions (PBC). For the simulations of a single molecule with FHI-aims, a unit cell equivalent to the simulation of the 2×2 unit cell has been used from which the aluminum slab has been removed. For the VASP calculations a cubic unit cell with a sidelength of 20 Å was used.*

Method	HOMO / eV	LUMO / eV	GAP / eV
Gaussian 6-311G(d,p)[15–18], OBC	-9,392	1,021	10,414
Gaussian 6-311++G(d,p)[15–18], OBC	-9,413	-0,332	9,081
Gaussian cc-pVTZ[19–24], OBC	-9,404	0,810	10,214
Gaussian cc-pVQZ[19–24], OBC	-9,419	0,430	9,849
Gaussian cc-pV5Z[19–24], OBC	-9,424	0,160	9,583
Gaussian AUG-cc-pVTZ[19–24], OBC	-9,418	-0,376	9,042
FHI-aims, tight basis set (see section 2.1), OBC	-9,404	0,003	9,408
FHI-aims, tight basis set (see section 2.1), PBC	-9,436	-0,030	9,406
VASP, ENCUT = 700 eV, PBC	-9.383	-0.388	9.035
VASP, ENCUT = 1400 eV PBC	-9.417	-0.429	8.988

11. Electrical field for a CREST-type compensation charge

In the main manuscript it has been argued that the spurious collective electrostatic shifts of core-level binding energies in final-state calculations could be avoided by a CREST-like approach[25,26] localizing the compensation charges statically in a charged sheet, rather than putting them into the lowest unoccupied states in the metal next to the Fermi level. In that case, the charged sheet would have to be placed above the adsorbate layer so that the field between the core holes and the compensation charges is primarily found above the adsorbate molecules and in this way cannot shift the positions of the core levels relative to the metal's Fermi level. A similar effect as with a charged sheet can also be achieved for point charges sufficiently far away from the interface (in the following plot at a distance of 30 Å).

As shown in Figure S20 for two differently sized unit cells, the field of that array of point charges (formed by the core holes and their compensation charges) decays rapidly on the substrate-side of the core holes (i.e. at negative distances), while it quickly approaches a constant value on the other side. This shows that in this way, spurious collective electrostatic shifts of core-level binding energies can indeed be avoided. What the plot, however, also shows is that the decay of the field on the substrate side is much faster than it would be for an isolated point charge. The field of the latter is, however, the field that triggers the screening effects in the metal, that are meant to be described by the final-state calculations. Consequently, a CREST-like compensation charge will result in an incorrect description of the core-hole screening, especially for small unit cells.

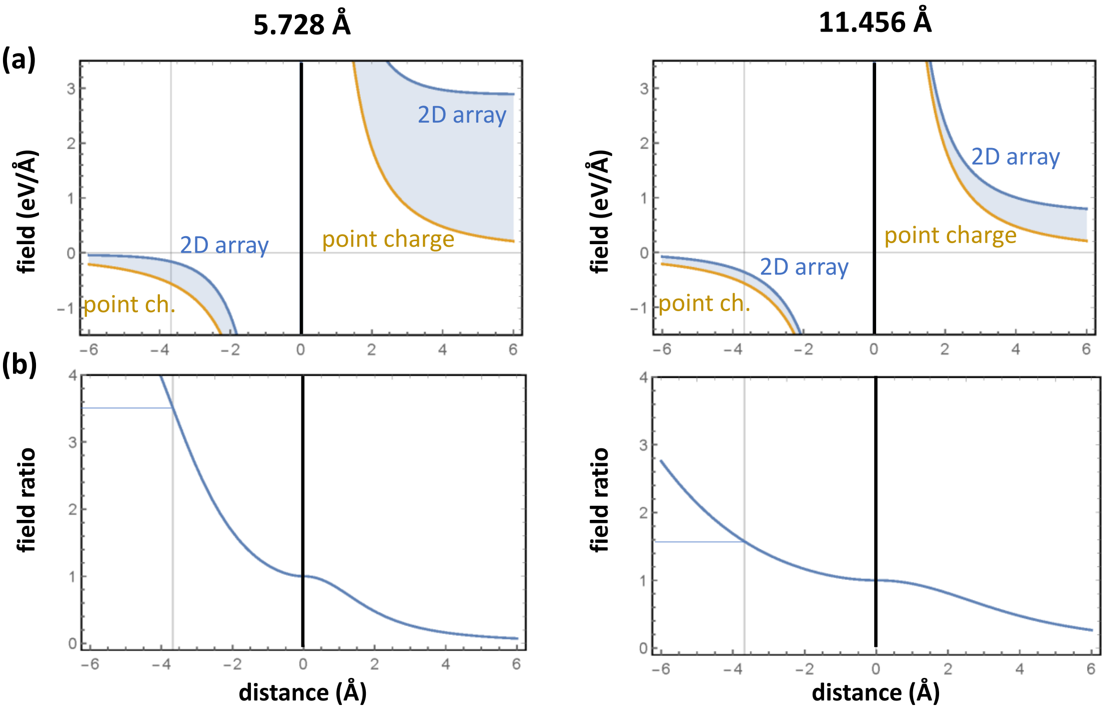

Figure S20. *(a) Electric fields in z-direction generated by a point charge (light brown) and by two parallel 2D arrays of oppositely charged point charges (blue) as a function of the distance from one of the point charges. The absolute magnitude of each corresponds to the elementary charge (when considering half core-holes, the magnitudes of the fields need to be divided by two). The 2D point charge arrays are each arranged on a quadratic grid with a distance between the charges of 5.728 Å (left panels, corresponding to the 2×2 unit cell) and 11.456 Å (right panels, corresponding to the 4×4 supercell). The positively charged sheet is positioned at "distance" zero and represents periodically repeated core holes. The negative charges represent the compensation charges in a CREST-like approach and are positioned at a "distance" of +30 Å. The field is plotted along a line perpendicular to the planes of the arrays of charges. That line goes right through a pair of point charges. The thin line at -3.68 Å relative to the core hole denotes the distance of the topmost aluminum layer from the core hole generated on the carbon atom of the methane. (b) Ratio of the two fields plotted in panel (a). The simulations have been performed using Mathematica*[27]*.*

12. References

(1) Blum, V.; Gehrke, R.; Hanke, F.; Havu, P.; Havu, V.; Ren, X.; Reuter, K.; Scheffler, M. Ab Initio Molecular Simulations with Numeric Atom-Centered Orbitals. *Comput. Phys. Commun.* **2009**, *180* (11), 2175–2196. https://doi.org/10.1016/j.cpc.2009.06.022.

(2) Hjorth Larsen, A.; Jørgen Mortensen, J.; Blomqvist, J.; Castelli, I. E.; Christensen, R.; Dułak, M.; Friis, J.; Groves, M. N.; Hammer, B.; Hargus, C.; Hermes, E. D.; Jennings, P. C.; Bjerre Jensen, P.; Kermode, J.; Kitchin, J. R.; Leonhard Kolsbjerg, E.; Kubal, J.; Kaasbjerg, K.; Lysgaard, S.; Bergmann Maronsson, J.; Maxson, T.; Olsen, T.; Pastewka, L.; Peterson, A.; Rostgaard, C.; Schiøtz, J.; Schütt, O.; Strange, M.; Thygesen, K. S.; Vegge, T.; Vilhelmsen, L.; Walter, M.; Zeng, Z.; Jacobsen, K. W. The Atomic Simulation Environment—a Python Library for Working with Atoms. *J. Phys. Condens. Matter* **2017**, *29* (27), 273002. https://doi.org/10.1088/1361-648X/aa680e.

(3) Macdonald, J. R.; Barlow, C. A. Work Function Change on Monolayer Adsorption. *J. Chem. Phys.* **1963**, *39* (2), 412–422. https://doi.org/10.1063/1.1734263.

(4) Maschhoff, B. L.; Cowin, J. P. Corrected Electrostatic Model for Dipoles Adsorbed on a Metal Surface. *J. Chem. Phys.* **1994**, *101* (9), 8138–8151. https://doi.org/10.1063/1.468241.

(5) Monti, O. L. A. Understanding Interfacial Electronic Structure and Charge Transfer: An Electrostatic Perspective. *J. Phys. Chem. Lett.* **2012**, *3* (17), 2342–2351. https://doi.org/10.1021/jz300850x.

(6) Natan, A.; Kuritz, N.; Kronik, L. Polarizability, Susceptibility, and Dielectric Constant of Nanometer-Scale Molecular Films: A Microscopic View. *Adv. Funct. Mater.* **2010**, *20* (13), 2077–2084. https://doi.org/10.1002/adfm.200902162.

(7) De Renzi, V.; Rousseau, R.; Marchetto, D.; Biagi, R.; Scandolo, S.; del Pennino, U. Metal Work-Function Changes Induced by Organic Adsorbates: A Combined Experimental and Theoretical Study. *Phys. Rev. Lett.* **2005**, *95* (4). https://doi.org/10.1103/PhysRevLett.95.046804.

(8) Zojer, E.; Taucher, T. C.; Hofmann, O. T. The Impact of Dipolar Layers on the Electronic Properties of Organic/Inorganic Hybrid Interfaces. *Adv. Mater. Interfaces* **2019**, *6* (14), 1900581. https://doi.org/10.1002/admi.201900581.

(9) Slater, J. C. Atomic Shielding Constants. *Phys. Rev.* **1930**, *36* (1), 57–64. https://doi.org/10.1103/PhysRev.36.57.

(10) Frisch, M. J.; Trucks, G. W.; Schlegel, H. B.; Scuseria, G. E.; Robb, M. A.; Cheeseman, J. R.; Scalmani, G.; Barone, V.; Petersson, G. A.; Nakatsuji, H.; Li, X.; Caricato, M.; Marenich, A. V.; Bloino, J.; Janesko, B. G.; Gomperts, R.; Mennucci, B.; Hratchian, H. P.; Ortiz, J. V.; Izmaylov, A. F.; Sonnenberg, J. L.; Williams-Young, D.; Ding, F.; Lipparini, F.; Egidi, F.; Goings, J.; Peng, B.; Petrone, A.; Henderson, T.; Ranasinghe, D.; Zakrzewski, V. G.; Gao, J.; Rega, N.; Zheng, G.; Liang, W.; Hada, M.; Ehara, M.; Toyota, K.; Fukuda, R.; Hasegawa, J.; Ishida, M.; Nakajima, T.; Honda, Y.; Kitao, O.; Nakai, H.; Vreven, T.; Throssell, K.; Montgomery, J. A., Jr.; Peralta, J. E.; Ogliaro, F.; Bearpark, M. J.; Heyd, J. J.; Brothers, E. N.; Kudin, K. N.; Staroverov, V. N.; Keith, T. A.; Kobayashi, R.; Normand, J.; Raghavachari, K.; Rendell, A. P.; Burant, J. C.; Iyengar, S. S.; Tomasi, J.; Cossi, M.; Millam, J. M.; Klene, M.; Adamo, C.; Cammi, R.; Ochterski, J. W.; Martin, R. L.; Morokuma, K.; Farkas, O.; Foresman, J. B.; Fox, D. J. *Gaussian˜16 Revision A.03*; 2016.

(11) Kresse, G.; Hafner, J. Ab Initio Molecular Dynamics for Liquid Metals. *Phys. Rev. B* **1993**, *47* (1), 558–561. https://doi.org/10.1103/PhysRevB.47.558.
(12) Kresse, G.; Hafner, J. Ab Initio Molecular-Dynamics Simulation of the Liquid-Metal–Amorphous-Semiconductor Transition in Germanium. *Phys. Rev. B* **1994**, *49* (20), 14251–14269. https://doi.org/10.1103/PhysRevB.49.14251.
(13) Kresse, G.; Furthmüller, J. Efficiency of Ab-Initio Total Energy Calculations for Metals and Semiconductors Using a Plane-Wave Basis Set. *Comput. Mater. Sci.* **1996**, *6* (1), 15–50. https://doi.org/10.1016/0927-0256(96)00008-0.
(14) Kresse, G.; Furthmüller, J. Efficient Iterative Schemes for *Ab Initio* Total-Energy Calculations Using a Plane-Wave Basis Set. *Phys. Rev. B* **1996**, *54* (16), 11169–11186. https://doi.org/10.1103/PhysRevB.54.11169.
(15) Petersson, G. A.; Bennett, A.; Tensfeldt, T. G.; Al-Laham, M. A.; Shirley, W. A.; Mantzaris, J. A Complete Basis Set Model Chemistry. I. The Total Energies of Closed-shell Atoms and Hydrides of the First-row Elements. *J. Chem. Phys.* **1988**, *89* (4), 2193–2218. https://doi.org/10.1063/1.455064.
(16) Petersson, G. A.; Al-Laham, M. A. A Complete Basis Set Model Chemistry. II. Open-shell Systems and the Total Energies of the First-row Atoms. *J. Chem. Phys.* **1991**, *94* (9), 6081–6090. https://doi.org/10.1063/1.460447.
(17) McLean, A. D.; Chandler, G. S. Contracted Gaussian Basis Sets for Molecular Calculations. I. Second Row Atoms, Z =11–18. *J. Chem. Phys.* **1980**, *72* (10), 5639–5648. https://doi.org/10.1063/1.438980.
(18) Krishnan, R.; Binkley, J. S.; Seeger, R.; Pople, J. A. Self-consistent Molecular Orbital Methods. XX. A Basis Set for Correlated Wave Functions. *J. Chem. Phys.* **1980**, *72* (1), 650–654. https://doi.org/10.1063/1.438955.
(19) Dunning, T. H. Gaussian Basis Sets for Use in Correlated Molecular Calculations. I. The Atoms Boron through Neon and Hydrogen. *J. Chem. Phys.* **1989**, *90* (2), 1007. https://doi.org/10.1063/1.456153.
(20) Kendall, R. A.; Dunning, T. H.; Harrison, R. J. Electron Affinities of the First-Row Atoms Revisited. Systematic Basis Sets and Wave Functions. *J. Chem. Phys.* **1992**, *96* (9), 6796. https://doi.org/10.1063/1.462569.
(21) Woon, D. E.; Dunning, T. H. Gaussian Basis Sets for Use in Correlated Molecular Calculations. III. The Atoms aluminum through Argon. *J. Chem. Phys.* **1993**, *98* (2), 1358. https://doi.org/10.1063/1.464303.
(22) Peterson, K. A.; Woon, D. E.; Dunning, T. H. Benchmark Calculations with Correlated Molecular Wave Functions. IV. The Classical Barrier Height of the $H+H_2 \rightarrow H_2 + H$ Reaction. *J. Chem. Phys.* **1994**, *100* (10), 7410–7415. https://doi.org/10.1063/1.466884.
(23) Wilson, A. K.; van Mourik, T.; Dunning, T. H. Gaussian Basis Sets for Use in Correlated Molecular Calculations. VI. Sextuple Zeta Correlation Consistent Basis Sets for Boron through Neon. *J. Mol. Struct. THEOCHEM* **1996**, *388*, 339–349. https://doi.org/10.1016/S0166-1280(96)80048-0.
(24) Davidson, E. R. Comment on “Comment on Dunning’s Correlation-Consistent Basis Sets.” *Chem. Phys. Lett.* **1996**, *260* (3–4), 514–518. https://doi.org/10.1016/0009-2614(96)00917-7.
(25) Sinai, O.; Hofmann, O. T.; Rinke, P.; Scheffler, M.; Heimel, G.; Kronik, L. Multiscale Approach to the Electronic Structure of Doped Semiconductor Surfaces. *Phys. Rev. B* **2015**, *91* (7), 075311. https://doi.org/10.1103/PhysRevB.91.075311.

(26) Erker, S.; Rinke, P.; Moll, N.; Hofmann, O. T. Doping Dependence of the Surface Phase Stability of Polar O-Terminated $(000\bar{1})$ ZnO. *New J. Phys.* **2017**, *19* (8), 083012. https://doi.org/10.1088/1367-2630/aa79e7.
(27) Wolfram Research, Inc. *Mathematica*; Version 11.3; Champaign, IL, 2018.

4.8 PARTLY FLUORINATED ALKYL THIOLATES ON AU(111)

As was shown quite instructively with a carefully chosen model system [59] (embedded as Chapter 4.6), computational artifacts can have a fundamental impact when calculating core-level binding energies. In this chapter the influence of the aforementioned artifacts are studied for a more realistic system: an experimentally [38, 213] and theoretically [153] thoroughly studied hybrid organic metal interface, namely a self-assembled monolayer (SAM) of a partly fluorinated alkyl thiolate on a Au(111) surface. These substituted alkyl thiolotes on a gold substrate are one of the most established types of SAMs.[214] The calculations in ref. [153] where done within the initial-state method as described in Chapter 4.1, meaning electrostatic screening was accounted for a posteriori, but final state effects where entirely neglected. In the following chapter the same system was investigated with the a priori more sophisticated final-state method. As discussed in the previous section, this approach, however, suffers from spurious collective electrostatic effects. What will additionally be shown is how these spurious effects are superimposed on the actual chemical and electrostatic shifts of the electronic levels of the SAM.

4.8.1 *Investigated system*

In Figure 7(a) the chemical structure of the investigated system is shown.

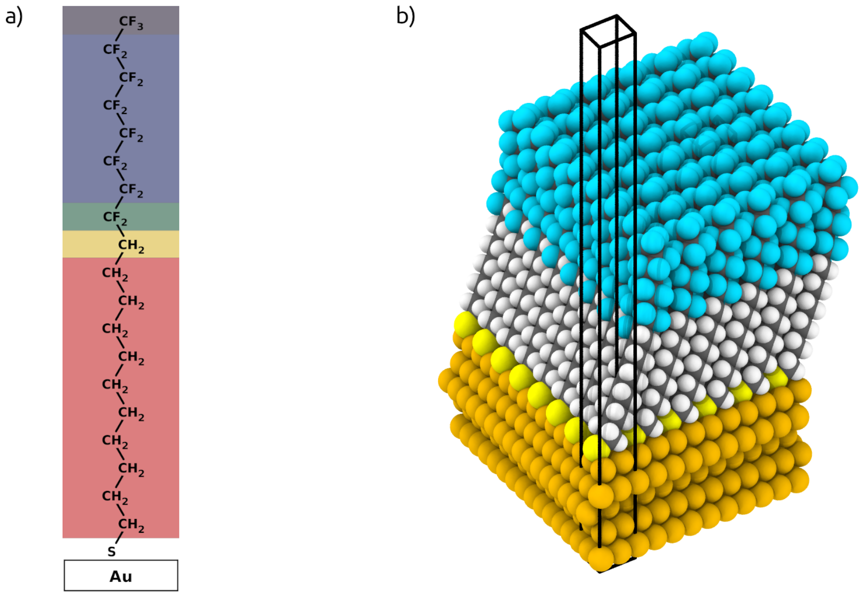

Figure 7: (a) Chemical structure of a partly fluorinated alkyl thiolate on a Au(111)-surface with the chemical formula 12,12,13,13,14,14,15,15,16,16,17,17,18,18,19,19,19-heptadecafluorononadecane-1-thiolate. The different background colors depict C atoms whose core-levels experience chemically distinct environments. (b) 3D model of the system with the black box indicating the unit cell used for the DFT-calculation utilizing the repeated slab approach (RSA). Figure modified from [153].

In part (b) of Figure 7 a $3D$ model of the unit cell repeated in x- and y-direction is shown to depict the effectively modeled system with the black box highlighting the actual unit cell which was used in conjunction with the repeated slab approach (RSA). The vacuum region added on top of the SAM is necessary to decouple the system quantum-mechanically in z-direction, because periodic boundary conditions are applied in all three spatial directions. A more thorough explanation of the RSA is given in Chapter 2.5.1.

4.8.2 *Core-level orbital energies*

In Figure 8 the calculated core-level binding energies are shown obtained within the initial-state approach with (blue stars) and without (orange crosses) a posteriori screening, as well as the results acquired utilizing the Slater-Janak transition-state theory, i. e., within a final-state approach (cyan dots).

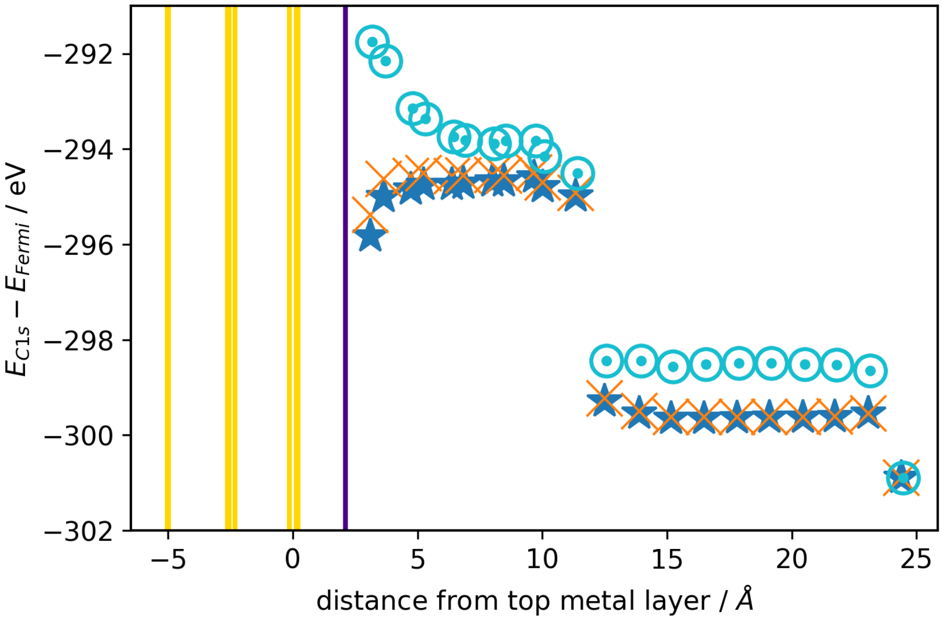

Figure 8: Carbon 1s core-level orbital energies of a partly fluorinated alkyl thiolate-SAM on a Au(111)-substrate. The values calculated within the final-state approach (cyan dots) differ compared to the ones calculated within the initial-state approach (blue stars). The orange crosses depict the initial-state values without an a posteriori screening correction. Furthermore, the initial-state results are rigidly shifted in such a way that the orbital energy of the topmost carbon atom coincide with the one acquired within the final-state approach for easier comparison. The gold lines represent the three topmost layers of the Au(111)-slab and the violet line depicts the position of the sulfur atom.

As can be seen, the chemical shifts are reproduced in both methods quite well, even though the relative shift of the triple fluorinated carbon atom is bigger in the case of the final-state method. In the case of the results acquired within the initial-state method, the following observations can be made: The very first carbon atom in the alkyl chain right next to the sulfur atom is chemically shifted to more negative binding energies with respect to the other carbon atoms in the alkyl chain of the molecule. The same behavior can be seen for the top most carbon atom in the alkyl chain, which experiences a different chemical neighborhood due to the fluorinated carbon atom right next to it.

The situation is drastically different for the final-state results. Here the core-level binding energies of the atoms in the alkyl chain, which exhibit the same chemical neighborhood, are shifted with respect to each other by up to 2 eV depending on the distance to the metal substrate. This is due to spurious collective electrostatic effects introduced by the utilized final-state methodology in conjunction with periodic boundary conditions (PBC).[59] As already mentioned, the chemical shifts are correctly reproduced in both, the initial and final state results. But in the case of the final-state calculations these are superimposed by spurious shifts introduced due to an artificial dipole layer created by the charge being moved from the core-level of the carbon atom, which is ionized in the final-state calculation, to the lowest, unoccupied orbital. When dealing with organic molecules on metal substrates, the lowest, unoccupied orbital lies right at the Fermi edge of the metal. The effect due to this spurious layer of dipoles can be seen quite strikingly by looking at the evolution of the core-level energies of the bottom most carbon atoms calculated within the final-state approach (cyan dots). As one can see, the core-levels experiencing the same chemical neighborhood are shifted with respect to each other, depending on their distance to the metal layer. This corresponds to the increasing size of the artificially introduced densely packed dipoles. This happens up to the fourth carbon atom, starting from there, the energy levels are not shifted further. The reason for this is the onset of Fermi-level pinning, as can be seen in the valence density of states (DOS) shown in Figure 9 for the alkyl chain of the molecule. There, the darkest line shows the projected DOS of the bottom most carbon atom at around 2 eV. As can be seen, the second carbon atom of the alkyl chain is shifted by ca. 1 eV relative to the first atom of the alkyl chain. The third carbon atom experiences the same relative shift, while starting from the fourth carbon atom, the levels are not shifted any further due to the fact that the DOS-peaks are already at the Fermi level, and, thus, *Fermi-level pinned*.

What can also be deduced from Figure 8 and 9 is that chemical and electrostatic effects are superimposed on each other. The projected DOS of the frontier valence state of the bottom most carbon atom is clearly shifted by around 1 eV with respect to the second carbon atom of the alkyl chain (as is the second with respect to the third, for that matter). Now when comparing the shifts to the ones of the core-level energies, it can be seen that the relative shift between the second and third carbon atom of the alkyl chain is also around 1 eV. In contrast to that, the shift between the first and the second carbon atom's core-level energy is almost vanishing. This is due to the fact that the spurious collective electrostatic effect would shift the

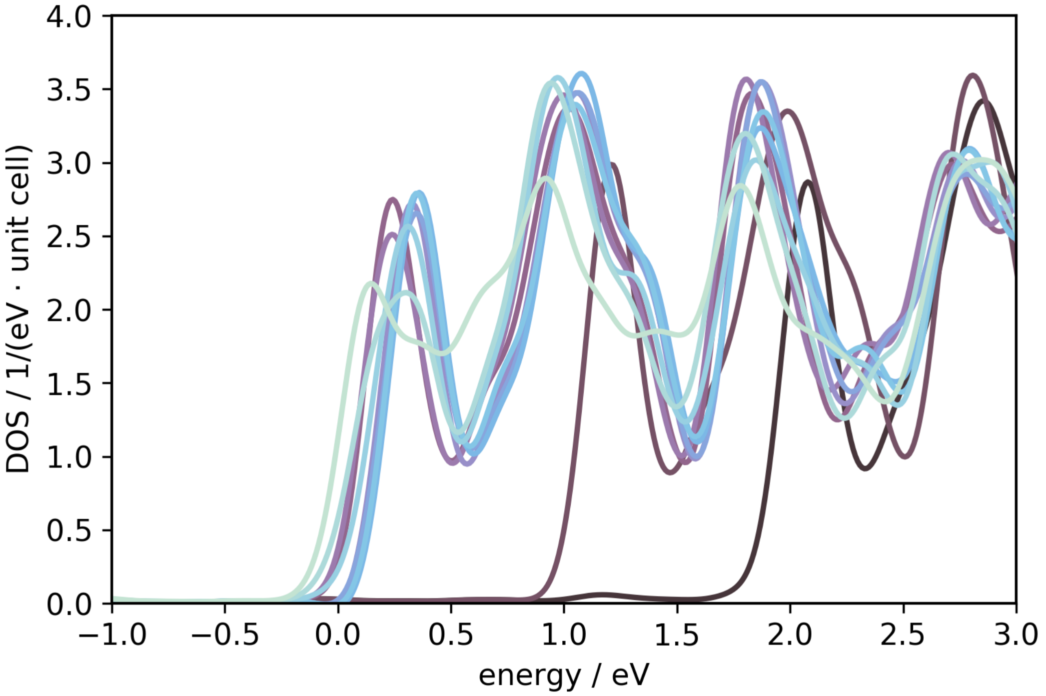

Figure 9: Projected density of states (DOS) of the carbon atoms in the alkyl chain of the molecule, i. e., the bottom most eleven atoms, aligned to the Fermi energy of each system. The darkest line (peak at ca. 2 eV) denotes the carbon atom closest to the metal substrate and the lightest color the atom right next to the fluorinated part. The DOSs of the first few atoms are shifted relative to each other by around 1 eV until the valence level is Fermi pinned. Additionally, the chemically different neighborhood can be deduced from the qualitatively different style of the peak originating from the top most alkyl carbon atom (lightest color), which is placed next to the fluorinated part of the molecule.

core-level by around 1 eV to less negative values, whereas the chemical shift due to the adjacent sulfur atom, however, shifts the core-level to more negative values. This can be deduced from the results acquired with an initial-state calculation, which is included in Figure 8. Due to these two effects shifting the core-level in opposite directions, the resulting shift is rather small. The chemical shift of the two topmost atoms of the alkyl chain can be seen again, as they are experiencing a different chemical neighborhood due to the adjacent fluorinated part of the molecule. The fluorinated part of the carbon chain (starting at the 12^{th} carbon atom at a distance of 12.5 Å from the top metal layer) is not shifted with respect to the size of the artificially induced dipole in the final-state calculations, because in this case already the bottom most atom is pinned at the Fermi level, as can be deduced from the DOS shown in Figure 10. This means, great care has to be taken, because these spurious collective effects might not be evident at a first glance. Furthermore, the relative shift between the topmost carbon atom, which is chemically shifted due to bonding to three fluorine atoms with respect to the fluorinated chain, is different in the final-state calculations when compared to the initial-state calculations, which fit the experimentally measured data quite

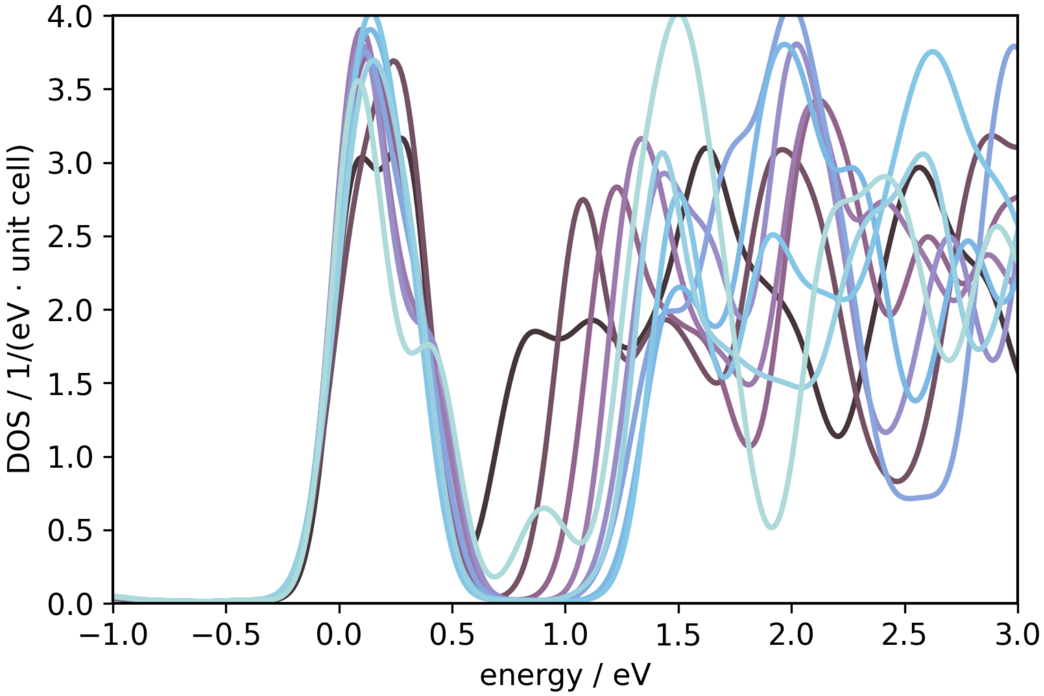

Figure 10: Projected density of states (DOS) of the carbon atoms in the fluorinated part of the molecule, i. e., the top most ten atoms, aligned to the Fermi energy of each system. The darkest line denotes the carbon atom closest to the metal substrate, which exhibits a double peak feature. The lightest color denotes the atom at the very top of the molecule, bonded to three fluorine atoms, which shows a qualitatively different peak with a distinctive shoulder due to the different chemical neighborhood.

well.[153] As can be seen in Figure 10, the DOS-peak (lightest line) of the triple fluorinated carbon atom is also right at the Fermi level and produces a qualitatively different peak, featuring a shoulder.

Furthermore, the absolute orbital energies acquired within the final-state approach do not match the experimentally measured core-level binding energies, but are shifted to more negative binding energies by around 8 eV.[213] Even though this is a substantially smaller shift in comparison to almost 20 eV in the case of initial-state calculations [153], the absolute core-level binding energies still do not reproduce HRXPS measurements in a satisfactory way.

4.8.3 *Plane averaged potential*

In Figure 11 the plane averaged potential difference of an initial and a final state calculation of the partly fluorinated alkyl thiolate is shown. It can be seen that in different regions of the molecule the influence of different effects dominate. What is true for all cases is that the potential up to the atom treated in the final state approach changes linearly with the distance to the metal-SAM-interface in a first approximation. The slope for the first few atoms is the same, as one would expect for the case of a simple electrostatic dipole. Here, again, can be seen that the relative shift between the first and the second, and the second and the third carbon atom is around 1 eV, respectively. When the system runs into pinning, the potential difference does not change by that much anymore.

What is also noteworthy, is that the potential difference behaves differently right at the carbon atom treated in the final state approach and thereafter. The potential difference stays practically the same in the case of the bottom most carbon atoms (or the top most fluorinated carbon atoms), whereas a pronounced drop can be seen for the atoms in the middle of the molecule. This behavior is resembled when looking at the work function (cf. Chapter 4.8.5), and explains why the work function shift is different compared to the core-level shift, as the former is a measure for the potential in the far field, whereas the latter probes the local electrostatic potential.

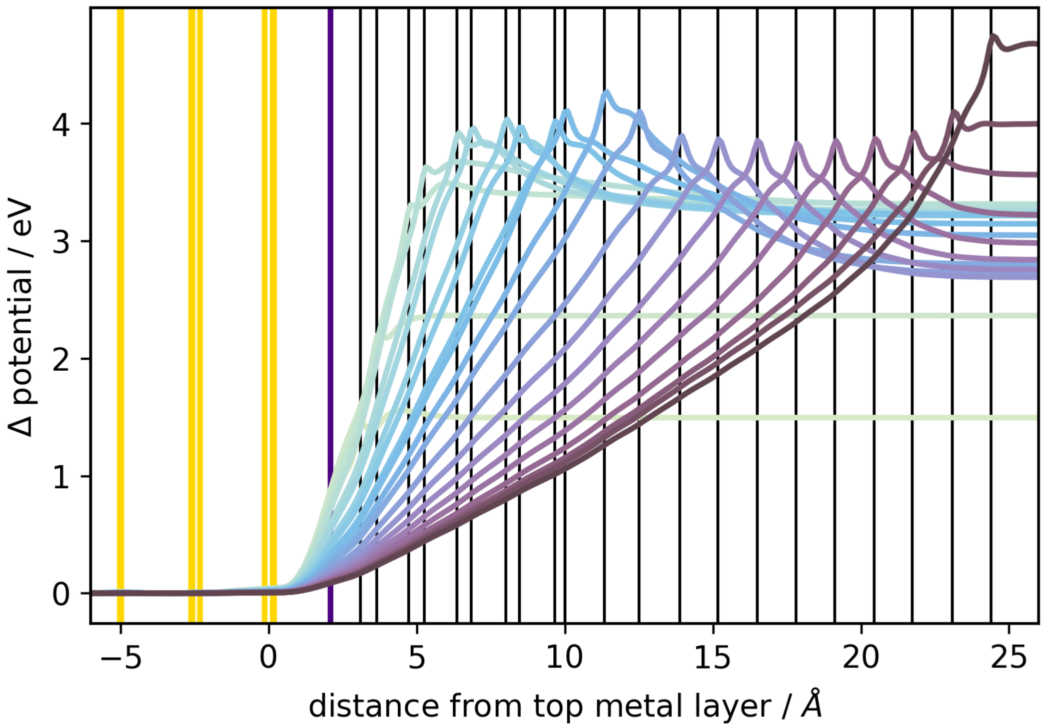

Figure 11: Difference of the plane averaged potential of a final state and an initial state calculation for every carbon atom of the system. The maximum of the potential difference coincides in all cases but the first few ones with the z-position of the carbon atom. The following color scheme is used for the different carbon atoms: the line with the lightest color denotes the bottom most carbon atom, and each line becomes darker the further to the top the carbon atom is it represents. The yellow lines indicate the gold layers, the violet and gray lines indicate the z-position of the sulfur and carbon atoms, respectively.

4.8.4 *Plane averaged charge density*

In Figure 12 the plane averaged charge density difference of an initial state calculation and the final state calculations is plotted. As can be seen, the charge difference is localized for each final-state calculation on a different atom. In passing it is noted that if the energies of several eigenstates are very similar, it happens that calculations done for different KS-eigenstates are localized on the same atom. This is due to FHI-AIMS ordering the eigenstates by energy, and, if the difference between two levels is small, they can switch when the SCF-calculation is restarted for the final-state approach. Therefore, it is important to check whether the core-hole is localized at the desired atom by, i. e., writing out the eigenstate density or by plotting the plane averaged charge density difference. The different heights of the peaks in Figure 12 are most probably due to numerical reasons. This is due to the charge density being written out in a cube file using voxels of finite size and then the plane averaged difference of two calculations is plotted.

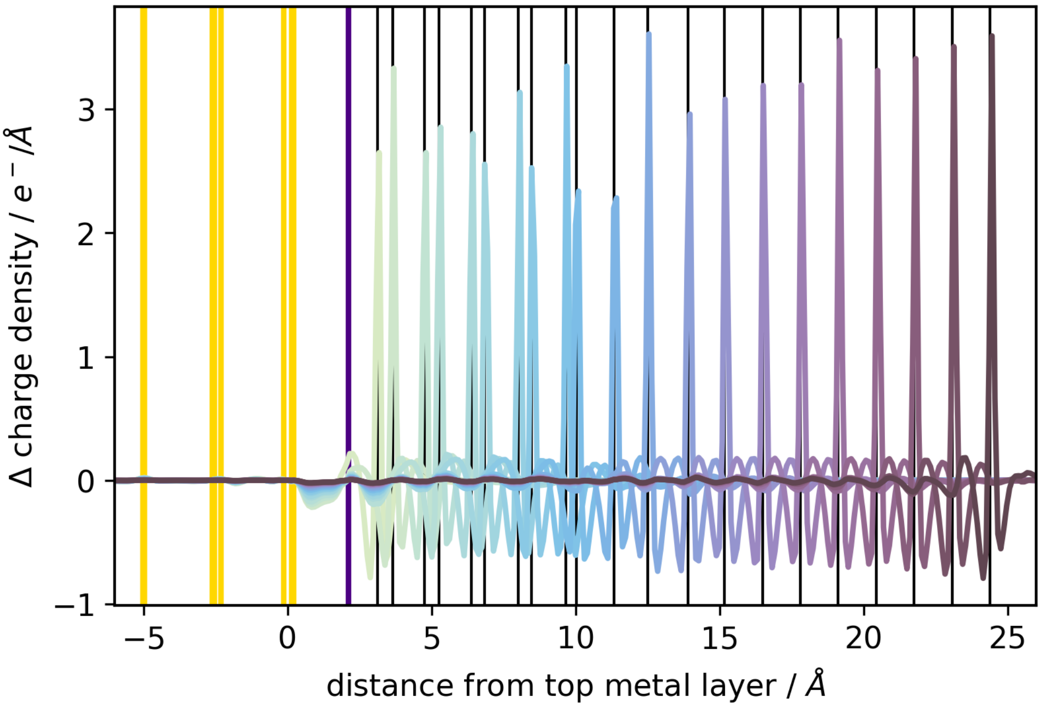

Figure 12: Plane averaged charge difference of the final state and the initial state calculation, i. e., the localization of the moved charge is visualized. The following color scheme is used to denote the different carbon atoms: the line with the lightest color indicates the bottom most carbon atom, and each line becomes darker the further to the top the carbon atom is it represents. The yellow lines indicate the gold layers, the violet and gray lines indicate the z-position of the sulfur and carbon atoms, respectively.

4.8.5 *Work function*

The same behavior as has been seen for the potential difference can be anticipated when plotting the work function of the system from the calculation of every carbon atom treated in the final state approach. In Figure 13 the upper (blue line) and lower (gold line) work function of the system is plotted in the initial state calculation. Additionally, the upper work function acquired within each final state calculation (cyan dots) is plotted over the position of the ionized carbon atom. The work function for the gold side of the slab is also plotted for each final-state calculation and they all coincide with the work function calculated within the initial-state calculation. Therefore, they were also plotted as gold lines.

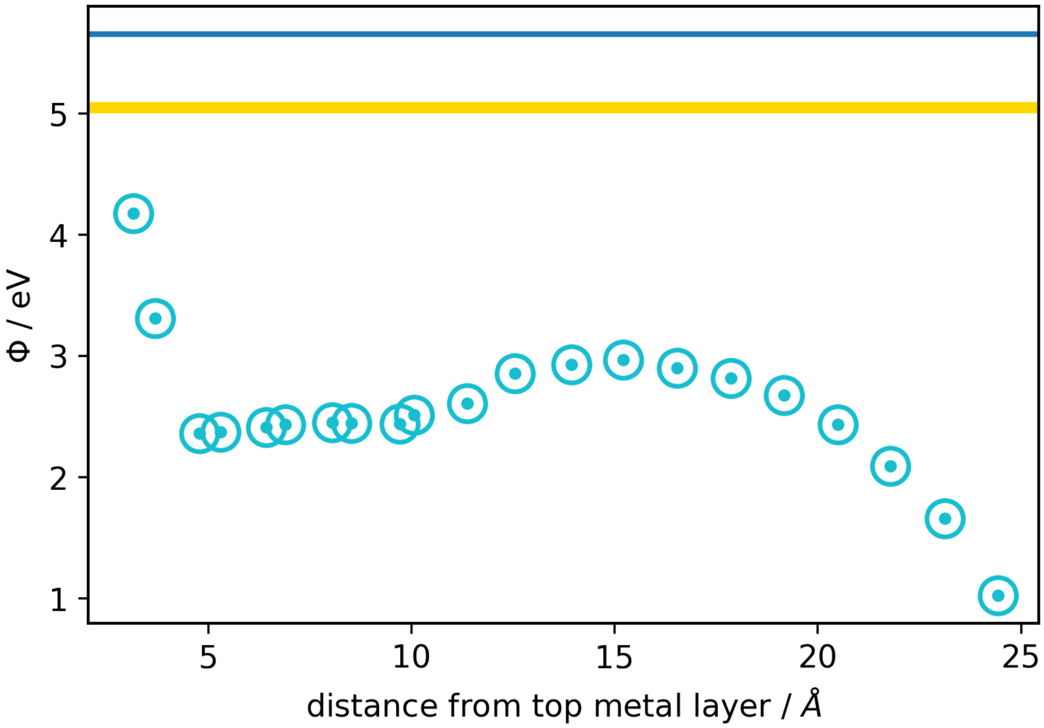

Figure 13: Work function for different carbon atoms treated in the final state approach. The cyan dots show the upper work function, i. e., at the side of the partly fluorinated alkyl thiolate. These values vary greatly depending on the atom treated within the final-state approach. In contrast to this is the lower work function, i. e., at the bottom of the gold slab, depicted by a gold line, which does not change significantly for any atom and is the same for the initial and final state calculations. The blue line denotes the upper work function acquired within the initial state calculation.

What is evident is the fact that the upper work function varies greatly depending on the carbon 1*s* orbital where half of an electron was removed, i. e., which was treated in the final state approach. This effect is due to the same reasons already explained in Chapter 4.8.3. Here the spurious collective electrostatic effects due to the artificially introduced densely packed dipole layer can be seen quite nicely for the three bottom most carbon atoms, as there is no pinning. Starting at the fourth atom, Fermi level pinning comes into effect. For the fluorinated carbon atoms the work function changes in accordance to the plane averaged potential difference already discussed in Chapter 4.8.3.

In stark contrast to this behavior are the values for the lower work function (gold line), i. e., at the bottom of the gold slab, which do not change significantly in the initial or final state approach. This is exactly the behavior one would expect in a converged simulation without any spurious artifacts.

4.8.6 *Summary and conclusions*

Overall, the effect of these spurious collective electrostatic effects described in the preceding chapters can neither be neglected in a simple model system as was shown in Chapter 4.4 nor can they be ignored in an extended system of an organic adsorbate on a metal substrate. This means, if applying the Slater-Janak transition state method (or the ΔSCF-approach for that matter) in conjunction with the repeated slab approach (RSA) it is of utmost importance to check whether such spurious dense dipole layers are introduced. This is especially important for long, upright standing molecules, as there the distance of the adsorbate atoms and the metal substrate is substantial. Depending on the distance between the atoms contributing to the overall spectrum and the mirror image plane of the metal substrate (which is in most cases around 1 Å above the metal surface), the size of the unit cell in x- and y-direction has to be chosen accordingly. When core-levels of carbon atoms are shifted with respect to each other, it might be ambiguous whether the changed local potential is due to their different chemical neighborhood or due to spurious collective electrostatic effects. In this case, a first clue can be the behavior of the upper work function, as it should not change at all when calculating core-level energies for different carbon atoms. In any case the size of the unit cell size must be chosen carefully and convergence tests must be done when utilizing final state calculations in conjunction with periodic boundary conditions.

5

ON USING X-RAY PHOTOELECTRON SPECTROSCOPY FOR DETERMINING INTERFACE DIPOLES

In the following chapter we again focus on collective electrostatic effects, but this time they are not due to spurious artificial artifacts, but rather are real and can be utilized in a beneficial manner to investigate the bonding dipole between a self-assembled monolayer (SAM) and a metal substrate. In the paper presented in this chapter we investigated the applicability of XPS to determine the interfacial dipole of SAMs on metal substrates. This can be achieved by taking advantage of collective electrostatic effects which come into play at ordered interfaces. We demonstrate this for the case of biphenyl-based SAMs incorporating different docking groups placed on a gold substrate. Furthermore, the influence of polar tail groups was investigated as well. The impact of varying interface dipoles due to different docking groups, which change the local electrostatic potential right at the interface, lead to a shift of the overall XP-spectrum, which correlates with a shift of the work function if there are no polar tail groups. What should be noted is the fact that the aforementioned observations only hold when investigating full coverage systems. Therefore, we have investigated how reducing the coverage of the adsorbate mitigates collective effects. This is because the density of the dipoles, which build the basis for these collective electrostatic effects, is diluted (cf. Chapter 3).

5.1 AUTHOR CONTRIBUTIONS

I contributed to all stages of the following paper. I performed all calculations presented in this work and analyzed the obtained results. I generated all Figures with the exception of Figure 1, which was created by Egbert Zojer. The data was jointly discussed and interpreted by both authors. I wrote the first draft of the manuscript for the publication, which was subsequently revised by both Egbert Zojer and me. Furthermore, I generated all the data for and compiled the Supporting Information, which was then revised by Egbert Zojer. The work was supervised and guided by Egbert Zojer, who also had the original idea for the research project.

5.2 ORIGINAL MANUSCRIPT: THE POTENTIAL OF X-RAY PHOTOELECTRON SPECTROSCOPY FOR DETERMINING INTERFACE DIPOLES OF SELF-ASSEMBLED MONOLAYERS

applied sciences

MDPI

Article

The Potential of X-ray Photoelectron Spectroscopy for Determining Interface Dipoles of Self-Assembled Monolayers

Thomas C. Taucher and **Egbert Zojer** *

Institute of Solid State Physics, Graz University of Technology, NAWI Graz, Petersgasse 16, 8010 Graz, Austria; thomas.taucher@tugraz.at
* Correspondence: egbert.zojer@tugraz.at; Tel.: +43-316-873-8475

Received: 16 July 2020; Accepted: 13 August 2020; Published: 19 August 2020

Abstract: In the current manuscript we assess to what extent X-ray photoelectron spectroscopy (XPS) is a suitable tool for probing the dipoles formed at interfaces between self-assembled monolayers and metal substrates. To that aim, we perform dispersion-corrected, slab-type band-structure calculations on a number of biphenyl-based systems bonded to an Au(111) surface via different docking groups. In addition to changing the docking chemistry (and the associated interface dipoles), the impacts of polar tail group substituents and varying dipole densities are also investigated. We find that for densely packed monolayers the shifts of the peak positions of the simulated XP spectra are a direct measure for the interface dipoles. In the absence of polar tail group substituents they also directly correlate with adsorption-induced work function changes. At reduced dipole densities this correlation deteriorates, as work function measurements probe the difference between the Fermi level of the substrate and the electrostatic energy far above the interface, while core level shifts are determined by the local electrostatic energy in the region of the atom from which the photoelectron is excited.

Keywords: X-ray photoelectron spectroscopy; XPS; self-assembled monolayer; SAM; collective electrostatics; band-structure calculation; density-functional theory; DFT

---

1. Introduction

In the field of organic electronics, chemically bonded self-assembled monolayers (SAMs) have been used to change the electronic properties of a huge variety of interfaces [1–18]. They have allowed the realization of n-type organic transistors by screening interface traps [3], they have been used to shift turn-on voltages of devices by several dozens of volts via the introduction of polar and reactive groups into transistor channels [4–7], and they have been employed for tuning injection barriers by adsorption on electrode surfaces, changing contact resistances by orders of magnitude [8–18]. Especially for the latter applications, the shift in the (electrostatic) energy landscape generated by the SAM is of crucial importance. On the one hand, this shift is a consequence of the intrinsic dipoles of the adsorbed molecules due to polar groups (like carboranes, pyrimidines, aromatic sulfones and sulfides, or esters) embedded into the molecular backbones [15,17,19–23] or due to polar tail group substituents (like halogens, amines, nitriles, nitro groups, pyrimidines, alcohols, ethers, or carboxylic acids) [9,24–38]. On the other hand, there is always an interface dipole localized in the immediate contact region between the substrate and the adsorbed molecule, as discussed in a variety of experimental and theoretical studies [11,25,27,28,31,32,39–44]. This interface dipole consists of the surface dipole of the (metal) substrate, the dipole associated with the (typically polar) docking group, and the bond dipole due to interfacial charge rearrangements following bond formation. The superposition of the

Appl. Sci. **2020**, *10*, 5735; doi:10.3390/app10175735

electric fields due to the interface dipoles of all adsorbed molecules causes a step in the electrostatic energy, as explained in detail in several review papers [31,40,42,45,46]. This step in electrostatic energy triggers a shift in the position of the vacuum level above the surface and, consequently, as the most common observation, changes the sample work function [8,11,14–17,19,21,22,25,27,28,31,32,35,39,41,43,44,47–52]. Additionally, theoretical as well as experimental studies reveal that it modifies the interfacial energy-level alignment, i.e., the positions of the electronic states of the adsorbed monolayer relative to those of the substrate [27,28,31,39,40,42,45–47,53–62]. A change in the interfacial level alignment has an immediate impact on charge-transport through the adsorbed layer [53–62] and also on the positions of the core levels of the adsorbate [42]. The latter has been primarily discussed for embedded dipole SAMs, with a focus on shifts caused by esters [20,63,64] or pyrimidines [21,22,48,49]. Notably, El-Sayed et al. also used it to assess the level alignment in mixed monolayers consisting of flat-lying donor and acceptor molecules [65].

Changes in core level binding energies can be probed by X-ray photoelectron spectroscopy (XPS) [66–70], which is one of the default techniques for characterizing SAMs, used, for example, for analyzing the quality of self-assembled monolayers and to verify bonding [67,71–82]. In this paper we will argue that the electrostatic core level shifts make XPS an ideally suited tool for probing interface dipoles. For supporting that claim, we will use state of the art quantum-mechanical simulations to determine core level shifts encountered in biphenyl-based SAMs attached to an Au(111) substrate by a variety of chemically different docking groups. To the best of our knowledge, a corresponding set of experimental XPS data with systematically varied docking groups and consistent film structures and morphologies does not exist yet. Nevertheless, first steps in that direction have been undertaken and biphenyl-based SAMs on various metallic substrates have been studied, albeit with a clear focus on thiol docking groups [60,73,81–89]. We, however, do not consider this to be an all too serious problem for a study focusing on the conceptual physical aspects that allow a determination of interface dipoles by XPS. Moreover, we have high confidence in the employed computational approach, which is described in the following section. This confidence is based on the fact that in the past we have performed several joint theoretical and experimental studies on aliphatic [63,64] and aromatic [22,48,49] SAMs bonded to the substrate by thiol and dithiocarbamate [90] groups, for which we observed an excellent agreement between measured and simulated core level shifts.

In the present study we will show that core level spectroscopy is not only useful for measuring chemical shifts or to explore the role of dipoles contained in the adsorbates. Rather, it can also be used as a tool for systematically determining the "interface dipole" at the interface between a substrate and an adsorbate.

2. Computational Methodology

The structural and electronic properties of the metal–SAM interfaces were simulated by density functional theory (DFT) employing the all-electron, full potential FHI-aims code (version 190715 [91–95] (see also aimsclub.fhi-berlin.mpg.de) and periodic boundary conditions. The Perdew–Burke–Ernzerhof (PBE) [96,97] functional was used for describing exchange and correlation. Furthermore, long-range van der Waals interactions were accounted for by employing the surface version [98] of the Tkatchenko–Scheffler dispersion correction [99], which was specifically parameterized for treating adsorbing molecules on metal substrates. The dispersion correction between the Au atoms of the metal slab was turned off. All calculations were done with the so-called tight basis set for all atomic species (as supplied by FHI-aims). A thorough description of the corresponding basis functions is included in the Supplementary Materials. Reciprocal space was sampled by a converged Γ-centered $15 \times 10 \times 1$ grid for the full coverage systems and by accordingly smaller sized grids for larger super cells. The change of the volume-integrated electron density was converged to 10^{-5} e^- and the total energy to 10^{-6} eV.

Interfaces were modeled employing the repeated-slab approach with the Au(111) substrate represented by five metal layers. The bottom three Au layers were kept fixed in all calculations to avoid spurious relaxations at the bottom surface. The periodic replicas of the slabs were quantum-mechanically and electrostatically decoupled by a vacuum gap of more than 20 Å and a self-consistent dipole correction [100,101]. The geometries of the adsorbate molecules and the top two Au-layers in the full coverage unit cells were fully relaxed until the remaining forces on each atom were below 10^{-3} eV/Å. The geometries of the other supercells considered here were directly derived from the full coverage unit cell by replicating it in x- and y-directions and removing all but one molecule from the resulting cell (see Supplementary Materials). These supercells were considered as model systems to study the impact of diluting the interfacial dipoles. Thus, we fixed the remaining molecule in the geometry it adopts in the densely packed layer to prevent it from falling over [102].

The change of the work function was obtained from the difference of the calculated work functions at the bottom side of the Au(111)-slab (Φ_{Au} = 5.10 eV for all systems) and above the self-assembled monolayer. Furthermore, the work function change of the nominally non-interacting system, i.e., the SAM without a docking group moved 1 Å away from the substrate compared to its equilibrium adsorption distance (see Section 3.2), was defined as a reference point relative to which the work function changes ($\Delta\Phi$) for all other systems are reported. The difference between lower and upper slab work function for the reference system amounts to $\delta\Phi_{\mathrm{ref}} = -0.11$ eV.

The core level binding energies were calculated using the initial state approach, relying on the Kohn–Sham eigenvalues of the respective orbitals. This approach does not provide absolute values of the core level binding energies, but yields relative shifts between different systems [65,68,103–108]. We have also found it to provide a very good description of core level shifts in SAMs [21,22,48,49,63,64]. In fact, when modeling the X-ray photoelectron (XP) spectra of (partially) aromatic hydrocarbon SAMs bonded to Au substrates, we typically find that shifting the calculated spectra to higher binding energies by between 18.9 to 19.0 eV [22,49,90,109] yields an excellent correlation with experimental data. Therefore, throughout the manuscript (like for the work functions) core level shifts are reported relative to the nominally non-interacting reference system consisting of a SAM without the docking group moved 1 Å away from the substrate compared to its equilibrium adsorption distance (see Section 3.2). The calculated value of that reference energy was −263.95 eV.

Another complication when employing the initial-state approach is that (in contrast to final-state approaches) [68,70,110,111] it does not account for core hole screening effects. Unfortunately, final-state approaches are not applicable to systems like the ones considered here, as in conjunction with periodic boundary conditions one would need unit cells comprising of thousands of atoms in order to avoid spurious collective electrostatic effects due to periodic replicas of the core holes (and the compensation charges) [63,112]. Therefore, we resorted to an a posteriori correction of screening by the metal substrate relying on an image charge model, which is explained in detail in the Supplementary Materials [113,114]. In passing we note that screening by the metal substrate has only a comparably minor impact on the spectra shown below, as we are dealing with rather extended, upright standing molecules, whose spectra are dominated by excitations of atoms, which are rather far away from the substrate. To account for the finite escape depth of the photoelectrons from lower-lying atoms, we scaled their contributions by an exponential attenuation function [115] setting the incident photon energy to 580 eV, as described in detail in the Supplementary Materials. To obtain the final spectra, the discrete peaks were convoluted with a Gaussian function with a variance of 0.3 eV. A flowchart summarizing the simulation procedure can be found in the Supplementary Materials. Furthermore, for the sake of reproducibility, we also provide all FHI-aims input and output files for all simulations contained in this manuscript. The data set has been uploaded to the NOMAD database and can be accessed and downloaded via the doi: 10.17172/NOMAD/2020.08.13-1.

For the analysis and visual representation of the data, Python was used in combination with NumPy [116] and matplotlib [117]. Ovito [118] was applied for generating the 3D view of the systems and for the 2D potential plot we used VESTA [119]. Finally, the figures were compiled with GIMP [120].

3. Results and Discussion

3.1. Energetics of a Metal–SAM Interface

For understanding the correlation between XP spectra and interface dipoles, it is useful to first consider how interface dipoles impact the electronic properties of a system consisting of an inorganic substrate and a chemically bonded monolayer (formed by upright-standing molecules). For the sake of simplicity, in the following we will focus on metal substrates. In this way, further complications due to band-bending effects [35,63,121,122] in semiconducting substrates (and their modification by the adsorbate layer) can be avoided.

A schematic representation of the electronic structure of the metal–SAM interface is shown in Figure 1 for the case of a SAM in which an interface dipole occurs (virtually all SAMs) and in which also a functional tail group is used bearing a tail group dipole. Due to the superposition of the fields generated by the dipoles in the densely packed monolayer (i.e., due to collective electrostatic effects) [27,31,40,42,45,46,63,123,124], steps in the electrostatic energy occur. The steps due to the interface dipole, ID, and due to the tail group dipole, TD, are indicated by vertical blue arrows. The sum of these two energy shifts causes the change in substrate work function due to monolayer adsorption, $\Delta\Phi$. Conversely, only the interface dipole is responsible for the change in injection barriers, ΔIB, which determines the final electron- and hole-injection barriers, EIB and HIB, respectively. The core levels are shifted in line with the frontier levels. Consequently, the interface dipole should result in a shift of the positions of the core levels relative to the Fermi level of the substrate, ΔE_{C1s}, that is equivalent to ΔIB. This shift is directly translated into a modification of the kinetic energies of the electrons, E_{kin}, and, thus, in a shift of the XP spectra.

In this context it is important to stress that the above considerations disregard energetic shifts due to interfacial charge transfer processes, which could significantly modify the energies of strongly localized orbitals (i.e., the core levels). Indeed, for the atoms in a SAM that are in the immediate vicinity of the interface, such a charge transfer typically modifies the core level binding energies [68,69,125,126], which has also been observed for simulations on SAMs [90]. In experiments on extended, upright standing molecules it will, however, be often inconsequential for the measured spectra, as the atoms in the immediate vicinity of the interface mostly affected by these "chemical" shifts hardly contribute to the measured spectra, especially when using primary photon energies of a few hundred eV in synchrotron measurements. This is a consequence of the finite escape depth of the photoelectrons. The situation changes for experiments with typical lab sources with primary photon energies of, e.g., 1253.6 eV (Mg-Kα) and 1486.6 eV (Al-Kα), for which the attenuation length can be larger than the typical thickness of SAMs. Thus, for properly resolving the electrostatic shifts discussed her, the said synchrotron experiments are preferable (also because of the often higher energy resolution).

Finally, it should be mentioned that in the absence of an energetic shift due to a tail group dipole (or when comparing differently docked systems with identical tail group dipoles), the above considerations imply that SAM-induced changes of the substrate work function should directly correlate with shifts in core level binding energies. Below, we will test under which circumstances such a situation is encountered at a metal–SAM interface.

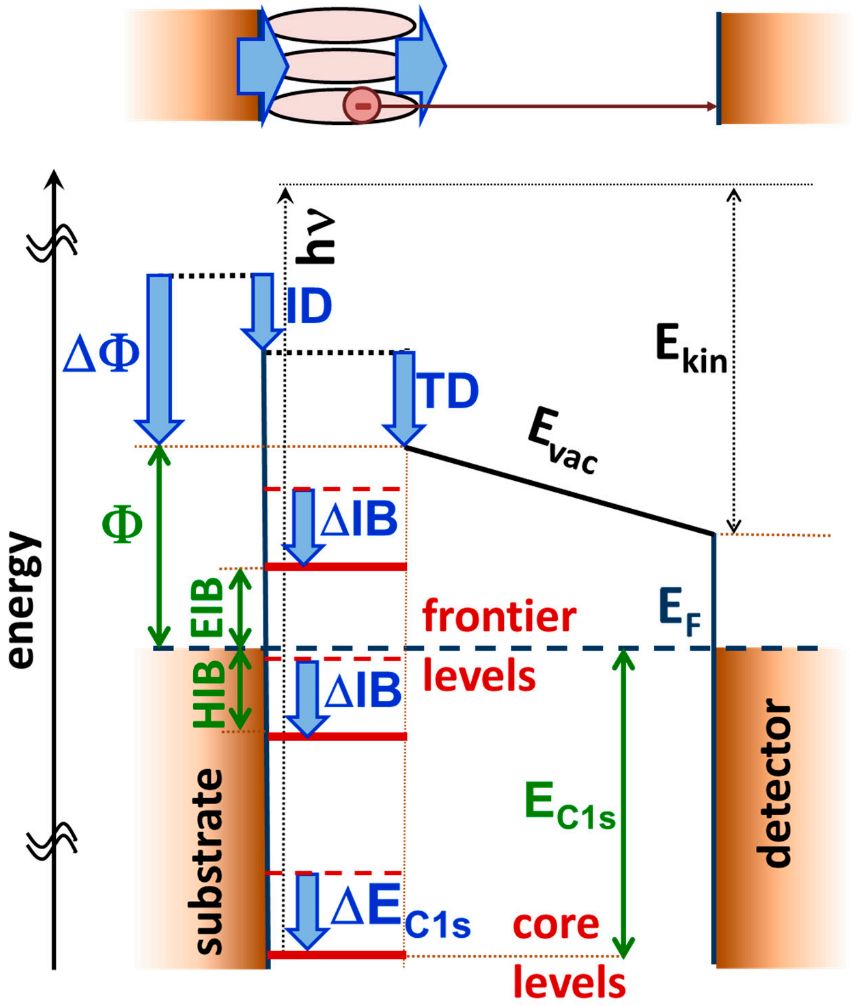

Figure 1. Schematics of the energy landscape of a metal–self-assembled monolayer (SAM) interface and an XPS experiment (disregarding the bias voltage applied between substrate and detector). The interface electronic structure is characterized by the work function, Φ, by the alignment of the frontier levels determining electron- and hole-injection barriers, EIB and HIB, and by the energetic positions of the core levels, here exemplarily denoted as E_{C1s}. The shift of the electrostatic energy due to the interface dipole, ID, determines the changes in the injection barriers, ΔIB, and the core level shifts, ΔE_{C1s}. The work function change, ΔΦ, is additionally influenced by the energetic shift due to the tail group dipole, TD. Absorption of an X-ray photon with energy hν creates a photoelectron, which at the position of the detector has a kinetic energy of E_{kin}. Additional positive potentials (not included in the plot) applied to the detector relative to the substrate increase the measured kinetic energy of the photoelectron. The top panel sketches the metal–SAM interface, whose properties are determined by the interface and the tail group dipole. In passing we note that the actual situation can be further complicated, e.g., when additional dipoles are contained along the backbones of the molecules [15,17,19–22].

3.2. Investigated Systems

To assess the possibility of probing bond dipoles by X-ray photoelectron spectroscopy, we simulated SAMs on Au(111) surfaces, as such systems have been studied extensively [71,72,74,79,127], which qualifies them as prototypical model systems. As molecular backbones we chose biphenyls with two molecules per $(3 \times \sqrt{3})$rect surface unit cell arranged in a herringbone structure [85]. As docking groups we considered thiolates (system I) [71,72,74,79], methyl thiolates (system II) [71,72,74,79], pyridines (system III) [54,128–133], isocyanides (system IV) [39,133–135] and cyanides (system V). The structures of all investigated systems can be seen in Figure 2. Furthermore, for the sake of comparison, we also simulated an upright-standing biphenyl layer not bearing a dedicated docking group (system VI), which represents a metastable structure, as the equilibrium configuration for the biphenyl-Au interface would very likely be flat-lying molecules. Due to different interfacial charge rearrangements and intrinsic dipole moments associated with the docking groups in these six systems, we expect distinct variations of the respective interface dipoles. Notably, in system VI, the only reason for an interface dipole would be Pauli-pushback [47,136,137]. To eliminate also that effect and to generate an essentially dipole-free interface, we also considered a system with the biphenyl layer shifted by 1 Å further away from the substrate (system VIa). In passing we note that increasing the distance from the substrate by yet another 1 Å does not change the spectrum (see Supplementary Materials). The electronic structure of system VIa is essentially identical to what is obtained when assuming vacuum-level alignment between an Au(111) surface and a free-standing biphenyl monolayer (the calculated work function reduction is on the order of 0.1 eV; for further information see Supplementary Material). Additionally, we considered two systems bearing electron accepting (system VII) and electron donating (system VIII) tail group substituents. These are known to change the work function without affecting the alignment of the frontier levels [27].

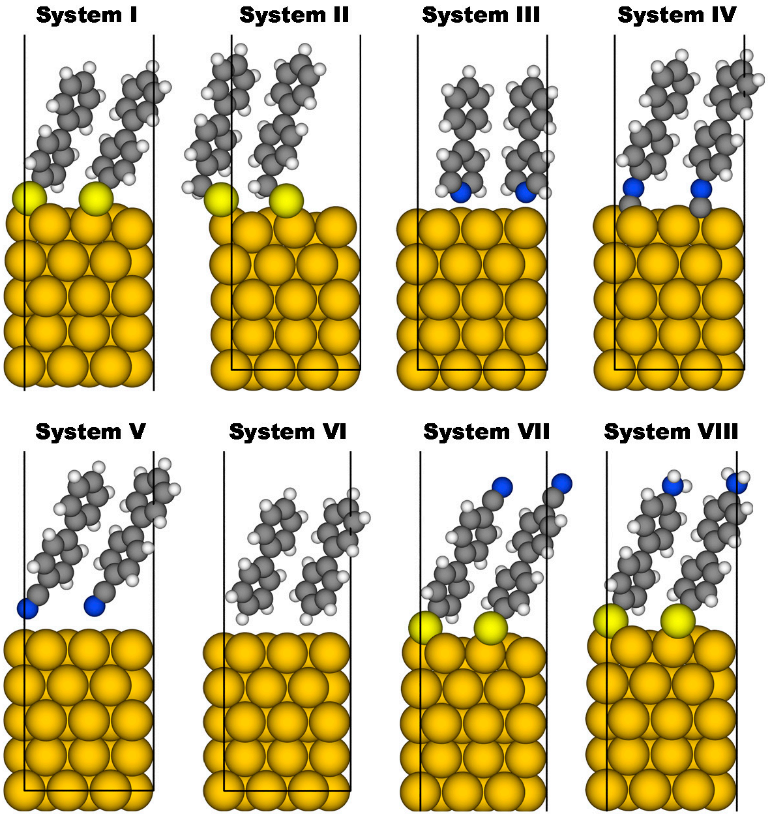

Figure 2. Front view of the unit cells investigated in the present study. The self-assembled monolayers are all derived from a biphenyl backbone and bear different docking groups (**Systems I** to **VI**) or different tail groups (**System VII** and **VIII**). The SAMs are bonded to an Au(111) metal slab consisting of 5 layers of gold atoms. The docking groups comprise of thiolate (**System I**), methyl-thiolate (**System II**), pyridine (**System III**), isocyanide (**System IV**) and cyanide (**System V**). System VI is an upright standing biphenyl layer not bearing any docking group. Systems VII and VIII are both bonded via thiolates, but contain different (polar) tail groups (a nitrile in the case of system VII and an amine in the case of system VIII). The molecules are arranged in a herringbone pattern, as can be seen in the top views of the unit cell shown in the Supplementary Materials. Color code: dark yellow: Au, bright yellow: S, grey: C, blue: N, and white: H.

3.3. Calculated Core-Level Binding Energies, XP Spectra, and Work Function Changes

3.3.1. Energetic Shifts Due to Variations in the Interface Dipole

In Figure 3, we show the core level binding energies and XP spectra of systems I, III, V, and VIa as prototypical examples for the impact of the docking groups on the core level binding energies. In the following, the "vacuum level alignment" system VIa was used as an energy reference for the work function as well as for the core level binding energies (for the absolute values of the reference energies see the Methods Section). This directly yields ΔE_{C1s} and $\Delta\Phi$ (i.e., the quantities shown in Figure 1). As far as the systems not displayed in Figure 3 are concerned, the data points for II essentially coincide with those of I and (apart from chemical shifts for the carbon atoms directly bonded to nitrogen atoms) the binding energies of III and V are also similar. System VI is similar to VIa with binding energies shifted to higher values by 0.34 eV. The corresponding data can be seen in the Supplementary Materials, where we show a (somewhat busy) plot analogous to Figure 3 containing values for all investigated systems. Compared to System VIa, the core level binding energies in all chemically bonded SAMs are shifted to higher (more negative) binding energies by several electronvolts. The effect is largest for III, for which the shift amounts to 2.8 eV (see black arrow). Even between docked systems, the peak positions vary by 1.6 eV with the smallest value (−265.2 eV) for the methyl thiolate and the largest (−266.8 eV) for the pyridine. This is exactly the situation one would expect according to Figure 1 for varying interface dipoles as a consequence of collective electrostatic effects [31,40,45,46,63].

In passing we note that, to the best of our knowledge, there is no systematic experimental study of docking group induced shifts in a series of well-ordered monolayers, but there are examples comparing thiols and isocyanides: Zangmeister et al. compared 4,4'-ethynylphenyl-1-benzenethiols on polycrystalline Au bonded either by thiols or by isocyanides and for the isocyanide-docked SAMs they observed a C1s peak at 0.6 eV higher binding energy than for the thiol case [138]. There is also indirect evidence that such shifts occur in other types of SAMs: when comparing thiolate and isocyanide bonded acene SAMs, Kim et al. measured a distinctly larger ionization energy of the isocyanide-bonded system with the shift between the valence orbitals amounting to 0.7 eV [139]. Unfortunately, they did not report corresponding C1s core level spectra, but, as discussed above, the shifts of valence and core levels have the same physical origin. Overall, the results in [138,139] are well in line with the data for systems I and IV in Figure 3, where the somewhat larger shift in the simulations is presumably due to assumed perfect ordering of the SAMs.

Superimposed on the electrostatic shifts of the XPS peaks, one can also identify the chemical shifts due to the differently bonded carbon atoms (cf. Figure 3a). For example, the carbon atoms connecting the two benzene rings are shifted by 0.5 eV relative to the other carbon atoms of the rings. Additionally, the carbon atoms attached to the docking groups are chemically shifted, resulting in distinct variations of the binding energies. This is, however, rather inconsequential for the positions and shapes of the XP spectra as a consequence of the finite escape depth of the photoelectrons. This is well visible, for example, for the isocyanide-docked SAM (system IV), where the lowest carbon atoms are shifted by 2 eV relative to the ones in the rings. The latter still rather exclusively determine the position of the peak in the corresponding XP spectrum.

Provided that the primary core level shifts are truly a consequence of collective electrostatic effects caused by interface dipoles they should directly correlate with the SAM-induced changes in the work function for systems I to VIa. To test that, we plotted $\Delta\Phi$ as a function of ΔE_{C1s} for all investigated SAMs in Figure 4. Indeed, the data for all SAMs without polar tail group substituents align perfectly along a straight line with a slope of 1 passing through the origin. This supports the assessment that in these systems core level shifts and work function changes have the same origin (namely the interface dipole). In passing we note that the dipole due to the terminal C-H bond of the biphenyl cancels out for the evolution of $\Delta\Phi$ vs. ΔE_{C1s} (at least for similar coverages and tilt angles), as the non-interacting biphenyl monolayer is used as the reference for both quantities.

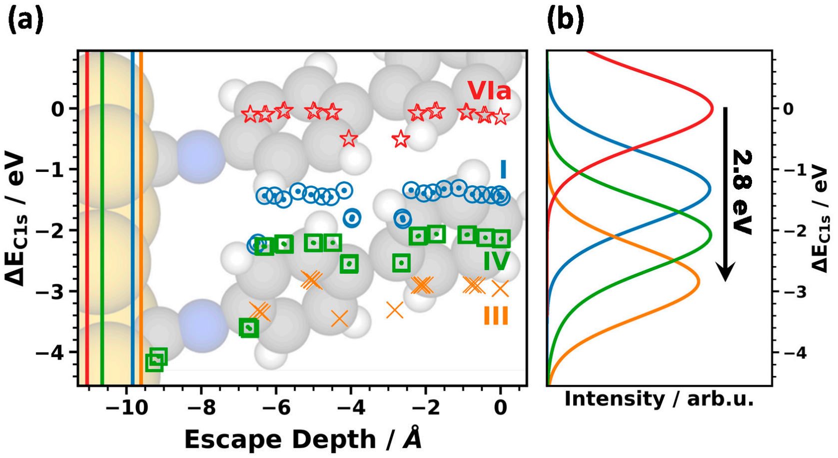

Figure 3. (**a**) Simulated shifts of carbon 1s orbital energies, ΔE_{C1s}, as a function of the escape depth of the electrons for the prototypical systems I, III, IV, and VIa and (**b**) the corresponding XP spectra generated from the calculated energy levels. The energy scale is chosen relative to the position of the peak in the XP spectrum for the vacuum-level aligned system VIa. The escape depth defined as the distance from the topmost carbon atom is chosen as the parameter on the x-axis considering that the highest atoms primarily determine the XP spectra. As the extent of the SAMs between the bottom ring and the metal substrate varies due to the different docking groups, this choice of the x-axis also largely aligns biphenyls in the different systems. System IV is shown in the background as an example of the structure of one of the SAMs considered in the plot. Due to the different SAM thicknesses, we included vertical lines in panel (**a**), which designate the positions of the centers of the atoms of the topmost Au layer. The large number of data points for each system is a consequence of the two inequivalent molecules per unit cell.

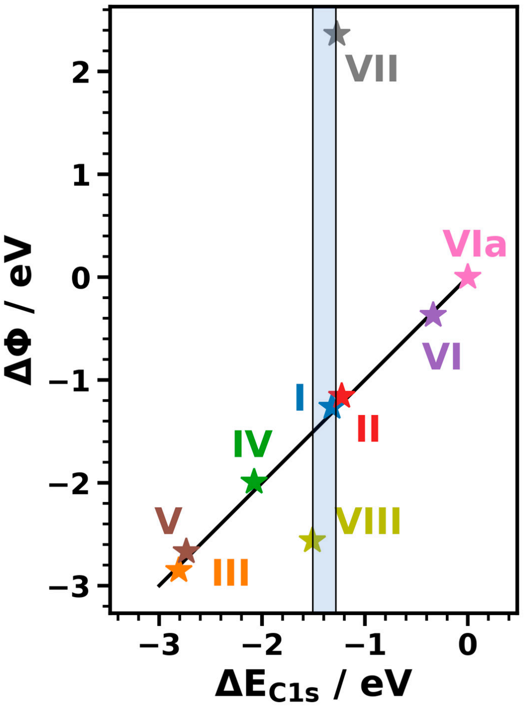

Figure 4. Correlation between the change in work function, $\Delta\Phi$, and the shift in binding energy, ΔE_{C1s}, for all systems relative to system VIa (as non-interacting reference system in which no interface dipole occurs). The black line indicates a linear curve with a slope of 1 through the origin. The shaded area represents the range over which the values for ΔE_{C1s} vary between systems I, VII, and VIII.

3.3.2. Influence of Different Tail Groups on the XP Spectra

This raises the question, what would happen if the SAM-forming molecules were substituted with tail groups bearing dipoles significantly different from the terminal C-H bond of a phenyl ring. According to Figure 1, this should (significantly) modify the work function shift, while leaving the core level binding energies essentially unchanged, with the exception of chemical shifts experienced by carbon atoms in or directly bonded to the substituents. To test that hypothesis, we simulated systems VII and VIII containing -CN and -NH_2 tail groups. As far as the simulated core level binding energies are concerned, we find them to be very similar for all three systems (I, VII, and VIII), as shown in Figure 5. Concerning the chemically shifted C1s binding energies of the uppermost carbon atoms, for system VII the shift of the top carbon atoms in the phenylene and the carbons in the -CN groups go in opposite directions. Thus, their impacts on the XP spectrum essentially cancel. As a consequence, the peak position of the C1s XP spectra of I and VII are virtually the same. Additionally, in VIII the shift of the peak remains comparably small (amounting to only 0.19 eV), as there are only the topmost carbon atoms in the two molecules per unit cell that are affected by the presence of the amine. This means that for all systems considered in the present study, the position of the peak in the C1s spectrum is a valid measure for the interface dipole.

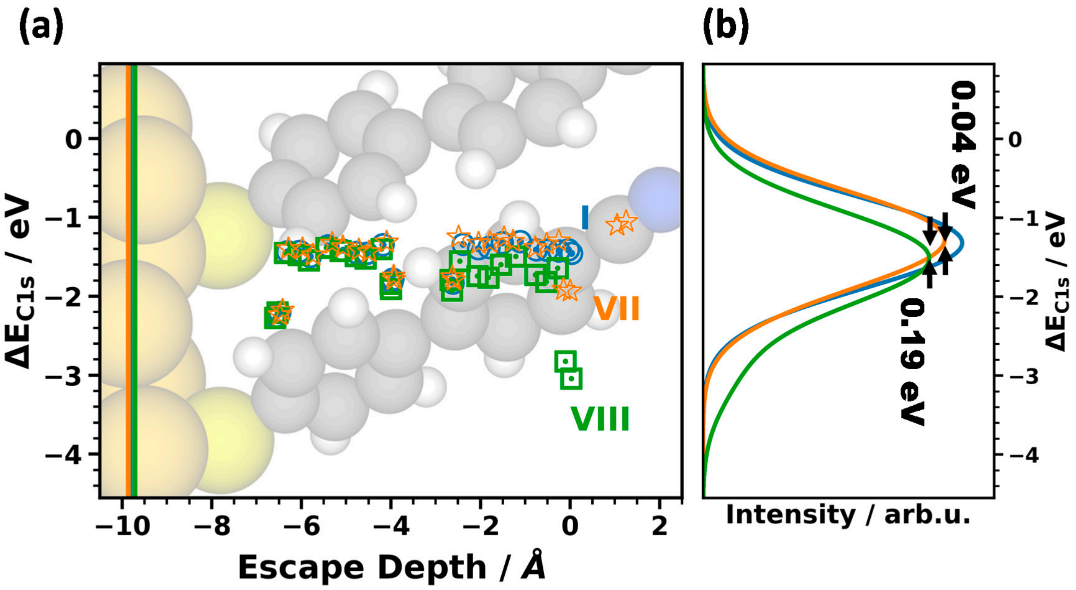

Figure 5. (**a**) Simulated shifts of carbon 1s orbital energies, ΔE_{C1s}, as a function of the escape depth of the electrons for the equally docked systems I, VII, and VIII and (**b**) corresponding XP spectra generated from the calculated energy levels. As the substituents significantly impact the extent of the SAMs above the top ring, but its volume density is rather low, the topmost carbon atom of the benzene ring was chosen as the origin of the *x*-axis. In this way, the axis is consistent with the *x*-axis of Figure 4 and the carbon rings are aligned at essentially the same positions. The large number of data points for each system is a consequence of the two inequivalent molecules per unit cell.

As shown in Figure 4, in sharp contrast to the core level spectra, the work function changes for VII and VIII differ significantly from that of I (by 3.63 eV for VII and by −1.30 eV for VIII). This is again fully consistent with the model described in Section 3.1.

3.3.3. Coverage Dependence

As a last aspect it should be addressed to what extent the above conclusions hold for less densely packed polar layers at the interface [42,113]. To assess that, in a gedankenexperiment we constructed hypothetical low-coverage systems with upright-standing molecules (for details see the Methods

Section and the Supplementary Materials). Based on the Helmholtz solution to the Poisson equation, one would expect a linear dependence of the dipole density and, thus, of $\Delta\Phi$ and ΔE_{C1s} on coverage. The actual coverage-dependence of $\Delta\Phi$ and ΔE_{C1s} is shown in Figure 6 for the same systems that had already been considered in Figure 3. Interestingly, one observes that $\Delta\Phi$ changes much more strongly at low than at high coverages. This is a consequence of depolarization effects. These strongly reduce the interface dipoles at high coverages [140–148]. Therefore, work function changes at full coverages are strongly reduced compared to what one would expect based on the dipoles associated with the adsorption of a single molecule [149].

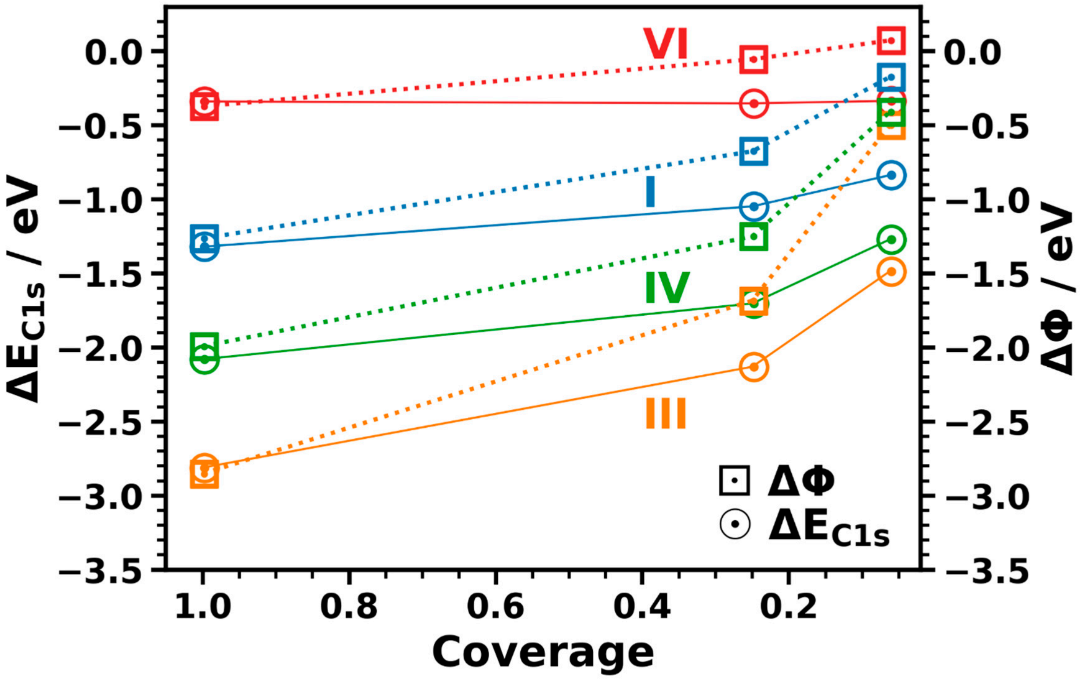

Figure 6. Core level shift, ΔE_{C1s}, (circles) and work function change $\Delta\Phi$ (square symbols) for systems I, III, IV, and VI as a function of coverage (varied between full, a quarter, and 1/16 coverage, where the latter approaches the single molecule limit, see Supplementary Materials). All energies are reported relative to the values of the non-interacting reference system VIa.

Another observation in Figure 6 is that the coverage-dependence of the core level binding energies (circles and solid line) is much weaker than that of $\Delta\Phi$ (squares and dotted line). This is particularly obvious for system VI, for which there is almost no change of ΔE_{C1s} with coverage, while the work function still changes by 0.5 eV. Qualitatively, the behavior is, however, the same for all studied systems, as shown in Figure 7. There, one sees that the energy range covered by the $\Delta\Phi$ values is significantly larger than that for ΔE_{C1s}. As a result, the slope of the linear fit to the dependence of $\Delta\Phi$ on ΔE_{C1s} (black lines in Figure 7) significantly decreases with decreasing coverage.

The main consequence of this observation is that at low dipole densities (in contrast to the full-coverage case, see above) ΔE_{C1s} is no longer a direct measure for the interface dipole. This can be explained by the different degrees of locality with which $\Delta\Phi$ and ΔE_{C1s} probe the electronic structure of the interface [48,148,150]. The value of $\Delta\Phi$ is determined by the energy difference between the Fermi level and the vacuum level far above the surface, i.e., in the far field. Conversely, core level binding energies probe the electrostatic energy in the immediate vicinity of the atom whose core electron is excited [48]. The latter is comparably close to the interface dipole at the bond between the molecule and the substrate. Thus, the shift in the electrostatic energy due to the dipole is still relevant, even if it is strongly reduced due to the drop of the shift with the inverse of the third power of the distance between atom and dipole. This is illustrated in Figure 8, where we show the change in electrostatic energy due to the formation of the bond between the pyridine-docked SAM and the metal substrate. Consequently, Figure 8 does not actually reflect the impact of the entire interface dipole, but only of the part resulting from the bond dipole. This quantity can, however, be calculated conveniently by subtracting the electrostatic energies of the subsystems from that of the bonded interface, which is not possible for the full interface dipole. It is also well suited to qualitatively illustrate the difference between the local and the far-field situation, even if one cannot expect quantitative agreement with the data from Figures 6 and 7, which are still determined by the entire interface dipole. For the full coverage system in the bottom panel of Figure 8, the main drop in electrostatic energy occurs at the immediate metal–pyridine interface and the electrostatic energy in the region of the top ring is essentially the same as far above the sample (despite a minor potential variation at the distance of the topmost C-H bond). Conversely, at 1/16 coverage the far-field electrostatic energy far above the interface (relevant for the work function) is several tenths of an eV higher than in the region of the upper carbon atoms (determining the position of the XPS peak).

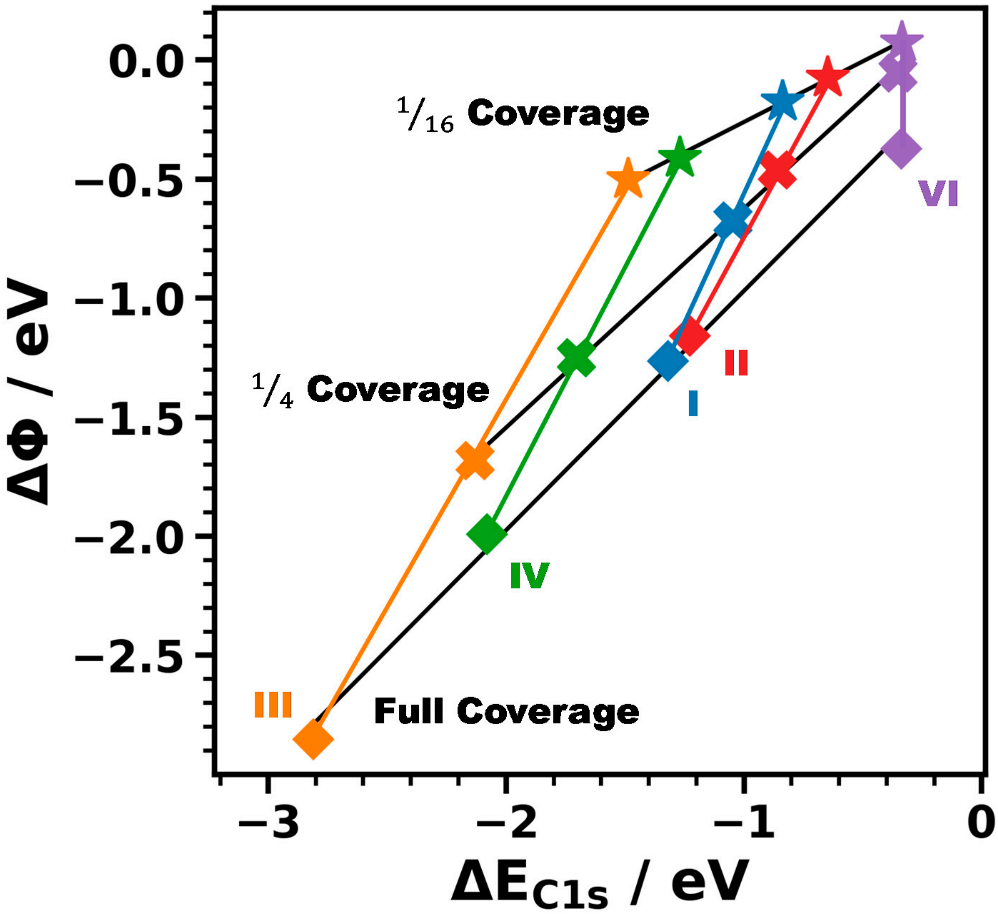

Figure 7. Core level shift, ΔE_{C1s}, as a function of the work function change, $\Delta\Phi$, for system I (**blue**), system II (**red**), system III (**orange**), system IV (**green**), and system VI (**violet**). Results for full, 1/4, and 1/16 coverage are compared. The black lines are fits to all systems for specific coverages, while the colored lines were fitted to the coverage-dependence for a specific system.

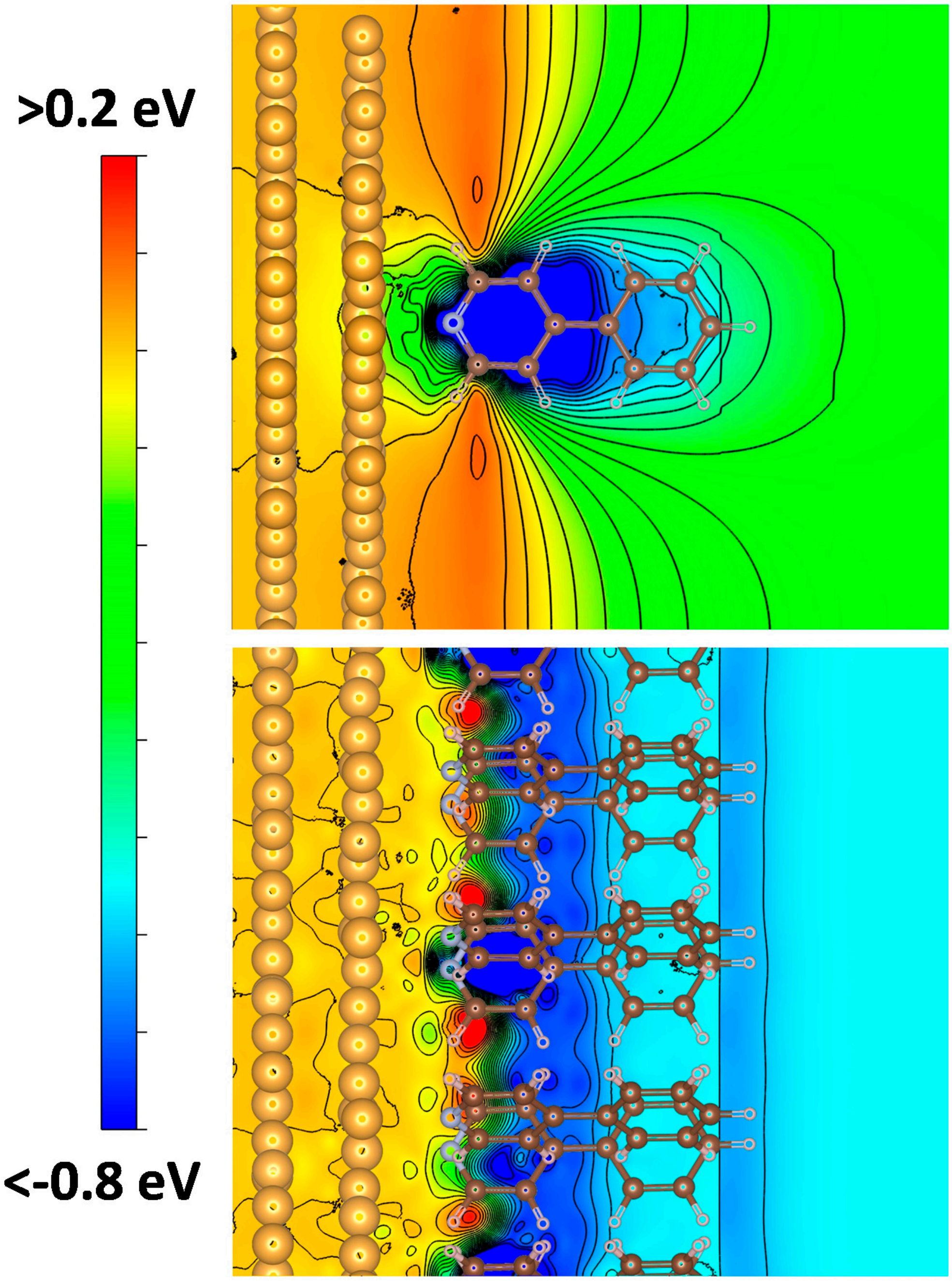

Figure 8. Contour plot of the change in the electrostatic energy due to metal–SAM bonding, i.e., due to the bond dipole (as part of the interface dipole) for system III. The potential is plotted for a plane defined by the plane of one of the molecules in the unit cell (see Supplementary Materials). The top (bottom) panel contains the result for 1/16 (full) coverage. Isolines are shown in steps of 0.05 eV.

3.3.4. The Role of Structural Imperfections of the Interface

For all systems we assumed perfectly ordered structures, which is triggered by the fact that especially for thiol-bonded SAMs highly ordered monolayers can be routinely obtained in carefully performed experiments. Still, in the following the possible consequences of deviations from perfect interfaces shall be briefly summarized: reduced dipole densities diminish the observed shifts, as can be inferred from the description in Section 3.1 and as discussed explicitly in Section 3.3.3. This also applies, when disorder reduces the net dipole per docking group perpendicular to the surface, i.e., although the shifts discussed in Section 3.3.1 are comparably large, for imperfect samples high-resolution measurements will be necessary. In passing we note that lateral inhomogeneities of the dipole density can result in a significant broadening of the spectra and in extreme cases even in the occurrence of multiple peaks, as we showed for mixed monolayers of embedded-dipole SAMs [48]. This is a consequence of XPS probing the local electrostatic potential at the atom from which the electron is excited. Similar considerations would apply to substrates with laterally inhomogeneous local work functions. Finally, it should be noted that the actually measured electrostatic shifts are determined by the "true" interface dipoles, where contaminants at the interface, e.g., for ex-situ prepared samples (or also the presence of ad atoms) can change the situation compared to the model case assumed in simulations. When dealing with strongly bonded adsorbates, like thiolates, one, however, is in the fortunate situation that their bonding to noble metal substrates typically displaces contaminants, which also explains, why for the XPS simulations on model systems mentioned in the introduction section, we typically obtained a favorable agreement with experiments on ex-situ prepared samples [22,48,49,63,64,90].

4. Conclusions

In the present contribution it is shown that X-ray photoelectron spectroscopy is a suitable tool for determining interface dipoles in densely packed self-assembled monolayers. This is shown via simulations on a number of biphenyl-based monolayers bonded to an Au(111) substrate by a broad range of different docking groups. The varying interface dipoles in these systems result in shifts of the core level binding energies by more than 1 eV, concomitantly shifting also the associated XP spectra. For SAMs not bearing polar tail groups the electrostatically triggered core level shifts directly correlate with SAM-induced work function changes. This correlation is broken, when work functions are further modified by polar tail group substituents. Nevertheless, even in these cases the XP spectra are a direct measure for the interface dipoles. The situation changes, when the dipole density at the interface is reduced. Then core level binding energies are still determined by the local electrostatic energy at the atoms from which the photoelectrons are excited. This energy is, however, no longer directly representative of the magnitude of the interface dipole, as it is strongly influenced, for example, by the distance of the excited atom from the location of the dipole. As a result, also the direct equivalence between core level shifts and work function changes is lost at reduced coverages, even though XPS still is suited for probing the local electrostatic energy (at least as long as chemical shifts, e.g., due to interfacial charge transfer are not superimposed on the electrostatic ones).

Supplementary Materials: Additional information on the computational methodology, a flow-chart summarizing the computational procedure, additional computational results, and views of unit cells and supercells are available online at http://www.mdpi.com/2076-3417/10/17/5735/s1.

Author Contributions: T.C.T. has performed all calculations, analyzed the results, compiled most figures, and wrote a first draft of the manuscript. E.Z. guided and supervised the research, contributed to the analysis of the data, compiled Figure 1, and revised the manuscript. All authors have read and agreed to the published version of the manuscript.

Funding: This work was funded (including the open access funding) by the Austrian Science Fund (FWF): P28051-N36. The quantum mechanical calculations have been performed using the Vienna Scientific Cluster (VSC3).

Conflicts of Interest: The authors declare no conflict of interest.

References

1. Casalini, S.; Bortolotti, C.A.; Leonardi, F.; Biscarini, F. Self-assembled monolayers in organic electronics. *Chem. Soc. Rev.* **2017**, *46*, 40–71. [CrossRef] [PubMed]
2. Halik, M.; Hirsch, A. The Potential of Molecular Self-Assembled Monolayers in Organic Electronic Devices. *Adv. Mater.* **2011**, *23*, 2689–2695. [CrossRef] [PubMed]
3. Chua, L.L.; Zaumseil, J.; Chang, J.F.; Ou, E.C.W.; Ho, P.K.H.; Sirringhaus, H.; Friend, R.H. General observation of n-type field-effect behaviour in organic semiconductors. *Nature* **2005**, *434*, 194–199. [CrossRef] [PubMed]

4. Kobayashi, S.; Nishikawa, T.; Takenobu, T.; Mori, S.; Shimoda, T.; Mitani, T.; Shimotani, H.; Yoshimoto, N.; Ogawa, S.; Iwasa, Y. Control of carrier density by self-assembled monolayers in organic field-effect transistors. *Nat. Mater.* **2004**, *3*, 317–322. [CrossRef]
5. Pernstich, K.P.; Haas, S.; Oberhoff, D.; Goldmann, C.; Gundlach, D.J.; Batlogg, B.; Rashid, A.N.; Schitter, G. Threshold voltage shift in organic field effect transistors by dipole monolayers on the gate insulator. *J. Appl. Phys.* **2004**, *96*, 6431–6438. [CrossRef]
6. Pacher, P.; Lex, A.; Proschek, V.; Etschmaier, H.; Tchernychova, E.; Sezen, M.; Scherf, U.; Grogger, W.; Trimmel, G.; Slugovc, C.; et al. Chemical Control of Local Doping in Organic Thin-Film Transistors: From Depletion to Enhancement. *Adv. Mater.* **2008**, *20*, 3143–3148. [CrossRef]
7. Aghamohammadi, M.; Rödel, R.; Zschieschang, U.; Ocal, C.; Boschker, H.; Weitz, R.T.; Barrena, E.; Klauk, H. Threshold-Voltage Shifts in Organic Transistors Due to Self-Assembled Monolayers at the Dielectric: Evidence for Electronic Coupling and Dipolar Effects. *ACS Appl. Mater. Interfaces* **2015**, *7*, 22775–22785. [CrossRef]
8. Campbell, I.H.; Rubin, S.; Zawodzinski, T.A.; Kress, J.D.; Martin, R.L.; Smith, D.L.; Barashkov, N.N.; Ferraris, J.P. Controlling Schottky energy barriers in organic electronic devices using self-assembled monolayers. *Phys. Rev. B* **1996**, *54*, R14321–R14324. [CrossRef]
9. Campbell, I.H.; Kress, J.D.; Martin, R.L.; Smith, D.L.; Barashkov, N.N.; Ferraris, J.P. Controlling charge injection in organic electronic devices using self-assembled monolayers. *Appl. Phys. Lett.* **1997**, *71*, 3528–3530. [CrossRef]
10. Yan, H.; Huang, Q.; Cui, J.; Veinot, J.G.C.; Kern, M.M.; Marks, T.J. High-Brightness Blue Light-Emitting Polymer Diodes via Anode Modification Using a Self-Assembled Monolayer. *Adv. Mater.* **2003**, *15*, 835–838. [CrossRef]
11. De Boer, B.; Hadipour, A.; Mandoc, M.M.; van Woudenbergh, T.; Blom, P.W.M. Tuning of Metal Work Functions with Self-Assembled Monolayers. *Adv. Mater.* **2005**, *17*, 621–625. [CrossRef]
12. Jang, Y.; Cho, J.H.; Kim, D.H.; Park, Y.D.; Hwang, M.; Cho, K. Effects of the permanent dipoles of self-assembled monolayer-treated insulator surfaces on the field-effect mobility of a pentacene thin-film transistor. *Appl. Phys. Lett.* **2007**, *90*, 132104. [CrossRef]
13. Kitamura, M.; Kuzumoto, Y.; Kang, W.; Aomori, S.; Arakawa, Y. High conductance bottom-contact pentacene thin-film transistors with gold-nickel adhesion layers. *Appl. Phys. Lett.* **2010**, *97*, 033306. [CrossRef]
14. Schulz, P.; Schäfer, T.; Zangmeister, C.D.; Effertz, C.; Meyer, D.; Mokros, D.; van Zee, R.D.; Mazzarello, R.; Wuttig, M. A New Route to Low Resistance Contacts for Performance-Enhanced Organic Electronic Devices. *Adv. Mater. Interfaces* **2014**, *1*, 1300130. [CrossRef]
15. Kim, J.; Rim, Y.S.; Liu, Y.; Serino, A.C.; Thomas, J.C.; Chen, H.; Yang, Y.; Weiss, P.S. Interface Control in Organic Electronics Using Mixed Monolayers of Carboranethiol Isomers. *Nano Lett.* **2014**, *14*, 2946–2951. [CrossRef]
16. Fenwick, O.; Van Dyck, C.; Murugavel, K.; Cornil, D.; Reinders, F.; Haar, S.; Mayor, M.; Cornil, J.; Samorì, P. Modulating the charge injection in organic field-effect transistors: Fluorinated oligophenyl self-assembled monolayers for high work function electrodes. *J. Mater. Chem. C* **2015**, *3*, 3007–3015. [CrossRef]
17. Petritz, A.; Krammer, M.; Sauter, E.; Gärtner, M.; Nascimbeni, G.; Schrode, B.; Fian, A.; Gold, H.; Cojocaru, A.; Karner-Petritz, E.; et al. Embedded Dipole Self-Assembled Monolayers for Contact Resistance Tuning in p-Type and n-Type Organic Thin Film Transistors and Flexible Electronic Circuits. *Adv. Funct. Mater.* **2018**, *28*, 1804462. [CrossRef]
18. Borchert, J.W.; Peng, B.; Letzkus, F.; Burghartz, J.N.; Chan, P.K.L.; Zojer, K.; Ludwigs, S.; Klauk, H. Small contact resistance and high-frequency operation of flexible low-voltage inverted coplanar organic transistors. *Nat. Commun.* **2019**, *10*. [CrossRef]
19. Evans, S.D.; Urankar, E.; Ulman, A.; Ferris, N. Self-assembled monolayers of alkanethiols containing a polar aromatic group: Effects of the dipole position on molecular packing, orientation, and surface wetting properties. *J. Am. Chem. Soc.* **1991**, *113*, 4121–4131. [CrossRef]
20. Cabarcos, O.M.; Shaporenko, A.; Weidner, T.; Uppili, S.; Dake, L.S.; Zharnikov, M.; Allara, D.L. Physical and Electronic Structure Effects of Embedded Dipoles in Self-Assembled Monolayers: Characterization of Mid-Chain Ester Functionalized Alkanethiols on Au{111}. *J. Phys. Chem. C* **2008**, *112*, 10842–10854. [CrossRef]

21. Abu-Husein, T.; Schuster, S.; Egger, D.A.; Kind, M.; Santowski, T.; Wiesner, A.; Chiechi, R.; Zojer, E.; Terfort, A.; Zharnikov, M. The Effects of Embedded Dipoles in Aromatic Self-Assembled Monolayers. *Adv. Funct. Mater.* **2015**, *25*, 3943–3957. [CrossRef]
22. Gärtner, M.; Sauter, E.; Nascimbeni, G.; Wiesner, A.; Kind, M.; Werner, P.; Schuch, C.; Abu-Husein, T.; Asyuda, A.; Bats, J.W.; et al. Self-Assembled Monolayers with Distributed Dipole Moments Originating from Bipyrimidine Units. *J. Phys. Chem. C* **2020**, *124*, 504–519. [CrossRef]
23. Baghbanzadeh, M.; Belding, L.; Yuan, L.; Park, J.; Al-Sayah, M.H.; Bowers, C.M.; Whitesides, G.M. Dipole-Induced Rectification Across Ag^{TS} /SAM//Ga_2O_3/EGaIn Junctions. *J. Am. Chem. Soc.* **2019**, *141*, 8969–8980. [CrossRef] [PubMed]
24. Kang, J.F.; Ulman, A.; Liao, S.; Jordan, R. Mixed Self-Assembled Monolayers of Highly Polar Rigid Biphenyl Thiols. *Langmuir* **1999**, *15*, 2095–2098. [CrossRef]
25. Zehner, R.W.; Parsons, B.F.; Hsung, R.P.; Sita, L.R. Tuning the Work Function of Gold with Self-Assembled Monolayers Derived from $X{-}[C_6H_4{-}C\vdots C{-}]_nC_6H_4{-}SH$ ($n = 0, 1, 2$; X = H, F, CH_3, CF_3, and OCH_3). *Langmuir* **1999**, *15*, 1121–1127. [CrossRef]
26. Ganzorig, C.; Kwak, K.J.; Yagi, K.; Fujihira, M. Fine tuning work function of indium tin oxide by surface molecular design: Enhanced hole injection in organic electroluminescent devices. *Appl. Phys. Lett.* **2001**, *79*, 272–274. [CrossRef]
27. Heimel, G.; Romaner, L.; Brédas, J.-L.; Zojer, E. Interface Energetics and Level Alignment at Covalent Metal-Molecule Junctions: π-Conjugated Thiols on Gold. *Phys. Rev. Lett.* **2006**, *96*. [CrossRef]
28. Sun, Q.; Selloni, A. Interface and Molecular Electronic Structure vs Tunneling Characteristics of CH_3- and CF_3-Terminated Thiol Monolayers on Au(111). *J. Phys. Chem. A* **2006**, *110*, 11396–11400. [CrossRef]
29. Yip, H.L.; Hau, S.K.; Baek, N.S.; Ma, H.; Jen, A.K.Y. Polymer Solar Cells That Use Self-Assembled-Monolayer-Modified ZnO/Metals as Cathodes. *Adv. Mater.* **2008**, *20*, 2376–2382. [CrossRef]
30. Demirkan, K.; Mathew, A.; Weiland, C.; Yao, Y.; Rawlett, A.M.; Tour, J.M.; Opila, R.L. Energy level alignment at organic semiconductor/metal interfaces: Effect of polar self-assembled monolayers at the interface. *J. Chem. Phys.* **2008**, *128*, 074705. [CrossRef]
31. Heimel, G.; Romaner, L.; Zojer, E.; Bredas, J.L. The Interface Energetics of Self-Assembled Monolayers on Metals. *Acc. Chem. Res.* **2008**, *41*, 721–729. [CrossRef] [PubMed]
32. Malicki, M.; Guan, Z.; Ha, S.D.; Heimel, G.; Barlow, S.; Rumi, M.; Kahn, A.; Marder, S.R. Preparation and Characterization of 4′-Donor Substituted Stilbene-4-thiolate Monolayers and Their Influence on the Work Function of Gold. *Langmuir* **2009**, *25*, 7967–7975. [CrossRef] [PubMed]
33. Yoon, H.J.; Bowers, C.M.; Baghbanzadeh, M.; Whitesides, G.M. The Rate of Charge Tunneling Is Insensitive to Polar Terminal Groups in Self-Assembled Monolayers in $Ag^{TS}S(CH_2)_nM(CH_2)_mT$//$Ga_2O_3$/EGaIn Junctions. *J. Am. Chem. Soc.* **2014**, *136*, 16–19. [CrossRef] [PubMed]
34. Lee, H.J.; Jamison, A.C.; Lee, T.R. Surface Dipoles: A Growing Body of Evidence Supports Their Impact and Importance. *Acc. Chem. Res.* **2015**, *48*, 3007–3015. [CrossRef]
35. Vilan, A.; Cahen, D. Chemical Modification of Semiconductor Surfaces for Molecular Electronics. *Chem. Rev.* **2017**, *117*, 4624–4666. [CrossRef]
36. Lindell, L.; Vahlberg, C.; Uvdal, K.; Fahlman, M.; Braun, S. Self-assembled monolayer engineered interfaces: Energy level alignment tuning through chain length and end-group polarity. *J. Electron Spectrosc. Relat. Phenom.* **2015**, *204*, 140–144. [CrossRef]
37. MacLeod, B.A.; Horwitz, N.E.; Ratcliff, E.L.; Jenkins, J.L.; Armstrong, N.R.; Giordano, A.J.; Hotchkiss, P.J.; Marder, S.R.; Campbell, C.T.; Ginger, D.S. Built-In Potential in Conjugated Polymer Diodes with Changing Anode Work Function: Interfacial States and Deviation from the Schottky–Mott Limit. *J. Phys. Chem. Lett.* **2012**, *3*, 1202–1207. [CrossRef]
38. Schmidt, C.; Witt, A.; Witte, G. Tailoring the Cu(100) Work Function by Substituted Benzenethiolate Self-Assembled Monolayers. *J. Phys. Chem. A* **2011**, *115*, 7234–7241. [CrossRef]
39. Heimel, G.; Romaner, L.; Zojer, E.; Brédas, J.L. Toward Control of the Metal−Organic Interfacial Electronic Structure in Molecular Electronics: A First-Principles Study on Self-Assembled Monolayers of π-Conjugated Molecules on Noble Metals. *Nano Lett.* **2007**, *7*, 932–940. [CrossRef]
40. Natan, A.; Kronik, L.; Haick, H.; Tung, R.T. Electrostatic Properties of Ideal and Non-ideal Polar Organic Monolayers: Implications for Electronic Devices. *Adv. Mater.* **2007**, *19*, 4103–4117. [CrossRef]

41. Wang, L.; Rangger, G.M.; Ma, Z.; Li, Q.; Shuai, Z.; Zojer, E.; Heimel, G. Is there a Au–S bond dipole in self-assembled monolayers on gold? *Phys. Chem. Chem. Phys.* **2010**, *12*, 4287–4290. [CrossRef] [PubMed]
42. Zojer, E.; Taucher, T.C.; Hofmann, O.T. The Impact of Dipolar Layers on the Electronic Properties of Organic/Inorganic Hybrid Interfaces. *Adv. Mater. Interfaces* **2019**, *6*, 1900581. [CrossRef]
43. Alloway, D.M.; Hofmann, M.; Smith, D.L.; Gruhn, N.E.; Graham, A.L.; Colorado, R.; Wysocki, V.H.; Lee, T.R.; Lee, P.A.; Armstrong, N.R. Interface Dipoles Arising from Self-Assembled Monolayers on Gold: UV-Photoemission Studies of Alkanethiols and Partially Fluorinated Alkanethiols. *J. Phys. Chem. B* **2003**, *107*, 11690–11699. [CrossRef]
44. Rusu, P.C.; Brocks, G. Surface Dipoles and Work Functions of Alkylthiolates and Fluorinated Alkylthiolates on Au(111). *J. Phys. Chem. B* **2006**, *110*, 22628–22634. [CrossRef]
45. Cahen, D.; Naaman, R.; Vager, Z. The Cooperative Molecular Field Effect. *Adv. Funct. Mater.* **2005**, *15*, 1571–1578. [CrossRef]
46. Monti, O.L.A. Understanding Interfacial Electronic Structure and Charge Transfer: An Electrostatic Perspective. *J. Phys. Chem. Lett.* **2012**, *3*, 2342–2351. [CrossRef]
47. Ishii, H.; Sugiyama, K.; Ito, E.; Seki, K. Energy Level Alignment and Interfacial Electronic Structures at Organic/Metal and Organic/Organic Interfaces. *Adv. Mater.* **1999**, *11*, 605–625. [CrossRef]
48. Hehn, I.; Schuster, S.; Wächter, T.; Abu-Husein, T.; Terfort, A.; Zharnikov, M.; Zojer, E. Employing X-ray Photoelectron Spectroscopy for Determining Layer Homogeneity in Mixed Polar Self-Assembled Monolayers. *J. Phys. Chem. Lett.* **2016**, *7*, 2994–3000. [CrossRef]
49. Gärtner, M.; Sauter, E.; Nascimbeni, G.; Petritz, A.; Wiesner, A.; Kind, M.; Abu-Husein, T.; Bolte, M.; Stadlober, B.; Zojer, E.; et al. Understanding the Properties of Tailor-Made Self-Assembled Monolayers with Embedded Dipole Moments for Interface Engineering. *J. Phys. Chem. C* **2018**, *122*, 28757–28774. [CrossRef]
50. Braun, S.; Salaneck, W.R.; Fahlman, M. Energy-Level Alignment at Organic/Metal and Organic/Organic Interfaces. *Adv. Mater.* **2009**, *21*, 1450–1472. [CrossRef]
51. Venkataraman, N.V.; Zürcher, S.; Rossi, A.; Lee, S.; Naujoks, N.; Spencer, N.D. Spatial Tuning of the Metal Work Function by Means of Alkanethiol and Fluorinated Alkanethiol Gradients. *J. Phys. Chem. C* **2009**, *113*, 5620–5628. [CrossRef]
52. Lange, I.; Reiter, S.; Pätzel, M.; Zykov, A.; Nefedov, A.; Hildebrandt, J.; Hecht, S.; Kowarik, S.; Wöll, C.; Heimel, G.; et al. Tuning the Work Function of Polar Zinc Oxide Surfaces using Modified Phosphonic Acid Self-Assembled Monolayers. *Adv. Funct. Mater.* **2014**, *24*, 7014–7024. [CrossRef]
53. Kim, B.; Choi, S.H.; Zhu, X.-Y.; Frisbie, C.D. Molecular Tunnel Junctions Based on π-Conjugated Oligoacene Thiols and Dithiols between Ag, Au, and Pt Contacts: Effect of Surface Linking Group and Metal Work Function. *J. Am. Chem. Soc.* **2011**, *133*, 19864–19877. [CrossRef] [PubMed]
54. Kim, T.; Darancet, P.; Widawsky, J.R.; Kotiuga, M.; Quek, S.Y.; Neaton, J.B.; Venkataraman, L. Determination of Energy Level Alignment and Coupling Strength in 4,4′-Bipyridine Single-Molecule Junctions. *Nano Lett.* **2014**, *14*, 794–798. [CrossRef]
55. Egger, D.A.; Rissner, F.; Zojer, E.; Heimel, G. Polarity Switching of Charge Transport and Thermoelectricity in Self-Assembled Monolayer Devices. *Adv. Mater.* **2012**, *24*, 4403–4407. [CrossRef]
56. Egger, D.A.; Liu, Z.F.; Neaton, J.B.; Kronik, L. Reliable Energy Level Alignment at Physisorbed Molecule–Metal Interfaces from Density Functional Theory. *Nano Lett.* **2015**, *15*, 2448–2455. [CrossRef]
57. Obersteiner, V.; Egger, D.A.; Heimel, G.; Zojer, E. Impact of Collective Electrostatic Effects on Charge Transport through Molecular Monolayers. *J. Phys. Chem. C* **2014**, *118*, 22395–22401. [CrossRef]
58. Obersteiner, V.; Huhs, G.; Papior, N.; Zojer, E. Unconventional Current Scaling and Edge Effects for Charge Transport through Molecular Clusters. *Nano Lett.* **2017**, *17*, 7350–7357. [CrossRef]
59. Xie, Z.; Bâldea, I.; Smith, C.E.; Wu, Y.; Frisbie, C.D. Experimental and Theoretical Analysis of Nanotransport in Oligophenylene Dithiol Junctions as a Function of Molecular Length and Contact Work Function. *ACS Nano* **2015**, *9*, 8022–8036. [CrossRef]
60. Xie, Z.; Bâldea, I.; Frisbie, C.D. Determination of Energy-Level Alignment in Molecular Tunnel Junctions by Transport and Spectroscopy: Self-Consistency for the Case of Oligophenylene Thiols and Dithiols on Ag, Au, and Pt Electrodes. *J. Am. Chem. Soc.* **2019**, *141*, 3670–3681. [CrossRef]
61. Xie, Z.; Bâldea, I.; Frisbie, C.D. Energy Level Alignment in Molecular Tunnel Junctions by Transport and Spectroscopy: Self-Consistency for the Case of Alkyl Thiols and Dithiols on Ag, Au, and Pt Electrodes. *J. Am. Chem. Soc.* **2019**, *141*, 18182–18192. [CrossRef] [PubMed]

62. Vilan, A.; Aswal, D.; Cahen, D. Large-Area, Ensemble Molecular Electronics: Motivation and Challenges. *Chem. Rev.* **2017**, *117*, 4248–4286. [CrossRef] [PubMed]
63. Taucher, T.C.; Hehn, I.; Hofmann, O.T.; Zharnikov, M.; Zojer, E. Understanding Chemical versus Electrostatic Shifts in X-ray Photoelectron Spectra of Organic Self-Assembled Monolayers. *J. Phys. Chem. C* **2016**, *120*, 3428–3437. [CrossRef] [PubMed]
64. Cabarcos, O.M.; Schuster, S.; Hehn, I.; Zhang, P.P.; Maitani, M.M.; Sullivan, N.; Giguère, J.-B.; Morin, J.-F.; Weiss, P.S.; Zojer, E.; et al. Effects of Embedded Dipole Layers on Electrostatic Properties of Alkanethiolate Self-Assembled Monolayers. *J. Phys. Chem. C* **2017**, *121*, 15815–15830. [CrossRef]
65. El-Sayed, A.; Borghetti, P.; Goiri, E.; Rogero, C.; Floreano, L.; Lovat, G.; Mowbray, D.J.; Cabellos, J.L.; Wakayama, Y.; Rubio, A.; et al. Understanding Energy-Level Alignment in Donor–Acceptor/Metal Interfaces from Core-Level Shifts. *ACS Nano* **2013**, *7*, 6914–6920. [CrossRef]
66. Siegbahn, K. (Ed.) *ESCA. Atomic, Molecular and Solid State Structure Studied by Means of Electron Spectroscopy*; Nova Acta Regiae Societatis Scientiarum Upsaliensis; Uppsala Almqvist & Wiksell: Stockholm, Sweden, 1967; Volume 20, Ser. 4.
67. Benesh, G.A.; King, D.A. Core-level shift spectroscopy for adsorbates: Ionic, covalent or metallic bonding? *Chem. Phys. Lett.* **1992**, *191*, 315–319. [CrossRef]
68. Bagus, P.S.; Ilton, E.S.; Nelin, C.J. The interpretation of XPS spectra: Insights into materials properties. *Surf. Sci. Rep.* **2013**, *68*, 273–304. [CrossRef]
69. Bagus, P.S.; Ilton, E.; Nelin, C.J. Extracting Chemical Information from XPS Spectra: A Perspective. *Catal. Lett.* **2018**, *148*, 1785–1802. [CrossRef]
70. Kirchhuebel, T.; Monti, O.L.A.; Munakata, T.; Kera, S.; Forker, R.; Fritz, T. The role of initial and final states in molecular spectroscopies. *Phys. Chem. Chem. Phys.* **2019**, *21*, 12730–12747. [CrossRef]
71. Ulman, A. Formation and Structure of Self-Assembled Monolayers. *Chem. Rev.* **1996**, *96*, 1533–1554. [CrossRef]
72. Schreiber, F. Structure and growth of self-assembling monolayers. *Prog. Surf. Sci.* **2000**, *65*, 151–257. [CrossRef]
73. Heister, K.; Zharnikov, M.; Grunze, M.; Johansson, L.S.O. Adsorption of Alkanethiols and Biphenylthiols on Au and Ag Substrates: A High-Resolution X-ray Photoelectron Spectroscopy Study. *J. Phys. Chem. B* **2001**, *105*, 4058–4061. [CrossRef]
74. Love, J.C.; Estroff, L.A.; Kriebel, J.K.; Nuzzo, R.G.; Whitesides, G.M. Self-Assembled Monolayers of Thiolates on Metals as a Form of Nanotechnology. *Chem. Rev.* **2005**, *105*, 1103–1170. [CrossRef]
75. Shaporenko, A.; Cyganik, P.; Buck, M.; Terfort, A.; Zharnikov, M. Self-Assembled Monolayers of Aromatic Selenolates on Noble Metal Substrates. *J. Phys. Chem. B* **2005**, *109*, 13630–13638. [CrossRef] [PubMed]
76. Käfer, D.; Bashir, A.; Witte, G. Interplay of Anchoring and Ordering in Aromatic Self-Assembled Monolayers. *J. Phys. Chem. C* **2007**, *111*, 10546–10551. [CrossRef]
77. Merzlikin, S.V.; Tolkachev, N.N.; Strunskus, T.; Witte, G.; Glogowski, T.; Wöll, C.; Grünert, W. Resolving the depth coordinate in photoelectron spectroscopy—Comparison of excitation energy variation vs. angular-resolved XPS for the analysis of a self-assembled monolayer model system. *Surf. Sci.* **2008**, *602*, 755–767. [CrossRef]
78. Beccari, M.; Kanjilal, A.; Betti, M.G.; Mariani, C.; Floreano, L.; Cossaro, A.; Di Castro, V. Characterization of benzenethiolate self-assembled monolayer on Cu(100) by XPS and NEXAFS. *J. Electron Spectrosc. Relat. Phenom.* **2009**, *172*, 64–68. [CrossRef]
79. Vericat, C.; Vela, M.E.; Benitez, G.; Carro, P.; Salvarezza, R.C. Self-assembled monolayers of thiols and dithiols on gold: New challenges for a well-known system. *Chem. Soc. Rev.* **2010**, *39*, 1805. [CrossRef]
80. Zaba, T.; Noworolska, A.; Bowers, C.M.; Breiten, B.; Whitesides, G.M.; Cyganik, P. Formation of Highly Ordered Self-Assembled Monolayers of Alkynes on Au(111) Substrate. *J. Am. Chem. Soc.* **2014**, *136*, 11918–11921. [CrossRef]
81. Euti, E.M.; Vélez Romero, P.; Linarez Pérez, O.; Ruano, G.; Patrito, E.M.; Zampieri, G.; Leiva, E.P.M.; Macagno, V.A.; Cometto, F.P. Electrochemical, HR-XPS and SERS study of the self-assembly of biphenyl 4,4′-dithiol on Au(111) from solution phase. *Surf. Sci.* **2014**, *630*, 101–108. [CrossRef]
82. Ossowski, J.; Nascimbeni, G.; Żaba, T.; Verwüster, E.; Rysz, J.; Terfort, A.; Zharnikov, M.; Zojer, E.; Cyganik, P. Relative Thermal Stability of Thiolate- and Selenolate-Bonded Aromatic Monolayers on the Au(111) Substrate. *J. Phys. Chem. C* **2017**, *121*, 28031–28042. [CrossRef]

83. Kang, J.F.; Liao, S.; Jordan, R.; Ulman, A. Mixed Self-assembled Monolayers of Rigid Biphenyl Thiols: Impact of Solvent and Dipole Moment. *J. Am. Chem. Soc.* **1998**, *120*, 9662–9667. [CrossRef]
84. Rong, H.T.; Frey, S.; Yang, Y.J.; Zharnikov, M.; Buck, M.; Wühn, M.; Wöll, C.; Helmchen, G. On the Importance of the Headgroup Substrate Bond in Thiol Monolayers: A Study of Biphenyl-Based Thiols on Gold and Silver. *Langmuir* **2001**, *17*, 1582–1593. [CrossRef]
85. Azzam, W.; Fuxen, C.; Birkner, A.; Rong, H.T.; Buck, M.; Wöll, C. Coexistence of Different Structural Phases in Thioaromatic Monolayers on Au(111). *Langmuir* **2003**, *19*, 4958–4968. [CrossRef]
86. Shaporenko, A.; Terfort, A.; Grunze, M.; Zharnikov, M. A detailed analysis of the photoemission spectra of basic thioaromatic monolayers on noble metal substrates. *J. Electron Spectrosc. Relat. Phenom.* **2006**, *151*, 45–51. [CrossRef]
87. Cyganik, P.; Buck, M.; Strunskus, T.; Shaporenko, A.; Wilton-Ely, J.D.E.T.; Zharnikov, M.; Wöll, C. Competition as a Design Concept: Polymorphism in Self-Assembled Monolayers of Biphenyl-Based Thiols. *J. Am. Chem. Soc.* **2006**, *128*, 13868–13878. [CrossRef]
88. Stoycheva, S.; Himmelhaus, M.; Fick, J.; Korniakov, A.; Grunze, M.; Ulman, A. Spectroscopic Characterization of ω-Substituted Biphenylthiolates on Gold and Their Use as Substrates for "On-Top" Siloxane SAM Formation. *Langmuir* **2006**, *22*, 4170–4178. [CrossRef]
89. Krzykawska, A.; Ossowski, J.; Żaba, T.; Cyganik, P. Binding groups for highly ordered SAM formation: Carboxylic versus thiol. *Chem. Commun.* **2017**, *53*, 5748–5751. [CrossRef]
90. Sauter, E.; Nascimbeni, G.; Trefz, D.; Ludwigs, S.; Zojer, E.; von Wrochem, F.; Zharnikov, M. A dithiocarbamate anchoring group as a flexible platform for interface engineering. *Phys. Chem. Chem. Phys.* **2019**, *21*, 22511–22525. [CrossRef]
91. Blum, V.; Gehrke, R.; Hanke, F.; Havu, P.; Havu, V.; Ren, X.; Reuter, K.; Scheffler, M. Ab initio molecular simulations with numeric atom-centered orbitals. *Comput. Phys. Commun.* **2009**, *180*, 2175–2196. [CrossRef]
92. Havu, V.; Blum, V.; Havu, P.; Scheffler, M. Efficient integration for all-electron electronic structure calculation using numeric basis functions. *J. Comput. Phys.* **2009**, *228*, 8367–8379. [CrossRef]
93. Marek, A.; Blum, V.; Johanni, R.; Havu, V.; Lang, B.; Auckenthaler, T.; Heinecke, A.; Bungartz, H.-J.; Lederer, H. The ELPA library: Scalable parallel eigenvalue solutions for electronic structure theory and computational science. *J. Phys. Condens. Matter* **2014**, *26*, 213201. [CrossRef] [PubMed]
94. Togo, A.; Tanaka, I. Spglib: A software library for crystal symmetry search. *arXiv* **2018**, arXiv:1808.01590.
95. Yu, V.W.; Corsetti, F.; García, A.; Huhn, W.P.; Jacquelin, M.; Jia, W.; Lange, B.; Lin, L.; Lu, J.; Mi, W.; et al. ELSI: A unified software interface for Kohn–Sham electronic structure solvers. *Comput. Phys. Commun.* **2018**, *222*, 267–285. [CrossRef]
96. Perdew, J.P.; Burke, K.; Ernzerhof, M. Generalized Gradient Approximation Made Simple. *Phys. Rev. Lett.* **1996**, *77*, 3865–3868. [CrossRef] [PubMed]
97. Perdew, J.P.; Burke, K.; Ernzerhof, M. ERRATA: Generalized Gradient Approximation Made Simple. *Phys. Rev. Lett.* **1997**, *78*, 1396. [CrossRef]
98. Ruiz, V.G.; Liu, W.; Zojer, E.; Scheffler, M.; Tkatchenko, A. Density-Functional Theory with Screened van der Waals Interactions for the Modeling of Hybrid Inorganic-Organic Systems. *Phys. Rev. Lett.* **2012**, *108*. [CrossRef]
99. Tkatchenko, A.; Scheffler, M. Accurate Molecular Van Der Waals Interactions from Ground-State Electron Density and Free-Atom Reference Data. *Phys. Rev. Lett.* **2009**, *102*. [CrossRef]
100. Neugebauer, J.; Scheffler, M. Adsorbate-substrate and adsorbate-adsorbate interactions of Na and K adlayers on Al(111). *Phys. Rev. B* **1992**, *46*, 16067–16080. [CrossRef]
101. Freysoldt, C.; Eggert, P.; Rinke, P.; Schindlmayr, A.; Scheffler, M. Screening in two dimensions: G W calculations for surfaces and thin films using the repeated-slab approach. *Phys. Rev. B* **2008**, *77*, 235428. [CrossRef]
102. Verwüster, E.; Hofmann, O.T.; Egger, D.A.; Zojer, E. Electronic Properties of Biphenylthiolates on Au(111): The Impact of Coverage Revisited. *J. Phys. Chem. C* **2015**, *119*, 7817–7825. [CrossRef]
103. Vackář, J.; Hyt'ha, M.; Šimůnek, A. All-electron pseudopotentials. *Phys. Rev. B* **1998**, *58*, 12712–12720. [CrossRef]
104. Methfessel, M.; Fiorentini, V.; Oppo, S. Connection between charge transfer and alloying core-level shifts based on density-functional calculations. *Phys. Rev. B* **2000**, *61*, 5229–5236. [CrossRef]

105. Morikawa, Y.; Hayashi, T.; Liew, C.C.; Nozoye, H. First-principles theoretical study of alkylthiolate adsorption on Au (111). *Surf. Sci.* **2002**, *507*, 46–50. [CrossRef]
106. Heimel, G.; Romaner, L.; Brédas, J.L.; Zojer, E. Organic/metal interfaces in self-assembled monolayers of conjugated thiols: A first-principles benchmark study. *Surf. Sci.* **2006**, *600*, 4548–4562. [CrossRef]
107. Giesbers, M.; Marcelis, A.T.M.; Zuilhof, H. Simulation of XPS C1s Spectra of Organic Monolayers by Quantum Chemical Methods. *Langmuir* **2013**, *29*, 4782–4788. [CrossRef]
108. Pueyo Bellafont, N.; Illas, F.; Bagus, P.S. Validation of Koopmans' theorem for density functional theory binding energies. *Phys. Chem. Chem. Phys.* **2015**, *17*, 4015–4019. [CrossRef]
109. Ishiwari, F.; Nascimbeni, G.; Sauter, E.; Tago, H.; Shoji, Y.; Fujii, S.; Kiguchi, M.; Tada, T.; Zharnikov, M.; Zojer, E.; et al. Triptycene Tripods for the Formation of Highly Uniform and Densely Packed Self-Assembled Monolayers with Controlled Molecular Orientation. *J. Am. Chem. Soc.* **2019**, *141*, 5995–6005. [CrossRef]
110. Pueyo Bellafont, N.; Bagus, P.S.; Illas, F. Prediction of core level binding energies in density functional theory: Rigorous definition of initial and final state contributions and implications on the physical meaning of Kohn-Sham energies. *J. Chem. Phys.* **2015**, *142*, 214102. [CrossRef]
111. Viñes, F.; Sousa, C.; Illas, F. On the prediction of core level binding energies in molecules, surfaces and solids. *Phys. Chem. Chem. Phys.* **2018**, *20*, 8403–8410. [CrossRef]
112. Taucher, T.C.; Hofmann, O.T.; Zojer, E. Final-State Simulations of Core-Level Binding Energies at Metal-Organic Hybrid Interfaces: Artifacts Caused by Spurious Collective Electrostatic Effects. 2020, Submitted.
113. Jackson, J.D. *Classical Electrodynamics*, 3rd ed.; Wiley: New York, NY, USA, 1999; ISBN 978-0-471-30932-1.
114. Neaton, J.B.; Hybertsen, M.S.; Louie, S.G. Renormalization of Molecular Electronic Levels at Metal-Molecule Interfaces. *Phys. Rev. Lett.* **2006**, *97*, 216405. [CrossRef] [PubMed]
115. Lamont, C.L.; Wilkes, J. Attenuation length of electrons in self-assembled monolayers of n-alkanethiols on gold. *Langmuir* **1999**, *15*, 2037–2042. [CrossRef]
116. Van der Walt, S.; Colbert, S.C.; Varoquaux, G. The NumPy Array: A Structure for Efficient Numerical Computation. *Comput. Sci. Eng.* **2011**, *13*, 22–30. [CrossRef]
117. Hunter, J.D. Matplotlib: A 2D Graphics Environment. *Comput. Sci. Eng.* **2007**, *9*, 90–95. [CrossRef]
118. Stukowski, A. Visualization and analysis of atomistic simulation data with OVITO–the Open Visualization Tool. *Model. Simul. Mater. Sci. Eng.* **2010**, *18*, 015012. [CrossRef]
119. Momma, K.; Izumi, F. *VESTA 3* for three-dimensional visualization of crystal, volumetric and morphology data. *J. Appl. Cryst.* **2011**, *44*, 1272–1276. [CrossRef]
120. The GIMP Development Team *GIMP* 2019. Available online: https://www.gimp.org (accessed on 30 March 2020).
121. Sze, S.M.; Ng, K.K. *Physics of Semiconductor Devices*, 3rd ed.; Wiley-Interscience: Hoboken, NJ, USA, 2007; ISBN 978-0-471-14323-9.
122. Stähler, J.; Rinke, P. Global and local aspects of the surface potential landscape for energy level alignment at organic-ZnO interfaces. *Chem. Phys.* **2017**, *485-486*, 149–165. [CrossRef]
123. Heimel, G.; Rissner, F.; Zojer, E. Modeling the Electronic Properties of π-Conjugated Self-Assembled Monolayers. *Adv. Mater.* **2010**, *22*, 2494–2513. [CrossRef]
124. Natan, A.; Zidon, Y.; Shapira, Y.; Kronik, L. Cooperative effects and dipole formation at semiconductor and self-assembled-monolayer interfaces. *Phys. Rev. B* **2006**, *73*. [CrossRef]
125. Egelhoff, W.F. Core-level binding-energy shifts at surfaces and in solids. *Surf. Sci. Rep.* **1987**, *6*, 253–415. [CrossRef]
126. Bagus, P.S.; Nelin, C.J.; Zhao, X.; Levchenko, S.V.; Davis, E.; Weng, X.; Späth, F.; Papp, C.; Kuhlenbeck, H.; Freund, H.J. Revisiting surface core-level shifts for ionic compounds. *Phys. Rev. B* **2019**, *100*, 115419. [CrossRef]
127. Vericat, C.; Vela, M.E.; Corthey, G.; Pensa, E.; Cortés, E.; Fonticelli, M.H.; Ibañez, F.; Benitez, G.E.; Carro, P.; Salvarezza, R.C. Self-assembled monolayers of thiolates on metals: A review article on sulfur-metal chemistry and surface structures. *RSC Adv.* **2014**, *4*, 27730–27754. [CrossRef]
128. Ma, Z.; Rissner, F.; Wang, L.; Heimel, G.; Li, Q.; Shuai, Z.; Zojer, E. Electronic structure of pyridine-based SAMs on flat Au(111) surfaces: Extended charge rearrangements and Fermi level pinning. *Phys. Chem. Chem. Phys.* **2011**, *13*, 9747. [CrossRef] [PubMed]

129. Hofmann, O.T.; Deinert, J.-C.; Xu, Y.; Rinke, P.; Stähler, J.; Wolf, M.; Scheffler, M. Large work function reduction by adsorption of a molecule with a negative electron affinity: Pyridine on ZnO(10$\bar{1}$0). *J. Chem. Phys.* **2013**, *139*, 174701. [CrossRef]
130. Hébert, P.; Le Rille, A.; Zheng, W.Q.; Tadjeddine, A. Vibrational spectroscopic study of the adsorption of pyridine at the Au(111)-electrolyte interface by in situ difference frequency generation. *J. Electroanal. Chem.* **1998**, *447*, 5–9. [CrossRef]
131. Stadler, R.; Thygesen, K.S.; Jacobsen, K.W. Forces and conductances in a single-molecule bipyridine junction. *Phys. Rev. B* **2005**, *72*, 241401. [CrossRef]
132. Kamenetska, M.; Quek, S.Y.; Whalley, A.C.; Steigerwald, M.L.; Choi, H.J.; Louie, S.G.; Nuckolls, C.; Hybertsen, M.S.; Neaton, J.B.; Venkataraman, L. Conductance and Geometry of Pyridine-Linked Single-Molecule Junctions. *J. Am. Chem. Soc.* **2010**, *132*, 6817–6821. [CrossRef]
133. Obersteiner, V.; Egger, D.A.; Zojer, E. Impact of Anchoring Groups on Ballistic Transport: Single Molecule vs Monolayer Junctions. *J. Phys. Chem. C* **2015**, *119*, 21198–21208. [CrossRef]
134. Smith, C.E.; Xie, Z.; Bâldea, I.; Frisbie, C.D. Work function and temperature dependence of electron tunneling through an N-type perylene diimide molecular junction with isocyanide surface linkers. *Nanoscale* **2018**, *10*, 964–975. [CrossRef]
135. Tsunoi, A.; Lkhamsuren, G.; Mondarte, E.A.Q.; Asatyas, S.; Oguchi, M.; Noh, J.; Hayashi, T. Improvement of the Thermal Stability of Self-Assembled Monolayers of Isocyanide Derivatives on Gold. *J. Phys. Chem. C* **2019**, *123*, 13681–13686. [CrossRef]
136. Bagus, P.S.; Staemmler, V.; Wöll, C. Exchangelike Effects for Closed-Shell Adsorbates: Interface Dipole and Work Function. *Phys. Rev. Lett.* **2002**, *89*. [CrossRef] [PubMed]
137. Mizushima, H.; Koike, H.; Kuroda, K.; Ishida, Y.; Nakayama, M.; Mase, K.; Kondo, T.; Shin, S.; Kanai, K. Effect of physisorption of inert organic molecules on Au(111) surface electronic states. *Phys. Chem. Chem. Phys.* **2017**, *19*, 18646–18651. [CrossRef] [PubMed]
138. Zangmeister, C.D.; Robey, S.W.; van Zee, R.D.; Kushmerick, J.G.; Naciri, J.; Yao, Y.; Tour, J.M.; Varughese, B.; Xu, B.; Reutt-Robey, J.E. Fermi Level Alignment in Self-Assembled Molecular Layers: The Effect of Coupling Chemistry. *J. Phys. Chem. B* **2006**, *110*, 17138–17144. [CrossRef] [PubMed]
139. Kim, B.; Beebe, J.M.; Jun, Y.; Zhu, X.Y.; Frisbie, C.D. Correlation between HOMO Alignment and Contact Resistance in Molecular Junctions: Aromatic Thiols versus Aromatic Isocyanides. *J. Am. Chem. Soc.* **2006**, *128*, 4970–4971. [CrossRef] [PubMed]
140. Macdonald, J.R.; Barlow, C.A. Work Function Change on Monolayer Adsorption. *J. Chem. Phys.* **1963**, *39*, 412–422. [CrossRef]
141. Maschhoff, B.L.; Cowin, J.P. Corrected electrostatic model for dipoles adsorbed on a metal surface. *J. Chem. Phys.* **1994**, *101*, 8138–8151. [CrossRef]
142. Gershevitz, O.; Sukenik, C.N.; Ghabboun, J.; Cahen, D. Molecular Monolayer-Mediated Control over Semiconductor Surfaces: Evidence for Molecular Depolarization of Silane Monolayers on Si/SiOx. *J. Am. Chem. Soc.* **2003**, *125*, 4730–4731. [CrossRef]
143. De Renzi, V.; Rousseau, R.; Marchetto, D.; Biagi, R.; Scandolo, S.; del Pennino, U. Metal Work-Function Changes Induced by Organic Adsorbates: A Combined Experimental and Theoretical Study. *Phys. Rev. Lett.* **2005**, *95*, 046804. [CrossRef]
144. Fukagawa, H.; Yamane, H.; Kera, S.; Okudaira, K.K.; Ueno, N. Experimental estimation of the electric dipole moment and polarizability of titanyl phthalocyanine using ultraviolet photoelectron spectroscopy. *Phys. Rev. B* **2006**, *73*, 041302. [CrossRef]
145. Cornil, D.; Olivier, Y.; Geskin, V.; Cornil, J. Depolarization Effects in Self-Assembled Monolayers: A Quantum-Chemical Insight. *Adv. Funct. Mater.* **2007**, *17*, 1143–1148. [CrossRef]
146. Sushko, M.L.; Shluger, A.L. Intramolecular Dipole Coupling and Depolarization in Self-Assembled Monolayers. *Adv. Funct. Mater.* **2008**, *18*, 2228–2236. [CrossRef]
147. Piacenza, M.; D'Agostino, S.; Fabiano, E.; Della Sala, F. Ab initio depolarization in self-assembled molecular monolayers: Beyond conventional density-functional theory. *Phys. Rev. B* **2009**, *80*, 153101. [CrossRef]
148. Blumenfeld, M.L.; Steele, M.P.; Monti, O.L.A. Near- and Far-Field Effects on Molecular Energy Level Alignment at an Organic/Electrode Interface. *J. Phys. Chem. Lett.* **2010**, *1*, 145–148. [CrossRef]

149. Wang, L.; Rangger, G.M.; Romaner, L.; Heimel, G.; Bučko, T.; Ma, Z.; Li, Q.; Shuai, Z.; Zojer, E. Electronic Structure of Self-Assembled Monolayers on Au(111) Surfaces: The Impact of Backbone Polarizability. *Adv. Funct. Mater.* **2009**, *19*, 3766–3775. [CrossRef]
150. Koller, G.; Winter, B.; Oehzelt, M.; Ivanco, J.; Netzer, F.P.; Ramsey, M.G. The electronic band alignment on nanoscopically patterned substrates. *Org. Electron.* **2007**, *8*, 63–68. [CrossRef]

5.3 SUPPLEMENTARY MATERIALS

In the Supplementary Materials we provide additional information on the computational methodology, a flow-chart summarizing the computational procedure, additional computational results, and views of unit cells and supercells used in the main manuscript.

Supplementary Materials

The Potential of X-ray Photoelectron Spectroscopy for Determining Interface Dipoles of Self-Assembled Monolayers

Thomas C. Taucher, and Egbert Zojer*

Institute of Solid State Physics, Graz University of Technology, NAWI Graz, Petersgasse 16, 8010 Graz, Austria.

*Corresponding author: egbert.zojer@tugraz.at, +43/316/873-8475

1 Information on the employed basis functions

The basis functions employed in the FHI-aims simulations have the format

$$\Phi(r) = \frac{u(r)}{r} * Y_{lm}(\Theta, \Phi) \tag{S1}$$

in spherical coordinates (r, Θ, Φ) relative to a given atomic center. FHI-aims provides for every atomic species a preconstructed *species_defaults* file. The used tight basis sets were not further adjusted, because they afforded the required accuracy and efficiency. Note: If a higher tier for the basis set is used, i.e., when using tight settings, all lower basis functions must be included as well.

Table S1. Basis functions that have been used for all calculations performed with FHI-aims[1]*. The abbreviations read as follows*[1]*: X(nl, z), where X describes the type of basis function where H stands for hydrogen-like functions and ionic for a free-ion like radial function. The parameter n stands for the main/radial quantum number, l denotes the angular momentum quantum number (s, p, d, f, …), and z denotes an effective nuclear charge, which scales the radial function in the defining Coulomb potential for the hydrogen-like function. In the case of free-ion like radial functions, z specifies the onset radius of the confining potential. If auto is specified instead of a numerical value, the default onset is used.*

	H	C	N	S	Au
Minimal	valence(1s, 1.0)	valence(2s, 2.0) valence(2p, 2.0)	valence(2s, 2.0) valence(2p, 3.0)	valence(3s, 2.0) valence(3p, 4.0)	valence(6s, 1.0) valence(5p, 6.0) valence(5d, 10.0) valence(4f, 14.0)
First tier	H(2s, 2.1) H(2p, 3.5)	H(2p, 1.7) H(3d, 6) H(2s, 4.9)	H(2p, 1.8) H(3d, 6.8) H(3s, 5.8)	ionic(3d, auto) H(2p, 1.8) H(4f, 7.0) Ionic(3s, auto)	ionic(6p, auto) H(4f, 4.7) ionic(6s, auto) H(5g, 10.0) H(3d, 2.5)
Second tier	H(1s, 0.85) H(2p, 3.7) H(2s, 1.2) H(3d, 7.0)	H(4f, 9.8) H(3p, 5.2) H(3s, 4.3) H(5g, 14.4) H(3d, 6.2)	H(4f, 10.8) H(3p, 5.8) H(1s, 0.8) H(5g, 16.0) H(3d, 4.9)	H(4d, 6.2) H(5g, 10.8)	

---

[1] As described in the FHI-aims manual, version January 23, 2017.

2 A posteriori screening via an image charge model

To account for the screening of the highly polarizable metal substrate, the calculated orbital energies were corrected by the following screening contribution:

$$\mathrm{E}_{C1s,screened}[eV] = \mathrm{E}_{C1s}[eV] + 27.2114 \cdot \frac{1}{4 \cdot \epsilon \cdot 1.889716 \cdot (z[\text{Å}] - z_0[\text{Å}])} \tag{S2}$$

Here, ϵ is the dielectric constant of the SAM; in our case we chose $\epsilon = 3.9$ according to measurements on biphenyl SAMs.[2] The constant z_0 is the position of the image plane of the Au(111) surface, which was set to 0.9 Å above the average z-position of the top Au layer.[3,4] The z-position of the atom, to whose core level the screening is applied, is denoted as z. The two conversion factors, 27.2114 and 1.889716, are there to convert Hartree to eV and Bohr to Å, respectively. In passing we note that this approach neglects direct screening effects within the SAM and also the fact that the SAM is only of finite thickness. The screening shifts the calculated core levels to more negative values, i.e. smaller binding energies, and, naturally, is most relevant for the ones closest to the substrate.

3 The damping factor

To account for the finite escape depth of the ejected electrons[5], a damping factor depending on the kinetic energy of the incident photons was applied to scale the contributions of the individual C atoms to the XP spectra. It is given by:

$$w_i(d) = w_0 \cdot e^{\frac{-d}{\lambda}} \tag{S3}$$

Here $w_i(d)$ is the scaling factor of the *i*-th C1s orbital. It depends on the vertical distance *d* between the *i*-th atom and the topmost Carbon atom of the SAM, and a damping factor λ, which is defined as $\lambda = 0.3E_{KIN}^{\beta}$. Here, $E_{KIN}[eV]$ is the kinetic energy of the escaping electron, i.e., the difference between the energy of the incident photons and the calculated core level orbital energy of the C1s electron (set to 580 eV for this study). β is an empirical attenuation factor, which was set to 0.5 in accordance with previous studies on similar systems.[6] Finally, w_0 is a scaling constant, which does not change the shape of the spectrum.

4 Flowchart describing the computational procedure

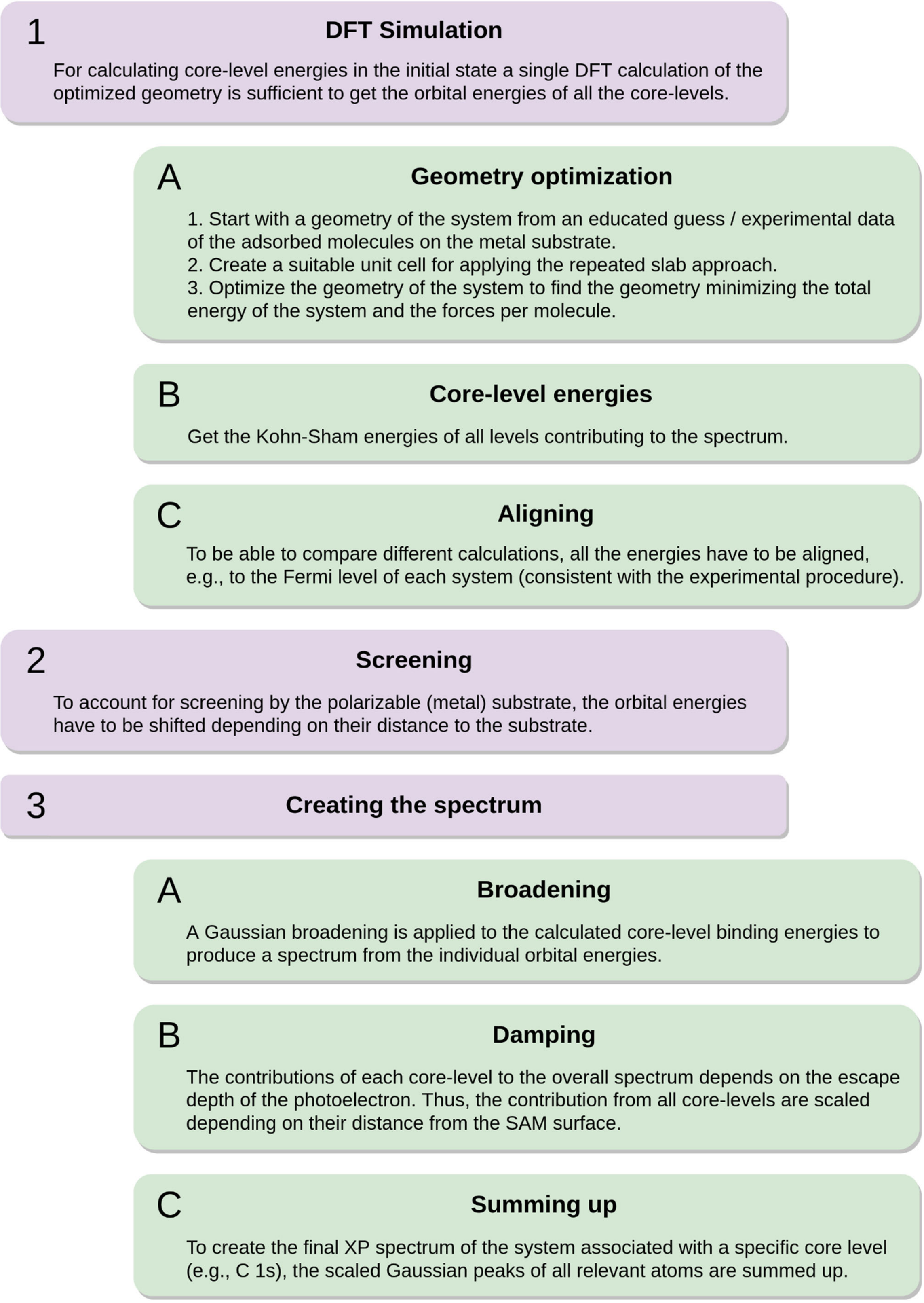

1 DFT Simulation

For calculating core-level energies in the initial state a single DFT calculation of the optimized geometry is sufficient to get the orbital energies of all the core-levels.

A Geometry optimization

1. Start with a geometry of the system from an educated guess / experimental data of the adsorbed molecules on the metal substrate.
2. Create a suitable unit cell for applying the repeated slab approach.
3. Optimize the geometry of the system to find the geometry minimizing the total energy of the system and the forces per molecule.

B Core-level energies

Get the Kohn-Sham energies of all levels contributing to the spectrum.

C Aligning

To be able to compare different calculations, all the energies have to be aligned, e.g., to the Fermi level of each system (consistent with the experimental procedure).

2 Screening

To account for screening by the polarizable (metal) substrate, the orbital energies have to be shifted depending on their distance to the substrate.

3 Creating the spectrum

A Broadening

A Gaussian broadening is applied to the calculated core-level binding energies to produce a spectrum from the individual orbital energies.

B Damping

The contributions of each core-level to the overall spectrum depends on the escape depth of the photoelectron. Thus, the contribution from all core-levels are scaled depending on their distance from the SAM surface.

C Summing up

To create the final XP spectrum of the system associated with a specific core level (e.g., C 1s), the scaled Gaussian peaks of all relevant atoms are summed up.

5 Testing the hypothesis of vacuum level alignment for system VIa

In the main manuscript, system VIa (a biphenyl monolayer moved from its equilibrium position by 1 Å away from the substrate) is considered as the reference case for vacuum level alignment. This is backed by the negligible work function change of ~-0.1 eV induced by that layer. As a further test, we compared the XP spectra for that system and a system in which the biphenyl is shifted by 2 Å (system VIb). In case there was no interaction between adsorbate and substrate in VIa, there should be no change in the calculated spectra between VIa and VIb. This is indeed what we find, as shown in Figure S1.

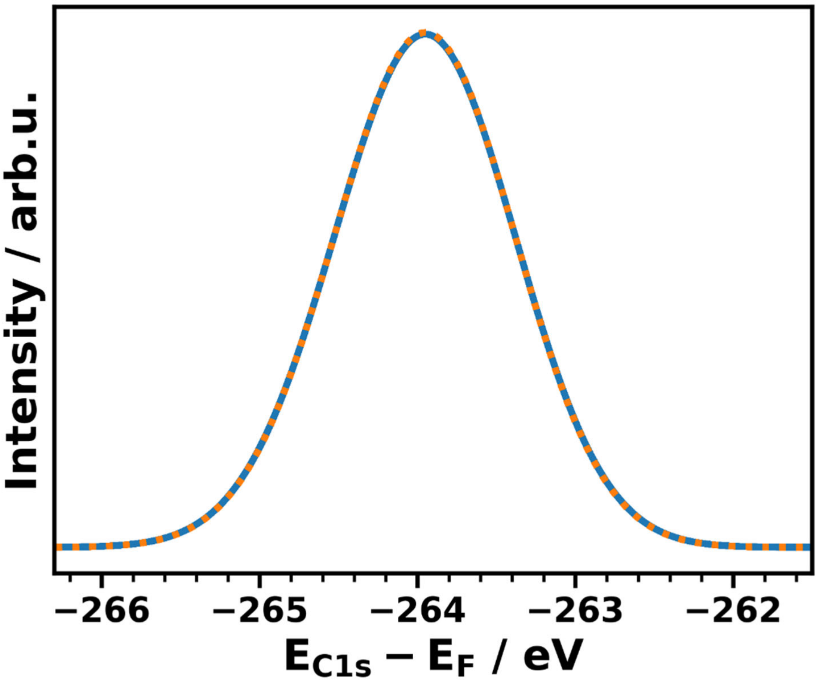

Figure S1. Calculated XP spectra of system VIa (blue, solid line) and VIb (orange, dotted line), where the biphenyl SAM is moved farther away by 1 Å and by 2 Å, respectively.

6 Calculated core-level binding energies and XP spectra for all systems at full coverage

For the sake of clarity, in Figure 3 of the main manuscript the core-level binding energies and XP spectra have been shown only for selected systems. A compilation of the results for all systems is contained in the following plot.

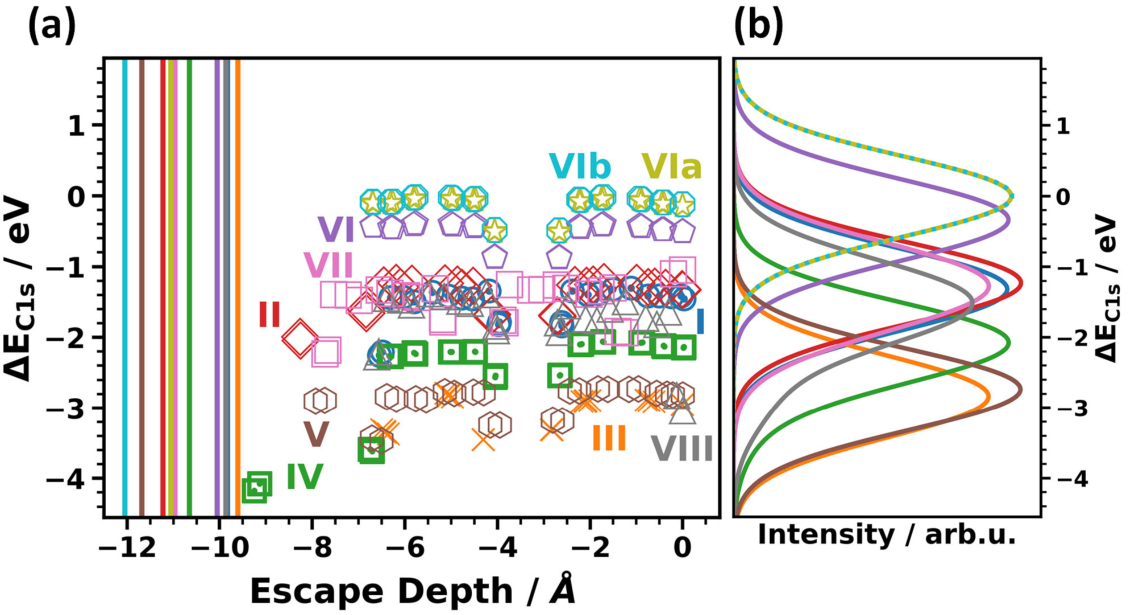

Figure S2. (a) Simulated shifts of carbon 1s orbital energies, ΔE_{C1s}, as a function of the escape depth of the electrons for all investigated systems; (b) corresponding XP spectra generated from the calculated energy levels. The energies scale is chosen relative to the position of the peak in the XP spectrum for the vacuum-level aligned system VIa. The escape depth defined as the distance from the topmost carbon atom is chosen as the parameter on the x-axis considering that the highest atoms primarily determine the XP spectra. As the extent of the SAMs between the bottom ring and the metal substrate varies due to the different docking groups, this choice of the x-axis also largely aligns biphenyls in the different systems. Due to the different SAM thicknesses, we included vertical lines in panel (a), which designate the positions of the centers of the atoms of the topmost Au layer. The large number of data points for each system is a consequence of the two inequivalent molecules per unit cell.

7 Single molecule limit

To check to what degree the data for 1/16 coverage reported in the main manuscript already describe an isolated molecule on a surface, we simulated XP spectra for system I also for 1/24 and 1/30 coverage (see Figure S3). The obtained spectra essentially coincide with that for 1/16 coverage, which suggests that the "isolated molecule" case is already achieved at that coverage.

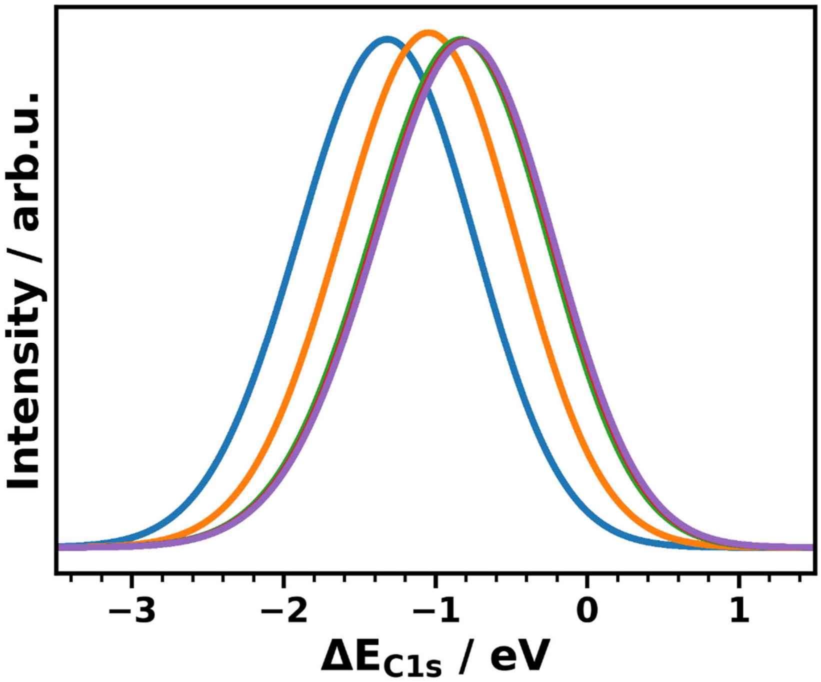

Figure S3. Calculated XP spectra of system I as a function of coverage (full coverage – blue, 1/4 coverage – orange, 1/16 coverage – green, 1/24 coverage – red, 1/30 coverage - violet). The energy scale is aligned relative to the position of the peak for the non-interacting system VIa.

8 Low coverage unit cells

The low coverage unit cells where created by replicating the full coverage unit cell (containing two molecules) in x- and y-direction and removing all but one molecule from the Au(111)-substrate. For a coverage of 1/4 the unit cell was duplicated only in x-direction; for the 1/16 coverage system the initial unit cell was repeated four times in x-direction and twice in y-direction; for the 1/24 cell six times in x- and twice in y-direction, and for the 1/30 coverage, this was done five times in x- and three times in y-direction.

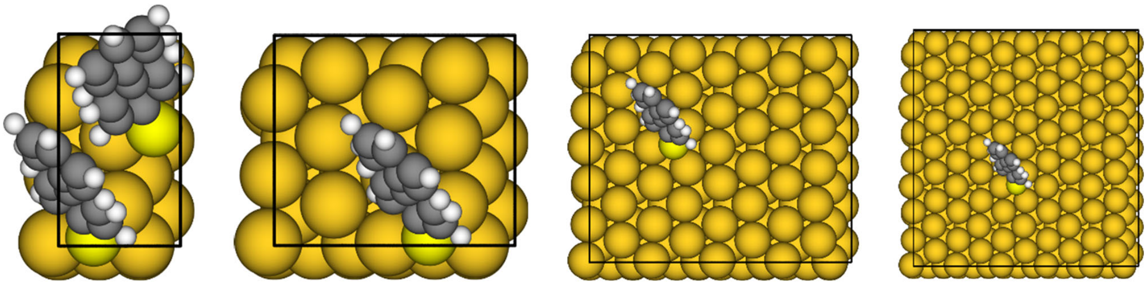

Figure S4. Top views of the unit cells for full, 1/4, 1/16, and 1/30 coverage (from left to right).

9 Top view of the unit cell

To be able to visually compare the tilt of each molecule in the geometrically optimized unit cell, top views of the unit cells of all systems are shown in Figure S5.

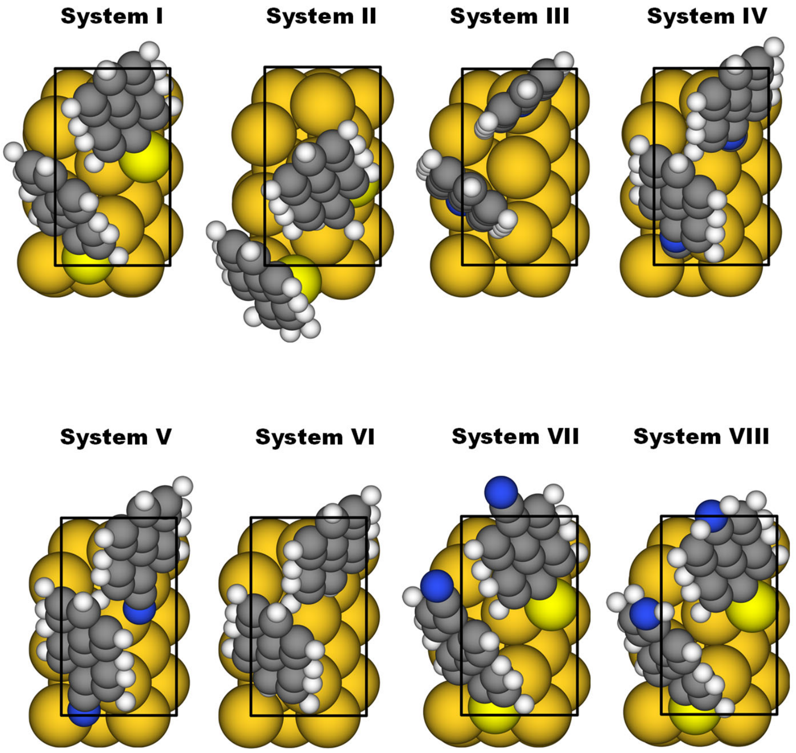

Figure S5. Top view of the investigated systems with different docking groups bonding to the Au(111) surface slab. The tilt of the molecules is similar all systems apart from system III, where the molecules are more upright-standing.

10 Plane for potential plot

To visualize the plane for which the electrostatic energy is shown in Figure 8, a top view of the (repeated) full coverage unit cell is shown in Figure S6 containing that plane.

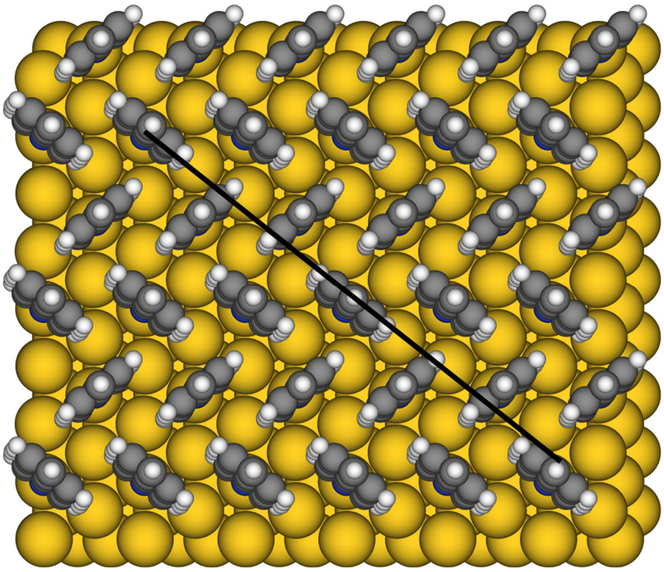

Figure S6. Top view of system II with a black line indicating the plane used for the 2D electrostatic energy plot in Figure 8.

11 References

(1) Blum, V.; Gehrke, R.; Hanke, F.; Havu, P.; Havu, V.; Ren, X.; Reuter, K.; Scheffler, M. Ab Initio Molecular Simulations with Numeric Atom-Centered Orbitals. *Computer Physics Communications* **2009**, *180* (11), 2175–2196. https://doi.org/10.1016/j.cpc.2009.06.022.

(2) Levstik, A.; Filipic, C.; Levstik, I. Dielectric Properties of Biphenyl. *J. Phys.: Condens. Matter* **1990**, *2* (13), 3031–3033. https://doi.org/10.1088/0953-8984/2/13/012.

(3) Li, Y.; Lu, D.; Galli, G. Calculation of Quasi-Particle Energies of Aromatic Self-Assembled Monolayers on Au(111). *Journal of Chemical Theory and Computation* **2009**, *5* (4), 881–886. https://doi.org/10.1021/ct800465f.

(4) Egger, D. A.; Liu, Z.-F.; Neaton, J. B.; Kronik, L. Reliable Energy Level Alignment at Physisorbed Molecule–Metal Interfaces from Density Functional Theory. *Nano Letters* **2015**, *15* (4), 2448–2455. https://doi.org/10.1021/nl504863r.

(5) Lamont, C. L.; Wilkes, J. Attenuation Length of Electrons in Self-Assembled Monolayers of n-Alkanethiols on Gold. *Langmuir* **1999**, *15* (6), 2037–2042.

(6) Gärtner, M.; Sauter, E.; Nascimbeni, G.; Petritz, A.; Wiesner, A.; Kind, M.; Abu-Husein, T.; Bolte, M.; Stadlober, B.; Zojer, E.; Terfort, A.; Zharnikov, M. Understanding the Properties of Tailor-Made Self-Assembled Monolayers with Embedded Dipole Moments for Interface Engineering. *J. Phys. Chem. C* **2018**, *122* (50), 28757–28774. https://doi.org/10.1021/acs.jpcc.8b09440.

6

ON THE TRANSITION VOLTAGE IN MOLECULAR ELECTRONICS

As molecular electronic devices consist of junctions which are comprised of a single molecule up to a monolayer, they operate at the very edge were collective electrostatic effects come into play. Therefore, it is of high interest to investigate the impact of collective electrostatic effects in the realms of molecular electronics. For the ever ongoing miniaturization of electronic devices, semiconducting components consisting of individual molecules or condensed into a molecular assembly are a promising approach. To develop such devices, a microscopic understanding of charge transport on an atomistic length scale is of key importance. The current focus of research in the molecular electronics community lies in establishing a fundamental understanding of the interplay between the current-voltage (I-V) characteristics and the molecular structure of a junction. Building a junction with a known molecular structure can be readily done in theoretical, quantum-mechanical based approaches and allows to investigate the electronic levels of molecular junctions in great detail. A key technique used for that is the so-called transition voltage spectroscopy (TVS).

6.1 TRANSITION VOLTAGE SPECTROSCOPY

A quite widely used technique to characterize molecular and monolayer junctions is TVS. This spectroscopic approach allows to investigate the electronic level alignment in molecular devices without the need for extreme voltages.[215] This is especially important for the case of two-terminal molecular junctions, as these usually can withstand only a comparable low bias voltage. As the Fermi level is typically a couple tenth of an eV away from the closest molecular level, a high bias voltage is needed for resonant electron tunneling. Such high bias voltages produce huge electric fields in the range of $>10^9$ V/m, causing a breakdown of the junction before the molecular level of interest is accessed.[215] In the seminal work of Beebe *et al.* [61, 62] it is argued that the position of the molecular level closest to the Fermi level can be derived from a current-voltage characteristics. This is already possible for comparable low bias voltages where resonance is not yet reached. Beebe *et al.* draw the analogy between (molecular) charge transport and electron tunneling. For the electron tunneling they argue on the basis of a model first described by Simmons,[216] where the electrons tunnel through a rectangular potential barrier. A schematic plot of the Simmons model is given in the left part of Figure 14.

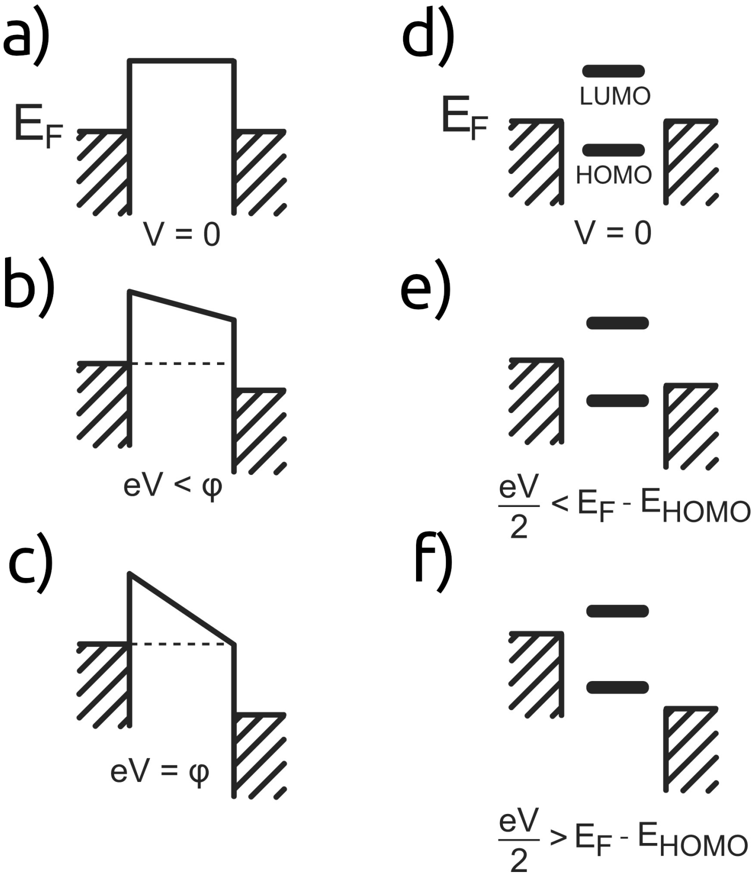

Figure 14: Schematics of a symmectric molecular junction described by the Simmons model (left hand side) and for comparison a resonant molecular model (right hand side). The depicted molecule yields a tunnel barrier of height ϕ. At the top, part (a) and (d), the situation at zero bias is depicted. When a bias voltage is applied the potential barrier tilts in the framework of the Simmons model (b), and in the picture of the resonant molecular model, the energy levels are shifted with respect to each other and open a window for transport of size eV (e). In the bottom part the situation is shown for the applied bias being equal or greater than ϕ. In this case, the barrier changes its shape and becomes triangular in the Simmons model. Therefore, the electron tunneling can be described via field emission (c). In (f) the situation is shown for resonant tunneling, i. e., when a level is within the bias window, which yields a dramatically increased current. Figure modified with permission from [215]. Copyright 2009 American Chemical Society.

In the framework of the Simmons model, the energy offset between the Fermi level and the closest, molecular orbital equals the tunnel barrier height ϕ. Depending on the molecule used, this is either the highest occupied molecular orbital (HOMO) or the lowest unoccupied molecular orbital (LUMO), resulting in hole mediated or electron mediated transport, respectively. The width of the tunnel barrier d is set to the distance between the two electrodes, i. e., the length of the molecule in the junction. Simmons showed that if the bias voltage is low enough, i. e., $eV < \phi$, the effective tunnel barrier is lowered to $\phi - eV/2$ (cf. Figure 14(b)). For high bias voltages, i. e., $eV \geq \phi$, the effective barrier changes its shape from trapezoidal to triangular and a part of the barrier becomes classically available, which is commonly referred to as Fowler–Nordheim (F-N)-tunneling.[217] The situation with a triangular potential barrier is shown in Figure 14(c), where $eV = \phi$. In the F-N-regime the current is proportional to $V^2 exp(c/V)$, where $c < 0$ depends on the height and width of the potential barrier. This means, for the case of $eV > \phi$ plotting the current-voltage data as $ln(I/V^2)$ over $1/V$, i. e., generating a so-called F-N-plot, results in a straight line with a negative slope. In the case of low voltages such a F-N-plot yields a positive slope.[61, 62] This is due to the current being proportional to the voltage at low biases, i. e., if $eV << \phi$, $ln(I/V^2) \propto ln(1/V)$. Therefore, plotting $ln(1/V)$ over $1/V$ yields a positive slope at low voltages. As already mentioned above, for high voltages the curve describes a negative slope, and, therefore, a minimum must occur between these two regimes. Consequently, any current voltage characteristic which evolves from linear to more than quadratic will produce a minimum in a F-N-plot. As this minimum was described by Beebe *et al.* to be at the transition to the field-emission regime, they coined the term *transition voltage*.

The considerations so far have been based on the Simmons model, which Huisman *et al.* argue is not suitable for describing the experimental data investigated by Beebe *et al.* [61, 62].[215] Instead, they propose to build on a Landauer approach (cf. Chapter 2.3.1), utilizing a coherent resonant molecular model, sketched in the right part of Figure 14. There, the transport is described by an energy dependent transmission function producing peaks at the molecular levels, which can be described by a Lorentzian function.[218–220] In Figure 14(d) the situation is depicted for zero bias. There the HOMO and LUMO lie below and above of the Fermi level of both electrodes, respectively. Now when a bias voltage is applied, the energy levels shift with respect to each other. If there is an overlap between the (broadened) energy level of the molecular orbital and the energy window between the two electrodes, i. e., the tail of the Lorentzian-type transport peak comes into resonance with the electrode's Fermi level, charge carriers start to flow. This situation is depicted in Figure 14(e). Increasing the voltage further shifts the molecular level further and resonant tunneling sets in. In two-terminal junctions, resonant tunneling can only occur if a molecular level is between the left and right chemical potential (cf. Figure 14(f).) Unfortunately, as discussed above, typical molecular junctions break down before reaching this point. As Huisman *et al.* showed in their work, the relevant physics needed for analyzing transition voltage spectroscopy (TVS) measurements is captured with their proposed model based on molecular levels. They presented a vastly improved model compared to Beebe *et al.*[61, 62] and were able to reproduce the experimentally measured transition voltages based on the framework of molecular energy levels using a length dependent transmission function.[215] The most fundamental difference is probably the totally different voltage profile over the molecular junction, dropping right at the metal-molecule interface in contrast to the Simmons model which proposes a continuous drop over the whole junction.

Furthermore, Huisman *et al.* argued that TVS can be used to identify tunnel junctions without molecules, on the ground that in their model the voltage drops at the interface between the electrodes and the molecule, whereas a vacuum tunnel junction behaves indeed as described by a Simmons model.[215] This was investigated by Trouwborst *et al.* [221] using a metal-vacuum-metal junction, to be precise, they did TVS-measurements on Au-vacuum-Au junctions. They found that the transition voltage, V_t, is sensitive to the shape of the gold leads, meaning that the geometry of the electrodes plays an important role. Furthermore, they showed that the distance between the electrodes indeed influences the measured V_t, but the variation of the transition voltage with respect to the distance is much weaker than anticipated. Thus, they concluded, it is not possible to utilize TVS to distinguish a vacuum junction from a molecular junction, even though the variation of V_t with respect to the distance provides a strong indication.[221]

Another concept proposed by Vilan *et al.* to interpret TVS with a so-called scaling factor for the applied bias voltage is based on a Taylor Expansion.[223] For this, they introduce the bias scaling voltage, V_0, which is conceptionally related to the transition voltage, V_t. This voltage scaling factor V_0 is derived from a Taylor expansion of the conductance $G(V)$ around $V = 0$, which describes the conductance-voltage curve of a molecular junction with a parabolic shape. The advantage of this approach is that it holds for vastly different tunneling models.[223] This means, even though TVS was first explained on the most probably not accurate basis of a change of the transport mechanism, namely from simple tunneling into the regime of field-emission tunneling, it still is a useful technique to describe a molecular junction. Nowadays, the widely accepted view is that V_t depicts the bias at which the tail of the (Lorentzian)-broadened peak of the molecular transmission function comes into resonance with the electrode's Fermi level.[224] Therefore, theoretical investigations of the transition voltage are mostly based on the Landauer formalism.[215, 224–228] Conceptually speaking, the transition voltage can be seen as an intrinsic property of the transport characteristic of a molecular junction, depending not only on the barrier height, but also on the length of the molecular junction[225], the coupling to the electrodes[225], and the asymmetry of the junctions[225, 227, 229]. Vilan *et al.* argue that "viewing TVS as a bias scaling factor not only substantiates the use of TVS as a genuine tunneling characteristic rather than a mathematical artifact,[228] but also stresses that TVS expresses the combined effect of several possible junction characteristics and does not necessarily reflect spectroscopic details."[222] Furthermore, they show that their approach can be applied to vastly different models, including the ones explained above. These two aforementioned, fundamentally different models represent the two edge-cases. Additionally, it also fits for off-resonant models which propose a step-wise potential profile along the molecule and the electrodes.[230] In their work Vilan *et al.* conclude that the transition voltage should be used as an "empirical parameter that can be highly characteristic for a given junction, even though it can be interpreted in various ways".[222]

6.1.1 *Landauer based single level model*

As already mentioned, the quantum-mechanical Landauer based approach (cf. Chapter 2.3.1) is nowadays the generally accepted formalism to treat tunneling transport.[227, 231–238] We will use the widely accepted model in molecular electronics that one orbital is primarily responsible for charge transport; namely the one closest to the Fermi level, i. e., the transmission is either facilitated via holes or electrons, depending on whether the highest occupied molecular orbital (HOMO) or lowest unoccupied molecular orbital (LUMO) of the molecule lies closer to the Fermi level of the electrode. This offset, ϵ_0, between the Fermi level and the appropriate frontier molecular orbital is one of the main factors determining the electrical properties of a molecular junction. The second crucial parameter is the coupling strength, Γ, which describes the interaction between the electrodes and the molecule(s) in a molecular junction. This means, the current–voltage characteristics of molecular electronic devices are mainly dominated by the alignment of the molecular energy levels relative to the Fermi level of the left and right electrode, and, furthermore, by the electronic coupling of the docking groups with the conducting states of the electrodes.

The overall current (cf. Equation (18) in Chapter 2.3.1) through the molecular junction is dependent on the transmission function, $T(E)$. On the basis of a single level model, the zero bias transmission function can be described by a single Lorentzian using the Breit-Wigner formula as: [227, 233, 239]

$$T(E) = \frac{4\Gamma_L\Gamma_R}{(E - [\epsilon_0 - \eta eV])^2 + (\Gamma_L + \Gamma_R)^2}, \tag{40}$$

where $\Gamma_{L,R}$ denotes the scattering rates, which describes the coupling strength of the molecule to the left and right electrodes, respectively, i. e., the broadening of the transport level by using the full width at half-maximum. ϵ_0 denotes the position of the transmission channel of the electric current, i. e., the center of the Lorentzian. The voltage division factor η depends on the applied voltage, yielding asymmetric current-voltage characteristics, and vanishes for a zero bias transmission model. Bâldea derived that $\eta = 0$ can be used safely for symmetric cases, i. e., if $V_{t+} = -V_{t-}$.[227, 240] Furthermore, if the Fermi-Dirac occupation of the density of states (DOS) at the electrodes is replaced by a delta function, i. e., treating the system at 0 K, an analytical equation can finally be given for the conductance of a molecular junction as: [223]

$$G = 4NG_0\Gamma_L\Gamma_R \left(\frac{1/2+\alpha}{[\epsilon_0 + (1/2+\alpha)eV]^2 + (\Gamma_L+\Gamma_R)^2} + \frac{1/2-\alpha}{[\epsilon_0 - (1/2-\alpha)eV]^2 + (\Gamma_L+\Gamma_R)^2} \right) \tag{41}$$

where N denotes the number of molecules conducting in parallel, G_0 is the quantum of conductance, i. e., $G_0 = 2e^2/h$, and ϵ_0 refers to the transmission level, i. e., the center of the Lorentzian peak of the transmission function. Γ_L and Γ_R denotes the coupling strength to the left and right electrodes, respectively, i. e., the width of the Lorentzian-peak, which represents the level broadening. $\alpha = \pm 1/2$ is an asymmetry factor which describes the relative position of the molecular level to the left and right electrode, respectively, with $\alpha = 0$ denoting the symmetric case.

As was shown in this chapter, there have been several models proposed for interpreting transition voltage spectroscopy (TVS). What is yet to be accomplished is formulating a simple model for molecular junctions in analogy to classical device models by utilizing the transition voltage which can be readily accessed via TVS. Right now, the interpretation of TVS within a single Lorentzian model is the most promising approach. What is undisputed, though, is the mathematical formalism for calculating the transition voltage V_t from a given current-voltage characteristic.

6.1.2 *Transition voltage*

The value of the transition voltage, V_t, acquired from a F-N-plot, is simply defined as the minimum of the so-called L_2-function [223]

$$L_2 = ln \left| \frac{I}{V^2} \right| . \tag{42}$$

Identical to this is the following relation: [223]

$$\left. \frac{dI}{dV} \frac{V}{I} \right|_{V_t} \overset{!}{=} 2 , \tag{43}$$

where the value 2 reflects the power of V^2 in Equation (42). Mathematically speaking, the transition voltage, V_t, denotes the bias where the current-voltage curve changes from subquadratic to superquadratic.[222, 235, 241] This means, V_t represents a measure of the non-linearity of the conductance with respect to the applied voltage.[241–243]

In the framework of a single Lorentzian model the transition voltage can be derived[223] using Equation (41) and Equation (43):

$$V_t = \frac{\epsilon_0}{-2\alpha \pm \sqrt{\alpha^2 + 3/4}} \overset{\alpha=0}{\Longrightarrow} \pm \frac{2}{\sqrt{3}} \epsilon_0 \,, \tag{44}$$

where ϵ_0 denotes the energy level of the transmission channel and the asymmetry factor $\alpha = 0$ for the symmetric case (cf. Chapter 6.1.1).

This means, the transition voltage can be extracted from current-voltage data and relates the minimum of a F-N-plot to the energetic position of the main transport level of a molecular junction as described in Equation (44). Furthermore, there exists a mathematical rigorous definition of how to determine the frontier molecular orbital acting as the main transport level according to the single level model when doing density functional theory (DFT)-based simulations. Additionally, quantum-mechanical simulations enable us to acquire the transmission curve of an accurately defined junction, and, consequently, be able to investigate the impact of different transmission curves. This allows us to assess how the detailed geometry of a junction impacts the form of the transmission curve with all of its features. Furthermore, the form of the transmission function of a given junction - whether it consists of clearly defined peaks or strongly broadened features - can be related to the measured transition voltage. We specifically focused our investigation on the applicability of the aforementioned single level model with respect to collective electrostatic effects and how these influence the transition voltage acquired utilizing the current-voltage data. For this, the theoretically calculated molecular level, which acts as the main transport channel, ϵ_0, will be compared to the energy level, ϵ_t, acquired utilizing the transition voltage, V_t, employing the relation

$$\epsilon_t = \frac{\sqrt{3}}{2} e V_t \,, \tag{45}$$

where V_t denotes the minimum of the F-N-plot of the current-voltage data.

As it turned out, even though mathematically rather simple and straightforward, using this approach is not possible in all investigated cases, because the transition voltage cannot be extracted for all systems investigated. Namely, when there is no transition from a subquadratic to a superquadratic regime [223] in the current-voltage data, i. e., when there is no (local) minimum in the F-N-plot. Therefore, we investigated different approaches how to acquire the transition voltage from the current-voltage characteristic even in such cases.

The current-voltage characteristics utilized were theoretically modeled instead of experimentally measured, which ensures a detailed and accurate description of the actually investigated molecular junction. Additionally, the transmission curve is readily available when doing such simulations and contributes to a deeper understanding of the current-voltage characteristics. This is justified, as it has been shown that quantum-mechanical simulations reproduce the experimental measurements of current-voltage data quite well.[236, 244] Extracting the energy level, ϵ_0, of the main transport orbital from the DFT-calculations is done by utilizing the projected density of states (PDOS) of each system investigated.

In passing we note that in our study we investigated solely symmetrical junctions and hysteresis effects are not considered. Therefore, we present only the *positive* part of the current-voltage characteristics, as extending the current-voltage curve to cover negative voltages would just mirror the shown data. Additionally, all transport data were calculated based on the zero bias transmission functions.

6.2 INVESTIGATED SYSTEMS

For the analysis of the transition voltage, previously calculated systems by a coworker of mine, Veronika Obersteiner, were used. The molecular junctions investigated are comprised of tourwire-based molecules [245], i. e., 1,2-bis(2-phyenylethynyl)benzene, attached to gold electrodes via different docking groups. The chemical structure of the systems deliberately selected for a more detailed investigation are shown in Figure 15 (right part) along with their transmission functions (left part). Depending on the docking group these have either electron donating or electron accepting properties. Furthermore, as can be seen in the left part of Figure 15, the systems produce vastly different transmission curves, ranging from small, well resolved peaks to smeared out, broad features. The docking group has also an influence on the bond dipole, and, consequently, the position of the electronic levels. A more extended description of the different systems is given by Obersteiner *et al.* in the following papers, where the junctions have been investigated in more detail: [119, 246, 247].

In the following we will first discuss the transition voltage with a focus on a prototypical molecular junction, namely one comprised of a pyridine-linked tourwire-based molecule, to be precise, of 4-[2-[4-(2-pyridin-4-ylethynyl)phenyl]ethynyl]-pyridine, called tourpyridine in the course of this work. The chemical structure is drawn in Figure 16. For the investigation, the so-called *low-conductance* mode of the pyridine-linked junctions was used (in contrast to the *high conductance* mode with additional gold adatoms right at the docking group).[247–249] This choice allows for a detailed investigation, because due to the rather weak coupling between the electrodes and the low-conductance mode pyridines, several transport channels are well resolved. Due to the fact that the transport channels responsible for charge transport can be shifted by collective electrostatic effects, they can also fundamentally change the current-voltage characteristic of a molecular junction. This can happen for a junction comprised of the same molecule, whether one deals with an actual single molecule junction or an extended junction, consisting of as less as nine molecules. Furthermore, these collective effects depend on the coverage of the molecules a molecular junction is comprised of, i. e., the density of the (polar) entities (cf. Chapter 3). Investigating the influence of collective electrostatic

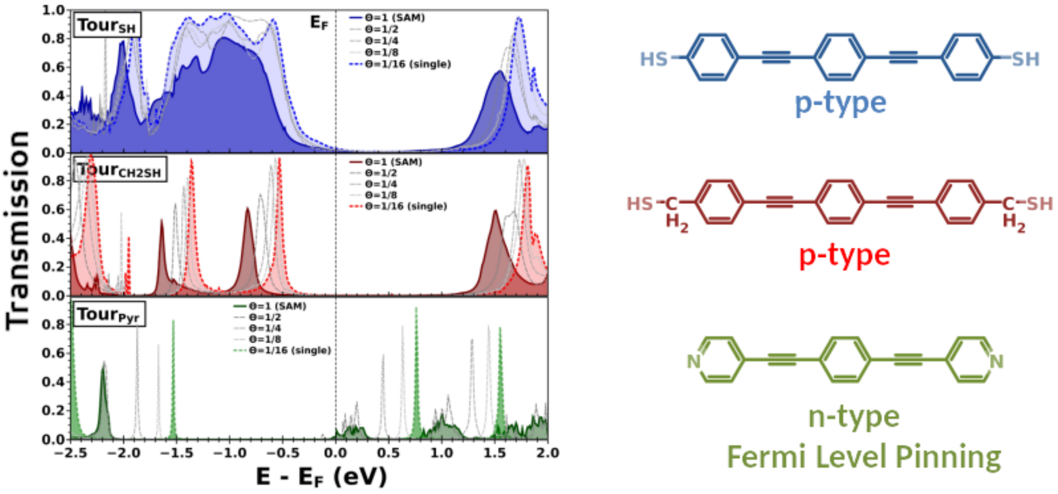

Figure 15: Left side: Transmission of the different systems for different coverages, the solid area showing the SAM and the shaded area the single molecule transmission. Right side: chemical formula, indicating whether n- or p-type transmission occurs. For the case of the tourpyridin junction Fermi level pinning occurs at a coverage of 50%. Figure modified with permission from [247]

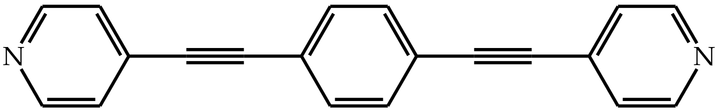

Figure 16: Chemical structure of 4-[2-[4-(2-pyridin-4-ylethynyl)phenyl]ethynyl]pyridine, also known as 1,4-bis(4-pyridylethynyl)benzene. This is a pyridine-linked tourwire-based molecule and will be called tourpyridine throughout this work.

effects can be done in two different ways, namely, first by diluting the density of the molecules a junction is comprised of evenly (see Chapter 6.3). Second, by analyzing molecular junctions consisting of differently sized clusters of molecules (see Chapter 6.4). Therefore, in the following chapters we will discuss the impact of collective electrostatic effects by investigating single molecule junctions, as well as molecular junctions comprised of differently sized clusters and junctions consisting of molecules with varying coverages up to a full monolayer. A sketch of the different situation is given in Figure 17, where in part (a) the unit cell of a single molecule junction (saturated) and a full coverage monolayer (decreased saturation) is shown. In Figure 17(b) the unit cell of a molecular junction consisting of a cluster of sixteen molecules is shown.

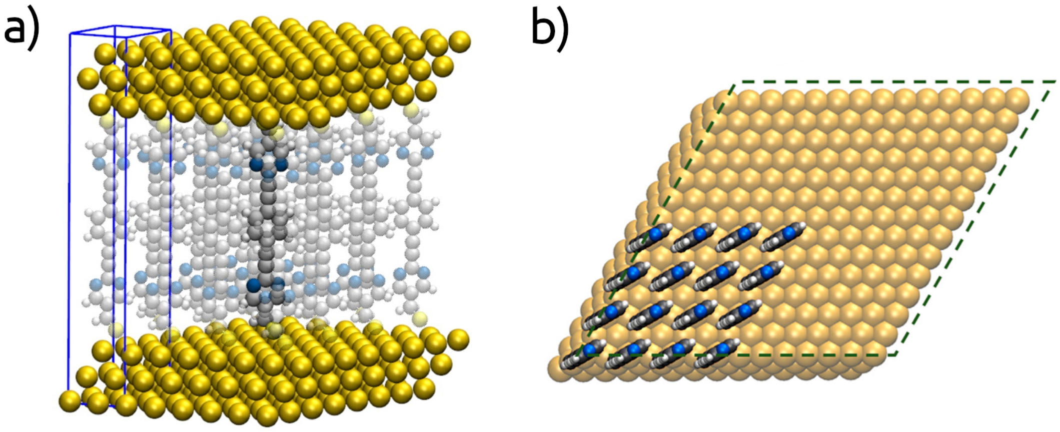

Figure 17: (a) Sketch of the semi-infinite system for a single molecule and full coverage (decreased saturation) junction consisting of a tourwire-based molecule. The unit cell for the full coverage system is indicated by the blue box, and for the single molecule case the whole unit cell is displayed, containing only the saturated molecule. Modified with permission from ref [246]. Copyright 2014 American Chemical Society. (b) Unit cell in top view of a molecular junction consisting of a cluster of 16 molecules. The top electrode is omitted in this sketch. Figure modified with permission from ref [250].

6.3 IMPACT OF DIFFERENT COVERAGES

First, molecular junctions with a layer of evenly diluted molecules will be investigated, i. e., the distance between each molecule increases by decreasing coverage. In Figure 18 the transmission function is plotted alongside the projected density of states (PDOS) for different coverages of a pyridine junction. As can be seen, both curves exhibit peaks in accordance to each other, namely features in the transmission function occur at the peak-position of the PDOS of the pyridine molecule. Consequently, as can be seen, the transmission channel depends on the position of, in this case, the LUMO level. This is because the LUMO-derived band is closer to the Fermi level compared to the HOMO-derived band and, therefore, acts as the main transport level. When the coverage increases, the transmission channel shifts in line with the PDOS peaks closer to the Fermi level. This is due to the increasing influence of collective electrostatic effects on the energy level alignment with increasing coverage. In case of the low coverage systems, i. e., for the single molecule junction up to a coverage of 25%, there is a pronounced transmission peak right at the position of the LUMO. This changes fundamentally when the coverage of the molecules is increased to 50% and beyond, i. e., also for the case of the full coverage junction. In these cases there is not a distinguished peak in the transmission curve, but a broader, somewhat smeared out transmission channel. This change of the transmission function is due to the transport channel being shifted to the Fermi level. When comparing the curves of the full coverage to the 50% coverage system, it can be seen that the levels shift not any further with increased coverage. This is due to Fermi level pinning. This means that there states are right at the Fermi level of the system in the DOS, i. e., the Fermi level cuts through the peak of the HOMO- or LUMO-derived band of the combined molecule-electrode system. A result of Fermi level pinning is that the energy levels are not shifted any further beyond the Fermi edge of the metal, e. g., by collective electrostatic effects, but pin at this position. This is due to charges rearranging in such a way that an thermodynamic equilibrium condition at the interface between the metal and the organic semiconductor (OSC) of the molecular junction is established. In Figure 19 a typical current-voltage characteristic is shown for the tourpyridine molecular junctions for varying coverages. It can be seen that the behavior of each curve differs when going from the single molecule junction, represented here by a molecular coverage of 6.25%, up to the full coverage junction. The change is also here particularly drastic if the coverage is increased from 25% to 50%. To investigate the onset of

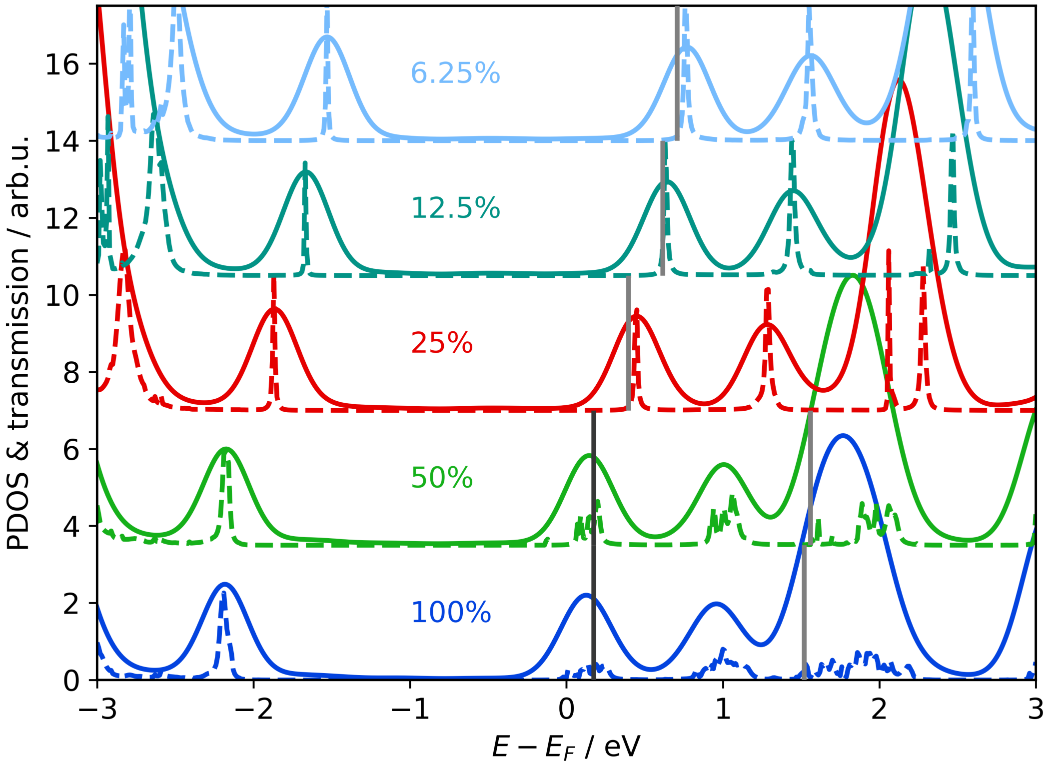

Figure 18: PDOS (solid lines) and transmission (dashed lines) for different coverages of tourpyridine utilized as the molecular junction. There is a broadened transmission peak due to pinning observable for the 50% and full coverage system. The gray lines indicate the transmission voltage. The rightmost, light gray lines at 1.5 eV for the 50% and full coverage system indicate the transition voltage as calculated from the maximum of the F-N-plot, whereas the left, dark gray line in the two spectra indicates the one calculated using another method, which is explained in more detail in the main text in Chapter 6.3)

.

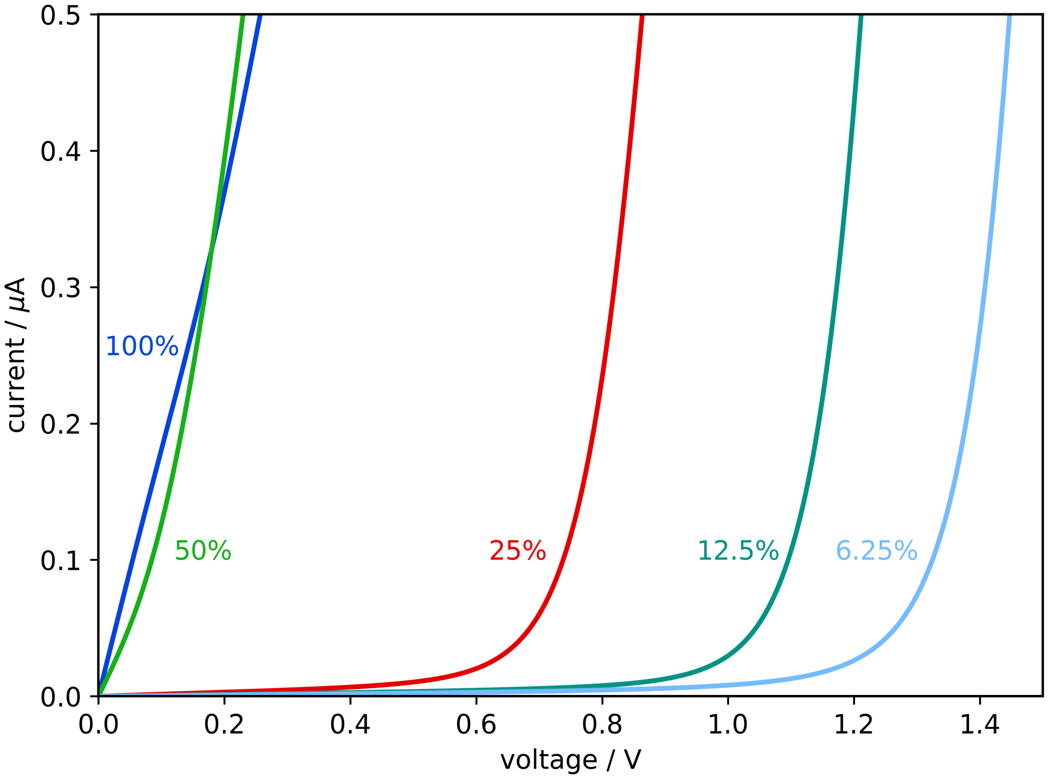

Figure 19: Current-voltage characteristics for different coverages of tourpyridine. The curves behave fundamentally different for the low, i. e., up to a coverage of 25%, and the high coverage systems (50% and full coverage).

the current-voltage curve in greater detail, in Figure 20 the same data is plotted only up to 0.1 V, where the different behavior of the current with respect to the voltage is even more obvious. This change of the nature of the current-voltage data is due to collective electrostatic effects, which start to influence the transport characteristic when the density of the molecules is increased. This means, that the transmission function is shifted until it pins at the Fermi level. In the case of the investigated molecular junction comprised of tourpyridine, they impact the overall current-voltage curve starting at a coverage of 50%. Consequently, the transition voltage is also influenced by these collective electrostatic effects. The transport level calculated (dark gray lines) using Equation (45) is also shown in Figure 18. The transition voltage, V_t, acquired from the current-voltage data shown in Figure 19 was used. For the case of the molecular junctions consisting of a layer of molecules with a coverage of up to 25%, the transition voltage is obtained in a straightforward manner from the F-N-plot shown in Figure 21. For the half and full coverage system this approach leads to an obviously wrong result (light gray lines at around 1.5 eV) as the correct position would be quite close to the Fermi level as indicated by the dark gray lines plotted there. Furthermore, as a consequence of a different way of acquiring the transition voltage for these cases, as might be noticeable in Figure 18, the calculated transmission channel is slightly shifted to the right of the peak maximum of the PDOS for the full coverage system and

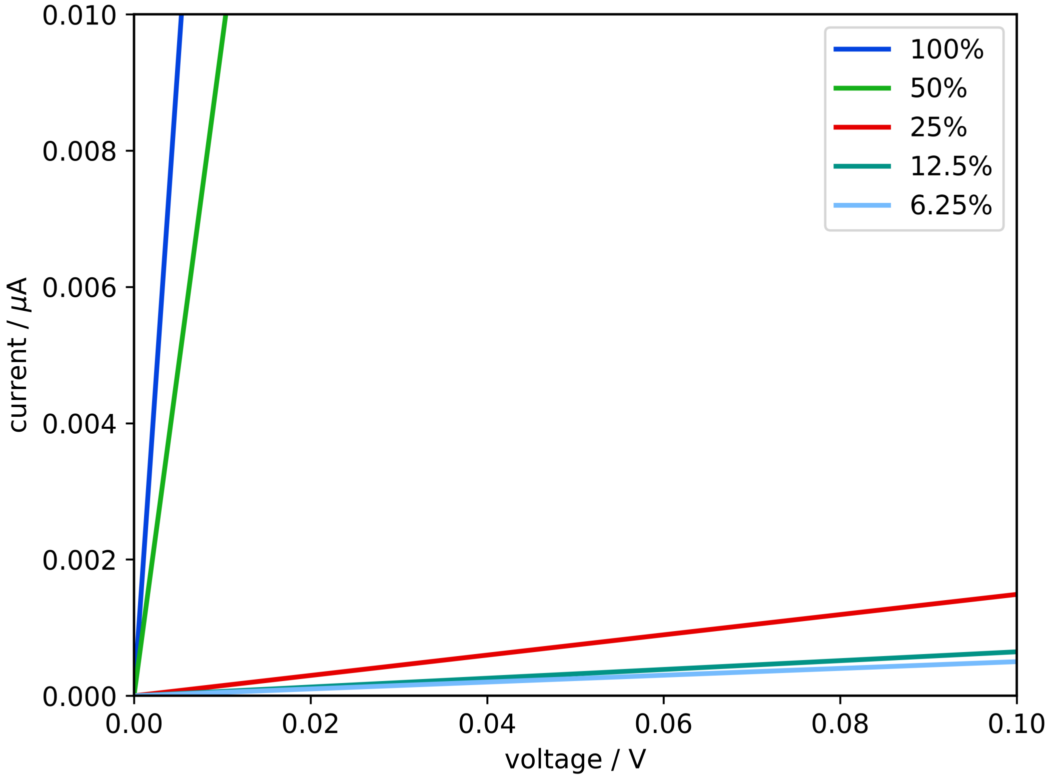

Figure 20: Zoomed into the data of the current-voltage characteristics displayed in Figure 19. There is a fundamentally different behavior of the I-V-curve of the full and low coverage systems due to collective electrostatic effects.

the 50% coverage, in contrast to the lower coverage situations. In the following paragraphs it is discussed in great detail, what options are available to acquire the transition voltage, V_t, if there is no clear minimum in a F-N-plot.

Acquiring the transition voltage

In Figure 21 the Fowler–Nordheim (F-N)-plot is shown for different coverages of a molecular junction comprised of tourpyridine molecules between two gold electrodes. For the molecular junction consisting of molecules packed with a coverage of up to 25% of the full coverage, a distinctive minimum can be clearly seen. Furthermore, the minimum shifts to higher voltages with increasing coverage, as would be expected from the behavior of the PDOS already shown in Figure 18. For the junction with a molecular coverage of 50% and the full coverage system, when using the minimum in the standard F-N-plot at 1.75 V and 1.8 V for the monolayer and the 50% coverage, respectively, the calculated transition voltage would be unreasonable (cf. Figure 18, indicated by the light gray lines at around 1.5 eV in the curve of the full coverage and 50% coverage system). Therefore, a slightly altered plot was created, which plots V^2/I over the voltage for an easier identification of the extremum with respect to the voltage. This way of plotting the current-voltage data and taking the maximum was introduced as an

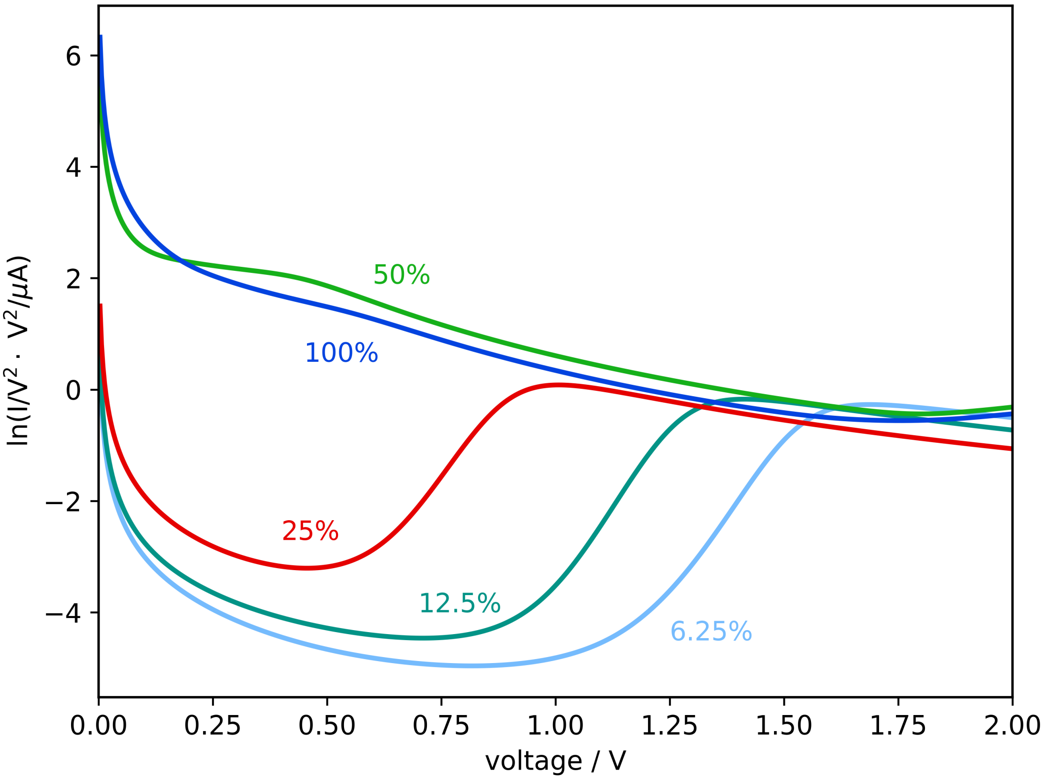

Figure 21: A F-N plot, where the logarithm of I/V^2 over the voltage is plotted for different coverages of the tourpyridine system. This means, the minimum of the curve needs to be considered for calculating the transition voltage.

alternative to the transition voltage by Bâldea *et al.*, calling it the *critical* voltage, for investigating a law of corresponding states.[251] There, instead of the logarithm of I/V^2 over the voltage, V^2/I over the voltage is plotted and the maximum instead of the minimum is considered. In passing it is noted that the same extremum is found whether plotting the voltage on the x-axis or 1/V as Beebe *et al.* did in their seminal work.[61, 62, 251] Unfortunately, as can be seen in Figure 21 and Figure 23 there is no clear extremum in the full and half coverage systems at a reasonable voltage, but a change of the gradient can be seen quite clearly in the latter representation. Therefore, in the case of a coverage of 50%, the point before the first change of curvature of the curve in Figure 23 can be taken instead of the global maximum. For the full coverage system there can be the gradient of the curve taken into account, but again there is no distinctive extremum at this point, which could be taken as the transition voltage for subsequently calculating the transmission level. These alternatives are not rigidly defined ways to acquire the transition voltage, but rather educated guesses based more on the known PDOS and less on a clearly defined extremum in the current-voltage data. The lack of an extremum is due to a fundamentally different current-voltage characteristics (cf. Figure 19) introduced by a pinning situation because of collective electrostatic effects. The reason for this can also be seen in the PDOS, and, consequently, in the transmission function, which is shown in Figure 18. There it can be seen that the

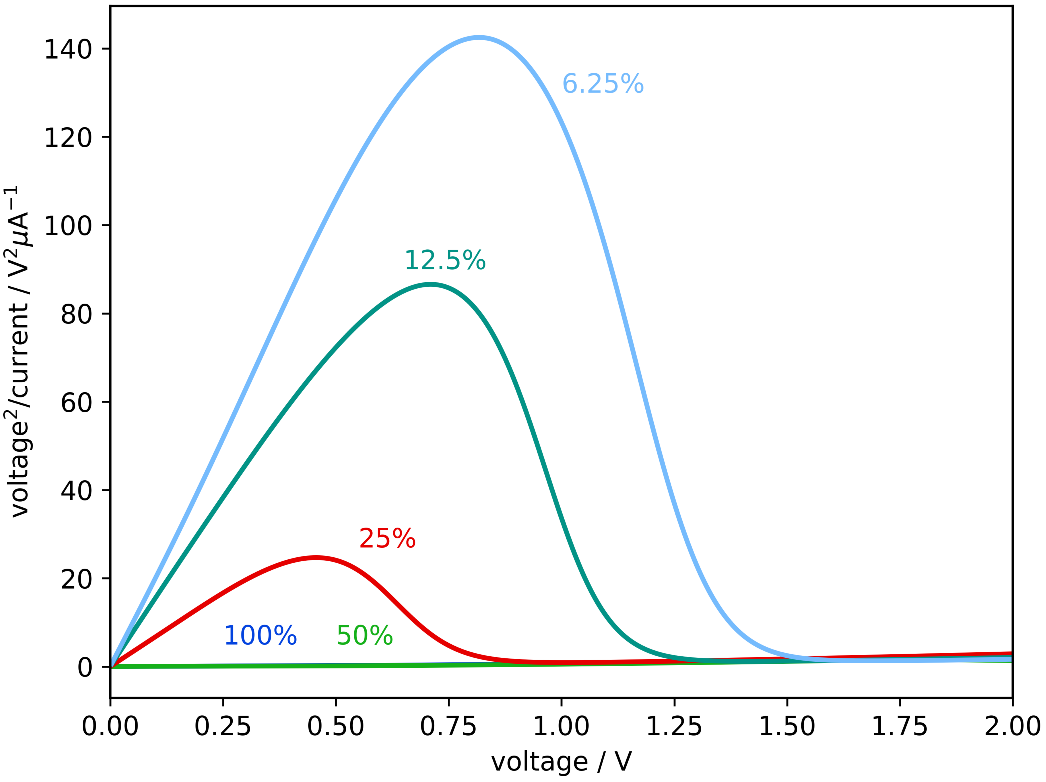

Figure 22: Representation of the current-voltage data inspired by a F-N plot of the tour-pyridine systems showing V^2/I over the voltage for different coverages. In the single molecule junction and the low coverage cases there is a clear maximum visible, which is not the case for the half and full coverage systems.

transmission function exhibits a distinctively different curve for a coverage of 50% and the monolayer junction. This is due to the transmission curve being shifted by collective electrostatic effects up to the Fermi level, where resonant tunneling is occurring.

The fact that the transmission channel is readily available and the impact of collective electrostatic effects can be investigated using quantum-mechanical simulations is an advantage of doing theoretical calculations. This value can than be compared to the transition voltage calculated utilizing the current-voltage characteristic in form of a F-N-plot, to check the applicability of this approach for different molecular junctions. The results for the different coverages, as well as for all the other systems investigated, are summarized in Table 1 in Chapter 6.6.

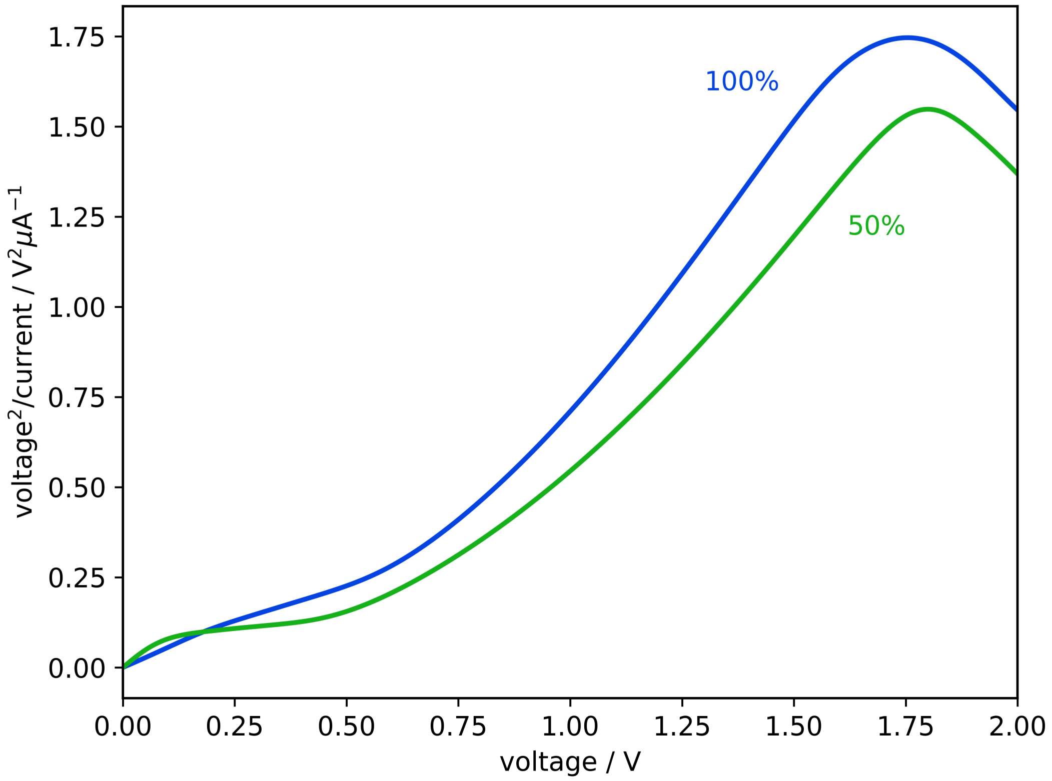

Figure 23: Data of the full monolayer and the 50% coverage molecular junction as shown in Figure 22, but zoomed in on the y-axis to more easily identify the maxima.

6.4 DIFFERENTLY SIZED CLUSTERS OF TOURPYRIDIN

Another interesting aspect is how the size of the molecular clusters a junction is comprised of relates to collective electrostatic effects. This is especially important, because depending on the experimental situation it is not always possible to generate a molecular junction, which consists of a clearly defined number of molecules, or a single molecule for that matter. Therefore, it was investigated how the transition voltage relates to differently sized clusters of molecules in the molecular junction.

What is noteworthy is the fact that the main transport peak in the transmission function splits up depending on the number of molecules in the junction as can be seen in Figure 24. This is because of electrostatic edge effects caused by changes in the electrostatic energy due to different dipole fields and quantum-mechanical coupling between the molecules themselves and the docking groups, depending on the size of the cluster. These effects are explained in more detail in a paper by Obersteiner *et al.* [250], where also the local density of states calculated for the specific energy window of each peak in the transmission function is investigated. This allows to correlate the differently shifted peaks in the transmission function to specific molecules in the junction, i. e., to the molecule in the center, the molecules at the edge and those at the corners of a cluster. Even though this is in contrast to a

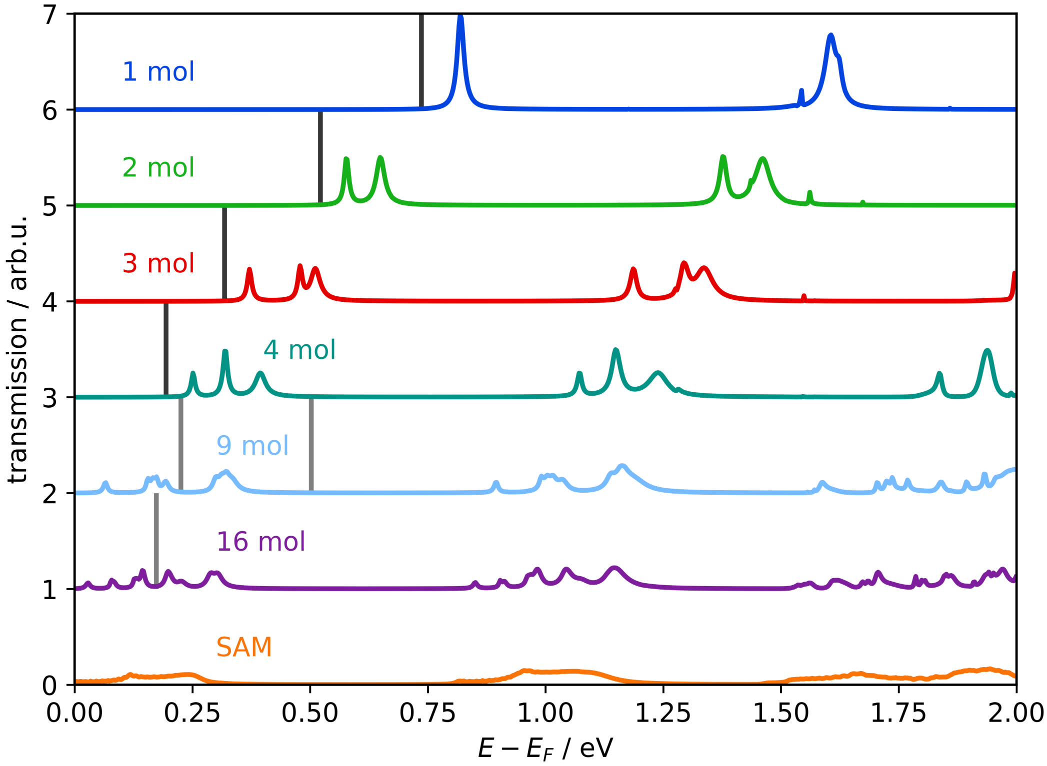

Figure 24: Transmission function of a molecular junction comprised of differently sized clusters of tourpyridine in a waterfall like plot. At the top, the transmission for the single molecule junction is plotted (blue). The second curve depicts the transmission of a junction comprised of two molecules (green), the third curve of three molecules (red). The teal curve shows the transmission for a junction made out of four molecules, the light blue one depicts the curve for a cluster of nine molecules. The two curves at the bottom are the transmission for a junction consisting of a cluster of 16 molecules (violet) and a full monolayer (orange). The dark gray bars indicate the calculated transition voltage, the light gray bars depict the transition voltage calculated without utilizing a maximum.

single level being solely responsible for the transport, the calculated transmission voltage seems reasonable. As can be concluded from Figure 24, the transition voltage calculated from the current-voltage data depends on the position of the transmission channel closest to the Fermi level. Therefore, the model also holds for a molecular junction comprised of a cluster of molecules, each providing its own transport channel. This can be explained by the transition voltage indicating the point where the tail of the first peak in the transmission function comes into resonance with the Fermi level.

Furthermore, the transmission function is shifted closer to the Fermi level until it pins due to collective electrostatic effects which increase according to the increasing cluster size. When plotting the transmission function in a waterfall like manner for differently sized clusters, starting from a single molecule junction (blue) at the top to a full coverage SAM at the bottom (orange), as is shown in Figure 24, it can be seen that up to a cluster size of nine molecules in the junction, the transmission peaks are shifted towards the Fermi level. Additionally, for the molecular junction consisting of clusters of up to four molecules the transport level calculated utilizing the transition voltage (vide infra) acquired from the current-voltage data is indicated by a dark gray bar. In these cases the transmission level could be calculated using a clearly defined transition voltage, whereas the light gray lines indicate an energy level calculated using an *educated guess* for the transition voltage. As can be seen, the position of the main transmission channel calculated utilizing the transition voltage, indicated by the gray line, shifts correspondingly to the transmission function. This implies that the current-voltage characteristic depends fundamentally on the transmission channel closest to the Fermi level. Furthermore, in the case of the molecular junction consisting of nine or more tourpyridine molecules, Fermi level pinning arises.

In Figure 25 a F-N-like plot is shown for different cluster sizes, starting from a single molecule junction up to a junction consisting of 16 molecules, and, for comparison, a full coverage junction as already discussed above. As one can see,

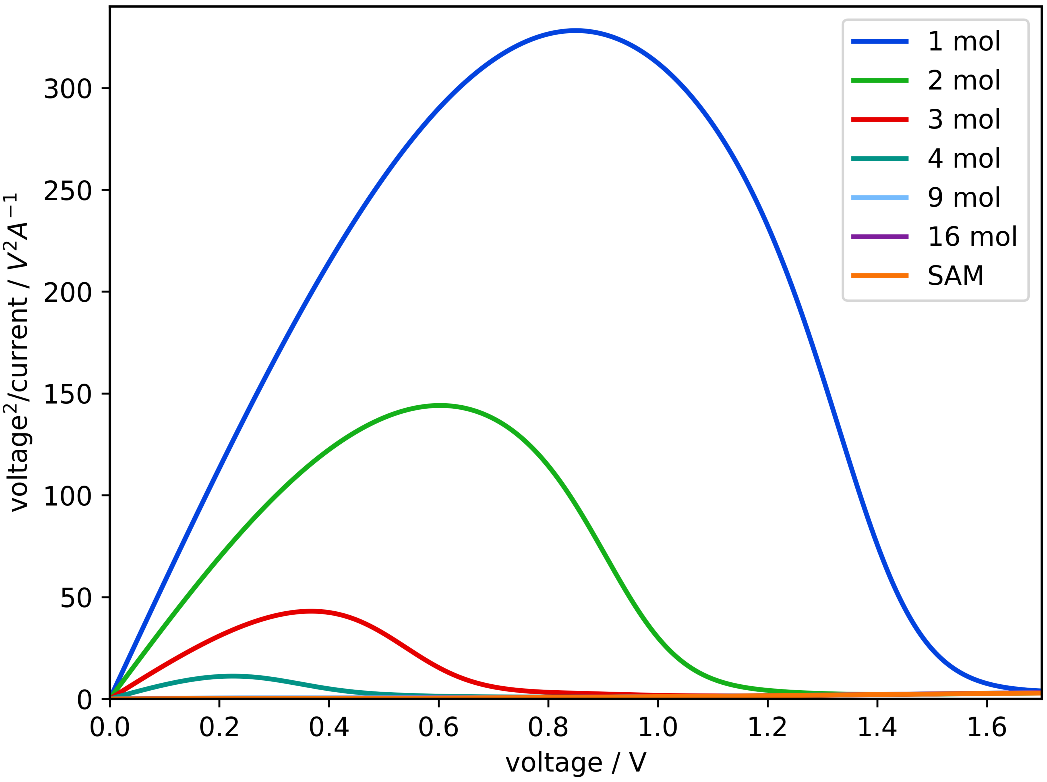

Figure 25: Representation inspired by a F-N plot showing the current-voltage data as V^2/I over the voltage of molecular junctions consisting of a single molecule junction of tourpyridine between two gold electrodes, and clusters of up to sixteen molecules per junction. Additionally, a full coverage junction is shown for comparison.

there is a maximum in the case of a single molecule junction (blue line) up to the system with a junction consisting of four molecules (teal line). For these cases the transition voltage can be utilized to calculate the main transport level in a straightforward manner by facilitating Equation (45). For a cluster of up to nine molecules, it is still possible to choose at least a local maximum (the first at 0.26 V and the second at 0.58 V, resulting in a transition voltage of 0.23 eV and 0.50 eV, respectively), as can be seen in Figure 26, where the same data is plotted, but zoomed in to lower voltages. When comparing the transition voltage acquired utilizing the local extrema to the transmission data shown in Figure 24 it seems that the local maximum at the lower voltage corresponds to the trend of the transport level shifting towards the Fermi level due to collective electrostatic effects coming into effect. The second local maximum of the transmission function of the system with nine molecules shown in Figure 26, on contrary, gives rise to a transport level between two peaks in the transmission function as can be seen in Figure 24. Investigating a molecular junction consisting of 16 or more molecules once again one would need to resort to some kind of infliction point. When investigating the junction comprised of 16 molecules, the calculated transition voltage based on an *educated guess* from Figure 26 is at approximately the same position, hinting again at Fermi level pinning for this molecular junction. In passing it is noted that the global minimum of the F-N-plot is at 1.91 V and 1.85 V for the molecular junction comprised out of nine and 16 molecules, respectively. This means, the acquired transition voltage is not based on a clearly defined extremum. This is similar to the case of the tourpyridine system with a coverage of more than 50% discussed above in Chapter 6.3.

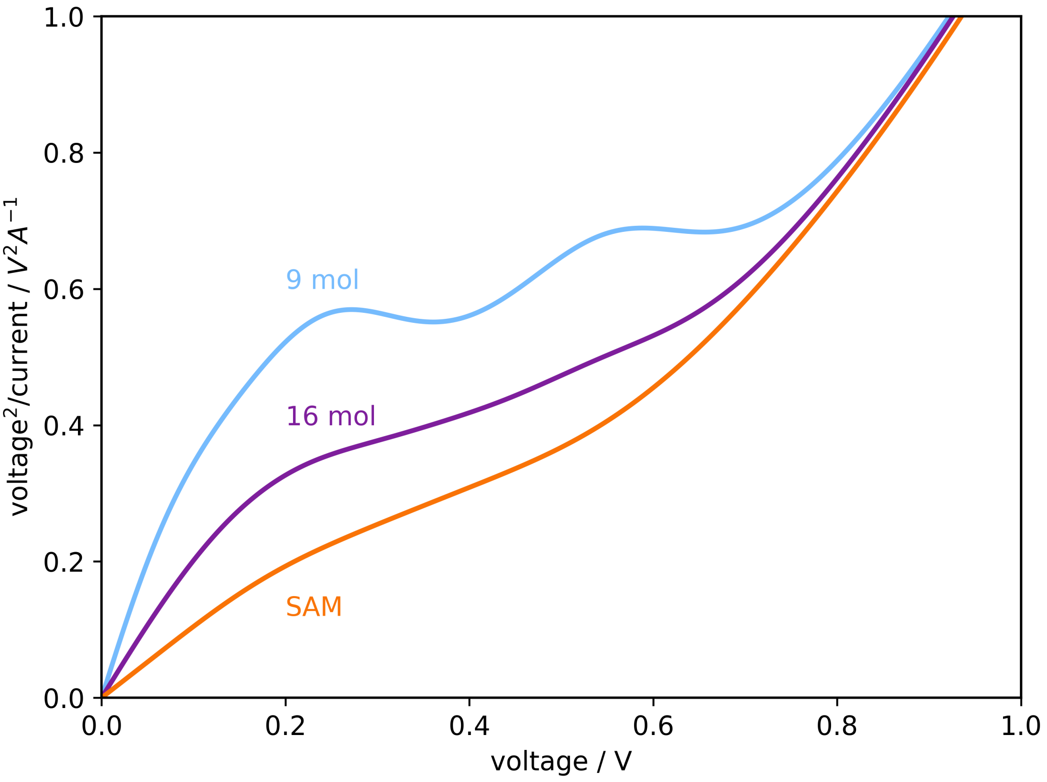

Figure 26: Zoomed in F-N-like plot of the current-voltage data for differently sized clusters of the tourpyridine molecular junction, showing that there is no global maximum in these cases. In the case of the junction consisting out of nine molecules, there are two local maxima identifiable.

6.5 IMPACT OF DOCKING GROUPS

Finally, another aspect worth investigating is the influence of the coupling strength of molecules to the electrodes due to different docking groups. For this, two molecular junctions made out of identical molecules only differing by the docking group attached to the gold electrodes are compared. To be precise, a tourwire-based [245] molecule attached via a thiolate (SH) and a methylthiolate (CH_2SH) docking group is used and the impact of the docking chemistry on the transition voltage is investigated.

The two molecular junctions differ only by an added methyl spacer in the CH_2SH-system compared to the SH-system, which leads to a different coupling strength at the molecule/electrode interface. In the case of CH_2SH acting as a docking group, the transmission shows a distinctive, narrow peak (dotted lines) right next to the HOMO level as can be seen in Figure 27, where the transmission function and the DOS is plotted. If compared to the system with a SH docking group (shown in Figure 28), one can see a quite different DOS (solid line) and, in accordance with it, a broad peak in the transmission function (dotted lines). This is due to the different coupling strength of each docking group to the electrodes. For the weakly coupled CH_2SH-system, when increasing the coverage from the single molecule

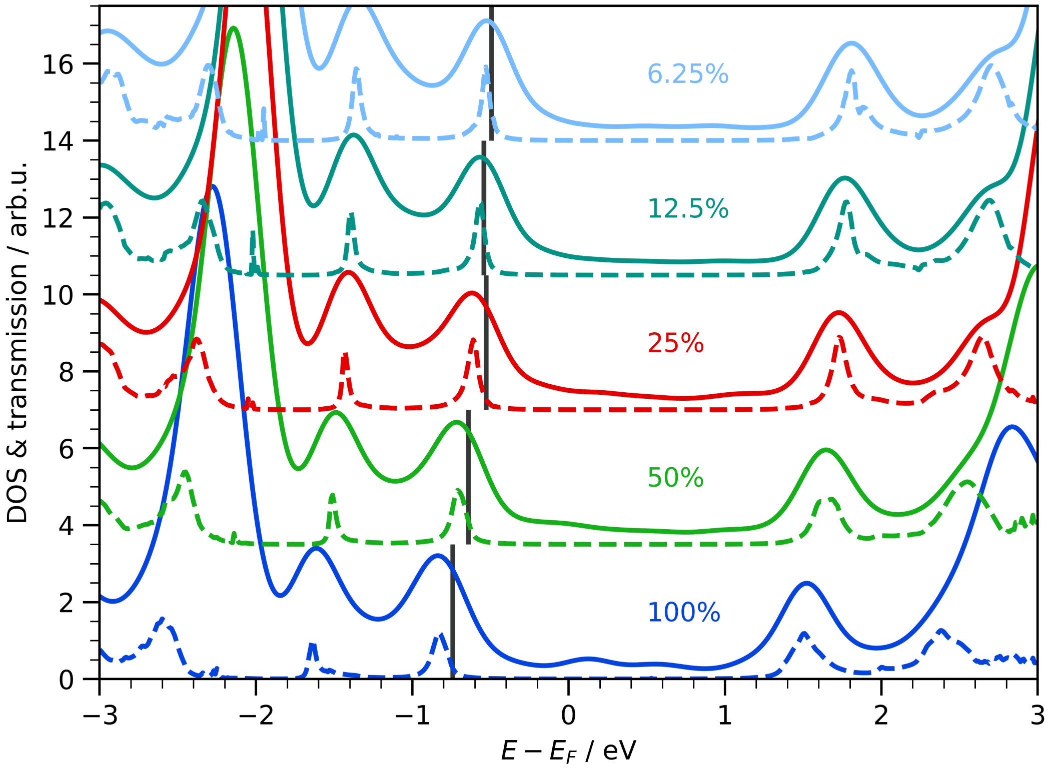

Figure 27: PDOS (solid lines) and transmission (dashed lines) of a tourwire-based molecule with a CH_2SH docking group for different coverages as depicted. The gray lines indicate the calculated transition voltage, which is almost the same for the low coverage systems, but shifted in the case of the half coverage (green) and full monolayer (blue) system.

system to the full monolayer coverage, it can be seen that the DOS changes only slightly for a coverage of up to 25% and more significantly for a coverage of 50% and the full coverage system. The reason for this are collective electrostatic effects, which come into play when increasing the density of dipoles, and have a noticeable impact starting at a coverage of 50%. This manifests in a shift of the electronic levels, and, consequently, affects the transition voltage, which can be seen in the case of CH_2SH quite clearly, where it is shifted accordingly to the transport level of the DOS. This is also seen when looking at Figure 29, where the maximum of the curve for a coverage of up to 25% is almost the same, and is shifted in the case of the full and half coverage systems.

When investigating the DOS of the SH system, which is shown in Figure 28 again with the transmission function, it can be seen that its features are quite broadened. This is an indication of a strong hybridization of the molecular levels with states in the electrode and results in a strong coupling. The position of the transport level is, as a result, not that obvious, and, consequently, the behavior of the transition voltage is much more inconclusive due to the smeared out nature of the curve. When looking at the F-N-like plot, which is shown in Figure 30, an interesting aspect can be seen. Namely that the current for the system with a coverage of 25%

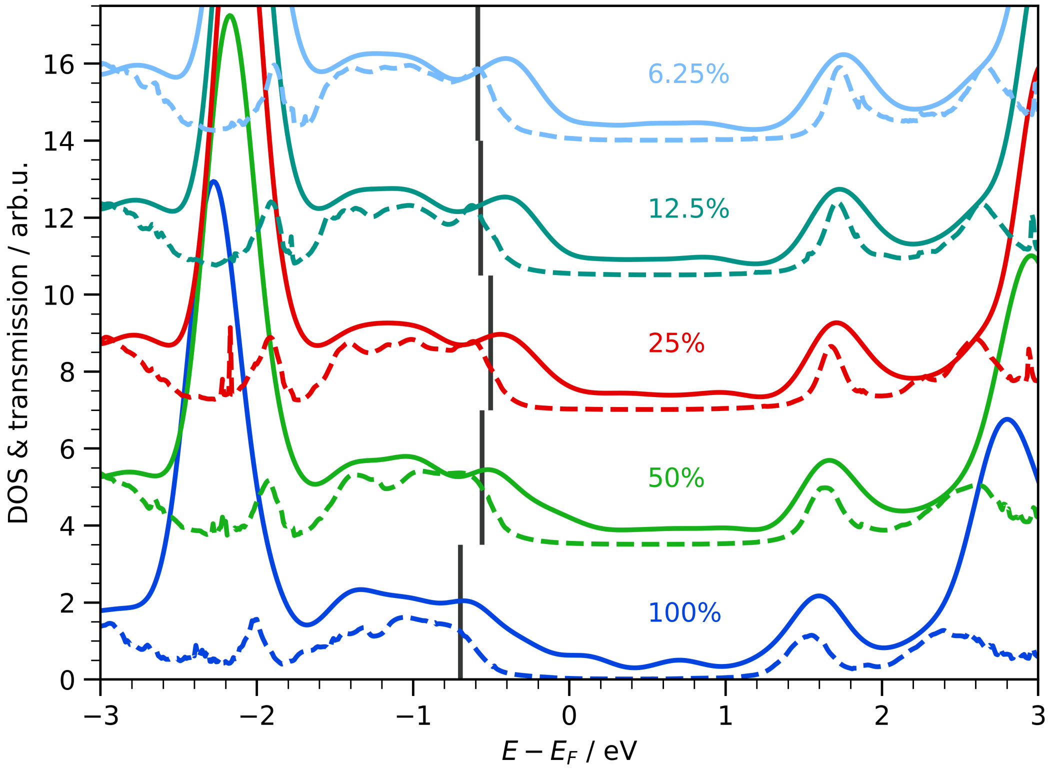

Figure 28: PDOS (solid lines) and transmission function (dashed lines) of a tourwire-based molecule with a SH docking group for different coverages as indicated. The gray lines depict the calculated transition voltage, which is clearly shifted to more negative values for the full monolayer system (blue) and slightly shifted closer to the Fermi level for a coverage of 25%. For the other systems it is practically the same.

is exceptionally high compared to the other coverages. This effect is most probably due to the exact situation at the molecule-electrode interface and results in a transition voltage which is slightly shifted with respect to the other low coverage systems, as can be seen in Figure 28. In passing it is noted that only the calculated current of the system with a coverage of 25% exhibits this behavior. As is shown in the supporting information of ref. [247], the evolution of the bond dipole is in accordance with the packing density. Furthermore, the transmission function is only different for the full coverage system and practically the same for all the other coverages. This results in the transition voltage of the full coverage system being clearly shifted to more negative values compared to the other coverages, whereas the transition voltage for the system with a coverage of 25% is slightly shifted closer to the Fermi level.

What can generally be said is that the onset of the first peak, even if the transmission function exhibits quite broadened features, determines the current-voltage characteristic and, consequently, also the transition voltage. This is in accordance with the situation in molecular clusters (cf. Chapter 6.4), where the first peak in the transmission function gives rise to the position of the transition voltage.

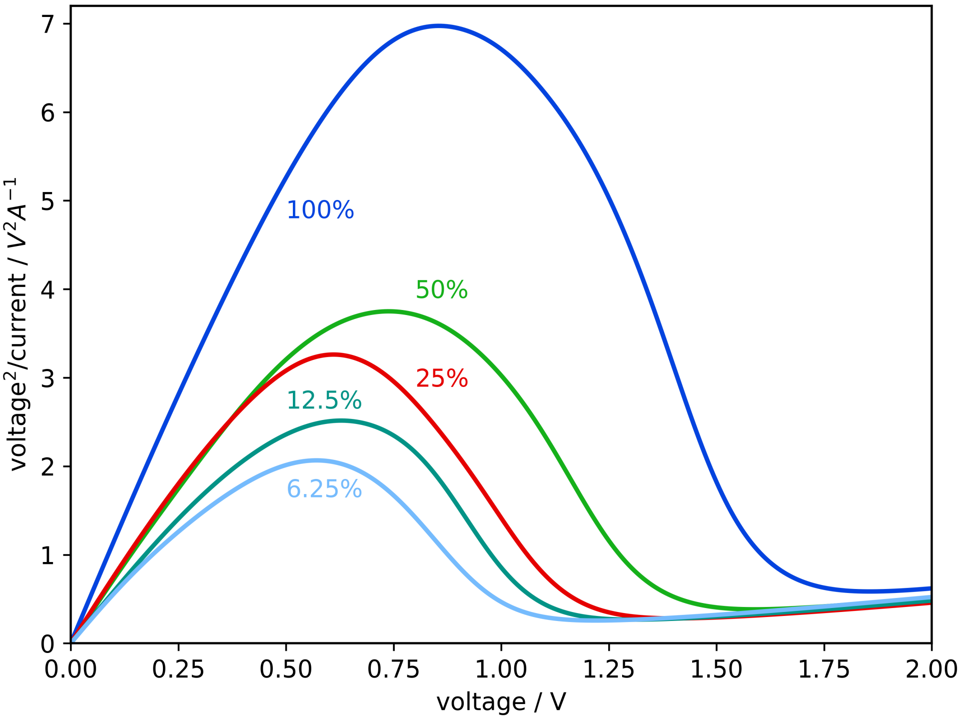

Figure 29: Plot inspired by a F-N plot of the system with CH_2SH as a docking group for different coverages. The maximum is slightly shifted for the half and full coverage system and almost the same for the low coverage systems.

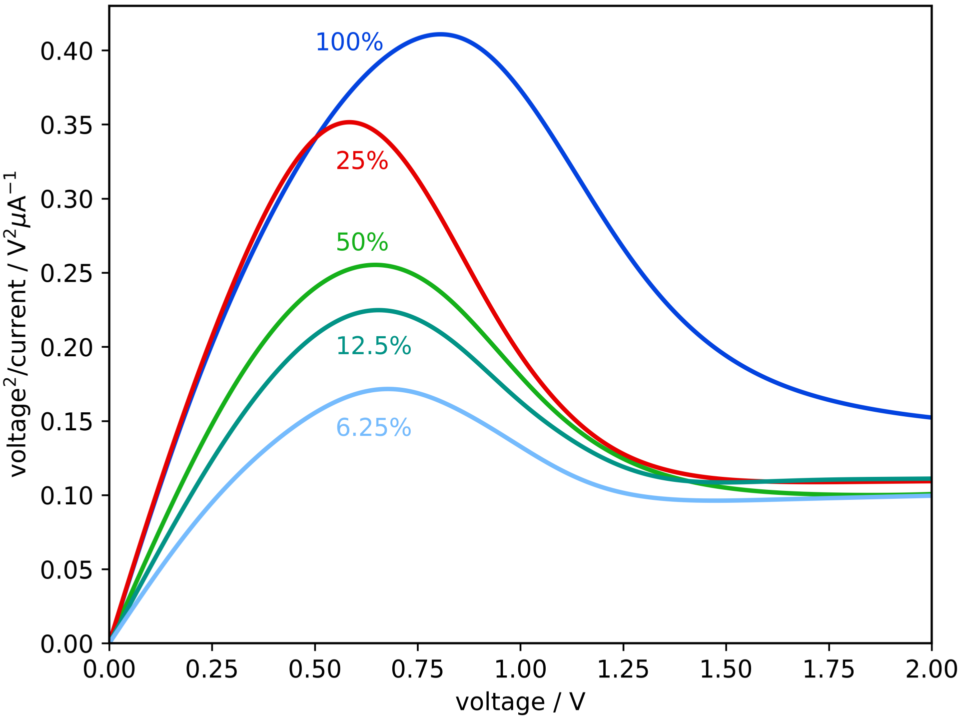

Figure 30: Plot inspired by a F-N plot of the system with SH as a docking group for different coverages. The maximum for the full coverage system is clearly shifted, for all other coverages it is almost the same. The curve of the 25% coverage exhibits a different behavior compared to the other systems.

6.6 SUMMARY AND CONCLUSIONS

As the transition voltage can be calculated utilizing the current-voltage characteristic on the one hand, and by using the DOS on the other hand, it is possible to investigate the applicability of a model based on a single transport level. This can be done, because in the single level model, the molecular orbital closest to the Fermi-level is deemed primarily responsible for charge transport.

The transition voltage for the tourpyridine system, the tourwire-based [245] molecular junction with sulfur as a docking group, and the system with a methylen-spacer as a docking group, all for different coverages calculated using the current-voltage data from a Fowler–Nordheim (F-N)-plot (V_t^{FN}) and V_t^{DOS}, calculated using Equation (45), can be found in Table 1.

Table 1: Transition voltage (V_t^{FN}) calculated from a F-N plot using current-voltage data calculated with a NEGF-approach (cf. Chapter 2.3.2) and utilizing the single-level model (SLM)-Equation (45) to calculate the energy level of the transmitting orbital (V_t^{DOS}). For comparison the energy level (ϵ_{DoS}) closest to the Fermi level from a DFT-calculation and the calculated transition voltage (V_t^{DoS}) using the aforementioned SLM-equation is also given here. In the last column the difference of the two energy levels is given. All energy levels are aligned to their respective Fermi energy and for the calculated $\epsilon_t(V_t^{FN})$ the sign is added accordingly to whether the HOMO or LUMO acts as the transmission orbital.

docking group	V_t^{FN} / V	$\epsilon_t(V_t^{FN})$ / eV	ϵ_{DoS} / eV	V_t^{DoS} / V	$\Delta\epsilon$ / eV
pyridine 100.0%	1.75	1.52	0.12	0.14	-1.40
Pyr 50.0%	1.80	1.56	0.14	0.17	-1.41
Pyr 25.0%	0.46	0.40	0.45	0.52	0.05
Pyr 12.5%	0.71	0.61	0.64	0.74	0.03
Pyr 6.5%	0.82	0.71	0.77	0.89	0.06
SH 100.0%	0.81	-0.70	-0.74	0.86	-0.05
SH 25.0%	0.58	-0.51	-0.50	0.57	0.01
SH 12.5%	0.66	-0.57	-0.45	0.52	0.12
SH 6.5%	0.68	-0.59	-0.45	0.51	0.14
CH_2SH 100.0%	0.86	-0.74	-0.83	0.96	-0.09
CH_2SH 50.0%	0.74	-0.64	-0.71	0.82	-0.07
CH_2SH 25.0%	0.61	-0.53	-0.61	0.70	-0.08
CH_2SH 12.5%	0.63	-0.54	-0.56	0.65	-0.02
CH_2SH 6.5%	0.57	-0.49	-0.52	0.61	-0.03

As one can see, the energy difference of the transmission levels taken from the DFT-calculation and acquired from the transition voltage is for all but the pinned cases negligible, but quite substantial for the latter ones. This means, the transport level can be determined correctly for most, but not all investigated systems by utilizing the transition voltage acquired by means of a F-N-plot utilizing the current-voltage data. This approach fails if the current-voltage data plotted in a F-N-like representation does not yield an extremum, which would allow to uniquely determine the transition voltage.

To sum up, the applicability of a single level model to calculate the transport level utilizing the current-voltage characteristic as explained in Chapter 6.1.2 was investigated for molecular junctions comprised of a single molecule and assemblies of molecules up to a full coverage monolayer. We focused the investigation on how collective electrostatic effects affect the transition voltage. When the coverage of molecules in the junction or the size of the molecular cluster comprising the junction exceeds a certain size, collective electrostatic effects come into play and impact the energetic level alignment at the interface. Consequently, the transmission function of the molecular junction is also affected. As a result, collective electrostatic effects influence the transition voltage, as it depends on the transmission channel closest to the Fermi level. Generally speaking, if there is no Fermi-level pinning, the transition voltage can be used to determine the main transport level on the basis of a single level model with an acceptable accuracy.

6.7 OUTLOOK ON UTILIZING COLLECTIVE ELECTROSTATIC EFFECTS IN MOLECULAR ELECTRONICS

It has been shown that electrostatic design utilizing collective electrostatic effects can be used to control ballistic transport through SAMs.[246, 247] A next step could be systematically varying the spatial localization of the transmissive channels and their energetic positions by inserting a varying number of polar functional elements into the backbones of SAM-forming molecules. Consequently, the position and magnitude of the resulting shifts of the peaks in the DOS can be studied. These originate from collective electrostatic effects caused by ordered assemblies of dipolar molecules. Such effects can also be used to tune the electronic properties of SAMs to create novel quantum structures like monolayer quantum cascades and monolayer quantum wells. To investigate these collective electrostatic effects the systems shown in Figure 31 can be utilized. As can be seen in the potential plot of these systems in Figure 32, the different polar elements indeed have an impact on the potential, which can be used to visualize the collective electrostatic effects. As one can see the potential is not changed in the case of the non-polar benzene bridged alkine dithiols, but is effected noticeably in the cases of the polar embedded groups. What can be seen is that the potential between the polar groups is shifted relative to its surroundings, but in different directions depending on the embedded polar group. In the recently released version[133] of SIESTA the TranSIESTA

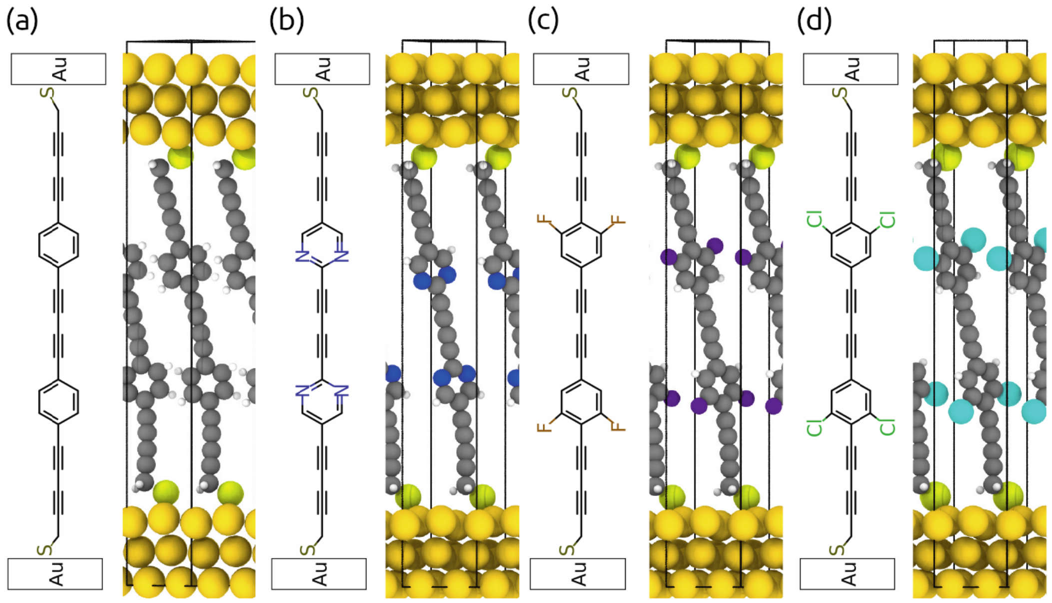

Figure 31: Lewis formula and 3D view of (a) benzene bridged alkine dithiols, (b) pyrimidin bridged alkine dithiols, (c) dichlorinated benzene bridged alkine dithiols and (d) difluorinated benzene bridged alkine dithiols, each sandwiched between two Au(111)-electrodes.

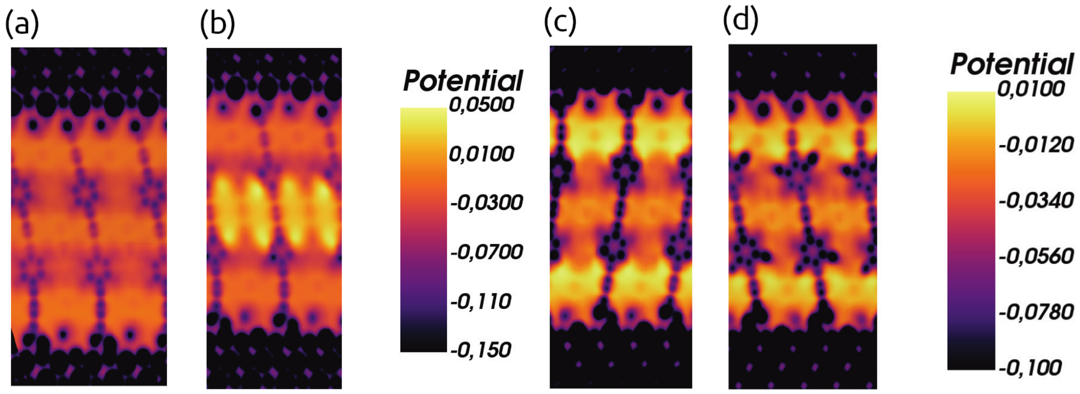

Figure 32: Potential of (a) benzene bridged alkine dithiols, (b) pyrimidin bridged alkine dithiols, (c) dichlorinated benzene bridged alkine dithiols and (d) difluorinated benzene bridged alkine dithiols. There is a shift of the potential depending on the atoms substituted in the benzene rings.

module is capable to calculate finite voltage bias transport simulations (in contrast to the results presented in this thesis in Chapter 6, which presents results acquired utilizing a zero-bias transmission curve.

7

CONCLUDING REMARKS

The research compiled in this thesis contributes to a better understanding of hybrid inorganic-organic systems and collective electrostatic effects arising at interfaces of such systems. As one of the most important experimental techniques to investigate these systems is X-ray photoelectron spectroscopy, the main focus of this work was dedicated to advance the quantum-mechanical modeling thereof. Furthermore, the impact of collective effects has been investigated within the realms of molecular electronics, where they also influence key properties of molecular junctions like the transition voltage. As is shown throughout this work, these aforementioned collective electrostatic effects, also known as cooperative effects, play an important role in vastly different fields. Generally speaking, the moment an ordered, densely packed layer of polar entities is present in a system, the energetic landscape is influenced by it. As a consequence, great care has to be taken not only when interpreting experimental measurements, but also when doing quantum-mechanical simulations of such systems, regardless of whether in the realms of surface science or molecular electronics.

In the first part, this thesis discusses the simulation of core-level spectra of organic self-assembled monolayers on metal substrates. In Chapter 4 the calculation of core-level excitations in the framework of density functional theory is investigated in great detail. There are two fundamentally different approaches, the so-called initial and final state approach. The initial state approach maps the Kohn-Sham eigenvalue of an orbital to the core electron's energy, and, therefore, takes the orbital energies of the undisturbed system, i. e., no change in the potential is allowed after removing the core electron, neglecting any relaxation effects. The final state approach, in contrast, actually removes the electron and allows the remaining core orbitals to relax. This means, quantum mechanical relaxation and screening effects are taken into account. This a priori more sophisticated approach is indeed necessary for describing surface core level shifts, but great care has to be taken when periodic boundary conditions are applied. Especially if investigating surfaces consisting of organic adsorbates physisorbed on metal substrates utilizing the widely used repeated slab approach, spurious electrostatic effects occur. These artificial effects are discussed in great detail in a paper we published in 2020.[59] We showed that due to the core hole being generated in every unit cell, an artificial dipole layer is formed by the applied periodic boundary conditions. These dipoles are created by the positive hole due to the removed charge from the core level in the organic adsorbate when applying the Slater-Janak transition state theory and a consequently induced negative screening charge in the metal. When using rather small unit cells - normally the smallest commensurate unit cell is used when utilizing the repeated slab approach because of the computational resources needed - the calculated core level energies are shifted by more than 1 eV in our model test system due to these spurious effects. These spurious collective electrostatic effects increase even further when the distance between the metal substrate and the excited core hole is increased, e. g., when the adsorption distance of a physisorbed molecule is rather large or in the case of self-assembled monolayers comprised of long, upright standing adsorbate molecules. To assess whether these artificial effects play a significant role, a change of the work function in the final state calculation compared to a standard density functional theory-calculation is a strong indicator. This allows to predict problems without tediously converging unit cell sizes, which might even be virtually impossible due to computational limitations. For such cases we present a simple electrostatic correction scheme on the basis of a reasonable guess for the effective dielectric constant of the interface. Another option would be to apply an a posteriori mirror charge screening correction to an initial state calculation, which we showed to provide quite reasonable results for organic adsorbates on metal substrates.[153]

Utilizing the initial state approach with an a posteriori electrostatic correction scheme, the applicability of X-ray photoelectron spectroscopy-measurements for determining the interface dipole is investigated in another paper we published in 2020 [60] and is included in this thesis in Chapter 5. There, we showed with the help of theoretical simulations that it is indeed possible to measure how the interface dipole of an organic self-assembled monolayer on a metal substrate influences an X-ray photoelectron spectrum. This bonding dipole is highly depending on the docking chemistry at the interface and the packing density of the molecules. The impact of collective electrostatic effects occurring at densely packed monolayers was investigated by varying the coverage, and, consequently, the dipole density at the interface. We find that in densely packed monolayers the shift of the X-ray photoelectron spectrum is a direct measure for the interface dipole. If the coverage is decreased, the core level energies measured via X-ray photoelectron spectroscopy are still determined by the local electrostatic environment, but are not directly correlated to the overall interface dipole any more. The same arguments hold for the work function change induced by the adsorption of the monolayer. Furthermore, the direct relation of the work function change and the shift of the X-ray photoelectron spectrum holds only if there are no polar groups in the molecule forming the self-assembled monolayer. This is most evident in the case of the work function being modified further by polar tail groups without shifting the core levels electrostatically. This is due to polar groups again inducing a densely packed layer of dipoles. Consequently, a jump in the potential energy surface is introduced by collective electrostatic effects stemming from this dipolar layer. This means that the whole energy landscape above of the polar tail groups is shifted with respect to below of them.

Finally, the role of collective electrostatic effects in molecular electronics with a special consideration of their influence on the transition voltage is investigated in Chapter 6. As the ballistic transport through molecular junction can be described by a single level model, a shift of the main transport level also results in a shift of the transition voltage. Furthermore, the applicability of determining the transport level by means of acquiring the transition voltage from a current-voltage characteristic is investigated. We show that for molecular junctions the approach to calculate the main transport level by utilizing a Fowler–Nordheim plot to get the transition voltage works reliably as long as there is no Fermi level pinning. This Fermi level pinning can occur due to collective electrostatic effects coming into play at a certain coverage, i. e., dipole density. This means that the energy levels are shifted by collective electrostatic effects up to the Fermi level, but not any further. In the case of tourpyridine, Fermi level pinning is exhibited beginning at a molecular coverage of 50%. Furthermore, we investigated the applicability of the aforementioned procedure to junctions consisting of differently sized clusters of molecules, starting from a single molecule junction. For tourpyridine clusters of more than nine molecules the current-voltage characteristics are influenced by collective electrostatic effects in such a way that it was not possible anymore to unambiguously acquire the transition voltage from a Fowler–Nordheim-like plot. Additionally, the impact of the coupling strength was investigated for a tourwire-based molecule attached to the metal electrodes via a SH and CH_2SH docking group, respectively. For these systems, even though they produce vastly different transport functions due to the different docking chemistry, it was possible to acquire the transition voltage for all coverages of the investigated molecular junctions, ranging from a single molecule junction up to the full coverage system.

A brief outlook of how collective electrostatic effects could be utilized in molecular electronics to create novel quantum structures like monolayer quantum cascades or monolayer quantum wells is given in Chapter 6.7.

To sum up, the influence of collective electrostatic effects at metal-organic interfaces was investigated using quantum-mechanical ab-initio simulations. The first part of this thesis deals with the simulation of X-ray photoelectron spectra and presents the advantages and disadvantages of different density functional theory-based approaches. The second part demonstrates the applicability of X-ray photoelectron spectroscopy measurements to determine the interface dipole of metal-organic interfaces. The third part investigates the scope of acquiring the transition voltage of molecular junctions based on a single level model.

Part III

Appendix

ACRONYMS

DFT density functional theory

C10EC5 pentyl-11-sulfanylundecanoate

FHI-AIMS Fritz Haber Institute ab initio molecular simulations package

DOS density of states

F-N Fowler–Nordheim

GGA general gradient approximation

HF Hartree-Fock

HIOS hybrid inorganic-organic system

HOMO highest occupied molecular orbital

HRXPS high resolution X-ray photoelectron spectroscopy

KS Kohn-Sham

LDA local density approximation

LUMO lowest unoccupied molecular orbital

NEGF non-equilibrium Greens function technique

OLED organic light emitting diode

OSC organic semiconductor

PBE Perdew-Burke-Ernzerhof

PBC periodic boundary conditions

PDOS projected density of states

RSA repeated slab approach

SAM self-assembled monolayer

SIESTA The Spanish Initiative for Electronic Simulations with Thousands of Atoms

SCF self-consistent field

SLM single-level model

TRANSIESTA TranSIESTA

TVS transition voltage spectroscopy

VASP Vienna Ab initio Simulation Package

VDW van der Waals

VSC-3 Vienna Scientific Cluster 3

XC exchange-correlation

XP X-ray photoelectron

XPS X-ray photoelectron spectroscopy

BIBLIOGRAPHY

1. M. O. Steinhauser. *Computational Multiscale Modeling of Fluids and Solids* doi:`10.1007/978-3-662-53224-9` (Springer Berlin Heidelberg, Berlin, Heidelberg, 2017) (see p. 3).
2. F. Jensen. *Introduction to Computational Chemistry* 2nd ed. 599 pp. (John Wiley & Sons, Chichester, England ; Hoboken, NJ, 2007) (see pp. 3, 5).
3. A. Jain, G. Hautier, C. J. Moore, S. Ping Ong, C. C. Fischer, T. Mueller, K. A. Persson, and G. Ceder. "A High-Throughput Infrastructure for Density Functional Theory Calculations". *Computational Materials Science* **50,** 2295. doi:`10.1016/j.commatsci.2011.02.023` (2011) (see p. 3).
4. G. Hautier, A. Jain, and S. P. Ong. "From the Computer to the Laboratory: Materials Discovery and Design Using First-Principles Calculations". *Journal of Materials Science* **47,** 7317. doi:`10.1007/s10853-012-6424-0` (2012) (see pp. 3, 6).
5. A. Jain, Y. Shin, and K. A. Persson. "Computational Predictions of Energy Materials Using Density Functional Theory". *Nature Reviews Materials* **1,** 1. doi:`10.1038/natrevmats.2015.4` (1 2016) (see pp. 3, 6).
6. N. Koch. "Organic Electronic Devices and Their Functional Interfaces". *ChemPhysChem* **8,** 1438. doi:`10.1002/cphc.200700177` (2007) (see p. 3).
7. C. Liu, Y. Xu, and Y.-Y. Noh. "Contact Engineering in Organic Field-Effect Transistors". *Materials Today* **18,** 79. doi:`10.1016/j.mattod.2014.08.037` (2015) (see p. 3).
8. X. Guo, Y. Xu, S. Ogier, T. N. Ng, M. Caironi, A. Perinot, L. Li, J. Zhao, W. Tang, R. A. Sporea, A. Nejim, J. Carrabina, P. Cain, and F. Yan. "Current Status and Opportunities of Organic Thin-Film Transistor Technologies". *IEEE Transactions on Electron Devices* **64,** 1906. doi:`10.1109/TED.2017.2677086` (2017) (see p. 3).
9. H. Matsui, Y. Takeda, and S. Tokito. "Flexible and Printed Organic Transistors: From Materials to Integrated Circuits". *Organic Electronics* **75,** 105432. doi:`10.1016/j.orgel.2019.105432` (2019) (see p. 3).
10. N. Thejo Kalyani and S. J. Dhoble. "Organic Light Emitting Diodes: Energy Saving Lighting Technology—A Review". *Renewable and Sustainable Energy Reviews* **16,** 2696. doi:`10.1016/j.rser.2012.02.021` (2012) (see p. 3).

11. A. Salehi, X. Fu, D.-H. Shin, and F. So. "Recent Advances in OLED Optical Design". *Advanced Functional Materials* **29,** 1808803. doi:`10.1002/adfm.201808803` (2019) (see p. 3).

12. M. Wright and A. Uddin. "Organic—Inorganic Hybrid Solar Cells: A Comparative Review". *Solar Energy Materials and Solar Cells* **107,** 87. doi:`10.1016/j.solmat.2012.07.006` (2012) (see p. 3).

13. D.-Y. Khang. "Recent Progress in Si-PEDOT:PSS Inorganic–Organic Hybrid Solar Cells". *Journal of Physics D: Applied Physics* **52,** 503002. doi:`10.1088/1361-6463/ab3f64` (2019) (see p. 3).

14. L. Kronik and N. Koch. "Electronic Properties of Organic-Based Interfaces". *MRS Bulletin* **35,** 417. doi:`10.1557/mrs2010.578` (2010) (see p. 3).

15. A. El-Sayed, P. Borghetti, E. Goiri, C. Rogero, L. Floreano, G. Lovat, D. J. Mowbray, J. L. Cabellos, Y. Wakayama, A. Rubio, J. E. Ortega, and D. G. de Oteyza. "Understanding Energy-Level Alignment in Donor–Acceptor/Metal Interfaces from Core-Level Shifts". *ACS Nano* **7,** 6914. doi:`10.1021/nn4020888` (2013) (see pp. 3, 34).

16. I. H. Campbell, S. Rubin, T. A. Zawodzinski, J. D. Kress, R. L. Martin, D. L. Smith, N. N. Barashkov, and J. P. Ferraris. "Controlling Schottky Energy Barriers in Organic Electronic Devices Using Self-Assembled Monolayers". *Physical Review B* **54,** R14321. doi:`10.1103/PhysRevB.54.R14321` (1996) (see p. 3).

17. I. H. Campbell, J. D. Kress, R. L. Martin, D. L. Smith, N. N. Barashkov, and J. P. Ferraris. "Controlling Charge Injection in Organic Electronic Devices Using Self-Assembled Monolayers". *Applied Physics Letters* **71,** 3528. doi:`10.1063/1.120381` (1997) (see p. 3).

18. R. W. Zehner, B. F. Parsons, R. P. Hsung, and L. R. Sita. "Tuning the Work Function of Gold with Self-Assembled Monolayers Derived from X-[C_6H_4-C⁝C-]$_n$ C_6H_4-SH (n = 0, 1, 2; X = H, F, CH_3, CF_3, and OCH_3)". *Langmuir* **15,** 1121. doi:`10.1021/la981114f` (1999) (see p. 3).

19. C. Ganzorig, K.-J. Kwak, K. Yagi, and M. Fujihira. "Fine Tuning Work Function of Indium Tin Oxide by Surface Molecular Design: Enhanced Hole Injection in Organic Electroluminescent Devices". *Applied Physics Letters* **79,** 272. doi:`10.1063/1.1384896` (2001) (see p. 3).

20. B. de Boer, A. Hadipour, M. M. Mandoc, T. van Woudenbergh, and P. W. M. Blom. "Tuning of Metal Work Functions with Self-Assembled Monolayers". *Advanced Materials* **17,** 621. doi:`10.1002/adma.200401216` (2005) (see p. 3).

21. H.-L. Yip, S. K. Hau, N. S. Baek, H. Ma, and A. K.-Y. Jen. "Polymer Solar Cells That Use Self-Assembled-Monolayer- Modified ZnO/Metals as Cathodes". *Advanced Materials* **20,** 2376. doi:`10.1002/adma.200703050` (2008) (see pp. 3, 4).

22. M. Malicki, Z. Guan, S. D. Ha, G. Heimel, S. Barlow, M. Rumi, A. Kahn, and S. R. Marder. "Preparation and Characterization of 4'-Donor Substituted Stilbene-4-Thiolate Monolayers and Their Influence on the Work Function of Gold". *Langmuir* **25,** 7967. doi:`10.1021/la9004104` (2009) (see p. 3).

23. X. Cheng, Y.-Y. Noh, J. Wang, M. Tello, J. Frisch, R.-P. Blum, A. Vollmer, J. P. Rabe, N. Koch, and H. Sirringhaus. "Controlling Electron and Hole Charge Injection in Ambipolar Organic Field-Effect Transistors by Self-Assembled Monolayers". *Advanced Functional Materials* **19,** 2407. doi:`10.1002/adfm.200900315` (2009) (see p. 3).

24. M. Kitamura, Y. Kuzumoto, W. Kang, S. Aomori, and Y. Arakawa. "High Conductance Bottom-Contact Pentacene Thin-Film Transistors with Gold-Nickel Adhesion Layers". *Applied Physics Letters* **97,** 033306. doi:`10.1063/1.3465735` (2010) (see p. 3).

25. C. Schmidt, A. Witt, and G. Witte. "Tailoring the Cu(100) Work Function by Substituted Benzenethiolate Self-Assembled Monolayers". *The Journal of Physical Chemistry A* **115,** 7234. doi:`10.1021/jp200328r` (2011) (see p. 3).

26. J. Kim, Y. S. Rim, Y. Liu, A. C. Serino, J. C. Thomas, H. Chen, Y. Yang, and P. S. Weiss. "Interface Control in Organic Electronics Using Mixed Monolayers of Carboranethiol Isomers". *Nano Letters* **14,** 2946. doi:`10.1021/nl501081q` (2014) (see pp. 3, 4).

27. P. Schulz, T. Schäfer, C. D. Zangmeister, C. Effertz, D. Meyer, D. Mokros, R. D. van Zee, R. Mazzarello, and M. Wuttig. "A New Route to Low Resistance Contacts for Performance-Enhanced Organic Electronic Devices". *Advanced Materials Interfaces* **1,** n/a. doi:`10.1002/admi.201300130` (2014) (see p. 3).

28. T. Abu-Husein, S. Schuster, D. A. Egger, M. Kind, T. Santowski, A. Wiesner, R. Chiechi, E. Zojer, A. Terfort, and M. Zharnikov. "The Effects of Embedded Dipoles in Aromatic Self-Assembled Monolayers". *Advanced Functional Materials* **25,** 3943. doi:`10.1002/adfm.201500899` (2015) (see pp. 3, 4, 32).

29. O. Fenwick, C. V. Dyck, K. Murugavel, D. Cornil, F. Reinders, S. Haar, M. Mayor, J. Cornil, and P. Samorì. "Modulating the Charge Injection in Organic Field-Effect Transistors: Fluorinated Oligophenyl Self-Assembled Monolayers for High Work Function Electrodes". *Journal of Materials Chemistry C* **3,** 3007. doi:`10.1039/C5TC00243E` (2015) (see p. 3).

30. S. Casalini, C. A. Bortolotti, F. Leonardi, and F. Biscarini. "Self-Assembled Monolayers in Organic Electronics". *Chemical Society Reviews* **46,** 40. doi:`10.1039/C6CS00509H` (2017) (see p. 3).

31. T. Mosciatti, P. Greco, T. Leydecker, M. Eredia, F. Biscarini, and P. Samorì. "Asymmetric Injection in Organic Transistors via Direct SAM Functionalization of Source and Drain Electrodes". *ACS Omega* **2,** 3502. doi:`10.1021/acsomega.7b00690` (2017) (see p. 3).

32. A. Petritz, M. Krammer, E. Sauter, M. Gärtner, G. Nascimbeni, B. Schrode, A. Fian, H. Gold, A. Cojocaru, E. Karner-Petritz, R. Resel, A. Terfort, E. Zojer, M. Zharnikov, K. Zojer, and B. Stadlober. "Embedded Dipole Self-Assembled Monolayers for Contact Resistance Tuning in p-Type and n-Type Organic Thin Film Transistors and Flexible Electronic Circuits". *Advanced Functional Materials* **28,** 1804462. doi:`10.1002/adfm.201804462` (2018) (see pp. 3, 4).

33. J. W. Borchert, B. Peng, F. Letzkus, J. N. Burghartz, P. K. L. Chan, K. Zojer, S. Ludwigs, and H. Klauk. "Small Contact Resistance and High-Frequency Operation of Flexible Low-Voltage Inverted Coplanar Organic Transistors". *Nature Communications* **10,** 1119. doi:`10.1038/s41467-019-09119-8` (1 2019) (see p. 3).

34. S. D. Evans, E. Urankar, A. Ulman, and N. Ferris. "Self-Assembled Monolayers of Alkanethiols Containing a Polar Aromatic Group: Effects of the Dipole Position on Molecular Packing, Orientation, and Surface Wetting Properties". *Journal of the American Chemical Society* **113,** 4121. doi:`10.1021/ja00011a010` (1991) (see p. 4).

35. G. Heimel, L. Romaner, J.-L. Brédas, and E. Zojer. "Interface Energetics and Level Alignment at Covalent Metal-Molecule Junctions: π-Conjugated Thiols on Gold". *Physical Review Letters* **96,** 196806. doi:`10.1103/PhysRevLett.96.196806` (2006) (see pp. 4, 20, 24, 32).

36. Q. Sun and A. Selloni. "Interface and Molecular Electronic Structure vs Tunneling Characteristics of CH3- and CF3-Terminated Thiol Monolayers on Au(111)". *The Journal of Physical Chemistry A* **110,** 11396. doi:`10.1021/jp064905w` (2006) (see p. 4).

37. Q. Sun and A. Selloni. "Interface and Molecular Electronic Structure vs Tunneling Characteristics of CH3- and CF3-Terminated Thiol Monolayers on Au(111)". *The Journal of Physical Chemistry A* **111,** 10170. doi:`10.1021/jp0766297` (2007) (see p. 4).

38. O. M. Cabarcos, A. Shaporenko, T. Weidner, S. Uppili, L. S. Dake, M. Zharnikov, and D. L. Allara. "Physical and Electronic Structure Effects of Embedded Dipoles in Self-Assembled Monolayers: Characterization of Mid-Chain Ester Functionalized Alkanethiols on Au{111}". *The Journal of Physical Chemistry C* **112,** 10842. doi:`10.1021/jp801618j` (2008) (see pp. 4, 92).

39. K. Demirkan, A. Mathew, C. Weiland, Y. Yao, A. M. Rawlett, J. M. Tour, and R. L. Opila. "Energy Level Alignment at Organic Semiconductor/Metal Interfaces: Effect of Polar Self-Assembled Monolayers at the Interface". *The Journal of Chemical Physics* **128,** 074705. doi:`10.1063/1.2832306` (2008) (see p. 4).

40. G. Heimel, L. Romaner, E. Zojer, and J.-L. Brédas. "The Interface Energetics of Self-Assembled Monolayers on Metals". *Accounts of Chemical Research* **41,** 721. doi:`10.1021/ar700284q` (2008) (see pp. 4, 19, 24).

41. M. Halik and A. Hirsch. "The Potential of Molecular Self-Assembled Monolayers in Organic Electronic Devices". *Advanced Materials* **23,** 2689. doi:`10.1002/adma.201100337` (2011) (see p. 4).

42. L. Lindell, C. Vahlberg, K. Uvdal, M. Fahlman, and S. Braun. "Self-Assembled Monolayer Engineered Interfaces: Energy Level Alignment Tuning through Chain Length and End-Group Polarity". *Journal of Electron Spectroscopy and Related Phenomena. Organic Electronics* **204,** 140. doi:`10.1016/j.elspec.2015.04.006` (2015) (see p. 4).

43. M. Gärtner, E. Sauter, G. Nascimbeni, A. Wiesner, M. Kind, P. Werner, C. Schuch, T. Abu-Husein, A. Asyuda, J. W. Bats, M. Bolte, E. Zojer, A. Terfort, and M. Zharnikov. "Self-Assembled Monolayers with Distributed Dipole Moments Originating from Bipyrimidine Units". *The Journal of Physical Chemistry C* **124,** 504. doi:`10.1021/acs.jpcc.9b08835` (2020) (see pp. 4, 34).

44. K. Siegbahn. *ESCA: Atomic, Molecular and Solid State Structure Studies by Means of Electron Spectroscopy; Pres. to the Royal Society of Sciences of Uppsala, Dec. 3rd, 1965* red. by K. Siegbahn (Almqvist & Wiksell, Uppsala, 1967) (see pp. 4, 27).

45. *Handbook of X-Ray Photoelectron Spectroscopy: A Reference Book of Standard Spectra for Identification and Interpretation of XPS Data* Update (eds J. F. Moulder and J. Chastain) 261 pp. (Perkin-Elmer Corporation, Eden Prairie, Minn, 1992) (see pp. 4, 27).

46. C. S. Fadley. "Atomic-Level Characterization of Materials with Core- and Valence-Level Photoemission: Basic Phenomena and Future Directions". *Surface and Interface Analysis* **40,** 1579. doi:`10.1002/sia.2902` (2008) (see pp. 4, 27).

47. S. Hofmann. *Auger- and X-Ray Photoelectron Spectroscopy in Materials Science: A User-Oriented Guide Springer Series in Surface Sciences* **49.** 528 pp. (Springer, Heidelberg ; New York, 2013) (see pp. 4, 27).

48. P. S. Bagus, E. Ilton, and C. J. Nelin. "Extracting Chemical Information from XPS Spectra: A Perspective". *Catalysis Letters* **148,** 1785. doi:`10.1007/s10562-018-2417-1` (2018) (see pp. 4, 27).

49. W. F. Egelhoff. "Core-Level Binding-Energy Shifts at Surfaces and in Solids". *Surface Science Reports* **6,** 253. doi:`10.1016/0167-5729(87)90007-0` (1987) (see pp. 4, 27).

50. G. A. Benesh and D. A. King. "Core-Level Shift Spectroscopy for Adsorbates: Ionic, Covalent or Metallic Bonding?" *Chemical Physics Letters* **191,** 315. doi:`10.1016/0009-2614(92)85307-V` (1992) (see pp. 4, 27).

51. P. S. Bagus, G. Pacchioni, C. Sousa, T. Minerva, and F. Parmigiani. "Chemical Shifts of the Core-Level Binding Energies for the Alkaline-Earth Oxides". *Chemical physics letters* **196,** 641 (1992) (see pp. 4, 27).

52. P. S. Bagus, E. S. Ilton, and C. J. Nelin. "The Interpretation of XPS Spectra: Insights into Materials Properties". *Surface Science Reports* **68,** 273. doi:`10.1016/j.surfrep.2013.03.001` (2013) (see pp. 4, 27, 32–34).

53. M. Giesbers, A. T. M. Marcelis, and H. Zuilhof. "Simulation of XPS C1s Spectra of Organic Monolayers by Quantum Chemical Methods". *Langmuir* **29,** 4782. doi:`10.1021/la400445s` (2013) (see pp. 4, 34).

54. T. Ozaki and C.-C. Lee. "Absolute Binding Energies of Core Levels in Solids from First Principles". *Physical Review Letters* **118,** 026401. doi:`10.1103/PhysRevLett.118.026401` (2017) (see pp. 4, 30).

55. F. Viñes, C. Sousa, and F. Illas. "On the Prediction of Core Level Binding Energies in Molecules, Surfaces and Solids". *Physical Chemistry Chemical Physics* **20,** 8403. doi:`10.1039/C7CP08503F` (2018) (see pp. 4, 31, 33, 34).

56. D. Golze, L. Keller, and P. Rinke. "Accurate Absolute and Relative Core-Level Binding Energies from GW". *The Journal of Physical Chemistry Letters* **11,** 1840. doi:`10.1021/acs.jpclett.9b03423` (2020) (see pp. 4, 30, 31).

57. N. Pueyo Bellafont, P. S. Bagus, and F. Illas. "Prediction of Core Level Binding Energies in Density Functional Theory: Rigorous Definition of Initial and Final State Contributions and Implications on the Physical Meaning of Kohn-Sham Energies". *The Journal of Chemical Physics* **142,** 214102. doi:`10.1063/1.4921823` (2015) (see pp. 4, 33, 34).

58. T. Kirchhuebel, O. L. A. Monti, T. Munakata, S. Kera, R. Forker, and T. Fritz. "The Role of Initial and Final States in Molecular Spectroscopies". *Physical Chemistry Chemical Physics* **21,** 12730. doi:`10.1039/C8CP07318J` (2019) (see pp. 4, 33).

59. T. C. Taucher, O. T. Hofmann, and E. Zojer. "Final-State Simulations of Core-Level Binding Energies at Metal-Organic Hybrid Interfaces: Artifacts Caused by Spurious Collective Electrostatic Effects". *ACS Omega* **5,** 25868. doi:`10.1021/acsomega.0c03209` (2020) (see pp. 4, 92, 94, 161).

60. T. C. Taucher and E. Zojer. "The Potential of X-Ray Photoelectron Spectroscopy for Determining Interface Dipoles of Self-Assembled Monolayers". *Applied Sciences* **10,** 5735. doi:`10.3390/app10175735` (17 2020) (see pp. 4, 162).

61. J. M. Beebe, B. Kim, J. W. Gadzuk, C. Daniel Frisbie, and J. G. Kushmerick. "Transition from Direct Tunneling to Field Emission in Metal-Molecule-Metal Junctions". *Physical Review Letters* **97,** 026801. doi:`10.1103/PhysRevLett.97.026801` (2006) (see pp. 4, 135, 137, 138, 148).

62. J. M. Beebe, B. Kim, C. D. Frisbie, and J. G. Kushmerick. "Measuring Relative Barrier Heights in Molecular Electronic Junctions with Transition Voltage Spectroscopy". *ACS Nano* **2,** 827. doi:`10.1021/nn700424u` (2008) (see pp. 4, 135, 137, 138, 148).

63. R. G. Parr. *Density-Functional Theory of Atoms and Molecules* (Oxford University Press, USA, Oxford, 1989) (see p. 5).

64. R. M. Martin. *Electronic Structure: Basic Theory and Practical Methods* 1st pbk. ed. with corrections. 624 pp. (Cambridge University Press, Cambridge, UK ; New York, 2008) (see p. 5).

65. M. Born and R. Oppenheimer. "Zur Quantentheorie Der Molekeln". *Annalen der Physik* **389,** 457. doi:`10.1002/andp.19273892002` (1927) (see p. 6).

66. A. D. Becke. "Perspective: Fifty Years of Density-Functional Theory in Chemical Physics". *The Journal of Chemical Physics* **140,** 18A301. doi:`10.1063/1.4869598` (2014) (see p. 6).

67. R. O. Jones. "Density Functional Theory: Its Origins, Rise to Prominence, and Future". *Reviews of Modern Physics* **87,** 897. doi:`10.1103/RevModPhys.87.897` (2015) (see p. 6).

68. K. Lejaeghere, G. Bihlmayer, T. Björkman, P. Blaha, S. Blügel, V. Blum, D. Caliste, I. E. Castelli, S. J. Clark, A. D. Corso, S. de Gironcoli, T. Deutsch, J. K. Dewhurst, I. D. Marco, C. Draxl, M. Dułak, O. Eriksson, J. A. Flores-Livas, K. F. Garrity, L. Genovese, P. Giannozzi, M. Giantomassi, S. Goedecker, X. Gonze, O. Grånäs, E. K. U. Gross, A. Gulans, F. Gygi, D. R. Hamann, P. J. Hasnip, N. a. W. Holzwarth, D. Iuşan, D. B. Jochym, F. Jollet, D. Jones, G. Kresse, K. Koepernik, E. Küçükbenli, Y. O. Kvashnin, I. L. M. Locht, S. Lubeck, M. Marsman, N. Marzari, U. Nitzsche, L. Nordström, T. Ozaki, L. Paulatto, C. J. Pickard, W. Poelmans, M. I. J. Probert, K. Refson, M. Richter, G.-M. Rignanese, S. Saha, M. Scheffler, M. Schlipf, K. Schwarz, S. Sharma, F. Tavazza, P. Thunström, A. Tkatchenko, M. Torrent, D. Vanderbilt, M. J. van Setten, V. V. Speybroeck, J. M. Wills, J. R. Yates, G.-X. Zhang, and S. Cottenier. "Reproducibility in Density Functional Theory Calculations of Solids". *Science* **351.**

doi:10.1126/science.aad3000. pmid: 27013736 (2016) (see p. 6).

69. H.-W. Wang, B.-C. Wang, W.-H. Chen, and M. Hayashi. "Localized Gaussian Type Orbital—Periodic Boundary Condition—Density Functional Theory Study of Infinite-Length Single-Walled Carbon Nanotubes with Various Tubular Diameters". *The Journal of Physical Chemistry A* **112,** 1783. doi:10.1021/jp0741071 (2008) (see p. 6).
70. R. Demichelis, Y. Noël, P. D'Arco, M. Rérat, C. M. Zicovich-Wilson, and R. Dovesi. "Properties of Carbon Nanotubes: An Ab Initio Study Using Large Gaussian Basis Sets and Various DFT Functionals". *The Journal of Physical Chemistry C* **115,** 8876. doi:10.1021/jp110704x (2011) (see p. 6).
71. S. J. Fox, J. Dziedzic, T. Fox, C. S. Tautermann, and C.-K. Skylaris. "Density Functional Theory Calculations on Entire Proteins for Free Energies of Binding: Application to a Model Polar Binding Site". *Proteins: Structure, Function, and Bioinformatics* **82,** 3335. doi:10.1002/prot.24686 (2014) (see p. 6).
72. D. J. Cole and N. D. M. Hine. "Applications of Large-Scale Density Functional Theory in Biology". *Journal of Physics: Condensed Matter* **28,** 393001. doi:10.1088/0953-8984/28/39/393001 (2016) (see p. 6).
73. B. G. Sumpter, R. K. Vasudevan, T. Potok, and S. V. Kalinin. "A Bridge for Accelerating Materials by Design". *npj Computational Materials* **1,** 1. doi:10.1038/npjcompumats.2015.8 (1 2015) (see p. 7).
74. A. Jain, K. A. Persson, and G. Ceder. "Research Update: The Materials Genome Initiative: Data Sharing and the Impact of Collaborative Ab Initio Databases". *APL Materials* **4,** 053102. doi:10.1063/1.4944683 (2016) (see p. 7).
75. A. Lopez-Bezanilla and P. B. Littlewood. "Growing Field of Materials Informatics: Databases and Artificial Intelligence". *MRS Communications* **10,** 1. doi:10.1557/mrc.2020.2 (2020) (see p. 7).
76. W. Pauli. *Exclusion Principle and Quantum Mechanics* (Springer, 1994) (see pp. 7, 9).
77. P. Hohenberg and W. Kohn. "Inhomogeneous Electron Gas". *Physical Review* **136,** B864. doi:10.1103/PhysRev.136.B864 (3B 1964) (see p. 7).
78. L. H. Thomas. "The Calculation of Atomic Fields". *Mathematical Proceedings of the Cambridge Philosophical Society* **23,** 542. doi:10.1017/S0305004100011683 (1927) (see p. 7).
79. E. Fermi. "Un Metodo Statistico per La Determinazione Di Alcune Priorieta Dell'atome". *Rend. Accad. Naz. Lincei* **6,** 32 (1927) (see p. 7).

80. W. Ritz. “Über Eine Neue Methode Zur Lösung Gewisser Variationsprobleme Der Mathematischen Physik.” *Journal für die reine und angewandte Mathematik (Crelle’s Journal)* **1909,** 1. doi:`10.1515/crll.1909.135.1` (1909) (see p. 8).

81. J. C. Slater. “The Theory of Complex Spectra”. *Physical Review* **34,** 1293. doi:`10.1103/PhysRev.34.1293` (1929) (see p. 9).

82. J. P. Perdew and A. Zunger. “Self-Interaction Correction to Density-Functional Approximations for Many-Electron Systems”. *Physical Review B* **23,** 5048. doi:`10.1103/PhysRevB.23.5048` (1981) (see p. 9).

83. R. O. Jones and O. Gunnarsson. “The Density Functional Formalism, Its Applications and Prospects”. *Reviews of Modern Physics* **61,** 689. doi:`10.1103/RevModPhys.61.689` (1989) (see pp. 9, 35).

84. J. P. Perdew and W. Yue. “Accurate and Simple Density Functional for the Electronic Exchange Energy: Generalized Gradient Approximation”. *Physical Review B* **33,** 8800. doi:`10.1103/PhysRevB.33.8800` (1986) (see p. 9).

85. P. Ziesche, S. Kurth, and J. P. Perdew. “Density Functionals from LDA to GGA”. *Computational Materials Science* **11,** 122. doi:`10.1016/S0927-0256(97)00206-1` (1998) (see p. 10).

86. J. P. Perdew, K. Burke, and M. Ernzerhof. “Generalized Gradient Approximation Made Simple”. *Physical Review Letters* **77,** 3865. doi:`10.1103/PhysRevLett.77.3865` (1996) (see p. 10).

87. J. P. Perdew, K. Burke, and M. Ernzerhof. “ERRATA: Generalized Gradient Approximation Made Simple [Phys. Rev. Lett. 77, 3865 (1996)]”. *Physical Review Letters* **78,** 1396. doi:`10.1103/PhysRevLett.78.1396` (1997) (see p. 10).

88. J. P. Perdew and K. Schmidt. “Jacob’s Ladder of Density Functional Approximations for the Exchange-Correlation Energy”. *AIP Conference Proceedings* **577,** 1. doi:`10.1063/1.1390175` (2001) (see p. 10).

89. A. D. Becke. “A New Mixing of Hartree–Fock and Local Density-Functional Theories”. *The Journal of Chemical Physics* **98,** 1372. doi:`10.1063/1.464304` (1993) (see p. 10).

90. J. P. Perdew, M. Ernzerhof, and K. Burke. “Rationale for Mixing Exact Exchange with Density Functional Approximations”. *The Journal of Chemical Physics* **105,** 9982. doi:`10.1063/1.472933` (1996) (see p. 10).

91. S. Refaely-Abramson, S. Sharifzadeh, M. Jain, R. Baer, J. B. Neaton, and L. Kronik. “Gap Renormalization of Molecular Crystals from Density-Functional Theory”. *Physical Review B* **88,** 081204. doi:`10.1103/PhysRevB.88.081204` (2013) (see p. 10).

92. T. Körzdörfer and J.-L. Brédas. "Organic Electronic Materials: Recent Advances in the DFT Description of the Ground and Excited States Using Tuned Range-Separated Hybrid Functionals". *Accounts of Chemical Research* **47,** 3284. doi:`10.1021/ar500021t` (2014) (see p. 10).

93. S. Refaely-Abramson, M. Jain, S. Sharifzadeh, J. B. Neaton, and L. Kronik. "Solid-State Optical Absorption from Optimally Tuned Time-Dependent Range-Separated Hybrid Density Functional Theory". *Physical Review B* **92,** 081204. doi:`10.1103/PhysRevB.92.081204` (2015) (see p. 10).

94. L. Kronik and S. Kümmel. "Dielectric Screening Meets Optimally Tuned Density Functionals". *Advanced Materials* **30,** 1706560. doi:`10.1002/adma.201706560` (2018) (see p. 10).

95. S. Bhandari, M. S. Cheung, E. Geva, L. Kronik, and B. D. Dunietz. "Fundamental Gaps of Condensed-Phase Organic Semiconductors from Single-Molecule Calculations Using Polarization-Consistent Optimally Tuned Screened Range-Separated Hybrid Functionals". *Journal of Chemical Theory and Computation* **14,** 6287. doi:`10.1021/acs.jctc.8b00876` (2018) (see p. 10).

96. R. Peverati and D. G. Truhlar. "Quest for a Universal Density Functional: The Accuracy of Density Functionals across a Broad Spectrum of Databases in Chemistry and Physics". *Philosophical Transactions of the Royal Society A: Mathematical, Physical and Engineering Sciences* **372,** 20120476. doi:`10.1098/rsta.2012.0476` (2014) (see p. 10).

97. M. G. Medvedev, I. S. Bushmarinov, J. Sun, J. P. Perdew, and K. A. Lyssenko. "Density Functional Theory Is Straying from the Path toward the Exact Functional". *Science* **355,** 49. doi:`10.1126/science.aah5975`. pmid: `28059761` (2017) (see p. 10).

98. D. Langbein. in *Springer Tracts in Modern Physics* (ed D. Langbein) 1 (Springer, Berlin, Heidelberg, 1974). doi:`10.1007/BFb0042407` (see p. 10).

99. V. A. Parsegian. *Van Der Waals Forces: A Handbook for Biologists, Chemists, Engineers, and Physicists* doi:`10.1017/CBO9780511614606` (Cambridge University Press, Cambridge, 2005) (see p. 10).

100. R. H. French, V. A. Parsegian, R. Podgornik, R. F. Rajter, A. Jagota, J. Luo, D. Asthagiri, M. K. Chaudhury, Y.-m. Chiang, S. Granick, S. Kalinin, M. Kardar, R. Kjellander, D. C. Langreth, J. Lewis, S. Lustig, D. Wesolowski, J. S. Wettlaufer, W.-Y. Ching, M. Finnis, F. Houlihan, O. A. von Lilienfeld, C. J. van Oss, and T. Zemb. "Long Range Interactions in Nanoscale Science". *Reviews of Modern Physics* **82,** 1887. doi:`10.1103/RevModPhys.82.1887` (2010) (see p. 10).

101. J. Klimeš and A. Michaelides. "Perspective: Advances and Challenges in Treating van Der Waals Dispersion Forces in Density Functional Theory". *The Journal of Chemical Physics* **137,** 120901. doi:`10.1063/1.4754130` (2012) (see p. 10).

102. K. Müller-Dethlefs and P. Hobza. "Noncovalent Interactions: A Challenge for Experiment and Theory". *Chemical Reviews* **100,** 143. doi:`10.1021/cr9900331` (2000) (see p. 10).

103. J. Hermann, R. A. DiStasio, and A. Tkatchenko. "First-Principles Models for van Der Waals Interactions in Molecules and Materials: Concepts, Theory, and Applications". *Chemical Reviews* **117,** 4714. doi:`10.1021/acs.chemrev.6b00446` (2017) (see p. 10).

104. M. Stöhr, T. V. Voorhis, and A. Tkatchenko. "Theory and Practice of Modeling van Der Waals Interactions in Electronic-Structure Calculations". *Chemical Society Reviews* **48,** 4118. doi:`10.1039/C9CS00060G` (2019) (see p. 10).

105. A. D. Becke and E. R. Johnson. "A Density-Functional Model of the Dispersion Interaction". *The Journal of Chemical Physics* **123,** 154101. doi:`10.1063/1.2065267` (2005) (see p. 11).

106. A. Tkatchenko and M. Scheffler. "Accurate Molecular Van Der Waals Interactions from Ground-State Electron Density and Free-Atom Reference Data". *Physical Review Letters* **102.** doi:`10.1103/PhysRevLett.102.073005` (2009) (see p. 11).

107. S. Grimme, J. Antony, S. Ehrlich, and H. Krieg. "A Consistent and Accurate Ab Initio Parametrization of Density Functional Dispersion Correction (DFT-D) for the 94 Elements H-Pu". *The Journal of Chemical Physics* **132,** 154104. doi:`10.1063/1.3382344` (2010) (see p. 11).

108. A. Tkatchenko, R. A. DiStasio, R. Car, and M. Scheffler. "Accurate and Efficient Method for Many-Body van Der Waals Interactions". *Physical Review Letters* **108,** 236402. doi:`10.1103/PhysRevLett.108.236402` (2012) (see p. 11).

109. R. J. Maurer, V. G. Ruiz, and A. Tkatchenko. "Many-Body Dispersion Effects in the Binding of Adsorbates on Metal Surfaces". *The Journal of Chemical Physics* **143,** 102808. doi:`10.1063/1.4922688` (2015) (see p. 11).

110. M. Dion, H. Rydberg, E. Schröder, D. C. Langreth, and B. I. Lundqvist. "Van Der Waals Density Functional for General Geometries". *Physical Review Letters* **92,** 246401. doi:`10.1103/PhysRevLett.92.246401` (2004) (see p. 11).

111. M. Dion, H. Rydberg, E. Schröder, D. C. Langreth, and B. I. Lundqvist. "Erratum: Van Der Waals Density Functional for General Geometries [Phys. Rev. Lett. 92, 246401 (2004)]". *Physical Review Letters* **95,** 109902. doi:`10.1103/PhysRevLett.95.109902` (2005) (see p. 11).

112. F. Furche and T. Van Voorhis. "Fluctuation-Dissipation Theorem Density-Functional Theory". *The Journal of Chemical Physics* **122,** 164106. doi:`10.1063/1.1884112` (2005) (see p. 11).

113. V. G. Ruiz, W. Liu, E. Zojer, M. Scheffler, and A. Tkatchenko. "Density-Functional Theory with Screened van Der Waals Interactions for the Modeling of Hybrid Inorganic-Organic Systems". *Physical Review Letters* **108.** doi:`10.1103/PhysRevLett.108.146103` (2012) (see p. 11).

114. W. A. Al-Saidi, V. K. Voora, and K. D. Jordan. "An Assessment of the vdW-TS Method for Extended Systems". *Journal of Chemical Theory and Computation* **8,** 1503. doi:`10.1021/ct200618b` (2012) (see p. 11).

115. E. M. Lifshitz. "The Theory of Molecular Attractive Forces between Solids". *Soviet Physics J. Exper. Theoret. Phys.* **2,** 73 (1956) (see p. 11).

116. E. Zaremba and W. Kohn. "Van Der Waals Interaction between an Atom and a Solid Surface". *Physical Review B* **13,** 2270. doi:`10.1103/PhysRevB.13.2270` (1976) (see p. 11).

117. R. Landauer. "Spatial Variation of Currents and Fields Due to Localized Scatterers in Metallic Conduction". *IBM Journal of Research and Development* **1,** 223. doi:`10.1147/rd.13.0223` (1957) (see p. 11).

118. J. Maassen and M. Lundstrom. "(Invited) The Landauer Approach to Electron and Phonon Transport". *ECS Transactions* **69,** 23. doi:`10.1149/06909.0023ecst` (2015) (see p. 12).

119. V. Obersteiner. *Computational Modeling of Organic-Inorganic Nanomaterials* Dissertation (Graz University of Technology, Graz, 2017). 207 pp. (see pp. 13, 142).

120. M. P. L. Sancho, J. M. L. Sancho, J. M. L. Sancho, and J. Rubio. "Highly Convergent Schemes for the Calculation of Bulk and Surface Green Functions". *Journal of Physics F: Metal Physics* **15,** 851. doi:`10.1088/0305-4608/15/4/009` (1985) (see p. 13).

121. V. Blum, R. Gehrke, F. Hanke, P. Havu, V. Havu, X. Ren, K. Reuter, and M. Scheffler. "Ab Initio Molecular Simulations with Numeric Atom-Centered Orbitals". *Computer Physics Communications* **180,** 2175. doi:`10.1016/j.cpc.2009.06.022` (2009) (see p. 14).

122. V. Havu, V. Blum, P. Havu, and M. Scheffler. "Efficient O(N) Integration for All-Electron Electronic Structure Calculation Using Numeric Basis Functions". *Journal of Computational Physics* **228,** 8367. doi:`10.1016/j.jcp.2009.08.008` (2009) (see p. 14).

123. A. Marek, V. Blum, R. Johanni, V. Havu, B. Lang, T. Auckenthaler, A. Heinecke, H.-J. Bungartz, and H. Lederer. "The ELPA Library: Scalable Parallel Eigenvalue Solutions for Electronic Structure Theory and Computational Science". *Journal of Physics: Condensed Matter* **26,** 213201. doi:`10.1088/0953-8984/26/21/213201` (2014) (see p. 14).

124. A. Togo and I. Tanaka. *$\texttt{Spglib$: A Software Library for Crystal Symmetry Search* arXiv: 1808.01590 [cond-mat]. (See p. 14).

125. V. W.-z. Yu, F. Corsetti, A. García, W. P. Huhn, M. Jacquelin, W. Jia, B. Lange, L. Lin, J. Lu, W. Mi, A. Seifitokaldani, Á. Vázquez-Mayagoitia, C. Yang, H. Yang, and V. Blum. "ELSI: A Unified Software Interface for Kohn–Sham Electronic Structure Solvers". *Computer Physics Communications* **222,** 267. doi:10.1016/j.cpc.2017.09.007 (2018) (see p. 14).

126. G. Kresse and J. Hafner. "Ab Initio Molecular Dynamics for Liquid Metals". *Physical Review B* **47,** 558. doi:10.1103/PhysRevB.47.558 (1993) (see p. 14).

127. G. Kresse and J. Hafner. "Ab Initio Molecular-Dynamics Simulation of the Liquid-Metal–Amorphous-Semiconductor Transition in Germanium". *Physical Review B* **49,** 14251. doi:10.1103/PhysRevB.49.14251 (1994) (see p. 14).

128. G. Kresse and J. Furthmüller. "Efficiency of Ab-Initio Total Energy Calculations for Metals and Semiconductors Using a Plane-Wave Basis Set". *Computational Materials Science* **6,** 15. doi:10.1016/0927-0256(96)00008-0 (1996) (see p. 14).

129. G. Kresse and J. Furthmüller. "Efficient Iterative Schemes for *Ab Initio* Total-Energy Calculations Using a Plane-Wave Basis Set". *Physical Review B* **54,** 11169. doi:10.1103/PhysRevB.54.11169 (1996) (see p. 14).

130. J. M. Soler, E. Artacho, J. D. Gale, A. García, J. Junquera, P. Ordejón, and D. Sánchez-Portal. "The SIESTA Method Forab Initioorder-Nmaterials Simulation". *Journal of Physics: Condensed Matter* **14,** 2745. doi:10.1088/0953-8984/14/11/302 (2002) (see pp. 14, 15).

131. E. Artacho, E. Anglada, O. Diéguez, J. D. Gale, A. García, J. Junquera, R. M. Martin, P. Ordejón, J. M. Pruneda, D. Sánchez-Portal, and J. M. Soler. "The SIESTA Method$\mathsemicolon$ Developments and Applicability". *Journal of Physics: Condensed Matter* **20,** 064208. doi:10.1088/0953-8984/20/6/064208 (2008) (see pp. 14, 15).

132. O. Hofmann, E. Zojer, L. Hörmann, A. Jeindl, and R. Maurer. "First-Principles Calculations of Hybrid Inorganic-Organic Interfaces: From State-of-the-Art to Best Practice". *Physical Chemistry Chemical Physics.* doi:10.1039/D0CP06605B (2021) (see pp. 14–16, 36).

133. A. García, N. Papior, A. Akhtar, E. Artacho, V. Blum, E. Bosoni, P. Brandimarte, M. Brandbyge, J. I. Cerdá, F. Corsetti, R. Cuadrado, V. Dikan, J. Ferrer, J. Gale, P. García-Fernández, V. M. García-Suárez, S. García, G. Huhs, S. Illera, R. Korytár, P. Koval, I. Lebedeva, L. Lin, P. López-Tarifa, S. G. Mayo, S. Mohr, P. Ordejón, A. Postnikov, Y. Pouillon, M. Pruneda, R. Robles, D. Sánchez-Portal, J. M. Soler, R. Ullah, V. W.-z. Yu, and J. Junquera. "Siesta: Recent Developments and Applications". *The*

Journal of Chemical Physics **152,** 204108. doi:10.1063/5.0005077 (2020) (see pp. 15, 159).

134. J. Neugebauer and M. Scheffler. "Adsorbate-Substrate and Adsorbate-Adsorbate Interactions of Na and K Adlayers on Al(111)". *Physical Review B* **46,** 16067. doi:10.1103/PhysRevB.46.16067 (1992) (see p. 16).
135. C. Freysoldt, P. Eggert, P. Rinke, A. Schindlmayr, and M. Scheffler. "Screening in Two Dimensions: GW Calculations for Surfaces and Thin Films Using the Repeated-Slab Approach". *Physical Review B* **77,** 235428. doi:10.1103/PhysRevB.77.235428 (2008) (see p. 16).
136. E. Zojer, T. C. Taucher, and O. T. Hofmann. "The Impact of Dipolar Layers on the Electronic Properties of Organic/Inorganic Hybrid Interfaces". *Advanced Materials Interfaces* **6,** 1900581. doi:10.1002/admi.201900581 (2019) (see pp. 19, 21–23).
137. A. Natan, L. Kronik, H. Haick, and R. T. Tung. "Electrostatic Properties of Ideal and Non-Ideal Polar Organic Monolayers: Implications for Electronic Devices". *Advanced Materials* **19,** 4103. doi:10.1002/adma.200701681 (2007) (see pp. 19, 20).
138. D. Cahen, R. Naaman, and Z. Vager. "The Cooperative Molecular Field Effect". *Advanced Functional Materials* **15,** 1571. doi:10.1002/adfm.200500187 (2005) (see p. 20).
139. A. Natan, Y. Zidon, Y. Shapira, and L. Kronik. "Cooperative Effects and Dipole Formation at Semiconductor and Self-Assembled-Monolayer Interfaces". *Physical Review B* **73.** doi:10.1103/PhysRevB.73.193310 (2006) (see p. 20).
140. G. Heimel, F. Rissner, and E. Zojer. "Modeling the Electronic Properties of π-Conjugated Self-Assembled Monolayers". *Advanced Materials* **22,** 2494. doi:10.1002/adma.200903855 (2010) (see p. 20).
141. O. L. A. Monti. "Understanding Interfacial Electronic Structure and Charge Transfer: An Electrostatic Perspective". *The Journal of Physical Chemistry Letters* **3,** 2342. doi:10.1021/jz300850x (2012) (see p. 20).
142. L. Romaner, G. Heimel, C. Ambrosch-Draxl, and E. Zojer. "Correction: The Dielectric Constant of Self-Assembled Monolayers". *Advanced Functional Materials* **21,** 3406. doi:10.1002/adfm.201190078 (2011) (see p. 20).
143. N. K. Adam, J. F. Danielli, J. B. Harding, and F. G. Donnan. "The Structure of Surface Films XXI—Surface Potentials of Dibasic Esters, Alcohols, Aldoximes, and Ketones". *Proceedings of the Royal Society of London. Series A - Mathematical and Physical Sciences* **147,** 491. doi:10.1098/rspa.1934.0231 (1934) (see p. 20).

144. G. Heimel, L. Romaner, E. Zojer, and J.-L. Brédas. "Toward Control of the Metal-Organic Interfacial Electronic Structure in Molecular Electronics: A First-Principles Study on Self-Assembled Monolayers of π-Conjugated Molecules on Noble Metals". *Nano Letters* **7,** 932. doi:`10.1021/nl0629106` (2007) (see pp. 20, 24).

145. W. Schottky. "Zur Halbleitertheorie der Sperrschicht- und Spitzengleichrichter". *Zeitschrift für Physik* **113,** 367. doi:`10.1007/BF01340116` (1939) (see p. 23).

146. N. F. Mott. "The Theory of Crystal Rectifiers". *Proceedings of the Royal Society of London. Series A. Mathematical and Physical Sciences* **171,** 27. doi:`10.1098/rspa.1939.0051` (1939) (see p. 23).

147. R. T. (Tung. "The Physics and Chemistry of the Schottky Barrier Height". *Applied Physics Reviews* **1,** 011304. doi:`10.1063/1.4858400` (2014) (see p. 23).

148. Y. Liu, J. Guo, E. Zhu, L. Liao, S.-J. Lee, M. Ding, I. Shakir, V. Gambin, Y. Huang, and X. Duan. "Approaching the Schottky-Mott Limit in van Der Waals Metal-Semiconductor Junctions". *Nature* **557,** 696. doi:`10.1038/s41586-018-0129-8` (7707 2018) (see p. 23).

149. H. Hertz. "Ueber Einen Einfluss Des Ultravioletten Lichtes Auf Die Electrische Entladung". *Annalen der Physik* **267,** 983. doi:`10.1002/andp.18872670827` (1887) (see p. 27).

150. A. Einstein. "Über Einen Die Erzeugung Und Verwandlung Des Lichtes Betreffenden Heuristischen Gesichtspunkt". *Annalen der Physik* **322,** 132. doi:`10.1002/andp.19053220607` (1905) (see p. 27).

151. A. G. Shard. "Detection Limits in XPS for More than 6000 Binary Systems Using Al and Mg Kα X-Rays". *Surface and Interface Analysis* **46,** 175. doi:`10.1002/sia.5406` (2014) (see p. 28).

152. M. Zharnikov. "High-Resolution X-Ray Photoelectron Spectroscopy in Studies of Self-Assembled Organic Monolayers". *Journal of Electron Spectroscopy and Related Phenomena* **178-179,** 380. doi:`10.1016/j.elspec.2009.05.008` (2010) (see p. 28).

153. T. C. Taucher, I. Hehn, O. T. Hofmann, M. Zharnikov, and E. Zojer. "Understanding Chemical versus Electrostatic Shifts in X-Ray Photoelectron Spectra of Organic Self-Assembled Monolayers". *The Journal of Physical Chemistry C* **120,** 3428. doi:`10.1021/acs.jpcc.5b12387` (2016) (see pp. 29, 32, 40, 92, 96, 162).

154. A. Holme, K. J. Børve, L. J. Sæthre, and T. D. Thomas. "Accuracy of Calculated Chemical Shifts in Carbon 1s Ionization Energies from Single-Reference Ab Initio Methods and Density Functional Theory". *Journal of Chemical Theory and Computation* **7,** 4104. doi:`10.1021/ct200662e` (2011) (see p. 30).

155. M. L. Vidal, X. Feng, E. Epifanovsky, A. I. Krylov, and S. Coriani. "New and Efficient Equation-of-Motion Coupled-Cluster Framework for Core-Excited and Core-Ionized States". *Journal of Chemical Theory and Computation* **15,** 3117. doi:`10.1021/acs.jctc.9b00039` (2019) (see p. 30).

156. C. Møller and M. S. Plesset. "Note on an Approximation Treatment for Many-Electron Systems". *Physical Review* **46,** 618. doi:`10.1103/PhysRev.46.618` (1934) (see p. 30).

157. L. Hedin. "New Method for Calculating the One-Particle Green's Function with Application to the Electron-Gas Problem". *Physical Review* **139,** A796. doi:`10.1103/PhysRev.139.A796` (3A 1965) (see p. 31).

158. F. Aryasetiawan and O. Gunnarsson. "The GW Method". *Reports on Progress in Physics* **61,** 237. doi:`10.1088/0034-4885/61/3/002` (1998) (see p. 31).

159. G. Onida, L. Reining, and A. Rubio. "Electronic Excitations: Density-Functional versus Many-Body Green's-Function Approaches". *Reviews of Modern Physics* **74,** 601. doi:`10.1103/RevModPhys.74.601` (2002) (see p. 31).

160. D. Danovich. "Green's Function Methods for Calculating Ionization Potentials, Electron Affinities, and Excitation Energies". *WIREs Computational Molecular Science* **1,** 377. doi:`10.1002/wcms.38` (2011) (see p. 31).

161. M. J. van Setten, R. Costa, F. Viñes, and F. Illas. "Assessing GW Approaches for Predicting Core Level Binding Energies". *Journal of Chemical Theory and Computation* **14,** 877. doi:`10.1021/acs.jctc.7b01192` (2018) (see p. 31).

162. D. Golze, J. Wilhelm, M. J. van Setten, and P. Rinke. "Core-Level Binding Energies from GW: An Efficient Full-Frequency Approach within a Localized Basis". *Journal of Chemical Theory and Computation* **14,** 4856. doi:`10.1021/acs.jctc.8b00458` (2018) (see p. 31).

163. B. Peng and K. Kowalski. "Green's Function Coupled-Cluster Approach: Simulating Photoelectron Spectra for Realistic Molecular Systems". *Journal of Chemical Theory and Computation* **14,** 4335. doi:`10.1021/acs.jctc.8b00313` (2018) (see p. 31).

164. S. V. Faleev, M. van Schilfgaarde, and T. Kotani. "All-Electron Self-Consistent GW Approximation: Application to Si, MnO, and NiO". *Physical Review Letters* **93,** 126406. doi:`10.1103/PhysRevLett.93.126406` (2004) (see p. 31).

165. J. Wenzel, M. Wormit, and A. Dreuw. "Calculating Core-Level Excitations and x-Ray Absorption Spectra of Medium-Sized Closed-Shell Molecules with the Algebraic-Diagrammatic Construction Scheme for the Polarization Propagator". *Journal of Computational Chemistry* **35,** 1900. doi:10.1002/jcc.23703 (2014) (see p. 31).

166. T. Fransson and A. Dreuw. "Simulating X-Ray Emission Spectroscopy with Algebraic Diagrammatic Construction Schemes for the Polarization Propagator". *Journal of Chemical Theory and Computation* **15,** 546. doi:10.1021/acs.jctc.8b01046 (2019) (see p. 31).

167. R. J. Maurer, C. Freysoldt, A. M. Reilly, J. G. Brandenburg, O. T. Hofmann, T. Björkman, S. Lebègue, and A. Tkatchenko. "Advances in Density-Functional Calculations for Materials Modeling". *Annual Review of Materials Research* **49,** 1. doi:10.1146/annurev-matsci-070218-010143 (2019) (see p. 31).

168. F. A. Evangelista, P. Shushkov, and J. C. Tully. "Orthogonality Constrained Density Functional Theory for Electronic Excited States". *The Journal of Physical Chemistry A* **117,** 7378. doi:10.1021/jp401323d (2013) (see p. 31).

169. W. D. Derricotte and F. A. Evangelista. "Simulation of X-Ray Absorption Spectra with Orthogonality Constrained Density Functional Theory". *Physical Chemistry Chemical Physics* **17,** 14360. doi:10.1039/C4CP05509H (2015) (see p. 31).

170. E. Runge and E. K. U. Gross. "Density-Functional Theory for Time-Dependent Systems". *Physical Review Letters* **52,** 997. doi:10.1103/PhysRevLett.52.997 (1984) (see p. 31).

171. M. E. Casida. in *Recent Advances in Density Functional Methods* 0 vols. *Recent Advances in Computational Chemistry* Volume 1, 155 (WORLD SCIENTIFIC, 1995). doi:10.1142/9789812830586_0005 (see p. 31).

172. K. Burke, J. Werschnik, and E. K. U. Gross. "Time-Dependent Density Functional Theory: Past, Present, and Future". *The Journal of Chemical Physics* **123,** 062206. doi:10.1063/1.1904586 (2005) (see p. 31).

173. A. Dreuw and M. Head-Gordon. "Single-Reference Ab Initio Methods for the Calculation of Excited States of Large Molecules". *Chemical Reviews* **105,** 4009. doi:10.1021/cr0505627 (2005) (see p. 31).

174. N. A. Besley and F. A. Asmuruf. "Time-Dependent Density Functional Theory Calculations of the Spectroscopy of Core Electrons". *Physical Chemistry Chemical Physics* **12,** 12024. doi:10.1039/C002207A (2010) (see p. 31).

175. N. A. Besley. "Density Functional Theory Based Methods for the Calculation of X-Ray Spectroscopy". *Accounts of Chemical Research* **53,** 1306. doi:`10.1021/acs.accounts.0c00171` (2020) (see p. 31).

176. N. Pueyo Bellafont, P. S. Bagus, C. Sousa, and F. Illas. "Assessing the Ability of DFT Methods to Describe Static Electron Correlation Effects: CO Core Level Binding Energies as a Representative Case". *The Journal of Chemical Physics* **147,** 024106. doi:`10.1063/1.4991833` (2017) (see p. 31).

177. N. Pueyo Bellafont, F. Viñes, and F. Illas. "Performance of the TPSS Functional on Predicting Core Level Binding Energies of Main Group Elements Containing Molecules: A Good Choice for Molecules Adsorbed on Metal Surfaces". *Journal of Chemical Theory and Computation* **12,** 324. doi:`10.1021/acs.jctc.5b00998` (2016) (see p. 31).

178. C.-O. Almbladh and U. von Barth. "Exact Results for the Charge and Spin Densities, Exchange-Correlation Potentials, and Density-Functional Eigenvalues". *Physical Review B* **31,** 3231. doi:`10.1103/PhysRevB.31.3231` (1985) (see p. 32).

179. T. Koopmans. "Über die Zuordnung von Wellenfunktionen und Eigenwerten zu den Einzelnen Elektronen Eines Atoms". *Physica* **1,** 104. doi:`10.1016/S0031-8914(34)90011-2` (1934) (see p. 32).

180. W. Kohn and L. J. Sham. "Self-Consistent Equations Including Exchange and Correlation Effects". *Physical Review* **140,** A1133. doi:`10.1103/PhysRev.140.A1133` (4A 1965) (see p. 32).

181. J. P. Perdew and M. R. Norman. "Electron Removal Energies in Kohn-Sham Density-Functional Theory". *Physical Review B* **26,** 5445. doi:`10.1103/PhysRevB.26.5445` (1982) (see pp. 32, 35).

182. R. Stowasser and R. Hoffmann. "What Do the Kohn-Sham Orbitals and Eigenvalues Mean?" *Journal of the American Chemical Society* **121,** 3414. doi:`10.1021/ja9826892` (1999) (see p. 32).

183. D. P. Chong, O. V. Gritsenko, and E. J. Baerends. "Interpretation of the Kohn–Sham Orbital Energies as Approximate Vertical Ionization Potentials". *The Journal of Chemical Physics* **116,** 1760. doi:`10.1063/1.1430255` (2002) (see p. 32).

184. D. P. Joubert. "Mapping Kohn-Sham Eigenenergies onto Vertical Ionization Energies and Electron Affinities". *Physical Review A* **85.** doi:`10.1103/PhysRevA.85.062509` (2012) (see p. 32).

185. E. J. Baerends, O. V. Gritsenko, and R. van Meer. "The Kohn–Sham Gap, the Fundamental Gap and the Optical Gap: The Physical Meaning of Occupied and Virtual Kohn–Sham Orbital Energies". *Physical Chemistry Chemical Physics* **15,** 16408. doi:`10.1039/c3cp52547c` (2013) (see p. 32).

186. N. Pueyo Bellafont, F. Illas, and P. S. Bagus. "Validation of Koopmans' Theorem for Density Functional Theory Binding Energies". *Phys. Chem. Chem. Phys.* **17,** 4015. doi:`10.1039/C4CP05434B` (2015) (see pp. 32, 34).

187. D. P. Piet, D. Danovich, H. Zuilhof, and E. J. R. Sudhölter. "Ionization Potentials of Porphyrins and Phthalocyanines. A Comparative Benchmark Study of Fast Improvements of Koopman's Theorem". *Journal of the Chemical Society, Perkin Transactions 2,* 1653. doi:`10.1039/A903296G` (1999) (see p. 32).

188. E. Pehlke and M. Scheffler. "Evidence for Site-Sensitive Screening of Core Holes at the Si and Ge (001) Surface". *Physical Review Letters* **71,** 2338. doi:`10.1103/PhysRevLett.71.2338` (1993) (see pp. 32, 34).

189. M. Birgersson, C.-O. Almbladh, M. Borg, and J. N. Andersen. "Density-Functional Theory Applied to Rh(111) and CO/Rh(111) Systems: Geometries, Energies, and Chemical Shifts". *Physical Review B* **67.** doi:`10.1103/PhysRevB.67.045402` (2003) (see p. 32).

190. A. Stierle, C. Tieg, H. Dosch, V. Formoso, E. Lundgren, J. N. Andersen, L. Köhler, and G. Kresse. "Surface Core Level Shift Observed on NiAl(110)". *Surface Science* **529,** L263. doi:`10.1016/S0039-6028(03)00329-7` (2003) (see pp. 32, 34).

191. M. Methfessel, V. Fiorentini, and S. Oppo. "Connection between Charge Transfer and Alloying Core-Level Shifts Based on Density-Functional Calculations". *Physical Review B* **61,** 5229. doi:`10.1103/PhysRevB.61.5229` (2000) (see pp. 32, 34).

192. J. Vackář, M. Hyt'ha, and A. Šimůnek. "All-Electron Pseudopotentials". *Physical Review B* **58,** 12712. doi:`10.1103/PhysRevB.58.12712` (1998) (see p. 32).

193. Y. Morikawa, T. Hayashi, C. C. Liew, and H. Nozoye. "First-Principles Theoretical Study of Alkylthiolate Adsorption on Au (111)". *Surface science* **507,** 46. (2002) (see pp. 32, 34).

194. I. Hehn, S. Schuster, T. Wächter, T. Abu-Husein, A. Terfort, M. Zharnikov, and E. Zojer. "Employing X-Ray Photoelectron Spectroscopy for Determining Layer Homogeneity in Mixed Polar Self-Assembled Monolayers". *The Journal of Physical Chemistry Letters* **7,** 2994. doi:`10.1021/acs.jpclett.6b01096` (2016) (see p. 32).

195. M. Gärtner, E. Sauter, G. Nascimbeni, A. Petritz, A. Wiesner, M. Kind, T. Abu-Husein, M. Bolte, B. Stadlober, E. Zojer, A. Terfort, and M. Zharnikov. "Understanding the Properties of Tailor-Made Self-Assembled Monolayers with Embedded Dipole Moments for Interface Engineering". *The Journal of Physical Chemistry C* **122,** 28757. doi:`10.1021/acs.jpcc.8b09440` (2018) (see pp. 32, 34).

196. F. Ishiwari, G. Nascimbeni, E. Sauter, H. Tago, Y. Shoji, S. Fujii, M. Kiguchi, T. Tada, M. Zharnikov, E. Zojer, and T. Fukushima. "Triptycene Tripods for the Formation of Highly Uniform and Densely Packed Self-Assembled Monolayers with Controlled Molecular Orientation". *Journal of the American Chemical Society* **141,** 5995. doi:`10.1021/jacs.9b00950` (2019) (see pp. 32, 34).
197. J. D. Jackson. *Classical Electrodynamics* 3rd ed. 808 pp. (Wiley, New York, 1999) (see p. 33).
198. J. Neaton, M. Hybertsen, and S. Louie. "Renormalization of Molecular Electronic Levels at Metal-Molecule Interfaces". *Physical Review Letters* **97.** doi:`10.1103/PhysRevLett.97.216405` (2006) (see p. 33).
199. C. L. Lamont and J. Wilkes. "Attenuation Length of Electrons in Self-Assembled Monolayers of n-Alkanethiols on Gold". *Langmuir* **15,** 2037. (1999) (see pp. 33, 34).
200. Y. Li, D. Lu, and G. Galli. "Calculation of Quasi-Particle Energies of Aromatic Self-Assembled Monolayers on Au(111)". *Journal of Chemical Theory and Computation* **5,** 881. doi:`10.1021/ct800465f` (2009) (see p. 33).
201. D. A. Egger, Z.-F. Liu, J. B. Neaton, and L. Kronik. "Reliable Energy Level Alignment at Physisorbed Molecule–Metal Interfaces from Density Functional Theory". *Nano Letters* **15,** 2448. doi:`10.1021/nl504863r` (2015) (see p. 33).
202. V. Jain, M. C. Biesinger, and M. R. Linford. "The Gaussian-Lorentzian Sum, Product, and Convolution (Voigt) Functions in the Context of Peak Fitting X-Ray Photoelectron Spectroscopy (XPS) Narrow Scans". *Applied Surface Science* **447,** 548. doi:`10.1016/j.apsusc.2018.03.190` (2018) (see p. 33).
203. G. Heimel, L. Romaner, J.-L. Brédas, and E. Zojer. "Organic/Metal Interfaces in Self-Assembled Monolayers of Conjugated Thiols: A First-Principles Benchmark Study". *Surface Science* **600,** 4548. doi:`10.1016/j.susc.2006.07.023` (2006) (see p. 34).
204. E. Sauter, G. Nascimbeni, D. Trefz, S. Ludwigs, E. Zojer, F. von Wrochem, and M. Zharnikov. "A Dithiocarbamate Anchoring Group as a Flexible Platform for Interface Engineering". *Physical Chemistry Chemical Physics* **21,** 22511. doi:`10.1039/C9CP03306H` (2019) (see p. 34).
205. M. Methfessel, D. Hennig, and M. Scheffler. "Ab-Initio Calculations of the Initial- and Final-State Effects on the Surface Core-Level Shift of Transition Metals". *Surface Science* **287-288,** 785. doi:`10.1016/0039-6028(93)91072-W` (1993) (see p. 34).

206. S. Lizzit, A. Baraldi, A. Groso, K. Reuter, M. V. Ganduglia-Pirovano, C. Stampfl, M. Scheffler, M. Stichler, C. Keller, W. Wurth, and D. Menzel. "Surface Core-Level Shifts of Clean and Oxygen-Covered Ru(0001)". *Physical Review B* **63.** doi:`10.1103/PhysRevB.63.205419` (2001) (see p. 34).

207. M. Boman, H. Aagren, and S. Stafstroem. "A Delta Self-Consistent-Field Study of Core Electron Binding Energies of Model Molecules for the Aluminum/Polythiophene Interface". *The Journal of Physical Chemistry* **99,** 16597. doi:`10.1021/j100045a018` (1995) (see p. 34).

208. T. Susi, M. Kaukonen, P. Havu, M. P. Ljungberg, P. Ayala, and E. I. Kauppinen. "Core Level Binding Energies of Functionalized and Defective Graphene". *Beilstein Journal of Nanotechnology* **5,** 121. doi:`10.3762/bjnano.5.12` (2014) (see p. 34).

209. J. C. Slater. *Quantum Theory of Molecules and Solids. Vol. 4* (McGraw-Hill, 1974) (see pp. 34, 35).

210. J. F. Janak. "Proof That ∂ E ∂ n i = μ in Density-Functional Theory". *Physical Review B* **18,** 7165. doi:`10.1103/PhysRevB.18.7165` (1978) (see p. 35).

211. C. Göransson, W. Olovsson, and I. A. Abrikosov. "Numerical Investigation of the Validity of the Slater-Janak Transition-State Model in Metallic Systems". *Physical Review B* **72.** doi:`10.1103/PhysRevB.72.134203` (2005) (see p. 36).

212. A. R. Williams, R. A. deGroot, and C. B. Sommers. "Generalization of Slater's Transition State Concept". *The Journal of Chemical Physics* **63,** 628. doi:`10.1063/1.431382` (1975) (see p. 36).

213. H. Lu, D. Zeysing, M. Kind, A. Terfort, and M. Zharnikov. "Structure of Self-Assembled Monolayers of Partially Fluorinated Alkanethiols with a Fluorocarbon Part of Variable Length on Gold Substrate". *The Journal of Physical Chemistry C* **117,** 18967. doi:`10.1021/jp405475h` (2013) (see pp. 92, 96).

214. J. C. Love, L. A. Estroff, J. K. Kriebel, R. G. Nuzzo, and G. M. Whitesides. "Self-Assembled Monolayers of Thiolates on Metals as a Form of Nanotechnology". *Chemical Reviews* **105,** 1103. doi:`10.1021/cr0300789` (2005) (see p. 92).

215. E. H. Huisman, C. M. Guédon, B. J. van Wees, and S. J. van der Molen. "Interpretation of Transition Voltage Spectroscopy". *Nano Letters* **9,** 3909. doi:`10.1021/nl9021094` (2009) (see pp. 135–138).

216. J. G. Simmons. "Generalized Formula for the Electric Tunnel Effect between Similar Electrodes Separated by a Thin Insulating Film". *Journal of Applied Physics* **34,** 1793. doi:`10.1063/1.1702682` (1963) (see p. 135).

217. R. H. Fowler and L. Nordheim. "Electron Emission in Intense Electric Fields". *Proceedings of the Royal Society of London. Series A, Containing Papers of a Mathematical and Physical Character* **119,** 173. doi:`10.1098/rspa.1928.0091` (1928) (see p. 137).

218. M. P. Samanta, W. Tian, S. Datta, J. I. Henderson, and C. P. Kubiak. "Electronic Conduction through Organic Molecules". *Physical Review B* **53,** R7626. doi:`10.1103/PhysRevB.53.R7626` (1996) (see p. 137).

219. M. Paulsson and S. Datta. "Thermoelectric Effect in Molecular Electronics". *Physical Review B* **67,** 241403. doi:`10.1103/PhysRevB.67.241403` (2003) (see p. 137).

220. J. M. Thijssen and H. S. J. V. der Zant. "Charge Transport and Single-Electron Effects in Nanoscale Systems". *physica status solidi (b)* **245,** 1455. doi:`10.1002/pssb.200743470` (2008) (see p. 137).

221. M. L. Trouwborst, C. A. Martin, R. H. M. Smit, C. M. Guédon, T. A. Baart, S. J. van der Molen, and J. M. van Ruitenbeek. "Transition Voltage Spectroscopy and the Nature of Vacuum Tunneling". *Nano Letters* **11,** 614. doi:`10.1021/nl103699t` (2011) (see p. 138).

222. A. Vilan, D. Cahen, and E. Kraisler. "Rethinking Transition Voltage Spectroscopy within a Generic Taylor Expansion View". *ACS Nano* **7,** 695. doi:`10.1021/nn3049686` (2013) (see pp. 138–140).

223. A. Vilan, D. Aswal, and D. Cahen. "Large-Area, Ensemble Molecular Electronics: Motivation and Challenges". *Chemical Reviews* **117,** 4248. doi:`10.1021/acs.chemrev.6b00595` (2017) (see pp. 138, 140, 141).

224. M. Araidai and M. Tsukada. "Theoretical Calculations of Electron Transport in Molecular Junctions: Inflection Behavior in Fowler-Nordheim Plot and Its Origin". *Physical Review B* **81,** 235114. doi:`10.1103/PhysRevB.81.235114` (2010) (see p. 138).

225. F. Mirjani, J. M. Thijssen, and S. J. van der Molen. "Advantages and Limitations of Transition Voltage Spectroscopy: A Theoretical Analysis". *Physical Review B* **84,** 115402. doi:`10.1103/PhysRevB.84.115402` (2011) (see p. 138).

226. T. Markussen, J. Chen, and K. S. Thygesen. "Improving Transition Voltage Spectroscopy of Molecular Junctions". *Physical Review B* **83,** 155407. doi:`10.1103/PhysRevB.83.155407` (2011) (see p. 138).

227. I. Bâldea. "Ambipolar Transition Voltage Spectroscopy: Analytical Results and Experimental Agreement". *Physical Review B* **85,** 035442. doi:`10.1103/PhysRevB.85.035442` (2012) (see pp. 138, 139).

228. I. Bâldea. "Transition Voltage Spectroscopy: Artefacts of the Simmons Approach". *Journal of Physics and Chemistry of Solids* **73,** 1151. doi:`10.1016/j.jpcs.2012.05.006` (2012) (see p. 138).

229. J. Chen, T. Markussen, and K. S. Thygesen. "Quantifying Transition Voltage Spectroscopy of Molecular Junctions: Ab Initio Calculations". *Physical Review B* **82,** 121412. doi:`10.1103/PhysRevB.82.121412` (2010) (see p. 138).

230. V. Mujica and M. A. Ratner. "Current–Voltage Characteristics of Tunneling Molecular Junctions for off-Resonance Injection". *Chemical Physics* **264,** 365. doi:`10.1016/S0301-0104(00)00394-3` (2001) (see p. 139).

231. S. Datta. *Electronic Transport in Mesoscopic Systems* doi:`10.1017/CBO9780511805776` (Cambridge University Press, Cambridge, 1995) (see p. 139).

232. I. R. Peterson, D. Vuillaume, and R. M. Metzger. "Analytical Model for Molecular-Scale Charge Transport". *The Journal of Physical Chemistry A* **105,** 4702. doi:`10.1021/jp0024571` (2001) (see p. 139).

233. J. C. Cuevas and E. Scheer. *Molecular Electronics: An Introduction to Theory and Experiment* doi:`10.1142/7434` (WORLD SCIENTIFIC, 2010) (see p. 139).

234. W. Hong, H. Valkenier, G. Mészáros, D. Z. Manrique, A. Mishchenko, A. Putz, P. M. García, C. J. Lambert, J. C. Hummelen, and T. Wandlowski. "An MCBJ Case Study: The Influence of π-Conjugation on the Single-Molecule Conductance at a Solid/Liquid Interface". *Beilstein Journal of Nanotechnology* **2,** 699. doi:`10.3762/bjnano.2.76` (2011) (see p. 139).

235. G. Wang, Y. Kim, S.-I. Na, Y. H. Kahng, J. Ku, S. Park, Y. H. Jang, D.-Y. Kim, and T. Lee. "Investigation of the Transition Voltage Spectra of Molecular Junctions Considering Frontier Molecular Orbitals and the Asymmetric Coupling Effect". *The Journal of Physical Chemistry C* **115,** 17979. doi:`10.1021/jp204340w` (2011) (see pp. 139, 140).

236. L. A. Zotti, T. Kirchner, J.-C. Cuevas, F. Pauly, T. Huhn, E. Scheer, and A. Erbe. "Revealing the Role of Anchoring Groups in the Electrical Conduction Through Single-Molecule Junctions". *Small* **6,** 1529. doi:`10.1002/smll.200902227` (2010) (see pp. 139, 142).

237. R. M. Metzger. "Unimolecular Electronics". *Chemical Reviews* **115,** 5056. doi:`10.1021/cr500459d` (2015) (see p. 139).

238. A. R. Garrigues, L. Yuan, L. Wang, E. R. Mucciolo, D. Thompon, E. del Barco, and C. A. Nijhuis. "A Single-Level Tunnel Model to Account for Electrical Transport through Single Molecule- and Self-Assembled Monolayer-Based Junctions". *Scientific Reports* **6,** 26517. doi:`10.1038/srep26517` (1 2016) (see p. 139).

239. G. Breit and E. Wigner. "Capture of Slow Neutrons". *Physical Review* **49,** 519. doi:`10.1103/PhysRev.49.519` (1936) (see p. 139).

240. I. Bâldea. "Revealing Molecular Orbital Gating by Transition Voltage Spectroscopy". *Chemical Physics* **377,** 15. doi:`10.1016/j.chemphys.2010.08.009` (2010) (see p. 139).

241. B. Kim, S. H. Choi, X.-Y. Zhu, and C. D. Frisbie. "Molecular Tunnel Junctions Based on π-Conjugated Oligoacene Thiols and Dithiols between Ag, Au, and Pt Contacts: Effect of Surface Linking Group and Metal Work Function". *Journal of the American Chemical Society* **133,** 19864. doi:`10.1021/ja207751w` (2011) (see p. 140).

242. D. J. Wold and C. D. Frisbie. "Fabrication and Characterization of Metal—Molecule—Metal Junctions by Conducting Probe Atomic Force Microscopy". *Journal of the American Chemical Society* **123,** 5549. doi:`10.1021/ja0101532` (2001) (see p. 140).

243. H. B. Akkerman and B. de Boer. "Electrical Conduction through Single Molecules and Self-Assembled Monolayers". *Journal of Physics: Condensed Matter* **20,** 013001. doi:`10.1088/0953-8984/20/01/013001` (2007) (see p. 140).

244. Z. Xie, I. Bâldea, C. E. Smith, Y. Wu, and C. D. Frisbie. "Experimental and Theoretical Analysis of Nanotransport in Oligophenylene Dithiol Junctions as a Function of Molecular Length and Contact Work Function". *ACS Nano* **9,** 8022. doi:`10.1021/acsnano.5b01629` (2015) (see p. 142).

245. L. A. Bumm, J. J. Arnold, M. T. Cygan, T. D. Dunbar, T. P. Burgin, L. Jones, D. L. Allara, J. M. Tour, and P. S. Weiss. "Are Single Molecular Wires Conducting?" *Science* **271,** 1705. doi:`10.1126/science.271.5256.1705` (1996) (see pp. 142, 154, 158).

246. V. Obersteiner, D. A. Egger, G. Heimel, and E. Zojer. "Impact of Collective Electrostatic Effects on Charge Transport through Molecular Monolayers". *The Journal of Physical Chemistry C* **118,** 22395. doi:`10.1021/jp5084955` (2014) (see pp. 142, 144, 159).

247. V. Obersteiner, D. A. Egger, and E. Zojer. "Impact of Anchoring Groups on Ballistic Transport: Single Molecule vs Monolayer Junctions". *The Journal of Physical Chemistry C* **119,** 21198. doi:`10.1021/acs.jpcc.5b06110` (2015) (see pp. 142, 143, 156, 159).

248. S. Y. Quek, H. J. Choi, S. G. Louie, and J. B. Neaton. "Length Dependence of Conductance in Aromatic Single-Molecule Junctions". *Nano Letters* **9,** 3949. doi:`10.1021/nl9021336` (2009) (see p. 142).

249. M. Kamenetska, S. Y. Quek, A. C. Whalley, M. L. Steigerwald, H. J. Choi, S. G. Louie, C. Nuckolls, M. S. Hybertsen, J. B. Neaton, and L. Venkataraman. "Conductance and Geometry of Pyridine-Linked Single-Molecule Junctions". *Journal of the American Chemical Society* **132,** 6817. doi:`10.1021/ja1015348` (2010) (see p. 142).

250. V. Obersteiner, G. Huhs, N. Papior, and E. Zojer. “Unconventional Current Scaling and Edge Effects for Charge Transport through Molecular Clusters”. *Nano Letters* **17**, 7350. doi:`10.1021/acs.nanolett.7b03066` (2017) (see pp. 144, 150).

251. I. Bâldea, Z. Xie, and C. Daniel Frisbie. “Uncovering a Law of Corresponding States for Electron Tunneling in Molecular Junctions”. *Nanoscale* **7**, 10465. doi:`10.1039/C5NR02225H` (2015) (see p. 148).